

*100<sup>th</sup> anniversary  
of S.A. Altshuler*

Kazan Federal University  
Zavoiskii Physical-Technical Institute  
Government and President of Tatarstan Republic  
Bruker Ltd (Moscow)  
Russian Academy of Sciences  
Russian Foundation for Basic Reserch

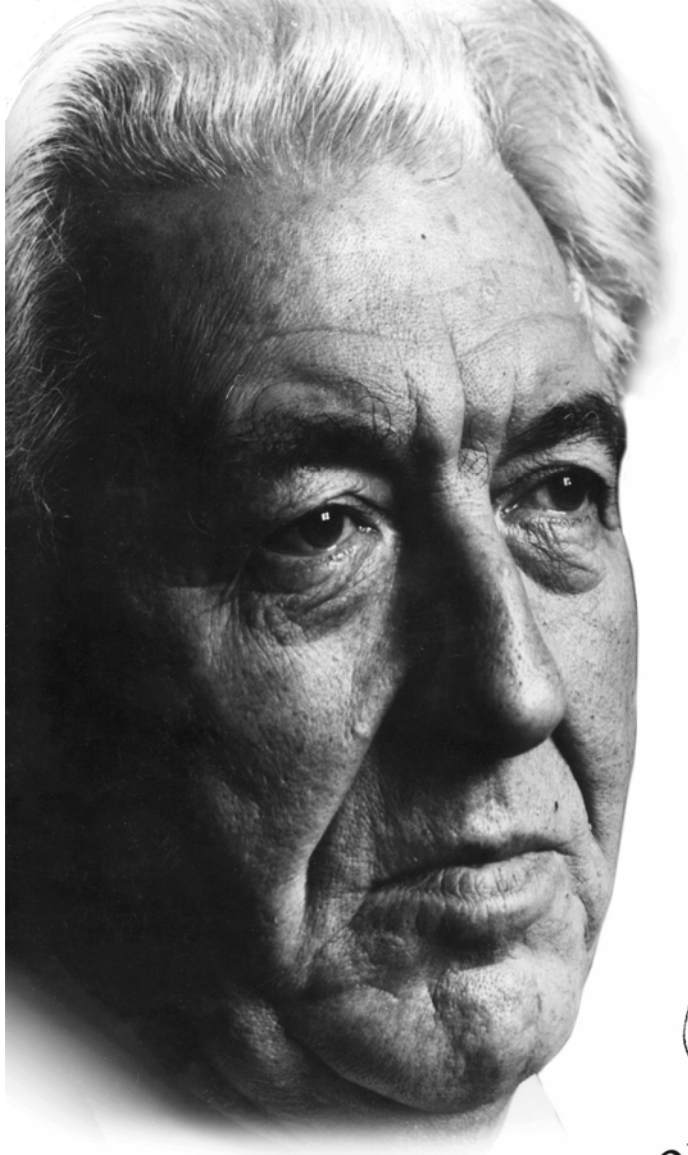
**ACTUAL PROBLEMS  
OF MAGNETIC RESONANCE  
AND ITS APPLICATION**

**XIV International  
Youth Scientific School**



**Program  
Proceedings**

**Kazan  
20 - 25 June 2011**



*C. DeGroot*

100<sup>th</sup> anniversary  
of S. A. Altshuler

Kazan Federal University  
Zavoiskii Physical-Technical Institute  
Government and President of Tatarstan Republic  
Bruker Ltd (Moscow)  
Russian Academy of Sciences  
Russian Foundation for Basic Reserch

# **ACTUAL PROBLEMS OF MAGNETIC RESONANCE AND ITS APPLICATION**

**XIV International Youth Scientific School**

## **Program Proceedings**

**Kazan  
20 – 25 June 2011**



**KAZAN UNIVERSITY  
2011**

Proceedings of the XIV International Youth Scientific School “Actual problems of magnetic resonance and its application”, 20 – 25 June 2011, Kazan. Edited by professor M.S. Tagirov (Kazan Federal University) and professor V.A. Zhikharev (Kazan State Technological University). – Kazan: Kazan Federal (Volga Region) University, 2011. – 138 p.

The reports of young scientists submitted on XIV International Youth Scientific School “Actual problems of magnetic resonance and its application” carry out by Kazan Federal (Volga Region) University and Zavoiskii Physical-Technical Institute are included in the present collection.

### **The administration of School**

Professor M.S. Tagirov (KSU, Kazan) — rector  
Professor V.A. Zhikharev (KSTU, Kazan) — vice-rector  
V.K. Voronkova (KFTI RAS, Kazan) — scientific secretary  
I.P. Volodina (KSU, Kazan) — secretary

### **The program committee**

The chairman  
Professor V.A. Atsarkin (IREE, Moscow)

#### Committee members

Professor A.V. Aganov (KSU, Kazan)  
Professor B.I. Kochelaev (KSU, Kazan)  
Professor I.V. Ovchinnikov (KFTI RAS, Kazan)  
Professor K.M. Salikhov (KFTI RAS, Kazan)

### **The organizing committee of School’2011**

M.S. Tagirov, V.A. Zhikharev, I.P. Volodina, I.G. Motygullin  
A.V. Klochkov, M.P. Rodionova, A.A. Rodionov,  
E.M. Alakshin, V.V. Kuzmin, R.R. Gazizullin, B.V. Yavkin

**ISBN 978-5-98180-925-5**

© **Authors Collective, 2011**  
© **Kazan Federal University, 2011**

# PROGRAM

## Program

### Monday, June 20

Zavoiski Lecture Hall (3<sup>rd</sup> Physical Auditorium)

9:30 – 9:45 **Opening Ceremony of School-2011**

#### Oral Session

Zavoiski Lecture Hall (3<sup>rd</sup> Physical Auditorium)

9:45 – 10:00 **B.V. Yavkin**, “Self-organization of sintered detonation nanodiamonds as revealed by high-frequency EPR spectroscopy”

10:00 – 10:15 **V.V. Kuzmin**, “Low temperature adsorption of <sup>3</sup>He on silica aerogel surface and its influence on <sup>3</sup>He spin kinetics”

10:15 – 10:30 **T.R. Safin**, “The experimental technique for observing magnon BEC”

10:30 – 10:45 **R.R. Gazizulin**, “The observation of magnon BEC in solid antiferromagnet CsMnF<sub>3</sub>”

10:45 – 11:00 **A.A. Ershova**, “Super-Hyperfine Structure of EPR Spectra of Ce<sup>3+</sup>, Nd<sup>3+</sup> and U<sup>3+</sup> Ions in Double Fluorides LiRF<sub>4</sub> (R=Y, Lu, Tm)”

11:00 – 11:15 **D.T. Sitdikov**, “Multifrequency EPR of Asphaltenes”

11:15 – 11:30 **Coffee break**

11:30 – 11:45 **D.D. Gabidullin**, “Radiofrequency synthesizer design for magnetic resonance imaging system’s spectrometer”

11:45 – 12:00 **N.A. Krylatykh**, “Simulation of Magnetic Resonance Imaging Experiments”

12:00 – 12:15 **T. Zinkevich**, “General R<sub>1</sub>/R<sub>1ρ</sub> equations for the NMR relaxation data analysis in solids”

12:15 – 12:30 **A.Y. Manin**, “Obtaining spatial structure of cyclosporine (Csa) in chloroform using 2D NMR”

12:30 – 12:45 **V. Sahin**, “ESR Research of High-temperature Superconductor Bi<sub>2</sub>Sr<sub>2</sub>Ca<sub>1-x</sub>Y<sub>x</sub>Cu<sub>2</sub>O<sub>8</sub>”

12:45 – 13:00 **E.I. Baibekov**, “Theory of electronuclear cross-relaxation in transient regime of EPR”

13:00 – 14:30 **Lunch**

14:30 – 14:45 **A.M. Sabitova**, “Synthesis of nanosized PrF<sub>3</sub> powders and their low temperature magnetism study”

14:45 – 15:00 **L.A. Batalova**, “<sup>59</sup>Co ZFNMR study of YBaCo<sub>2</sub>O<sub>5+x</sub> compound”

15:00 – 15:15 **T.A. Platova**, “<sup>59</sup>Co NQR study of Na<sub>0.71</sub>CoO<sub>2</sub> compound”

15:15 – 15:30 **N.S. Saenko**, “Electronic and magnetic properties of activated carbon fibers and carbon nanofibers: ESR and magnetic susceptibility data”

15:30 – 15:45 **Z.N. Volkova**, “Magnetic polarons in CaMnO<sub>3-x</sub>: the <sup>17</sup>O NMR study”

15:45 – 16:00 **A.G. Smolnikov**, “Local magnetic susceptibility in the multiferroic CuCrO<sub>2</sub>: <sup>63,65</sup>Cu NMR study”

16:00 – 16:15 **Coffee break**

16:15 – 16:30 **V.I. Klimentiev**, “Phototransformation of acetylene derivatives of lappaconitine studied by NMR and CIDNP techniques”

## PROGRAM

- 16:30 – 16:45 **O.Yu. Gluschenko**, “NMR study of cholesterol complexes with glycyrrhizic acid”
- 16:45 – 17:00 **A.I. Dmitriev**, “Electron Spin Resonance in Heterostructures with a InGaAs quantum well and Mn  $\delta$ -Doped GaAs Layer”
- 17:00 – 17:15 **A.V. Fokin**, “Structural transition in lanthanum gallate and transformation of the fine structure of the EPR spectrum of a Gd<sup>3+</sup> impurity center”
- 17:15 – 17:30 **L.V. Khaidarshina**, “Diagnostics of radiating ions-radicals in bioorganic materials using a method of an electronic paramagnetic resonance at Q-range. The spectra shapes”
- 17:30 – 17:45 **N.N. Efimov**, “High-frequency EPR of the polynuclear compounds of Cu(II)”

### **Tuesday, June 21**

#### **Oral Session**

Zavoiski Lecture Hall (3<sup>rd</sup> Physical Auditorium)

- 9:00 – 9:15 **T.S. Yankova**, “Spin probe orientation distribution functions in aligned nematic liquid crystal”
- 9:15 – 9:30 **O.A. Babanova**, “NMR study of ball-milled TiH<sub>2</sub> with C, B, and BN additives”
- 9:30 – 9:45 **A.N. Ivachev**, “Paramagnetic resonance of ions Pb<sup>3+</sup> in ferroelectric Pb<sub>5</sub>Ge<sub>3</sub>O<sub>11</sub>”
- 9:45 – 10:00 **R.A. Novikov**, “NMR studies of mechanisms and stereochemistry of new dimerization and cascade oligomerization reactions of dimethyl 2-phenylcyclopropan-1,1-dicarboxylate catalyzed by Lewis acids”

Main building, University Assembly Hall

11:00 – 11:10 **Opening Ceremony of ALT100**

#### **Lectures**

Main building, University Assembly Hall

- 11:10 – 11:40 **B.I. Kochelaev**, “Semen A. Altshuler: scientist, mentor and teacher”
- 11:40 – 12:10 **A.A. Manenkov**, “EPR and development of Quantum Electronics”
- 12:10 – 12:55 **ALT100 Oral Session**
- 13:00 – 13:30 **Excursion to Kazan Federal University museum**

13:30 – 15:30 **Lunch**

#### **Lectures**

Zavoiski Lecture Hall (3<sup>rd</sup> Physical Auditorium)

- 15:30 – 16:00 **V.S. Zapasskii**, “Spin Noise Spectroscopy”
- 16:00 – 16:30 **M.N. Popova**, “High-resolution spectroscopy of hyperfine interactions in rare earth doped crystals”
- 16:30 – 17:10 **ALT100 Oral Session**
- 17:10 – 17:30 **Coffee break**
- 17:30 – 18:30 **ALT100 Oral Session**

## PROGRAM

18:30 – 20:30 **Welcome party**

### **Wednesday, June 22**

#### **Lectures**

Altshuler Lecture Hall (1<sup>st</sup> Physical Auditorium)

9:30 – 10:00 **H. Keller**, “Probing fundamental properties of high-temperature superconductors with positive muons”

10:00 – 10:30 **A. Shengelaya**, “Spin, Charge and Lattice dynamics in copper and iron based high-TC superconductors as revealed by EPR”

10:30 – 11:00 **T. Herrmannsdoerfer**, “Coexistence of ferromagnetism and superconductivity in single-phase Bi<sub>3</sub>Ni nanostructures”

11:00 – 11:20 **Coffee break**

11:20 – 11:50 **K. Baberschke**, “Ferromagnetic resonance in nanostructures, rediscovering its roots in paramagnetic resonance”

11:50 – 12:20 **A. Bussmann-Holder**, “Soft-mode magnon coupling in magneto-electric EuTiO<sub>3</sub>”

12:20 – 13:00 **ALT100 Oral Session**

13:00 – 14:30 **Lunch**

#### **Lectures**

Altshuler Lecture Hall (1<sup>st</sup> Physical Auditorium)

14:30 – 15:00 **V.F. Tarasov**, “Electron quadrupole spin resonance of non-Kramers chromium impurity centers in synthetic forsterite”

15:00 – 16:00 **ALT100 Oral Session**

#### **Lectures**

Altshuler Lecture Hall (1<sup>st</sup> Physical Auditorium)

16:00 – 16:30 **V.A. Ulanov**, “EPR study of iron paramagnetic clusters in the barium fluoride crystals”

16:30 – 21:30 **Volga cruise**

### **Thursday, June 23**

#### **Lectures**

Altshuler Lecture Hall (1<sup>st</sup> Physical Auditorium)

9:30 – 10:00 **Yu.M. Bunkov**, “Magnon Bose-Einstein condensation, new results”

10:00 – 10:30 **D.A. Tayurskii**, “Magnetic relaxation of normal liquid <sup>3</sup>He inside nanoporous media: effects of confinement and inhomogeneous absorption potential”

10:30 – 11:00 **B. Barbara**, “Quantum magnetism of large spins: from relaxation to coherence”

11:00 – 11:20 **Coffee break**

## PROGRAM

11:20 – 11:50 **V.A. Atsarkin**, “Dynamic nuclear polarization: yesterday, today, and tomorrow”

11:50 – 12:20 **H. Suzuki**, “Hyperfine enhanced nuclear magnetism and lattice vibrations”

12:20 – 13:00 **ALT100 Oral Session**

13:00 – 14:30 **Lunch**

14:30 – 16:10 **ALT100 Oral Session**

16:10 – 16:30 **Coffee break**

### Lectures

Altshuler Lecture Hall (1<sup>st</sup> Physical Auditorium)

16:30 – 17:00 **A.I. Smirnov**, “Magnetic resonance of spin excitations in quantum magnets”

17:00 – 17:30 **S. Zvyagin**, “High-field ESR in low-dimensional spin systems”

### Oral Session

Altshuler Lecture Hall (1<sup>st</sup> Physical Auditorium)

17:30 – 17:50 **V.N. Glazkov**, “ESR study of the spin-gap magnet PHCC: magnetic resonance of the S=1 quasiparticles in the effective crystal field”

18:30 – 20:30 **Opera**

## Friday, June 24

### Lectures

Altshuler Lecture Hall (1<sup>st</sup> Physical Auditorium)

9:30 – 10:00 **L.R. Tagirov**, “Ferromagnetic resonance – a powerful tool to characterize magnetic heterostructures”

10:00 – 10:30 **F. Borsa**, “Static and Dynamic Properties of Molecular Nanomagnets Investigated by NMR”

10:30 – 11:00 **B. Tsukerblat**, “The nanoscopic spin frustrated molecular magnet V<sub>15</sub>: EPR and spin-phonon relaxation”

11:00 – 11:20 **Coffee break**

11:20 – 11:50 **S. Vasiliev**, “Magnetic Resonance in a Quantum Gas of Atomic Hydrogen”

11:50 – 12:10 **ALT100 Oral Session**

### Oral Session

Altshuler Lecture Hall (1<sup>st</sup> Physical Auditorium)

12:10 – 12:30 **S. Bertaina**, “Multiple quantum Rabi oscillations in quasi-harmonic high spin system”

### Lectures

Altshuler Lecture Hall (1<sup>st</sup> Physical Auditorium)

12:30 – 13:00 **F.S. Dzheparov**, “Spin relaxation in disordered media”

## PROGRAM

13:00 – 14:30 **Lunch**

### Lectures

Altshuler Lecture Hall (1<sup>st</sup> Physical Auditorium)

14:30 – 15:00 **E.B. Fel'dman**, “Multiple quantum NMR dynamics in nanopore materials”

### Oral Session

Altshuler Lecture Hall (1<sup>st</sup> Physical Auditorium)

15:00 – 15:20 **A.N. Pyrkov**, “The effect of spin-lattice relaxation on the intensities of multiple-quantum NMR coherences and entanglement in solids”

15:20 – 16:00 **ALT100 Oral Session**

16:00 – 16:20 **Coffee break**

16:20 – 17:20 **ALT100 Oral Session**

17:30 – 19:30 **Poster Session**

**P.A. Agzamova**, “Hyperfine interactions in (La,Y)TiO<sub>3</sub> system”

**A.A. Konakov**, “Temperature dependence of the conduction electron g-factor in silicon”

**K. Tadyszak**, “EPR study of spin relaxation in the single-layer graphene”

**V.V. Ogloblichev**, “<sup>51</sup>V NMR Study of the Multiferroic Ni<sub>3</sub>V<sub>2</sub>O<sub>8</sub>”

**Ya.V. Tkachev**, “EPR Meets MD: Dynamics of Myosin Motor Domain”

### Saturday, June 25

Altshuler Lecture Hall (1<sup>st</sup> Physical Auditorium)

9:30 – 11:10 **ALT100 Oral Session**

11:10 – 11:30 **Coffee break**

11:30 – 12:30 **ALT100 Oral Session**

12:30 – 13:00 **Closing Ceremony of School-2011 and ALT100**

13:00 – 14:30 **Lunch**

## Self-organization of sintered detonation nanodiamonds as revealed by high-frequency EPR spectroscopy

P.G. Baranov<sup>1</sup>, A.A. Soltamova<sup>1</sup>, I.V. Il'in<sup>1</sup>, F.M. Shakhov<sup>1</sup>, S.V. Kidalov<sup>1</sup>, A.Y. Vul'<sup>1</sup>,  
B.V. Yavkin<sup>2</sup>, G.V. Mamin<sup>2</sup>, S.B. Orlinskii<sup>2</sup>, N.I. Silkin<sup>2</sup>

<sup>1</sup>Ioffe Physical-Technical Institute, St. Petersburg 194021, Russia

<sup>2</sup>Kazan (Volga Region) Federal University, Kazan, 420008, Russia

e-mail: boris.yavkin@gmail.com

### Introduction

Nanodiamonds of detonation origin attract considerable interest due to their fascinating properties and following applications in technology [1], medicine, magnetic field sensing, quantum informatics, optics [2]. In many of these applications defects and impurities in diamond playing crucial role, urging for new methods of synthesis with pre-defined amount and type of defects. Considering nitrogen-vacancy (NV) defect center, up to now there are two major way of production diamond with these defects: CVD and HPHT, and both of them required post-synthesis irradiation under intense electron or ion beam followed by annealing at 700–800K, which is not very efficient for literally nanometer-sized particles [3]. Nanodiamonds of detonation origin are possibly able to overcome this obstacle because sufficient amount of vacancies are formed during detonation procedure and nitrogen atoms are also embedded into diamond lattice because of nitrogen-containing explosives.

### Materials and methods

Nanodiamonds of detonation origin were produced by detonation of TNT + RDX explosive mixture in special detonation chamber. Size of primary particles is 4-5nm, but these particles are strongly agglomerated in complexes of 100–200 nm [4]. For sintering procedure nanodiamond powder was placed into chamber for 11s under pressure of 6GPa and temperature of 800 K [3]. After sintering XRD diffraction pattern was analyzed and size of primary particles was calculated to be 5.8 nm.

Samples were studied by high-frequency (94 GHz) EPR spectroscopy. Spectra were recorded at room temperature on Bruker E 680 commercial spectrometer, standard procedures for acquiring CW and pulsed EPR were used.

### Results

EPR spectra were recorded for both initial and sintered nanodiamond powder. For initial nanodiamond powder EPR spectrum consists of two signals from different paramagnetic centers. One central line with  $g=2.0028$  originates from surface paramagnetic center and three other lines (due to hyperfine interaction with  $^{14}\text{N}$ , nuclear spin  $I=1$ ) represent powder pattern of single substitutional nitrogen impurity  $N_S^0$  with parameters  $g_{\parallel} = g_{\perp} = 2.0024$ ,  $A_{\parallel} = 40.7$  G,  $A_{\perp} = 29.0$  G [4].

Surprisingly enough, for sintered nanodiamond we have clearly seen perfect crystalline patterns. Analysis of experimental spectra led us to conclusion that we are dealing with three types of paramagnetic centers: surface paramagnetic centers with  $g = 2.0028$ ,  $N_S^0$  with parameters  $g_{\parallel} = g_{\perp} = 2.0024$ ,  $A_{\parallel} = 40.7$  G,  $A_{\perp} = 29.0$  G and nitrogen-vacancy defect with parameters  $g = 2.0028$ ,  $D = 2.88$  GHz. All of these parameters for  $N_S^0$  and NV defect are in

good agreement with previously published for bulk diamond [3]. Both N and NV EPR spectra demonstrate angular dependence which originates from crystalline sample. Analysis of angular dependencies was performed based on Hamiltonian for NV defects

$$H = g\mu_B\mathbf{BS} + D\left[S_z^2 - 1/3S(S+1)\right]. \quad (1)$$

Approximation allowed us to determine Hamiltonian parameters for NV, which is in good agreement with previously published results for NV centers in bulk diamond.

### Conclusion

Single-crystal angular dependencies as revealed by EPR spectra clearly show self-organization processes of detonation nanodiamond while sintering procedure. Temperature dependence of nanodiamond self-organization was clearly shown. New method of NV defects creation is promising because of price and ease compare to HPHT or CVD methods.

### References

- [1] Ultrananocrystalline Diamond. Synthesis, Properties, and Applications, *edited by O.A. Shendorova and D.M. Gruen, William Andrew Publishing, Norwich, New York, U.S.A., 2006.*
- [2] P.G. Baranov, A.A. Soltamova, D.O. Tolmachev, N.G. Romanov, R.A. Babunts, F.M. Shakhov, S.V. Kidalov, A.Y. Vul', G.V. Mamin, S.B. Orlinskii, N.I. Silkin, *Submitted to Small, 2011.*
- [3] A.A. Soltamova, I.V. Il'in, F.M. Shakhov, S.V. Kidalov, A.Y. Vul', B.V. Yavkin, G.V. Mamin, S.B. Orlinskii, P.G. Baranov, *JETP Letters* **2010**, *92*, 106-110
- [4] S. B. Orlinskii, R. S. Bogomolov, A. M. Kiyamova, B. V. Yavkin, G. M. Mamin, S. Turner, G. Van Tendeloo, A. Shiryaev, I. I. Vlasov and O. Shenderova, *Nanoscience and Nanotechnology Letters*, Vol. 3, 1–5, **2011**

## Low temperature adsorption of $^3\text{He}$ on silica aerogel surface and its influence on $^3\text{He}$ spin kinetics

E.M. Alakshin<sup>1</sup>, R.R. Gazizulin<sup>1</sup>, A.V. Klochkov<sup>1</sup>, V.V. Kuzmin<sup>1</sup>, M.S. Tagirov<sup>1</sup>,  
D.A. Tayurskii<sup>1</sup>, N. Mulders<sup>2</sup>

<sup>1</sup>Institute of Physics, Kazan (Volga region) Federal University, Kazan, Russia

<sup>2</sup>University of Delaware, Newark, Delaware, USA

e-mail: slava625@yandex.ru

Supreme role of adsorbed  $^3\text{He}$  layer on an aerogel surface in processes of nuclear magnetic relaxation was studied earlier [1, 2]. The spin kinetics of  $^3\text{He}$  in the silica aerogel was studied above the Fermi temperature of liquid  $^3\text{He}$ . The magnetic relaxation times  $T_1$  and  $T_2$  for adsorbed, gaseous, and liquid  $^3\text{He}$  in the 95 % porosity aerogel at a temperature of 1.5 K were obtained by means of pulse nuclear magnetic resonance techniques. It was found that  $T_1$  in all three cases is proportional to the frequency, whereas  $T_2$  is frequency independent. It was shown that the longitudinal relaxation proceeds due to the exchange motion in the solid adsorbed  $^3\text{He}$  film. The intrinsic relaxation mechanisms in the liquid and gas phases are much weaker than the relaxation through the adsorbed surface layer. A theoretical model of relaxation in the adsorbed  $^3\text{He}$  layer, taking into account the filamentary structure of the aerogel, has been proposed.

At present work we report experimental data on heterogeneous adsorption potential of  $^3\text{He}$  in two types of silica aerogels: powder and bulk and its influence on magnetic relaxation of  $^3\text{He}$ .

The longitudinal magnetization relaxation time  $T_1$  of  $^3\text{He}$  was measured by the saturation recovery method using FID signal. The spin-spin relaxation time  $T_2$  was measured by Hahn method. The hand made pulse NMR spectrometer has been used (frequency range 3 – 50 MHz). The pulse NMR spectrometer is equipped by resistive electrical magnet with a magnetic field strength up to 1 T. The particles size of powder aerogel was obtained by Transmission Electron Microscopy and is about 1 – 10 mkm. Bulk aerogel sample (95 %) has filamentary structure with strand diameter about 3 – 5 nm.

Adsorption isotherms of  $^3\text{He}$  in aerogel are presented in fig.1. At the temperature  $T=4.2$  K small portion of gaseous  $^3\text{He}$  was introduced into the cell, which was further thermalized during 30 min and equilibrium pressure was measured [3]. After each step a new portion of gaseous  $^3\text{He}$  was introduced. The adsorption capacity of complete layer was measured and was about 5 cm<sup>3</sup> for bulk aerogel and 12 cm<sup>3</sup> STP for powder aerogel.

In previous works [1,2] the spin kinetics of  $^3\text{He}$  in bulk silica aerogel was studied above the Fermi temperature of liquid  $^3\text{He}$  for complete adsorbed layer. In the fig.2 experimental data of  $^3\text{He}$  nuclear longitudinal relaxation time  $T_1$  for incomplete adsorbed layer ( $V_{\text{ads}}=0.8$  cm<sup>3</sup> STP for bulk aerogel and 2 cm<sup>3</sup> STP for powder aerogel) are presented as a function of the temperature. The adsorbed layer was prepared at two different temperatures (1.5 K and 4.2 K) and as can be seen from fig.2 the behavior is completely different. It can be explained by taking into account heterogeneity of adsorption potential of  $^3\text{He}$  on an aerogel surface. The adsorption of  $^3\text{He}$  at different temperatures in this case will fill the surface different manner.

The existence of strong temperature dependence of  $T_1$  for  $^3\text{He}$  adsorbed on aerogel surface shows that in case of incomplete adsorbed  $^3\text{He}$  layer fast thermal motion and

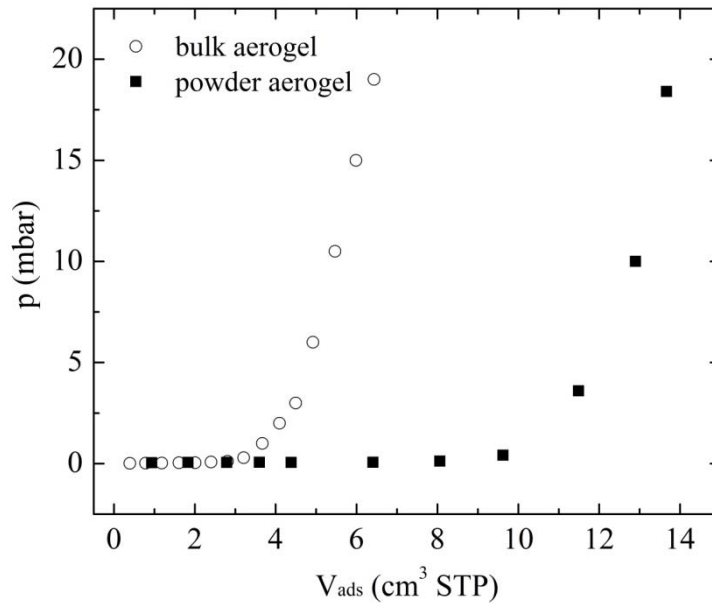


**Fig.1.** Adsorption isotherms of  $^3\text{He}$  in bulk and powder aerogels at temperature 4.2 K.

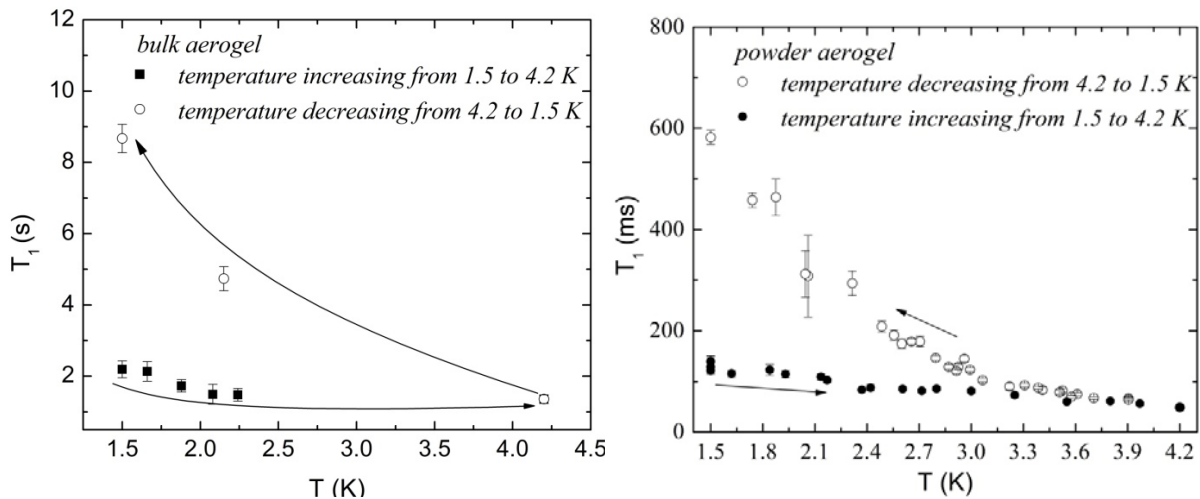


**Fig.2.** The temperature dependences of  $^3\text{He}$  nuclear longitudinal relaxation time  $T_1$  for incomplete adsorbed layer,  $f_0=20$  MHz. The adsorbed layer was prepared at two different temperatures (1.5 K and 4.2 K).

redistribution of  $^3\text{He}$  molecules on the aerogel surface play significant role in nuclear magnetic relaxation of  $^3\text{He}$ .

For obtaining  $^3\text{He}$  adsorption data and calculation binding energies of  $^3\text{He}$  on the aerogel surface following method was used. At room temperature whole gas handling system together with NMR cell was filled by gaseous  $^3\text{He}$  in amount of  $V(^3\text{He}) = 12 \text{ cm}^3 \text{ STP}$  in case of powder aerogel and  $V(^3\text{He}) = 4.7 \text{ cm}^3 \text{ STP}$  in case of bulk aerogel. The whole gas handling system consists of “cold part” (capillary in cryostat and NMR cell) and “hot part” (external capillary, calibrating volume and a pressure gauge). The amount of  $^3\text{He}$  was chosen, taking into account data from fig.1. After equilibrium pressure in whole system was achieved the cryostat begun cool down slowly (1 K/min at temperatures above 10 K and 0.05 K/min at low temperatures), using helium flow system. The cooling process leads to pressure decreasing in the system because of two processes: gas cooling in a “cold part” and adsorption on the aerogel surface. The amount of adsorbed  $^3\text{He}$  was calculated using:

$$M_{ads} = M_0 - M_{hot} - M_{cold}, \quad (1)$$

where  $M_0$  — amount of  $^3\text{He}$  in the whole system,  $M_{hot}$  — amount of gaseous  $^3\text{He}$  in the “hot part” of the system,  $M_{cold}$  — amount of gaseous  $^3\text{He}$  in the “cold part” of the system.  $M_{hot}$  and  $M_{cold}$  can be estimated using:

$$M_{hot} = M_0 \cdot p(b/a), \quad (2)$$

$$M_{cold} = M_0 \cdot p/(b \cdot T), \quad (3)$$

where  $a, b$  — fitting parameters for high temperature  $p(T)$  dependence,  $p$  — pressure,  $T$  — temperature. The experimental data after those corrections are presented in fig.3.

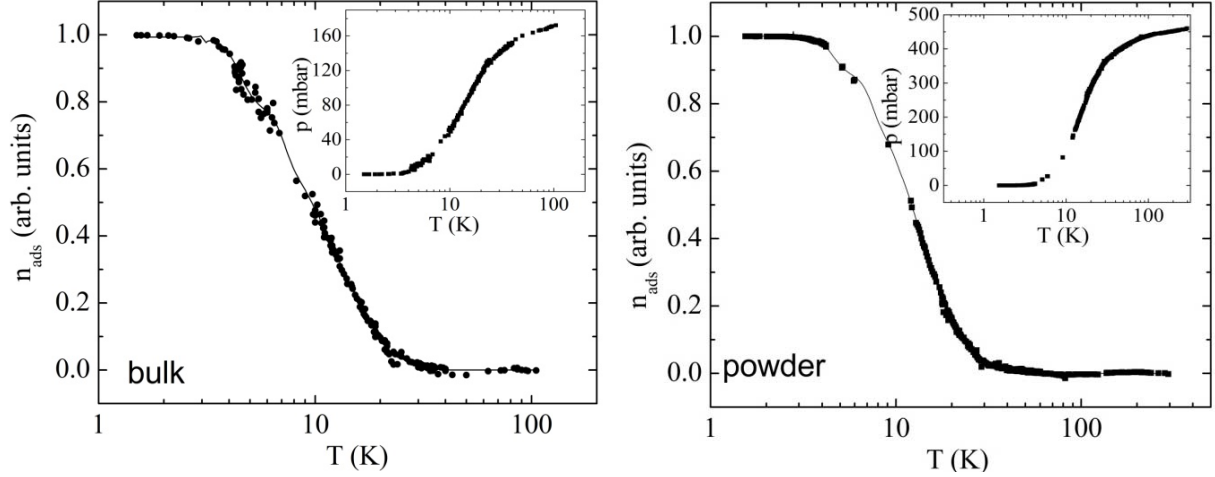


**Fig.3.** Temperature dependences of  $^3\text{He}$  amount adsorbed in aerogel: dots — experimental data, lines — Langmuir model (see text). On inserts shown the  $p(T)$  dependences

The binding energies can be estimated from Langmuir model [4] by eq.:

$$\Theta = p/(p^* + p), \quad (4)$$

where  $\Theta$  — degree of layer filling

$$p^* = \alpha T^{5/2} / \langle \exp(-H^S/kT) \rangle, \quad (5)$$

where  $\alpha$  — constant,  $T$  — temperature,  $H^S$  — Hamiltonian of  $^3\text{He}$  interaction with an aerogel surface. In the case of low temperatures it can be rewritten as:

$$\langle \exp(-H^S/kT) \rangle \approx \exp(-\varepsilon_m/kT) \quad (6)$$

where  $\varepsilon_m$  —  $^3\text{He}$  binding energy on aerogel surface. The experimental data on fig.3 was fitted by twenty processes like (6) with binding energy lies on 45 – 700 K (fig.4). As can be see from fig.4 both distributions are similar and describes by exponential decay with characteristic parameter  $130 \pm 11$  K.

Considering all presented experimental data, significant influence of aerogel surface heterogeneity on the processes of  $^3\text{He}$  nuclear magnetic relaxation at temperatures 1.5 – 4.2 K was described. For instance, this influence appears in differences of  $^3\text{He}$   $T_1$  nuclear relaxation times for small portion of  $^3\text{He}$ , adsorbed at different temperatures. Binding energy data of  $^3\text{He}$  on the surface of powder silica aerogel obtained experimentally and binding energy lies in the range 60 – 250 K.

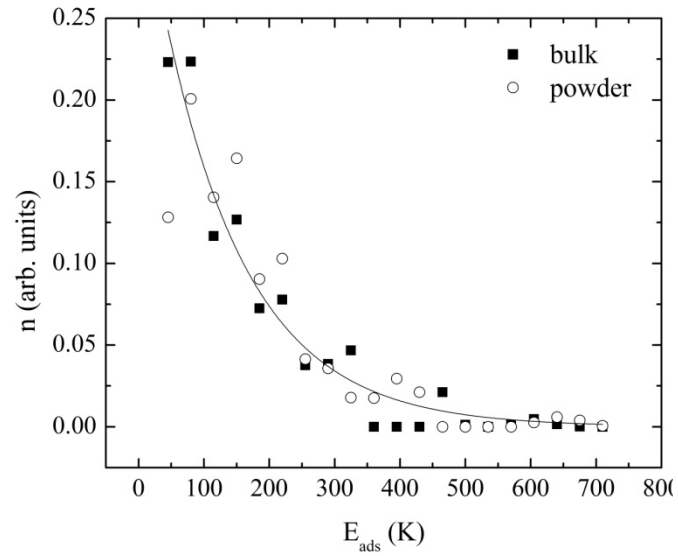


**Fig.4.** Binding energy distribution of  $^3\text{He}$  in two types of aerogel

### Acknowledgments

This work is partially supported by Russian Fund for Basic Research (grant N 09-02-01253).

### References

- [1] A.V. Klochkov, V.V. Kuzmin, K.R. Safiullin et al., JETP Lett., **88**, 823 (2008).
- [2] A. Klochkov, V. Kuzmin, K. Safiullin et al., J. of Phys.: CS, **150**, 032043 (2009).
- [3] E.M. Alakshin, R.R. Gazizulin, A.V. Klochkov et al., JETP Lett., **93**, 242 (2011).
- [4] W.A. Steele, J. Low Temp. Phys., **3**, 257 (1970).

## The experimental technique for observing magnon BEC

T.R. Safin<sup>1</sup>, E.M. Alakshin<sup>1</sup>, Yu.M. Bunkov<sup>2</sup>, A.V. Klochkov<sup>1</sup>, R.R. Gazizulin<sup>1</sup>,  
V.V. Kuzmin<sup>1</sup>, M.S. Tagirov<sup>1</sup>

<sup>1</sup>Kazan (Volga region) Federal University, Kazan, Russia,

<sup>2</sup>Institut Neel, Grenoble, France

e-mail: imfador@gmail.com

The magnon BEC was predicted for magnetically ordered matters such as CsMnF<sub>3</sub> [1]. The effect of NMR in magnetically ordered matters on nucleus of the magnetic ion has features, that imposes specific requirements on the measuring equipment[2]. The main feature is weak dependence on the frequencies of NMR ( $\nu_n$ ) from external field, therefore it is necessary to use the tuning of spectrometer frequency. Under this contradiction eventuates between the requirement for broadband resonant circuit with the sample (for transmission frequency) and its quality factor (for the increasing sensitivity) [3].

For the experimental observation such effect it is necessary to use frequencies about 500 – 600 MHz. For this reason was used «split-ring» resonator [4, 5] that shows high filling factor and quality factor (fig.1). And it also gives higher filling factor than spiral resonator does.

The analysis of resonator performed on scheme that is shown on the fig.2



**Fig.1.** «Split collar» resonator

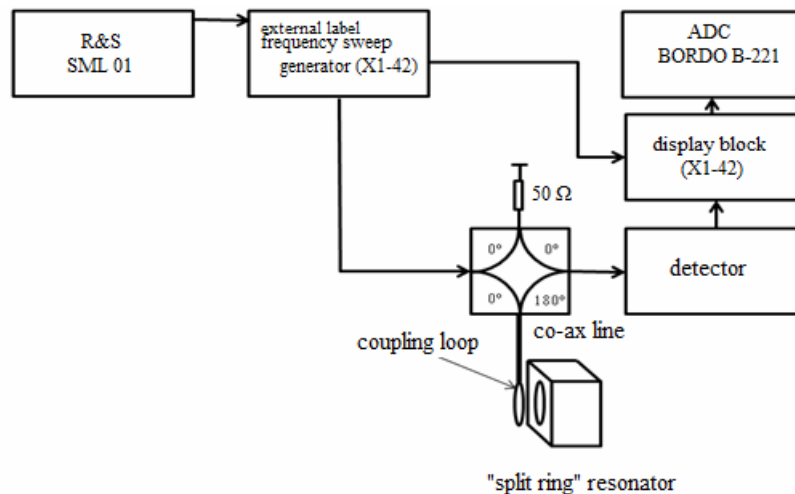


**Fig.2.** Scheme of measuring amplitude-frequency response of «split collar» resonator.

The reconciliation of a resonator on  $50 \Omega$  was done by fine changing of the length between them and coupling loop. An acceptable reconciliation was observed on the spacing about 2 mm. Such resonator at  $T=300$  K had the quality factor 139 and the resonance frequency 559 MHz, at  $T=77$  K it had the quality factor 872 and the center frequency 523 MHz.

In first case it was required to observe continuous NMR. The scheme is represented in fig.3.

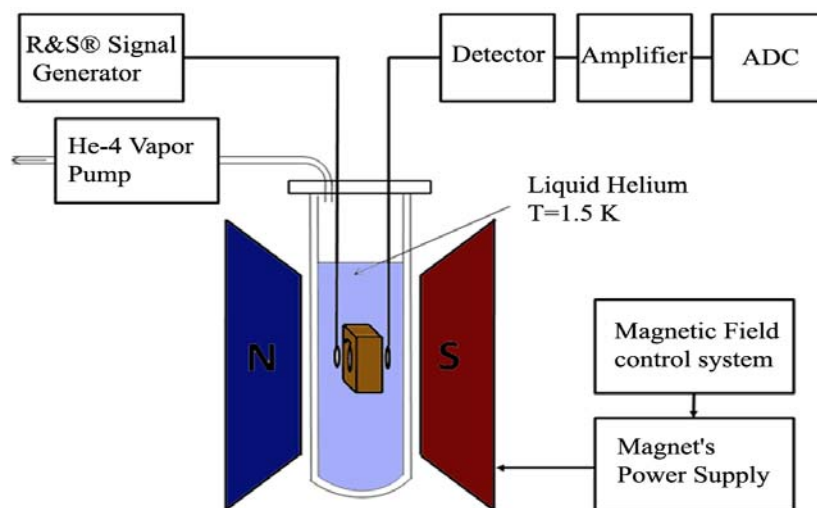


**Fig.3.** Detecting signal is a sum of adsorption and dispersion, by cable tweaking we can tune the phase to see “almost” adsorption signal in the crystal

The experiment was done at the temperature  $T=1.5$  K, which was achieved by helium bath pumping. The signal from R&S Signal Generator was filed to a transmitting coupling loop and was obtained on the receiver coupling loop. After that the signal is detected by detector and then after amplifying it proceed to ADC. The magnetic field sweeping was executed by magnetic field control system. Detecting signal is a sum of adsorption and dispersion, by cable tweaking we can tune the phase to see “almost” adsorption signal in the crystal.

Pulse NMR experiment was done by spectrometer, which is shown in fig.4.

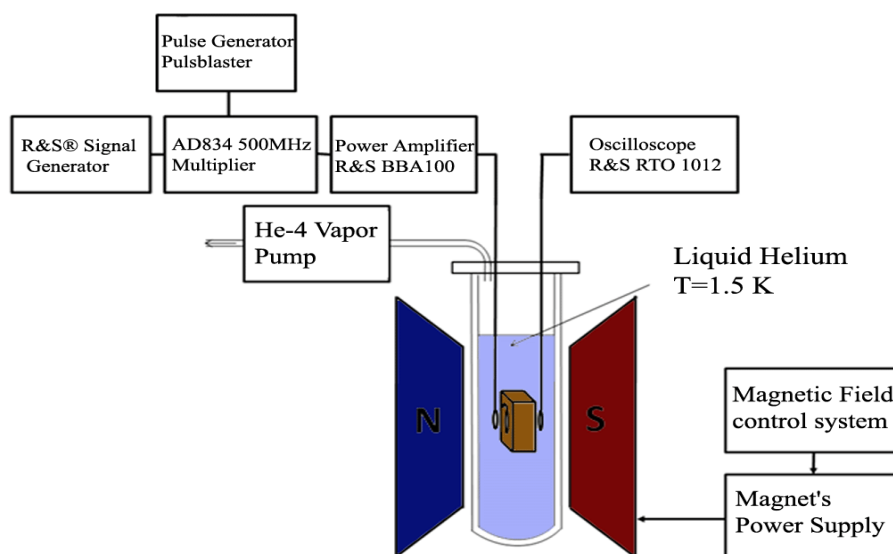


**Fig.4.** Pulse NMR Spectrometer

In this scheme we have used AD834 500MHz Multiplier for forming video pulses. On the one input of multiplier the high frequency signal from R&S Signal Generator was submitted. On the second the pulses from Pulse Generator PulseBlaster PB32-16k, SpinCore Technologies Inc., was submitted.

The AD834 is a monolithic, laser-trimmed four-quadrant analog multiplier intended for use in high frequency applications, with a transconductance bandwidth ( $R_L = 50 \Omega$ ) in excess of 500 MHz from either of the differential voltage inputs. In multiplier modes, the typical total full-scale error is 0.5%. Performance is relatively insensitive to temperature and supply variations due to the use of stable biasing based on a band gap reference generator and other design features.

Fig.5 is a functional equivalent of the AD834. There are three differential signal interfaces: the two voltage inputs ( $X = X1 - X2$  and  $Y = Y1 - Y2$ ), and the current output ( $W$ ) which flows in the direction shown in fig.5 when  $X$  and  $Y$  are positive. The outputs ( $W1$  and  $W2$ ) each have a standing current of typically 8.5mA.

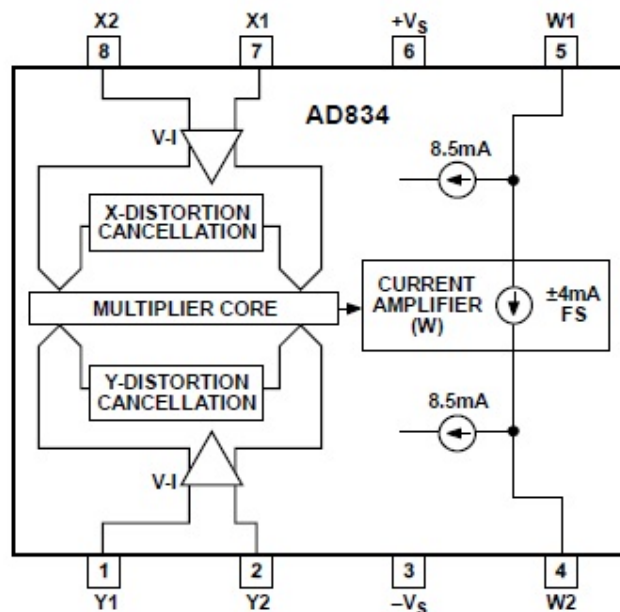


Fig.5. Functional Block Diagram

### Acknowledges

This is supported by the Ministry of Education and Science of the Russian Federation (FTP "Scientific and scientific-pedagogical personnel of the innovative Russia" contract N 02.740.11.5217)

### References

- [1] Yu.M. Bunkov, UFN, 180, 884 ; Physics–Uspekhi, **53**:8, 848–853(2010).
- [2] Turov E.A., Petrov M.P. NMR in ferro- and antiferromagnets. M.: 1969.
- [3] McCausland M. A., Mackensie I. S. Adv. Phys., 1979 v. 28, p. 305.
- [4] Dumesh B.S. Sensitive nuclear magnetic resonance spectrometers continuous UHF / Dumesh B.S. // PTA. -1986. - vol.1. - p.135.
- [5] Hardy W.N. Split-ring resonator for use in magnetic resonance from 200-2000 MHz / W.N. Hardy, L.A. Whitehead // Rev.Sci.Instrum. -1981. - 52. -2. -p.213.

## The observation of magnon BEC in solid antiferromagnet CsMnF<sub>3</sub>

E.M. Alakshin<sup>1</sup>, Yu. M. Bunkov<sup>2</sup>, R.R. Gazizulin<sup>1</sup>, A.V. Klochkov<sup>1</sup>, V.V. Kuzmin<sup>1</sup>,  
T.R. Safin<sup>1</sup>, M.S. Tagirov<sup>1</sup>

<sup>1</sup>Kazan (Volga region) Federal University, 420008, Kremlevskaya st. 18, Kazan, Russia.

<sup>2</sup>Institut Neel, Grenoble, France.

e-mail: g-rasul@yandex.ru

The spin supercurrent and Bose-Einstein condensation of magnons similar to an atomic BEC was observed in 1984 in superfluid <sup>3</sup>He-B. The same phenomena should exist in solid magnetic systems. In this presentation we will report the first observation of magnon BEC in solid easy plain antiferromagnet CsMnF<sub>3</sub>. We have observed magnon BEC on a mode of coupled Nuclear-Electron precession. The dynamical properties of this mode have many similarities with NMR of superfluid <sup>3</sup>He-A. The coupled nuclear electron precession in CsMnF<sub>3</sub> shows a very peculiar dynamics. The electron precession frequency drops down to a near zero at zero fields. The <sup>55</sup>Mn NMR frequency in hyperfine field is very high, about 600 MHz. Due to crossover the two mixed modes of precession appear. We will speak about low frequency electron-nuclear precession mode. Its frequency depends on orientation of nuclear magnetization as it shown in fig.1.

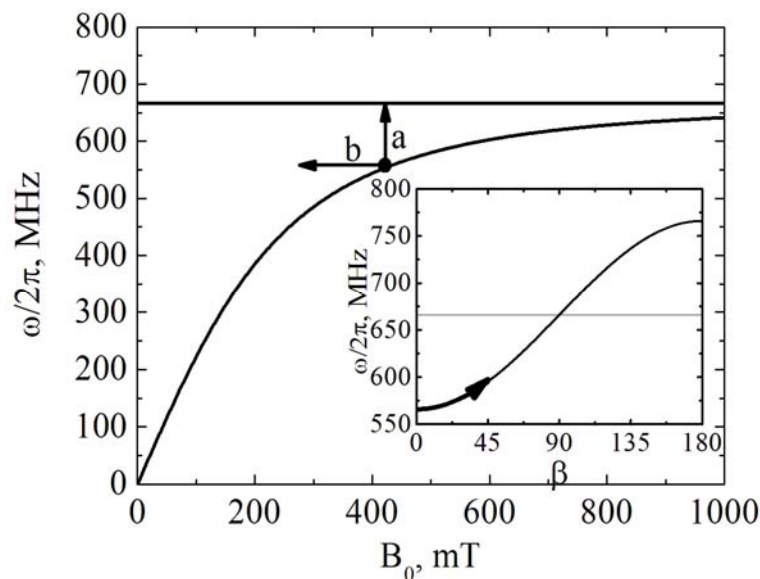


**Fig.1.** The frequency of NMR mode on magnetic field and its dependence on angle of magnetization deflection at given field.

That is similar to the frequency dependence in <sup>3</sup>He-A where BEC of magnons have been proved [1]. Furthermore, the involvement of electron ordered subsystem gives the magnon-magnon interaction, spin waves and spin supercurrent, while the nuclear subsystem gives the relatively long time of relaxation. That is why the magnon BEC was predicted for CsMnF<sub>3</sub> [2].

The experiment was done at the temperature of 1.5 K at a frequency of 560.6 MHz. The line of CW NMR at small RF excitation corresponds to 440 mT field. If we will increase the excitation and sweep down the field, the nuclear magnetizations deflects and keep the same frequency of radiation, as shown in fig.2. The amplitude of the radiation grows up. That means that we are created the magnon BEC with a deflected and homogeneously processing

magnetization. The stability of this state is due to the profile of magnon-magnon interaction and intrinsic spin supercurrent.

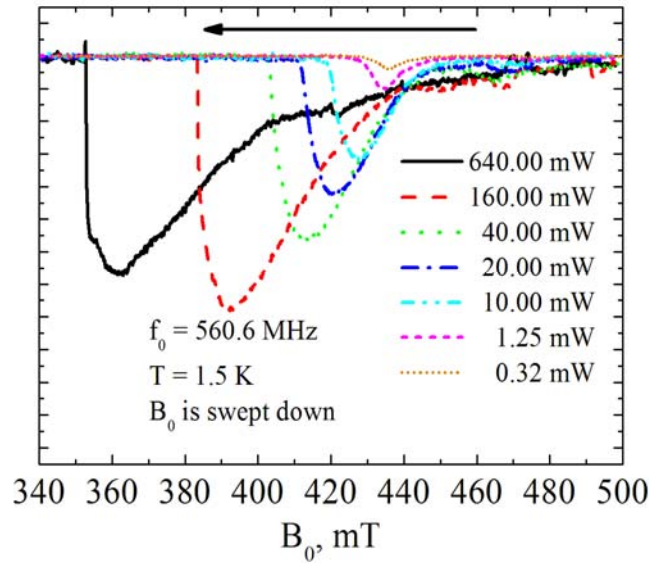


**Fig.2.** The signal of CW NMR at different excitation levels. The system radiates on a non-resonance frequency that is correspond to formation of BEC

### Acknowledgments

This work is supported by the Ministry of Education and Science of the Russian Federation (FTP “Scientific and scientific-pedagogical personnel of the innovative Russia” contract N 02.740.11.5217).

### References

- [1] P. Hunger, Yu.M. Bunkov, E. Collin, H. Godfrin, J. Low Temp. Phys **158**, 129–134 (2010).
- [2] Yu.M. Bunkov, Physics–Uspekhi, **53**, 8, 848–853(2010).

## Super-Hyperfine Structure of EPR Spectra of $\text{Ce}^{3+}$ , $\text{Nd}^{3+}$ and $\text{U}^{3+}$ Ions in Double Fluorides $\text{LiRF}_4$ ( $R=\text{Y, Lu, Tm}$ )

L.K. Aminov, A.A. Ershova, S.L. Korableva, I.N. Kurkin, B.Z. Malkin, A.A. Rodionov

Kazan State University, 420008 Kazan, Russian Federation

e-mail: Ershova.asia@bk.ru

Superhyperfine structure (SHFS) of the EPR spectra of paramagnetic crystals is due to the interaction of electrons localized on paramagnetic ions with magnetic moments of nuclei of surrounding ligands. Our previous studies of the EPR spectra of rare earth ions and  $\text{U}^{3+}$ , introduced as impurities in the crystals  $\text{LiRF}_4$  ( $R=\text{Y, Lu, Tm}$ , impurity ions substitute for  $\text{R}^{3+}$  ions at sites with tetragonal point symmetry  $S_4$ ) [1-3], revealed a number of interesting features of SHFS of measured spectra. Among them are the enhanced nuclear magnetism in the spectrum of  $\text{U}^{3+}$  in Van Vleck paramagnet  $\text{LiTmF}_4$  [2], a curious fact of resolved SHFS in EPR spectrum of  $\text{LiYF}_4:\text{Ce}^{3+}$  at an intermediate orientation of the external magnetic field  $\mathbf{B}$  relative to the crystal axes (at an angle of  $\sim 33^\circ$  to the symmetry axis  $c$ ), whereas for  $\mathbf{B}\parallel c$  the resolution is absent [3]. Further, we observed the EPR spectra of  $\text{Nd}^{3+}$  ions in  $\text{LiYF}_4$  and  $\text{LiTmF}_4$  at different orientations of the external field relative to the crystal axes. In addition, it appeared possible to observe the SHFS of EPR spectrum of  $\text{U}^{3+}$  in  $\text{LiYF}_4$  at  $\mathbf{B}\perp c$ . In this paper we present the results of these and some earlier measurements and discuss them. Some parameters of superhyperfine interaction (SHFI) of rare earths (unfilled electron shell  $4f^n$ ) and uranium ions (unfilled electron shell  $5f^3$ ) are obtained from the observed EPR spectra.

EPR spectra of  $\text{U}^{3+}$ ,  $\text{Ce}^{3+}$  and  $\text{Nd}^{3+}$  ions in double fluorides  $\text{LiRF}_4$  were taken with Bruker ESP-300 spectrometer at the frequency of  $\approx 9.36$  GHz (X-band) and at temperatures in the range of 5 – 25 K. The samples were grown by Bridgman-Stockbarger method, in the argon atmosphere. Intensive EPR spectra due to  $\text{U}^{3+}$ ,  $\text{Yb}^{3+}$ ,  $\text{Nd}^{3+}$ ,  $\text{Er}^{3+}$ ,  $\text{Ce}^{3+}$  ions were observed (g-factors of rare earth ions are given in ref. [4]). The  $\text{Nd}^{3+}$ ,  $\text{U}^{3+}$  and  $\text{Ce}^{3+}$  ions in  $\text{LiYF}_4$  are characterized by g-factors  $g_{\parallel} = 1.987$ ,  $g_{\perp} = 2.554$ ;  $g_{\parallel} = 1.149$ ,  $g_{\perp} = 2.508$ ,  $g_{\parallel} = 2.737$ ;  $g_{\perp} = 1.475$  respectively.

Search of the SHFS of EPR spectra was carried out primarily in the principal orientations  $\mathbf{B}\parallel c$  and  $\mathbf{B}\perp c$ , because in the intermediate orientation, when  $0 < \theta < \pi/2$  ( $\theta$  is the angle between the magnetic field and the  $c$  axis) the spectrum of the system is strongly complicated due to the large number of magnetically nonequivalent nuclei. The SHFS of the EPR spectrum of  $\text{Yb}^{3+}$  ions in  $\text{LiYF}_4$  disappears when the orientation of the magnetic field deviates from  $\mathbf{B}\parallel c$  just by  $\sim 2^\circ$  [5].

In single crystals  $\text{LiYF}_4:\text{Ce}$  and  $\text{LiLuF}_4:\text{Ce}$  at the orientation  $\mathbf{B}\parallel c$  the SHFS was not observed (there is an unresolved EPR line with a width  $\Delta\mathbf{B}_{pp} = 12.2$  G = 46.9 MHz). At  $\mathbf{B}\perp c$  (arbitrary direction of  $\mathbf{B}$  relative to the axes  $a$  and  $b$  in the plane  $ab$ ) the SHFS in these crystals is observed. The EPR lines are narrower in the crystal  $\text{LiYF}_4$ , the corresponding EPR spectrum is shown in fig.1. SHFS consists of 5 components with an interval between the components of  $\sim 9$  G (line width of individual components of SHFS  $\sim 6$  G = 12.4 MHz).

The SHFS has been observed in the crystal  $\text{LiYF}_4:\text{Ce}$  at an intermediate orientation of the external magnetic field  $\mathbf{B}$  relative to the  $c$  axis. g-factor ( $g = 2.425$ ) suggests that for this orientation, the angle between  $\mathbf{B}$  and  $c$  is  $\theta = 33.4^\circ$ . SHFS consists of 5 components with an interval between the components of  $\sim 3.6$  G and the line width of individual components of  $\sim 2.9$  G.

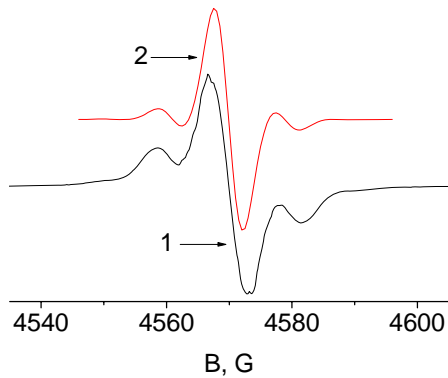


**Fig.1.** The measured (1) and simulated (2) EPR spectra of  $\text{Ce}^{3+}$  ions in  $\text{LiYF}_4$  single crystals,  $\mathbf{B}\perp c$ ,  $T=20$  K,  $\nu = 9.38$  GHz.

$\mathbf{B}\parallel c$  (fig.2). SHFS includes 9 components, with the distance between them  $\sim 5.5$  G (15.4 MHz). At  $\mathbf{B}\perp c$  the SHFS in EPR spectrum of  $\text{Nd}^{3+}$  is not observed (fig.3).

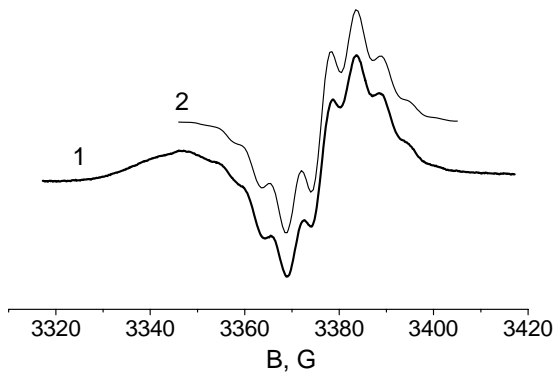


**Fig.2.** The measured (1) and simulated (2) EPR spectra of  $\text{Nd}^{3+}$  ions in  $\text{LiYF}_4$  single crystals,  $\mathbf{B}\parallel c$ ,  $T=15$  K,  $\nu = 9.36$  GHz.

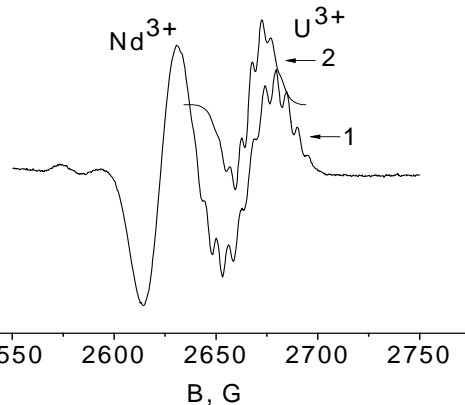


**Fig.3.** The measured (1) and simulated (2) EPR spectra of  $\text{Nd}^{3+}$  and  $\text{U}^{3+}$  ions in  $\text{LiYF}_4$  single crystals,  $\mathbf{B}\perp c$ ,  $T=16$  K,  $\nu = 9.36$  GHz.

An EPR spectrum of  $\text{LiTmF}_4: \text{Nd}^{3+}$  the SHFS is also observed only at  $\mathbf{B}\parallel c$ . As in the spectrum of  $\text{LiYF}_4: \text{Nd}^{3+}$ , nine components are observed, and the distance between them is also equal to  $\sim 5.5$  G, but the line widths of SHFS components are significantly higher than in  $\text{LiYF}_4$ .

In single crystals  $\text{LiYF}_4$  and  $\text{LiLuF}_4$  the SHFS of EPR spectra of  $\text{U}^{3+}$  ions is observed both at  $\mathbf{B}\parallel c$  and at  $\mathbf{B}\perp c$ . The SHFS at  $\mathbf{B}\perp c$  (see fig.3) contains 11 components with a separation of  $\sim 6$  G (21.1 MHz). It should be noted that the SHFS of  $\text{U}^{3+}$  in  $\text{LiLuF}_4$  at  $\mathbf{B}\perp c$  is similar to that in  $\text{LiYF}_4$ , but the resolution is notably worse. Resolution is improved by moving away from the strict perpendicular orientation. The most clear SHFS was observed at  $\theta = 81^\circ$ .

Superhyperfine structure of EPR spectra is determined by the interaction of  $f$ -electrons with the nearest nuclei  $\text{F}^-$  (two fours F1 and F2), as well as nuclei  $\text{Tm}^{3+}$  in the Van Vleck paramagnet  $\text{LiTmF}_4$  [3]. Contributions of the  $\text{Li}^+$  and  $\text{Y}^{3+}$  nuclei are negligible.

P R O C E E D I N G S

The following parameters of the ligands are used in further estimates:

$$\begin{aligned} \text{F1: } R_1 &= 0.222 \text{ nm, } \theta_1 = 67.6^\circ; \text{ F2: } R_2 = 0.227 \text{ nm, } \theta_2 = 38.6^\circ [6,7], \gamma_I/2\pi = 40 \text{ MHz/T [8]} \\ \text{Tm: } R_3 &= 0.370 \text{ nm, } \theta_3 = 44^\circ, \gamma_I/2\pi = -3.54 \text{ MHz/T [9]} \end{aligned}$$

where  $\theta_i$  is the angle between  $\mathbf{R}_i$  and the axis  $c$ ,  $\mathbf{R}_i$  is radius-vector connecting impurity ion with  $i$ -th ligand,  $\gamma_I$  is nuclear gyromagnetic ratio. Structural data are given for regular positions of the ions in the crystal. The introduction of impurities leads to some distortion of local structure [10,11], in particular, changes the crystal field at neighboring impurity ions  $\text{Tm}^{3+}$  in  $\text{LiTmF}_4$  [9].

Effective spin Hamiltonian for a paramagnetic ion, which interacts with magnetic moments of the nuclei of the ligands can be written as [2, 8]:

$$H = \mu_B \mathbf{B} \tilde{g} \mathbf{S} + \hbar \sum_i \left( -\mathbf{B} \tilde{\gamma}_I^i \mathbf{I}^i + \sum_{p,v} T_{pv}^i I_p^i S_v \right), \quad (1)$$

where  $\mu_B$  is Bohr's magneton,  $\tilde{g}$  — g-tensor of the impurity ion,  $\mathbf{I}^i$  — nuclear spin of the  $i$ -th ligand,  $\tilde{\gamma}_I^i$  — an effective nuclear gyromagnetic tensor of the  $i$ -th ligand that differs from the gyromagnetic factor  $\gamma_I^i$  by enhancement factor  $(1 + \tilde{\alpha}^i)$ , taking large values in the case of nuclei of Van Vleck ions (for Tm in  $\text{LiTmF}_4$   $\alpha_{\parallel} = 1.73$ ,  $\alpha_{\perp} = 66.5$  [9]). For nuclei of diamagnetic ions  $\text{F}^-$ ,  $\text{Li}^+$ ,  $\text{Y}^{3+}$  the shift tensor  $\tilde{\alpha}$  can be neglected. Superhyperfine interaction (SHFI) consists of a magnetic dipole-dipole interaction of the paramagnetic ion with the nucleus and nondipolar (covalent) part due to the overlap of  $f$ -electron functions with ligands. The dipolar contribution to the tensor  $\tilde{T}$  SHFI ion is:

$$T_{pvd}^i = -\frac{\mu_B \gamma_I^i}{R_i^3} \sum_q (\delta_{qp} - 3n_q^i n_p^i) g_{qv}.$$

Here  $\mathbf{n}^i = \mathbf{R}_i/R_i$ . The effective spin of ions is  $S = 1/2$ .

Electronic Zeeman energy is much higher than other terms in the formula (1). The nuclear part of the Hamiltonian (1) is diagonalized independently for each electronic state  $M$ . In the framework of the approximation of noninteracting ligands, this procedure reduces to the diagonalization of Hamiltonians of individual ligands

$$H^i(M) = \hbar \mathbf{I}^i \mathbf{B}_{eff}^i(M),$$

and the subsequent superposition of the obtained spectra. At  $\mathbf{B}||z(c)$  four of F1 and F2 ions are magnetically equivalent, and

$$\mathbf{B}_{eff}^i(M_z) = \left[ M_z T_{xy} (1 + \alpha_{\perp}), M_z T_{yz} (1 + \alpha_{\perp}), (M_z T_{zz} - \gamma_I^i B) (1 + \alpha_{\parallel}) \right].$$

At  $\mathbf{B}||x$ , we have

$$\mathbf{B}_{eff}^i(M_x) = \left[ (M_x T_{xx} - \gamma_I^i B) (1 + \alpha_{\perp}), M_x T_{xy} (1 + \alpha_{\perp}), M_x T_{zx} (1 + \alpha_{\parallel}) \right].$$

The effective field is expressed in frequency units. The intervals between the components of the spectrum and their intensity at  $\mathbf{B}||c$  are determined by the values  $\gamma_I B$ ,  $T_{zz}$ ,  $T_t = (T_{xz}^2 + T_{yz}^2)^{1/2}$ . Taking into account only dipole-dipole contribution to the SHFI leads to a qualitative agreement between the calculated and observed EPR spectra.

It is possible to match better the calculated and measured spectra of Ce in  $\text{LiYF}_4$  and  $\text{LiLuF}_4$  ( $\mathbf{B} \perp c$ ) by increasing the dipolar value of SHFI by 1.6 times for F1 nuclei and reducing them by 15% for F2 nuclei. The calculation of the EPR signal at  $\mathbf{B}||c$  gives one broad line with unresolved superhyperfine structure.

The contribution of the four nuclei of  $\text{Tm}^{3+}$  ions in the SHFS of the EPR spectrum is schematically represented in the form of five equidistant lines (see [2]). Convolution of this spectrum with a broad line with unresolved superhyperfine structure due to F1 and F2 ligands, observed in  $\text{LiYF}_4:\text{Ce}^{3+}$  and  $\text{LiLuF}_4:\text{Ce}^{3+}$  at  $\mathbf{B}\parallel c$ , corresponds to the experimental spectrum in  $\text{LiTmF}_4:\text{Ce}^{3+}$ .

For  $\text{LiYF}_4:\text{Nd}^{3+}$  ( $B = 3.4$  kG)  $\gamma_I B = 13.5$  MHz, and dipolar components of the SHFI tensor for F1 and F2 are as follows (in MHz):  $T_{zzd}^{(1)} = -3.8$ ,  $T_{td}^{(1)} = 7.15$ ,  $T_{zzd}^{(2)} = 5.2$ ,  $T_{td}^{(2)} = 9.2$ . As in previous studies [1-3], simulation of the spectrum, taking into account only the dipole-dipole contribution to the SHFI tensor, leads to the qualitative agreement with measurements. Fig.2 shows an almost full coincidence with the experiment of the model spectrum for the following parameters  $T_{kl}$ :  $T_{zz}^{(1)} = -6$ ,  $T_t^{(1)} = 13.4$ ,  $T_{zz}^{(2)} = 3.4$ ,  $T_t^{(2)} = 14.2$ . Width of the individual components are taken to be  $\sim 10$  MHz, which roughly corresponds to the interaction with remote  $\text{F}^-$  nuclei (see [12]).

When  $\mathbf{B}\perp c$ , four structurally equivalent ligands split into two pairs of magnetically equivalent ligands, and the dipolar term depends on the orientation of the field in the plane  $ab$ . We present here for  $\text{U}^{3+}$  ion at  $\mathbf{B}\perp c$  ( $B = 2660$  G) the dipolar components of SHFI with F1 and F2 nuclei in the case when the ligand is in a plane containing the external field and the axis  $z$  ( $c$ ):  $T_{xxd}^{(1)} = 13.3$ ,  $T_{td}^{(1)} = 9$ ,  $T_{xxd}^{(2)} = -1.3$ ,  $T_{td}^{(2)} = 11.7$ . These values also allow to qualitatively reproduce the observed EPR spectrum (fig.3).

EPR spectra of  $\text{U}^{3+}$  ( $5f^3$ ) and  $\text{Nd}^{3+}$  ( $4f^3$ ) ions are qualitatively similar. However, EPR spectra of the uranium ions reveal more SHFS components and some increasing of the distance between these components. Phenomenological parameters values used for modeling of the EPR spectra differ to some extent from purely dipole values. Summing as the general conclusion, we note that the main features of the observed superhyperfine structure of EPR spectra of rare earth ions and  $\text{U}^{3+}$  in double-fluoride  $\text{LiRF}_4$  are well explained by existing theoretical concepts.

## References

- [1] L.K. Aminov, A.A. Ershova, D.G. Zverev et al., Appl. Magn. Reson. **33**, 351 (2008).
- [2] L.K. Aminov, A.A. Ershova, S.L. Korableva et al., Pis'ma v ZhETF **87**, 362 (2008)
- [3] L.K. Aminov, A.A. Ershova, V.N. Efimov et al., Fiz. tverd. tela **52**, 1931 (2010).
- [4] L.K. Aminov, I.N. Kurkin, I.H. Salikhov et al., Fiz.tverd. tela **32**, 2705 (1990).
- [5] J.P. Sattler, J. Nemarich, Phys. Rev. **B 4**, 1 (1971).
- [6] E. Garcia, R.P. Ryan, Acta Cryst. C **49**, 2053 (1993).
- [7] A. Bensalah, Y. Guyot, A. Brenier et al., J. Alloys Compd. **380**, 15 (2004).
- [8] A. Abragam, B. Bleaney, Electron Paramagnetic Resonance of Transition Ions, vol. 1, Clarendon, Oxford, 1970.
- [9] L.K. Aminov, B.Z. Malkin, M.A. Teplov, in Handbook on the Physics and Chemistry of Rare Earths, vol. 22, Ed. K.A. Gschneidner, Jr. and L. Eyring, Elsevier Science, 1996, p.295.
- [10] M. Stephan, M. Zachau, M. Groting et al., J. Lumin. **114**, 255 (2005).
- [11] L.K. Aminov, B.Z. Malkin, M.A. Koreiba et al., Optika I Spectroskopiya **68**, 835 (1990).
- [12] U.Ranon, J.S.Hyde, Phys. Rev. **141**, 259 (1966).

## Multifrequency EPR of Asphaltenes

D.T. Sitdikov<sup>1</sup>, G.V. Mamin<sup>1</sup>, S.B. Orlinskii<sup>1</sup>, N.I. Silkin<sup>1</sup>, R.V. Yusupov<sup>1</sup>, T.N. Yusupova<sup>2</sup>

<sup>1</sup>Kazan Federal University, 420008, Kazan, Russia.

<sup>2</sup>A.E. Arbuzov Institute of Organic and Physical Chemistry, 420088, Kazan, Russia

e-mail: sitdikov-ksu@rambler.ru

### Introduction

Heavy oils rich in asphaltene are increasingly being exploited to sate the increasing thirst for petroleum around the world. Asphaltenes are a well known problem for the oil industry. Their tendency to form deposits on wells, tubing, piping, and also during refining processes causes heavy losses to the oil industry every year

Asphaltenes have been extensively studied in the literature and are defined by a solubility class of molecules, insoluble in n-paraffins/soluble in toluene, with a very high molecular weight. They are made of polar aromatic compounds with mainly carbon (80 – 86 %), hydrogen (6 – 8 %), oxygen (0.5 – 2 %), nitrogen (0.5 – 2 %), sulfur (2 – 9 %), and metals (Ni and V associated with porphyrin structures). Asphaltenes are characterized by broad size and molecular pattern distributions [1].

From all studies, asphaltenes seem to be described through two average models:

- the “continental” type [2], in which asphaltenes are represented as large central aromatic region (fig.1);
- the “archipelago” type [3], where asphaltenes are made of smaller aromatic regions linked by bridging alkanes (fig.2).

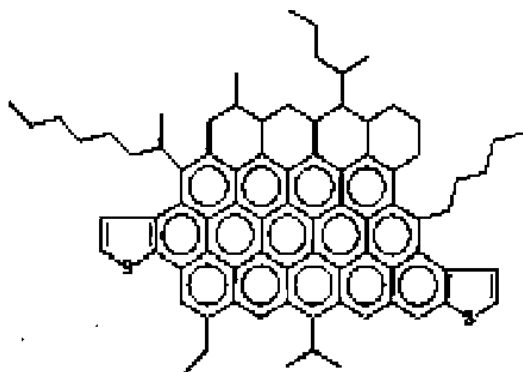


**Fig.1.** Representation of asphaltene models “continental” type [2].

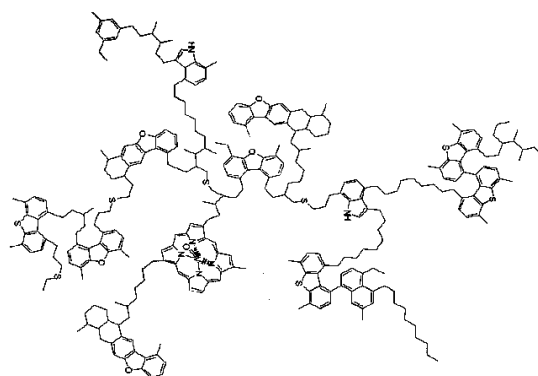


**Fig.2.** Representation of asphaltene models “archipelago” type [3].

The size of these structures ranges in a wide window from 10 to several hundreds of angstroms.

Existence of two types of asphaltene molecules with different chemical structure complicates heavy oils processing. It becomes necessary to evolve fraction with one type asphaltene molecules – “continental” or “archipelago”.

## Results and discussion

Samples of asphaltenes (A<sub>initial</sub>) were obtained from oil from four different petroleum deposit Zuzeevskoe, Akanskoe (2262), Akanskoe (2023), Kazahstanskoe. Samples of asphaltenes (A<sub>initial</sub>) were separated to three fractions:

- A1 fraction predominantly consists of “continental” asphaltene molecules;
- A2 fraction predominantly consists of “archipelago” asphaltene molecules;
- A1+A2 fraction consists of identical quantity “continental” and “archipelago”.

Powder spectra of asphaltenes consist of 16 superfine lines of vanadyl ( $V^{4+}+O^{2-} \rightarrow VO^{2+}$ ,  $3d^1$ ,  $S = 1/2$ ) and single intensive line corresponded to unpaired electrons of free radicals (fig.3).

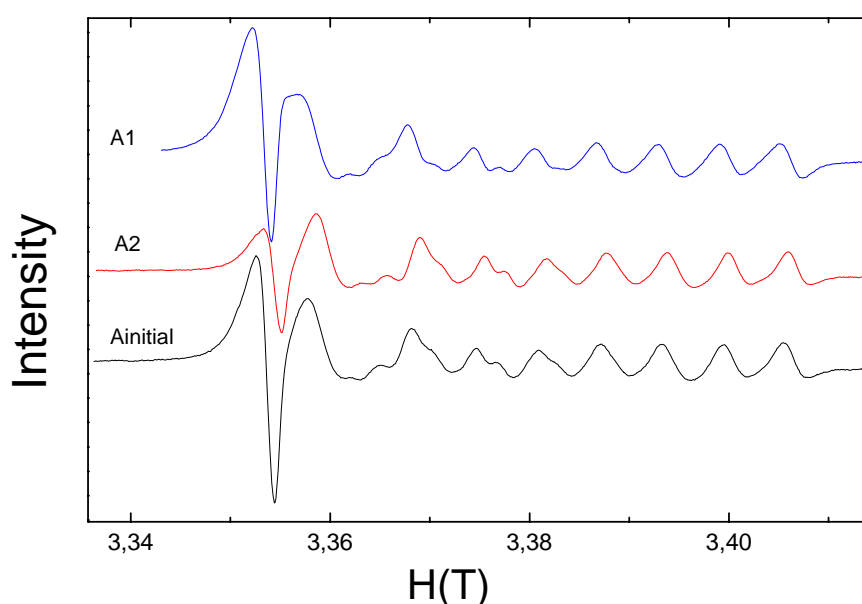


**Fig.3.** CW EPR spectra of asphaltenes from field Akanskoe (2262).

Every samples single line is believed to consist of two types of free radicals (A и B), that corresponded to asphaltene molecules with “continental” and “archipelago” type accordingly (fig.4).

## Conclusions

The CW and pulse W-band EPR spectra of asphaltenes from different deposit were measured and interpreted, their spectroscopic and relaxational characteristics were obtained.

It was shown, that EPR spectroscopy allows us to define two types of molecular structure in asphaltenes – “continental” and “archipelago”, as well as measuring their relative concentrations and studying their structure. The resolution of high-frequency EPR allow get the relation between intensity of radicals and intensity of vanadil complex. This parameter can be used in addition to traditional parameters for classification the crude oil.

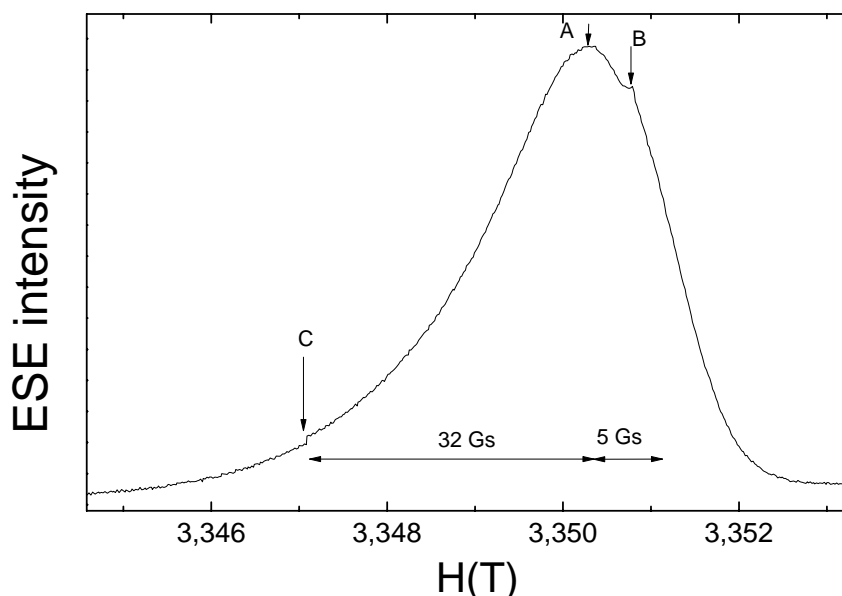


**Fig.4.** EPR Spectra of asphaltenes from field Akanskoe (2023) detected by amplitude of an electronic spin echo.

#### References

- [1] Marchal, C. Asphaltene diffusion and adsorption in modified NiMo alumina catalysts followed by ultraviolet (UV) spectroscopy / Charles Marchal, Eswar Abdessalem, Melaz Tayakout-Fayolle, and Denis Uzio // *Energy Fuels* – 2010 – 24 – P. 4290–4300.
- [2] Murgich, J. Molecular recognition and molecular mechanics of micelles of some model asphaltenes and resins / Juan Murgich, Jesus Rodriguez M., and Yosslen Aray // *Energy & Fuels* – 1996 – 10 – P. 68-76.
- [3] Sheremata, J.M. Quantitative molecular representation and sequential optimization of athabasca asphaltenes / Jeff M. Sheremata, Murray R. Gray, Heather D. Dettman, and William C. McCaffrey // *Energy & Fuels* – 2004 – 18 – P. 1377-1384.

## Radiofrequency synthesizer design for magnetic resonance imaging system's spectrometer

D.D. Gabidullin

Laboratory of the Methods of Medical Physics, Zavoisky Physical-Technical Institute of the Kazan scientific Center of the Russian Academy of Sciences, 420029, Sibirsky tract, 10/7, Kazan, Republic of Tatarstan, Russian Federation

e-mail: dinarld@mail.ru

### Introduction

Magnetic resonance imaging (MRI) system is an imaging technique primarily used in medical setting to produce high quality images of the inside of the human body. This technique is based on collecting the signal from an excited slice or volume within the sample. This excitation is achieved using special radiofrequency (RF) pulses that are designed to provide the required localization within the imaged volume. This work is deals with the designing of RF synthesizer which actual frequency and the applied slice selection magnetic field gradient determine the position of the excited slice.

### General description of the device

The operation principle of the designed device (fig.1) is relied on the so called digital direct synthesis (DDS) method. The advantages of this method are the following:

- fast, phase-continuous frequency switching;
- fine frequency and phase tuning resolution;
- fully digital control of frequency and phase value;
- easy implementation of digital modulation of frequency.

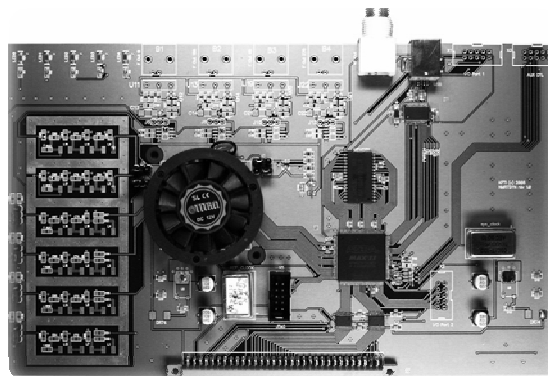


**Fig.1.** RF synthesizer.

The simplified block-scheme of the invention is presented below (fig.2), where

- DDS — chip realizing the DDS method;
- FPGA — field-programmable gate array. It carries out control function and correct interaction between other parts of the device;
- Ref.Gen. — the reference generator. It is required for DDS chip clocking;
- Clk.Osc — the clocking oscillator. It is required for FPGA chip clocking;

- LPF – low-pass filter. It is required for suppressing the clock frequency and its harmonics and the mirror signal generated by the reference generator;
- RAM — random access memory. It is necessary for storing the digital codes of the frequency values;
- USB/FIFO is a USB to parallel FIFO interface. It is required for easy interaction with personal computer;
- PPU — pulse program unit. It carries out the frequency switching function during experiment.

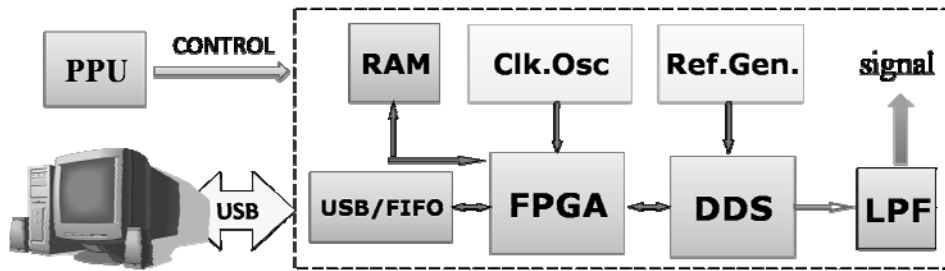


Fig.2. Block-scheme of the RF synthesizer.

The program for FPGA has been also written. In this program the four modules each of them interacting with a definite element of the device are considered (fig.3).

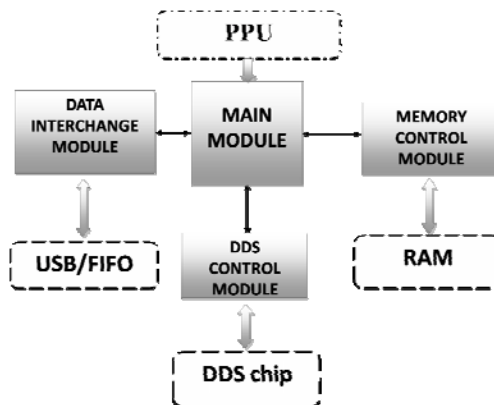


Fig.3. Functional block diagram of the program.

To produce the correct function of the made up device within software of MRI system the so called drivers of high and low level have been written. Also a program for testing and debugging of the device has been made.

The designed device has the following main characteristics:

- frequency range —  $0 \div 15$  MHz;
- frequency resolution — less than 1 mHz;
- switching frequency — no more than 1 kHz;
- four phase-shifted output channels;
- ability of generating the square pulses.

### Acknowledgements

This work is supported by the program of fundamental researches of the Presidium of Russian Academy of Sciences “Fundamental Sciences to Medicine”.

## Simulation of Magnetic Resonance Imaging Experiments

N.A. Krylatykh, Ya.V. Fattakhov

Zavoisky Physical-Technical Institute of the Kazan Scientific Center of the Russian Academy of Sciences, 420029, Kazan, Russian Federation

e-mail: natalya.p4elka@gmail.com.

### Introduction

Method of magnetic resonance imaging (MRI) had become popular and wide-available method of structure investigation ranging from medical to solid state applications. To develop new MRI pulse sequences it is important to have possibility of simulation of real experiments. In present work different publicly available simulators are considered and their characteristics are compared.

### Artefacts in Magnetic Resonance Imaging

The quality of images received in MRI depends on large amount of parameters (heterogeneity and instability of basic and gradient fields, outside noises, methods of coding k-space and etc.). To understand origin and to create an analytical model of one or another image artifact analytically is sometimes difficult enough and not always possible. And removal of artifacts is necessary for increasing of diagnostic image value and exclusion of probability to diagnose wrongly.

### MRI Simulators

The method of mathematical modeling for receiving images in MRI is used widely for problem solving of this type. There are known several program-stimulators of MRI, among them are SiMRI, ODIN, and POSSUM [1-3]. Programs design the process of receiving images from receiving the signal up to the terminal image, give the possibility to design both ideal and non-ideal conditions.

For simulation the process of receiving MR images on tomographs the ODIN program is the main tool for our laboratory. This program for calculation the evolution of a magnetization vector uses Bloch–Torrey equations:

$$\dot{\vec{M}} = \vec{M} \times \vec{\Omega} - \begin{pmatrix} M_x/T_2 \\ M_y/T_2 \\ (M_z - M_0)/T_1 \end{pmatrix} + \begin{pmatrix} \vec{\nabla} \cdot \vec{D} \vec{\nabla} M_x \\ \vec{\nabla} \cdot \vec{D} \vec{\nabla} M_y \\ \vec{\nabla} \cdot \vec{D} \vec{\nabla} M_z \end{pmatrix}. \quad (1)$$

To modeling the process of MR-images recording on tomographs the following steps have been done: new pulse sequence designed, a map of heterogeneity have been recorded and the character of instability in time of basic magnetic field have been studied.

To make a map of inhomogeneity of basic magnetic field we have find a values of frequency on the sphere. Calculation of field values in the work space of magnet was done by using spherical functions and there coefficients:

$$H_z(R, \theta, \varphi) = \sum_{l=0}^{\infty} \sum_{m=-l}^l A_{lm} R^l Y_l^m(\theta, \varphi) \quad (2)$$

where  $Y_l^m(\theta, \varphi)$  and  $A_{lm}$  denote spherical harmonics and their coefficients and  $(R, \theta, \varphi)$  — spherical coordinates [1].

## PROCEEDINGS

The pulse sequences on interface of ODIN described in terms of the physical properties of their elements and the arrangement of these sequence elements as a function of time. Programming of pulse sequences used on ZPhTI's tomographs was done on the templates of standard sequences. Timing diagram of ZPhTI's Multislise SE sequence is given on fig.1.

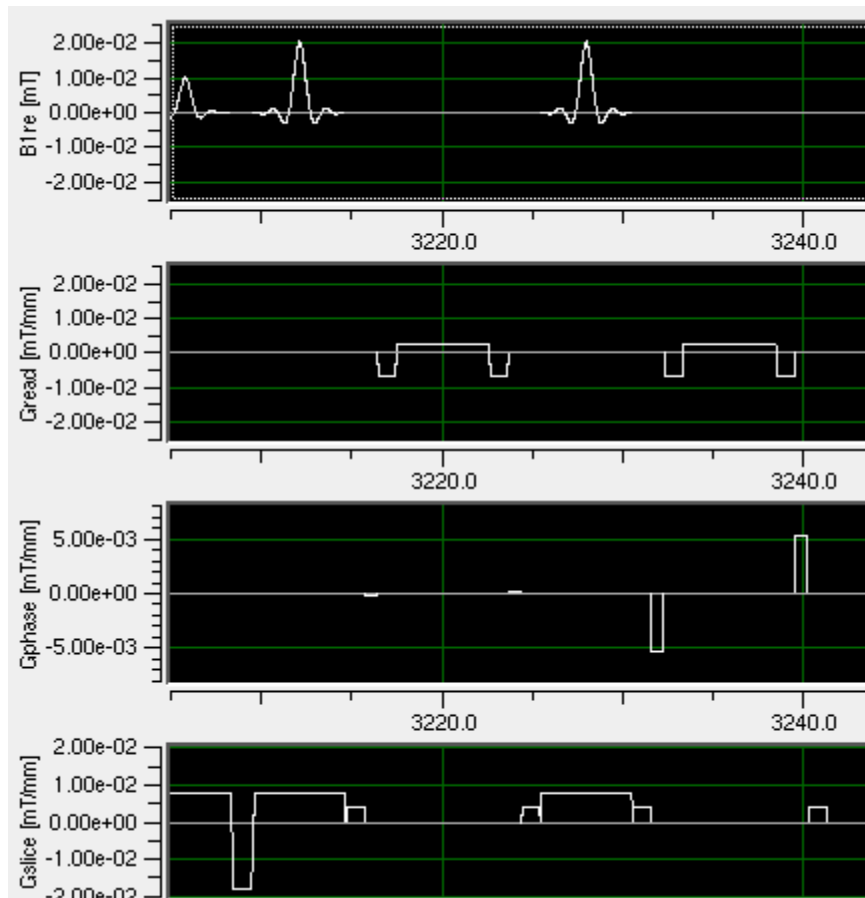


**Fig.1.** Multislise SE timing diagram .

### References

- [1] <http://www.creatis.insa-lyon.fr/menu/ivolumique/segmentation/simri-hbc/index-us.html>.
- [2] <http://od1n.sourceforge.net>.
- [3] <http://www.fmrib.ox.ac.uk/fsl/possum/index.html>.

## General $R_1/R_{1\rho}$ equations for the NMR relaxation data analysis in solids

T. Zinkevich<sup>1</sup>, R. Kurbanov<sup>2</sup>, A. Krushelnitsky<sup>2</sup>

<sup>1</sup>Zavoisky Physical-Technical Institute, 420029, Sibirsky tract, Kazan, Russia.

<sup>2</sup>Kazan Institute of Biochemistry and Biophysics, 420111, Lobachevsky str., Kazan, Russia.

e-mail: tatyana-vilkova@ya.ru

Nuclear magnetic relaxation is one of the most powerful tools for studying molecular dynamics in different substances. The strategy of the quantitative NMR relaxation application to the molecular dynamic studies is a back calculation of the correlation function of motion from experimentally measured relaxation rates (times). Without any a priori assumptions, single relaxation rate cannot provide enough data for the correlation function restoration since this is an ill-defined problem. Thus, multiple relaxation measurements are necessary: the more experimental parameters, the more exact form of the correlation function can be obtained. Usually this function is parameterized by a limited number of dynamic parameters and the values of these parameters are obtained from the simultaneous fitting the relaxation rates measured at various conditions, e.g. resonance frequencies, temperatures, etc. The most widely known procedure of such a treatment of the relaxation rates is a model-free approach [1].

The model-free approach has been extensively applied to the relaxation data analysis. Note that in solutions, the internal motions slower than the overall Brownian tumbling of a molecule are invisible for the relaxation experiments and the solid state approaches allow studying the whole frequency range of internal motions. However, the analysis of the solid state relaxation data is a bit more complicated. The relaxation rate  $R_{1\rho}$ , which is sensitive to the slow motions in the  $\mu\text{s}$  time scale, contains the so-called spin-spin contribution corresponding to the additional relaxation pathway to the lattice via proton dipole-dipole reservoir [2]. This contribution does not contain information on molecular dynamics and at certain conditions it can be dominant. There are some options either to take this contribution into account or to suppress it [3, 4]. One of such options is using the resonance off-set of the spin-lock field [5]. This makes possible achieving high spin-lock fields without dangerous increase of the RF power. In this way one may suppress the undesirable spin-spin contribution and expand the frequency range of the  $R_{1\rho}$  measurements. Note that the ordinary well known  $R_1/R_{1\rho}$  formulae do not describe the off-resonance spin-lock experiments in the solid state.

Another important point is the fact that quite often the spin-lock frequency in the  $R_{1\rho}$  experiments is comparable with the magic angle spinning (MAS) frequency. This is especially relevant for the  $^{15}\text{N}$  experiments, since high spin-lock fields on the  $^{15}\text{N}$  channel are difficult to achieve. Thus, the MAS frequency also needs to be taken into account in the  $R_{1\rho}$  formula.

In the present work we derive general equations for the  $R_1/R_{1\rho}$  relaxation that take into account both the resonance offset of the spin-lock pulse and the arbitrary values of the spin-lock and MAS frequencies. The same equation determines both  $R_1$  and  $R_{1\rho}$  relaxation rates: if the angle between  $B_{1e}$  and  $B_0$  is equal to  $0^\circ$  and  $90^\circ$ , then the equation converts to the standard  $R_1$  and  $R_{1\rho}$  definitions, respectively. These equations are derived for the heteronuclear dipolar and chemical shift anisotropy (CSA) relaxation mechanisms.

Relaxation rate for the heteronuclear dipolar relaxation mechanism is

$$R_{1\rho}^{IS} = R_1^{IS} + \sin^2 \beta_\rho \left( R_{1\Delta}^{IS} - \frac{1}{2} R_1^{IS} \right),$$

where  $R_{1\Delta}^{IS} = \mu^2 \left( 3J(\omega_S) + \frac{2}{3} \sum_{\substack{n=-2 \\ n \neq 0}}^2 \frac{1}{|n|} J(\omega_e + n\omega_R) \right)$ ,  $R_1^{IS}$  — well-known spin-lattice relaxation time,  $\mu^2 = \frac{\hbar^2 \gamma_I^2 \gamma_S^2 S(S+1)}{3r^6}$ ,  $\hbar$  is Plank's constant,  $\gamma_I, \gamma_S$  — gyromagnetic ratios for  $I$  and  $S$  nuclei,  $S$  — spin of the  $I$  nucleus,  $r$  — the distance between interaction nuclei,  $\beta_\rho$  — spin-lock field offset angle,  $\omega_e, \omega_R, \omega_S$  are the frequencies of effective field, MAS rotation, frequency of  $S$  nuclei, respectively, and  $J_n(\Omega)$  is spectral density function of the motion.

For the CSA mechanism of relaxation another formula is derived:

$$R_{1\rho}^{CSA} = R_1^{CSA} + \sin^2 \beta_\rho \left( R_{1\Delta}^{CSA} - \frac{1}{2} R_1^{CSA} \right).$$

Here  $R_{1\Delta}^{CSA} = \frac{1}{6} (\delta\omega_0)^2 \sum_{\substack{n=-2 \\ n \neq 0}}^2 \frac{1}{|n|} J(\eta, \omega_e + n\omega_R)$ ,  $\delta\omega_0$  — chemical shift anisotropy,  $\eta$  — asymmetry parameter. Using these formulas the program has been written to calculate relaxation rates  $R_{1\rho}$  with MAS and resonance offset of spin-lock frequency.

The obtained general  $R_1/R_{1\rho}$  formulas were verified using the SPINEVOLUTION program [6] for one simple model –jumps of the internuclear  $^{15}\text{N}$ - $^1\text{H}$  vector between two sites with an equal probability with the angle between them  $60^\circ$ . In this case spectral density function assumed to be of the form of  $J(\Omega) = \frac{2}{5} (1 - S^2) \frac{\tau}{1 + (\Omega\tau)^2}$ ,  $S^2$  is the order parameter

(for the  $60^\circ$  jumps  $S^2 = 0,438$ ) and  $\tau_c$  — correlation time of motion. The coefficient  $2/5$  is a result of the powder averaging. There are correlation time dependencies of relaxation rates resulted from the formulas and from the simulation using SPINEVOLUTION program for two mechanisms of relaxation in the fig.1.

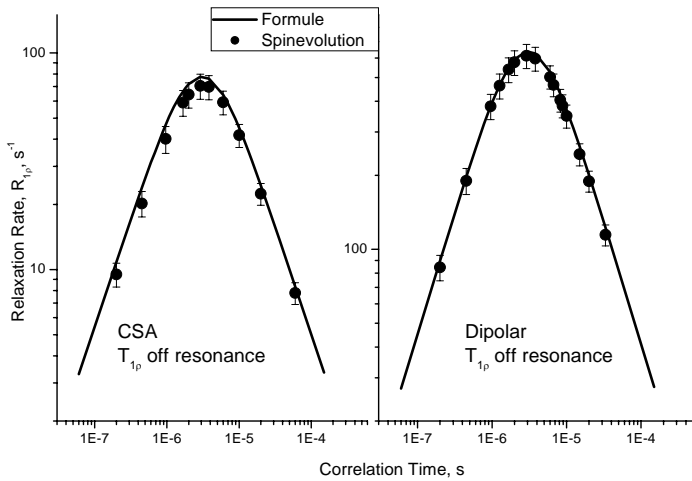


**Fig.1.** Correlation time dependencies of relaxation rate  $R_{1\rho}$  with spin-lock pulse frequency offset. Parameters:  $B_e=57,7$  kHz (effective field),  $\Delta\nu=28,9$  kHz (resonance offset),  $\theta=60^\circ$  (angle between two sites),  $\nu_{rot}=10$  kHz (rotational frequency),  $\delta\omega_{aniso}=100$  p.p.m. (chemical shift anisotropy),  $\beta_\rho=60^\circ$  (effective field angle).

As we can see from the picture there is a good agreement between data obtained. The implemented formula makes it possible to forecast with a high accuracy the spin-lattice relaxation rate accounting magic angle spinning and spin-lock pulse field frequency offset, which has not been taken into account before.

As soon as there are two terms of spectral density  $J(\omega_e \pm \omega_R)$  and  $J(\omega_e \pm 2 \cdot \omega_R)$  in the relaxation rate formula, it seems to be possible to investigate extremely slow motions

(with a correlation times close to milliseconds-seconds) setting the frequency of effective field close to MAS frequency. To examine this possibility the simulations of on-resonance  $T_{1\rho}$  have been carried out using SPINEVOLUTION program and derived formulas at different spinning frequencies and a wide range of effective spin-lock frequency. The results are shown in the fig.2.

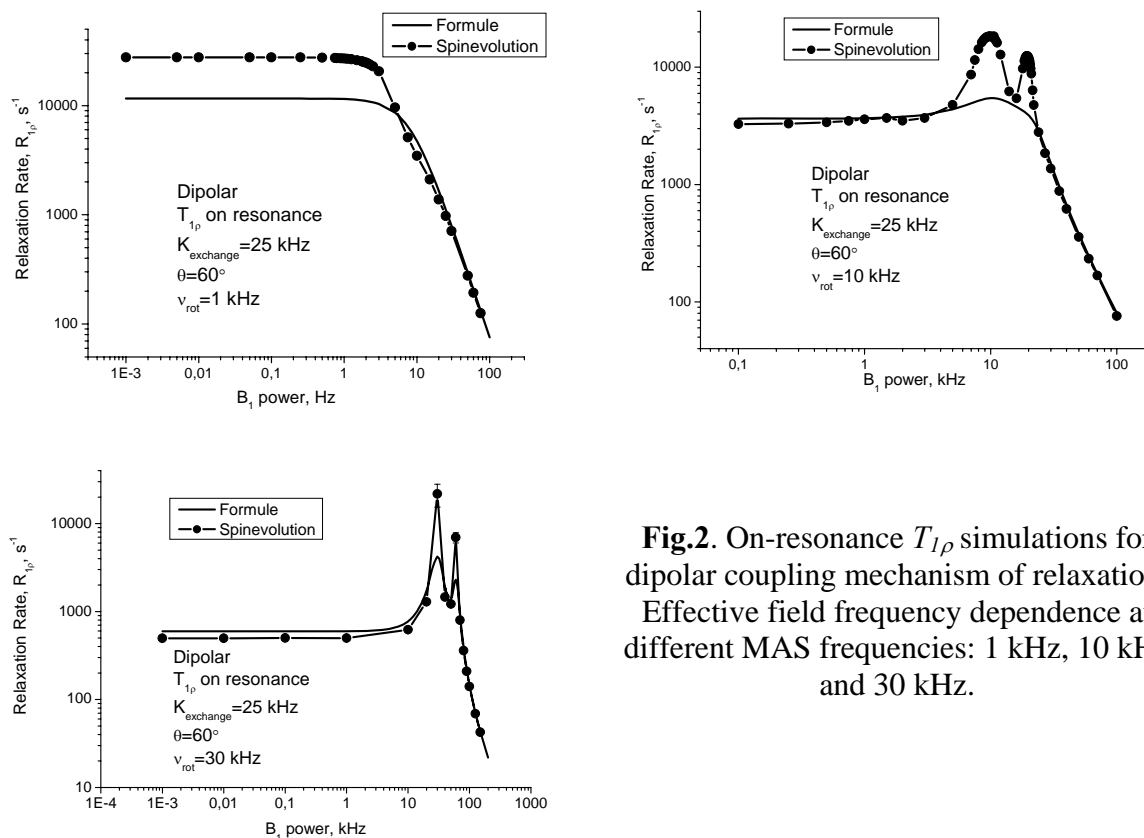


**Fig.2.** On-resonance  $T_{1\rho}$  simulations for dipolar coupling mechanism of relaxation. Effective field frequency dependence at different MAS frequencies: 1 kHz, 10 kHz and 30 kHz.

As it is seen from the pictures there is a coincidence of relaxation rates only if the effective spin-lock frequency is far away from single and double MAS frequency. If  $\omega_e$  and  $\omega_R$  are similar, rotary resonance effects destroy the relaxation decay (see fig.3a) and thus the above formulas are not applicable.

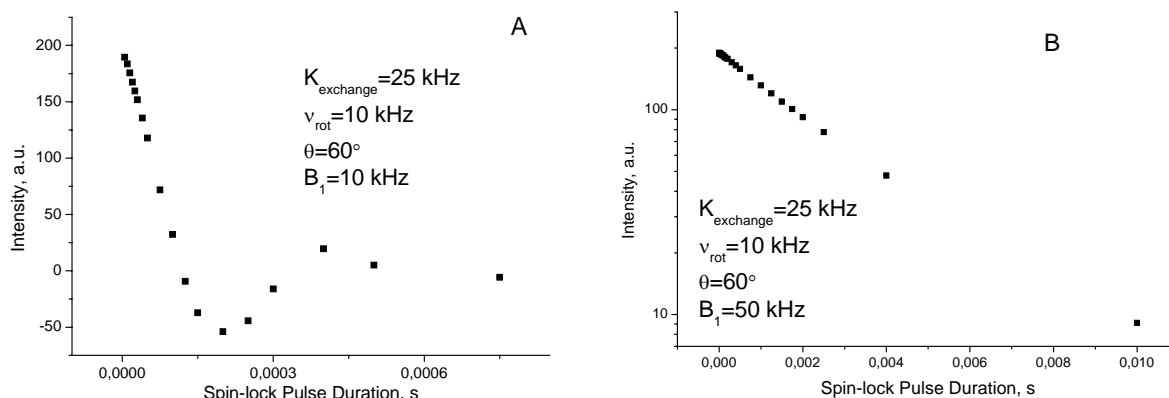


**Fig.3.** Examples of relaxation decays obtained with SPINEVOLUTION program. On-resonance  $T_{1\rho}$  with a dipolar mechanism of relaxation. A). MAS frequency equal to spin-lock field frequency – non-exponential decay. B). MAS frequency lower than spin-lock field frequency – exponential decay.

## PROCEEDINGS

In the context of theory proposed it's impossible to take resonance phenomenon into account. The rotational resonance in this case is a restriction in validity of present formulas.

### Conclusions

Thus, two formulas to predict spin-lattice relaxation rates for two mechanisms of relaxation – dipolar coupling and chemical shift anisotropy – have been derived. Validity of these formulas in the case of magic angle spinning and spin-lock pulse frequency offset were proved by SPINEVOLUTION simulations. This work makes possible quantitative analysis of molecular motions with extracting dynamic parameters: correlation times, order parameters and activation energies of different types of motions.

### References

- [1] Lipari, G. Model-free approach to the interpretation of nuclear magnetic resonance relaxation in macromolecules. 1. Theory and range of validity / G. Lipari, A. Szabo // *J.Am.Chem.Soc.* - 1982. - Vol. 104. - P. 4546-4559.
- [2] Vanderhart, D. L. <sup>13</sup>C NMR rotating frame relaxation in a solid with strongly coupled protons: Polyethylene / D. L. Vanderhart, A. N. Garroway // *J.Chem.Phys.* - 1979. - Vol. 71. - P. 2773-2787.
- [3] Akasaka, K. Spin-spin and spin-lattice contributions to the rotating frame relaxation of C-13 in L-alanine / K. Akasaka, S. Ganapathy, C. A. McDowell, A. Naito // *J.Chem.Phys.* - 1983. - Vol. 78. - P. 3567-3572.
- [4] Tekely, P. Attenuation of spin-spin effects in C-13 T1rho NMR experiments by multipulse proton homonuclear decoupling / P. Tekely, D. Canet, J. J. Delpuech, J. Virlet // *Magn.Reson.Chem.* - 1990. - Vol. 28. - P. S10-S14.
- [5] Krushelnitsky, A. Expanding the frequency range of the solid-state T1. experiment for heteronuclear dipolar relaxation / A. Krushelnitsky, R. Kurbanov, D. Reicher, G. Hempel, H. Schneider, V. Fedotov // *Solid State Nucl.Magn.Reson.* - 2002. - Vol. 22.- P. 423-438.
- [6] Veshtort, M., SPINEVOLUTION: A powerful tool for the simulation of solid and liquid state NMR experiments/ M. Veshtort, R.G. Griffin// *J. Magn. Reson.* – 2006. – Vol. 178. – P. 248-282.

## Obtaining spatial structure of cyclosporine (Csa) in chloroform using 2D NMR

A.Y. Manin, S.V. Efimov, V.V. Klochkov

Kazan Federal University, 420008, Kremlevskaya str. 18, Kazan, Russia

e-mail: anton.manin@live.ksu.ru

### Introduction

In medicine, important role for today plays efficiency of medications. Hence, there is a problem in the biochemistry to reveal their possible impact and efficiency.

We have chosen cyclosporine (Csa) as an object for our research. Cyclosporine is a cyclic peptide which is used as immunosuppressive medication in transplantation. In cells, cyclosporine binds with the protein cyclophilin and, as a result, stops the reaction chain that is responsible for the immune response [1, 2, 3]. This peptide is poorly dissolved in water (23  $\mu\text{M}$  at 25<sup>0</sup>C), but in organic solvents its solubility is high [4].

The aim of our work was to analyze 1D and 2D NMR spectra, and to obtain spatial structure of cyclosporine using methods of mathematical simulation.

### Experimental results and discussion

Schematic structure of cyclosporine is shown in fig.1.

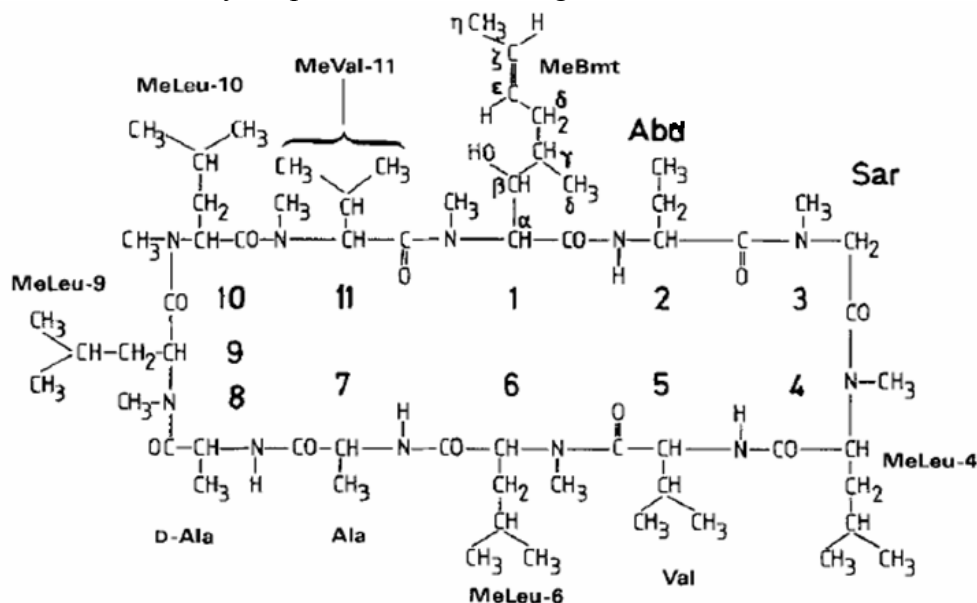


**Fig.1.** Schematic structure of cyclosporine - Bmt-Aba-Sar-Mle-Val-Mle-Ala-Dal-Mle-Mle-Val.

Let's consider main spectra that were used for the assignment of NMR signals.

At first, we used selective TOCSY spectra. Amide protons were excited, and as a result, we observed signals from the corresponding amino acids atoms. Also we have used 2D TOCSY which yields information about all signals of a certain amino acid. Due to this fact, it was used as the main method for assignment.

We obtained signals of carbons with the help of HSQC spectra and measured chemical shifts of attached protons. That method helped us in making assignment.

Also we have used important instrument called HMBC. Region of C=O groups allowed us to obtain chemical shifts of NCH<sub>3</sub> groups. If we connect that signals between each other and obtain the cycle, we can suggest that the assignment is correct. The demonstration of these words you can see in the fig.2.

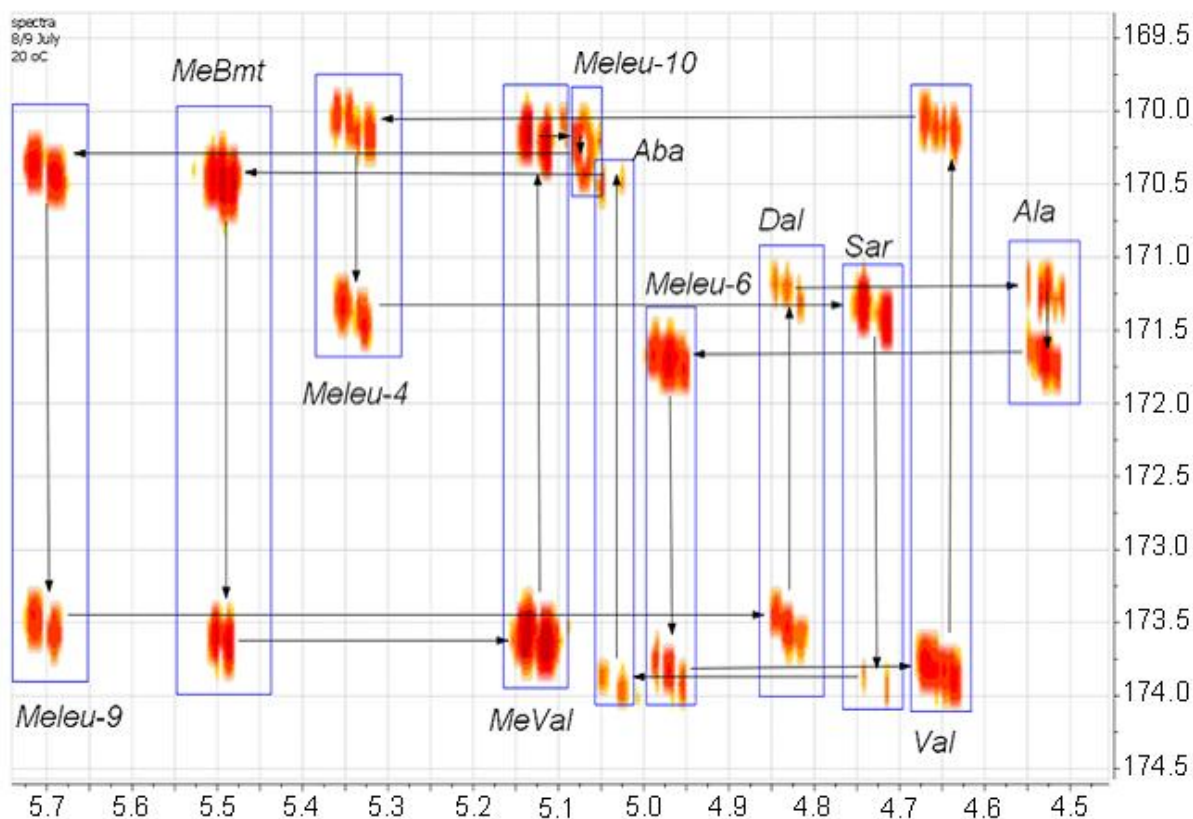


**Fig.2.** HMBC (<sup>1</sup>H 500 MHz) spectra of cyclosporine in chloroform at T=293 K. Region of C=O and NCH<sub>3</sub> groups is shown.

According to the analysis of 1D and 2D NMR spectra we have obtained the chemical shifts of all protons.

At the next step we had to obtain the distances between protons. For this purpose, we have used a set of NOESY spectra with different mixing times. After making integration, obtained intensities were normalized by the diagonal peaks. It was plotted as a function of the mixing time. The tangent of the angle of slope of obtained curve gave us the speed of the cross-relaxation. Then we used correlation  $\sigma_{pq} = \sigma_{ij}^0 \left( \frac{r_{pq}}{r_{ij}^0} \right)^6$ , where  $r_{ij}^0$  is reference distance between two nonequivalent  $\alpha$ -protons of Sar assumed to be 1.75 Å. After this calculation, interproton distances were obtained.

Knowledge of chemical shifts and distances between protons allowed us to use mathematical simulating to get the structure of cyclosporine molecule, which we are interested in. For this purpose, we used DYNAMO package [5], which is widely used for structural researches.

Obtained spatial structure of cyclosporine can be seen in fig.3.

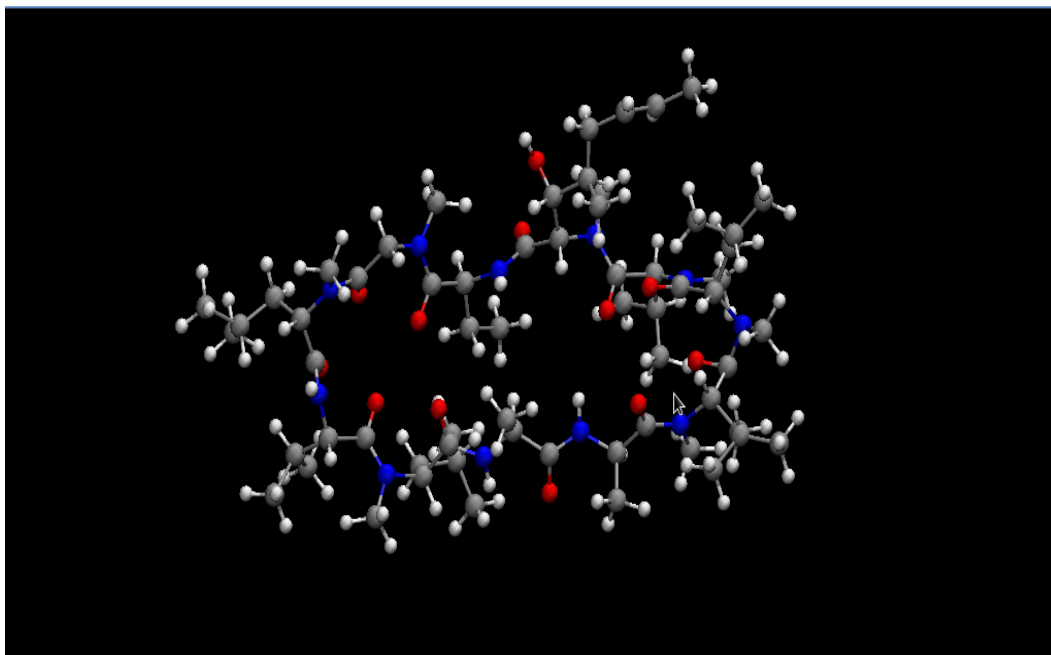


**Fig.3.** Spatial structure of cyclosporine(Csa) in chloroform.

This spatial structure is going to be used in our further research. It is interesting to see how cyclosporine interacts with cells membranes. For this purpose, we are going to use micelle solution of sodium dodecyl sulfate (SDS), which is shown in fig.4.

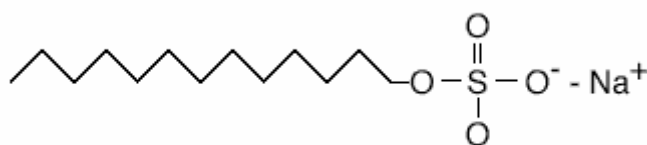


**Fig.4.** Structure of SDS molecule.

Obtained micelles may play role of cell membrane because of commensurable sizes [6].

### References

- [1] V.L. Hsu, S.L. Heald, M.W. Harding, R.E. Handschumacher and Ian M. Armitage, *Biochem. Pharm.* 40(1) (1990) 131-140.
- [2] C. Weber, G. Wider, B. von Freyberg, R. Traber, W. Braun, H. Widmer and K. Wuthrich, *Biochemistry* 30 (1991) 6563-6574.
- [3] S.W. Fesik, R.T. Gampe, H.L. Eaton, G. Gemmecker, E.T. Olejniczak, P. Neri, T.F. Holzman, D.A. Egan, R. Edalji, R. Simmer, R. Helfrich, J. Hochlowski and M. Jackson, *Biochemistry* 30 (1991) 6574-6583.
- [4] Yingqing Ran, Luwei Zhao, Qing Xu, S.H. Yalkowsky, *AAPS PharmSciTech* 2(1) (2001) 23-26.
- [5] F. Delaglio, S. Grzesiek, G. Vuister, G. Zhu, J. Pfeifer, A. Bax, *J. Biomol. NMR* 6 (1995) 277-293.
- [6] G.D. Henry and B.D. Sykes, *Meth. In Enzymol.* 239 (1994) 515-535.

## ESR Research of High-temperature Superconductor $\text{Bi}_2\text{Sr}_2\text{Ca}_{1-x}\text{Y}_x\text{Cu}_2\text{O}_8$

V. Sahin<sup>1</sup>, L. Salakhutdinov<sup>2</sup>, Yu. Talanov<sup>2</sup>

<sup>1</sup>Kazan Federal University, 420008, Kremlevskaya str. 18, Kazan, Russia

<sup>2</sup>Zavoisky Physical-Technical Institute, 420029, Sibirsky tract, Kazan, Russian Federation

e-mail: urfinjus67@gmail.com

### Introduction

Since it's discovering in 1986, high-temperature superconductivity wasn't explained with a conventional theory. And there is interesting fact that some properties, usually observed in superconductor state, is remains above  $T_c$ , for example, pseudogap [1], uncorrelated Cooper pairs [2], giant Nernst effect [3]. These properties are connected with magnetic state of HTSC, which is also doesn't have proper theoretical description. There was proposed a few models of magnetic state of HTSC above  $T_c$ , the model of vortex state (different from the Abrikosov vortex state), the model of stripe-structure (so-called "stripes" of antiferromagnetic state divided with paramagnetic state) [4]. None of the models was widely accepted, partly in case of low amount of experimental facts. So the aim of the work was to research the distribution of local magnetic fields in HTSC above  $T_c$  and try to correlate results with one of the models of magnetic state. The idea of the work is to use ESR, due to its powerful abilities to study the local magnetic field distribution of any origin.

An object of our research were two monocrystals of  $\text{Bi}_2\text{Sr}_2\text{Ca}_{1-x}\text{Y}_x\text{Cu}_2\text{O}_8$ , (Bi-2212) with  $x=0$  and  $x=0.4$ . Bi2212 is well-known HTSC material, so we hadn't necessity to research common properties of samples.

### Experimental results and discussion

To characterize samples we obtained temperature dependence of high-frequency magnetic susceptibility. It is shown in fig.1.

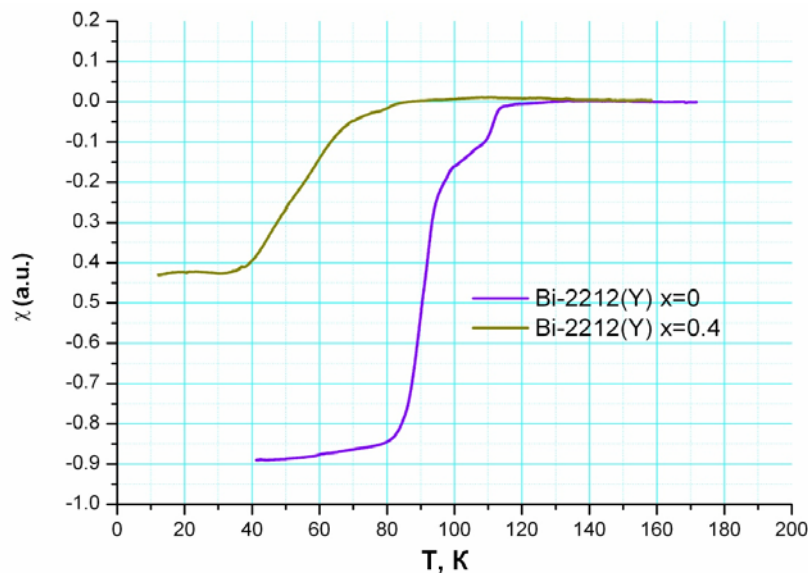


**Fig.1.** Temperature dependence of high-frequency magnetic susceptibility in  $\text{Bi}_2\text{Sr}_2\text{Ca}_{1-x}\text{Y}_x\text{Cu}_2\text{O}_8$  with  $x=0$  and  $x=0.4$

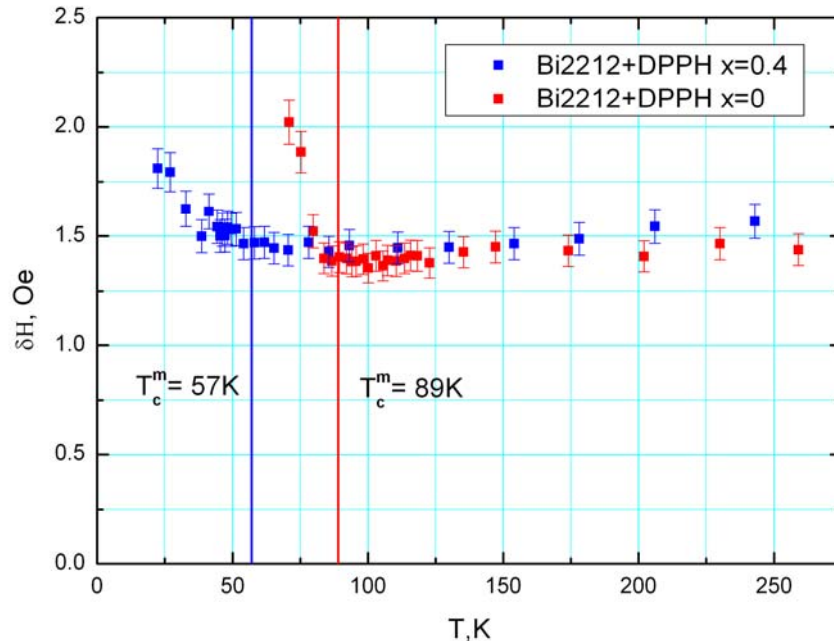
Value of  $T_c^m$  is defined as a middle of transition section. According to the fig.1  $T_c^m$  of sample with  $x=0$  is 89 K and  $T_c^m$  of sample with  $x=0.4$  is 57 K.

ESR signal of a Bi-2212 is very broad [4], so it can't be used to analyze in this research. To obtain the effects caused by magnetic state above  $T_c$  (which prospective value is 1-2 Oe) we need to use paramagnetic probes with a narrow ESR signal. In this study 2,2-diphenyl-1-picrylhydrazyl (DPPH) is used. It has a narrow Lorentzian ESR signal with line width of 1.2 Oe. Its resonance field at the spectrometer working frequency of 9.3 GHz is about 3300 Oe ( $g = 2.0036$ ). ESR signal of probe placed directly in area of distortions of local magnetic field is affected by this distortions and analyzing changes of parameters of the spectra can give us lot information about magnetic state of samples.

To place paramagnetic probe in the area of distortions of local magnetic fields we used the method of vacuum deposition, firstly proposed by Dulcic in 1989 [5]. The layer of DPPH was deposited on the surface of the Bi-2212. There are a few requirements to thickness of paramagnetic layer. First, layer shouldn't be too thin, because intensity of ESR spectra is in direct proportion to number of paramagnetic ions so the ESR signal of thin layer won't be clearly separated from the noise. Secondly, ESR signal of very thick layer will be determined by part of the layer, lying in homogeneous field. The characteristic distance between vortices in Abrikosov lattice estimated as 80-100 nm, so the thickness of the layer must be spanned in 100-200 nm. Thickness of deposited layer in this study was approximately 130 nm.

To take account of effects caused by DPPH itself we deposited same layer of paramagnetic on glass substrate.

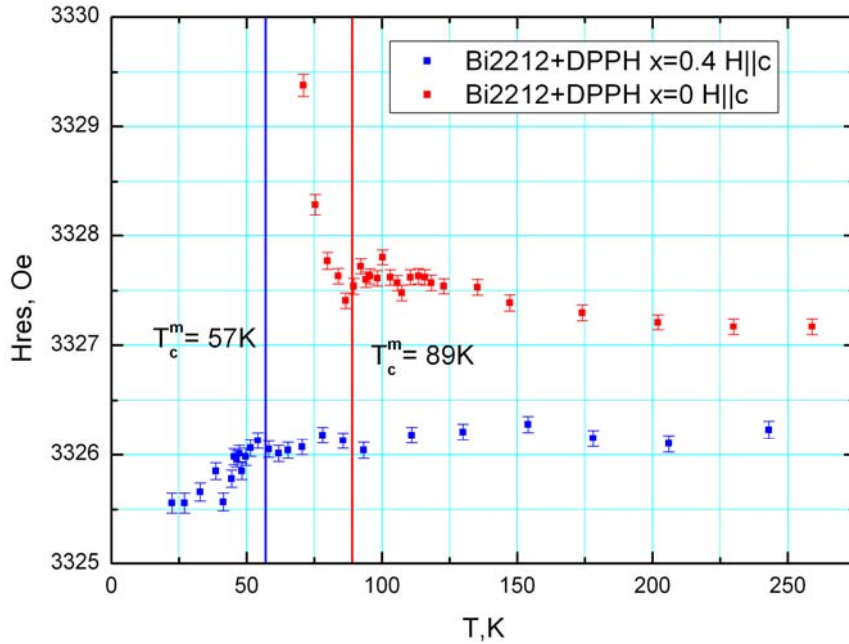
By recording and analyzing the EPR spectra, we obtained the temperature dependences of the ESR signal of DPPH for different samples. Fig.2 shows the temperature dependence of the line width of the ESR signal of DPPH deposited on a superconductor.



**Fig.2.** Temperature dependence of the line width of the ESR signal of DPPH for samples with  $x=0$  and  $x=0.4$

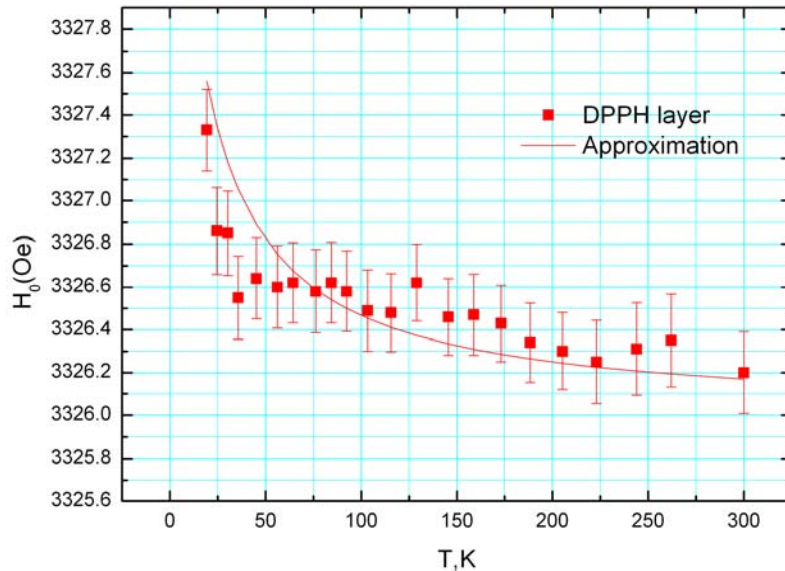
Above  $T_c$  width of the line is approximately equal for both samples, and below  $T_c$  line is broadening, what may be connected to superconducting transition and forming Abrikosov vortices. Broadening line of the sample with  $x=0.4$  is less dramatic and more unevenly than broadening line of the sample with  $x=0$ , we can propose phase inhomogeneity in sample with  $x=0.4$ .

Fig.3 shows the temperature dependence of the resonance field of the ESR signal of DPPH deposited on a superconductor.



**Fig.3.** Temperature dependence of the resonance field of the ESR signal of DPPH for samples with x=0 and x=0.4

As one may notice, DPPH is paramagnetic. So before analyzing this dependence we must take account of demagnetization field of paramagnetic, which can make a contribution in a value of resonance field. Fig.4 shows the temperature dependence of resonance field of the ESR signal of DPPH deposited on glass substrate.



**Fig.4.** Temperature dependence of the resonance field of the ESR signal of DPPH deposited on glass substrate and approximation by a theoretical function

As the temperature decreases, the value of the resonance field of DPPH follows the law  $H_{res}=H_0(1-4\chi\pi)$ , where susceptibility of DPPH follows the law  $\chi\sim 1/T$ . This results in additional contribution to the shift of the resonance field of a thin film of DPPH. This

contribution was subtracted and result – temperature dependence of the resonance field of ESR signal of DPPH caused by magnetic state of HTSC (fig.5)

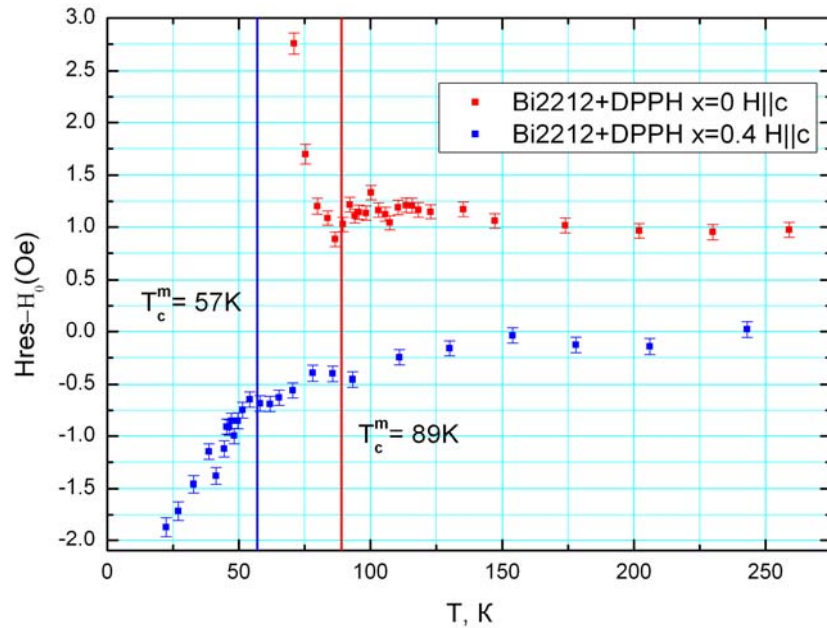


**Fig.5.** Temperature dependence of the resonance field of the ESR signal of DPPH for samples with  $x = 0$  and  $x = 0.4$

According to temperature dependence of the sample with  $x=0.4$ , we observe continuous shift of the resonance field to lower fields, although forming Abrikosov vortex lattice must result in shift of the resonance fields to the higher fields. In consideration of temperature dependence of line width of this sample, we can draw a conclusion about phase inhomogeneity of this sample.

For sample with  $x=0$  we observe moderate shift to the higher fields above  $T_c$ , with decreasing the temperature we observe shift to the lower fields, caused by transition processes and below  $T_c$  there is dramatic shift to the higher fields related to forming of the Abrikosov vortices. Shift above  $T_c$  may be caused by inhomogeneity of distribution of local magnetic fields, that can be both stripe-structure and vortices.

To make a certain choice of a model of magnetic state above  $T_c$  we plan to continue research.

## References

- [1] Patrick A. Lee, Naoto Nagaosa, Xiao-Gang Wen, Reviews of modern physics (2006), vol.78, 17-85
- [2] Kenjiro K. Gomes, Abhay N. Pasupathy, Aakash Pushp, Shimpei Ono, Yoichi Ando & Ali Yazdani, Nature B(2007) Vol. 47 569-572.
- [3] Y. Wang, L. Li, N. Ong, Phys. Rev. B.73, 024510 (2006).
- [4] Gaojie X. et al. Microstructure, localized  $Cu^{2+}$  spin, and transport properties of  $Bi_2Sr_2Ca_{1-x}Y_xCu_2O_{8+y}$ , Phys. Rev. B.- 2000.- V.62. N.13.- P.9172-9178
- [5] B. Rakvin, M. Pozek, A. Dulcic, Solid State Commun (1989) Vol.72 no.2 199-204

## Theory of electronuclear cross-relaxation in transient regime of EPR

E.I. Baibekov

Kazan Federal University, 420008, Kremlevskaya 18, Kazan, Russian Federation

e-mail: edbaibek@yandex.ru

### Introduction

Rabi oscillations (ROs), or transient nutations, represent transitions between the states of magnetic particle driven by electromagnetic wave of resonant frequency [1]. As is well-known [2, 3], the relaxation dynamics of the spin system in transient regime differs from the one when resonant microwave (MW) field is absent; more importantly, it often contradicts to the predictions of conventional Bloch equations (“anomalous decay” of ROs [2, 3]). At sufficiently low spin concentrations the relaxation originates mostly from long-range magnetic dipole (MD) interactions. As usual [4], we can distinguish between the spins of *A* and *B* types. The first, *A*, have Larmor frequencies close to resonance and thus are driven by the resonant transient pulse. The second group, *B*, contains spins with precession frequencies far from resonance. The decay of ROs in the system of only *A* spins was considered in refs. [3, 5]. An opposite case when a single *A* spin interacts with the bath of *B* spins was investigated in [6]. An example of such a system is a central electronic spin coupled to a nuclear spin bath (central spin model [7]). In the present work we consider the specific case when Rabi frequency of spin *A* is comparable to Larmor frequencies of spins *B*. This situation is quite reachable in EPR experiment since the ratio of the electronic and nuclear magnetic moments is  $\sim 10^3 - 10^4$  and thus of the same order as usual ratio of static and MW magnetic fields  $B_0 / B_1$ . In ref. [6] this particular case was entirely omitted: only secular parts of electronuclear interaction were left in the effective Hamiltonian and the decay of ROs of the central spin was caused by its dephasing due to random magnetic fields from nearby nuclei. On the contrary, we concentrate here on the nonsecular parts of MD interaction responsible for mutual electronuclear spin flips – an analogue of the cross-relaxation process in conventional relaxation theory except for these flips occur in a reference frame associated with rotating MW field vector  $\mathbf{B}_1$ . We will show that the decoherence of the central spin under above-mentioned condition is enhanced by the presence of nuclear spin bath and present a simple model based on perturbation theory which allows to calculate the corresponding relaxation rates of ROs. The predictions of the theory are justified by recent experimental studies of the relaxation dynamics in  $V_{15}$  molecular magnet [8].

### Theory

We consider a central electron spin  $S = 1/2$  surrounded with a bath of  $N$  nuclear spins  $I = 1/2$  placed in static magnetic field  $\mathbf{B}_0 \parallel z$  and transverse MW field  $2\mathbf{B}_1 \cos \omega_0 t \parallel x$  ( $B_0 \gg B_1$ ). We start from the following Hamiltonian:

$$H = \hbar \omega_e S_z + 2\hbar \Omega_R S_x \cos \omega_0 t + \hbar \sum_j \omega_j I_z^j + \hbar \sum_{\substack{j \\ \alpha=x,y,z}} A_{z\alpha}^j S_z I_\alpha^j, \quad (1)$$

where  $\omega_e = \gamma_e B_0$  is Larmor frequency of the central spin,  $\Omega_R = \gamma_e B_1$  is Rabi frequency and  $\omega_j$  are Larmor frequencies of nuclear spins distributed around  $\omega_N = \gamma_N B_0$  ( $\gamma_e$  and  $\gamma_N$  being electronic

and nuclear gyromagnetic ratios). The last term in (1) represents superhyperfine (in particular, MD) interactions between the central spin and nuclear spins. We neglect out-of-resonance interaction of nuclei with MW field, as well as terms  $\sim S_x, S_y$  in the superhyperfine interaction which do not commute with the electronic Zeeman interaction.

Let us rewrite Eq. (1) in the reference frame (RF) defined by the following transformation of the system wave function  $\Psi$  :

$$\Psi' = R\Psi, \quad R = \exp\left[i\left(\omega_0 S_z + \sum_j \omega_j I_z^j\right)t\right]. \quad (2)$$

The above transformation corresponds to local rotations of coordinate systems of the central spin and nuclear spins around  $\mathbf{B}_0$  with frequencies  $\omega_0$  and  $\omega_j$ , respectively. Neglecting highly oscillating terms  $\sim e^{2i\omega_0 t}$ , we obtain:

$$H' = \hbar\varepsilon S_z + \hbar\Omega_R S_x + \hbar S_z \sum_j \left\{ A_{zx}^j (I_x^j \cos \omega_j t - I_y^j \sin \omega_j t) + A_{zy}^j (I_x^j \sin \omega_j t + I_y^j \cos \omega_j t) + A_{zz}^j I_z^j \right\}, \quad (3)$$

where  $\varepsilon = \omega_e - \omega_0$  is the shift of the Larmor frequency of the central spin from resonance. Performing another transformation,

$$\tilde{S}_x = (\Omega_R S_x + \varepsilon S_z)/\Omega, \quad \tilde{S}_y = S_y, \quad \tilde{S}_z = (\Omega_R S_z - \varepsilon S_x)/\Omega, \quad (4)$$

we rewrite Eq. (3) as

$$H' = \hbar\Omega \tilde{S}_x + \frac{\hbar}{2\Omega} (\Omega_R \tilde{S}_z + \varepsilon \tilde{S}_x) \sum_j \left\{ \left[ (A_{zx}^j - iA_{zy}^j) e^{i\omega_j t} I_+^j + c.c. \right] + 2A_{zz}^j I_z^j \right\} = H_0' + V(t), \quad (5)$$

where  $I_{\pm}^j = I_x^j \pm iI_y^j$ , and  $\Omega = \sqrt{\varepsilon^2 + \Omega_R^2}$  is the frequency of nutation of the central spin around  $\tilde{x}$  axis in RF. In the absence of MD interactions, the eigenstates of the central spin in RF are those of  $\tilde{S}_x$  operator:  $\tilde{S}_x |\pm\rangle = \pm \frac{1}{2} |\pm\rangle$ . The interaction  $V(t)$  induces the decay of Rabi oscillations via:

(i) First-order ( $\tilde{S}_x I_z^j$  terms) and second-order ( $\tilde{S}_z I_z^j$ ) dephasing of spin magnetization. The former mechanism is relevant only for spins quite out of resonance (with  $\varepsilon > \Omega_R$ ). The latter dominates the relaxation of transient nutations when the nuclear spin bath has no spectral components near frequency  $\Omega$  [6].

(ii) Cross-relaxation processes  $|\pm\rangle |\downarrow_j\rangle \leftrightarrow |\mp\rangle |\uparrow_j\rangle$  induced by  $\tilde{S}_z I_{+(-)}^j$  terms, where  $|\uparrow_j\rangle, |\downarrow_j\rangle$  are nuclear spin-up and spin-down states  $I_z^j |\uparrow(\downarrow)_j\rangle = \pm \frac{1}{2} |\uparrow(\downarrow)_j\rangle$ . The energy exchange between the central spin and a nucleus is most effective when resonance condition is fulfilled, i.e.  $\omega_j$  is close to  $\Omega$ . The probability of transition  $P_{|+\rangle \rightarrow |-\rangle} = P_{|-\rangle \rightarrow |+\rangle} = P$  of the central spin with nutation frequency  $\Omega$  at time  $t$  is estimated in the first order of the time dependent perturbation theory as

$$P(\Omega, t) = 2^{-N} \sum_{\{m_l\}} \sum_j \left| \frac{1}{i\hbar} \int_0^t d\tau \langle -, \{m_l\} | V(\tau) | +, \{m_l\} \rangle e^{-i\Omega\tau} \right|^2. \quad (6)$$

Here, in order to get rid of nuclear variables, averaging over initial nuclear spin bath state  $2^{-N} \sum_{\{m_i\}}(\dots)$  and summation over its final state  $\sum_j(\dots)$  is maintained. A set  $\{m_i\} = (m_1, m_2, \dots, m_N)$  denotes the initial configuration of  $N$  nuclear spins ( $m_i = \uparrow, \downarrow$ ),  $\{m'_i\}$  is the final configuration with  $j$ -th spin flipped. The calculation of matrix elements in (6) is straightforward. If  $N$  is sufficiently high, we can introduce averaging over nuclear spins' frequencies  $\omega_j$  and coordinates  $\mathbf{r}_j$ . Thus, we replace  $2^{-N} \sum_{\{m_i\}}(\dots)$  with the integral  $\int d\omega_j \rho(\omega_j)(\dots)$  and  $\sum_j(\dots)$  with  $N \langle \dots \rangle_{\mathbf{r}_j}$ , where  $\rho(\omega_j)$  is the distribution density of nuclear frequencies and  $\langle \dots \rangle_{\mathbf{r}_j}$  denotes averaging over  $\mathbf{r}_j$ , so that

$$P(\Omega, t) = \frac{\sigma_e^2 \Omega_R^2}{\Omega^2} \int d\omega \rho(\omega) \left\{ \frac{\sin^2\left(\frac{\Omega - \omega}{2} t\right)}{(\Omega - \omega)^2} + \frac{\sin^2\left(\frac{\Omega + \omega}{2} t\right)}{(\Omega + \omega)^2} \right\}. \quad (7)$$

Here  $\sigma_e = \sqrt{\frac{N}{8} \langle (A_{zx}^j)^2 + (A_{zy}^j)^2 \rangle_{\mathbf{r}_j}}$  is the effective local field induced by nuclear spins at the site of the central spin. The function  $\rho(\omega)$  can be well approximated by the Gaussian  $\rho(\omega) = (\sqrt{2\pi}\sigma_N)^{-1} \exp[-(\omega - \omega_N)^2 / (2\sigma_N^2)]$ , as usual in the theory of magnetic resonance line broadening [9].

Now we consider an ensemble of  $n_0$  central spins with the same nutation frequency  $\Omega$ . If we denote the number of central spins at the moment  $t$  still in coherent motion as  $n(t)$  (with  $n(0) = n_0$ ), then  $dn/n = -dP(\Omega, t)$ , and thus  $n(t) = n_0 e^{-P(\Omega, t)}$ . Suppose that electron spins comprise an inhomogeneously broadened ESR line of spectral density  $g(\varepsilon)$ . Then the evolution of the recorded  $z$ -projection of magnetization is as follows:

$$M_z(t) \sim \int d\varepsilon g(\varepsilon) \frac{\varepsilon^2 + \Omega_R^2 \cos \Omega t}{\Omega^2} e^{-P(\Omega, t)}. \quad (8)$$

In the absence of relaxation ( $\Omega \neq \omega_N$ ) the exponential factor in Eq. (8) vanishes. Further we consider a typical case in EPR when the standard deviation  $\sigma$  of the distribution  $g(\varepsilon)$  exceeds  $\Omega_R$ . When  $\Omega_R t \gg 1$ , one obtains  $M_z(t) \sim t^{-1/2} \cos(\Omega_R t + \pi/4) + \text{const}$ , where a slow polynomial decay  $\sim t^{-1/2}$  is due to superposition of oscillations of spins with different shifts  $\varepsilon$  [10]. However, as  $\Omega$  approaches  $\omega_N$ , the factor  $e^{-P(\Omega, t)}$  in Eq. (8) becomes important. While the exact relaxation dynamics depends on the properties of the system under consideration (namely, the values of model parameters  $\sigma_e$  and  $\sigma_N$ ) and can be obtained only by numeric integration in Eq. (8), the general properties of the decay of ROs may be derived also. Roughly, electronic spins with nutation frequencies falling into the range  $\omega_N - \sigma_e < \Omega < \omega_N + \sigma_e$  result in  $P(\Omega, t) \sim 1$  and

thus effectively take part in cross-relaxation processes. Since  $\Omega \geq \Omega_R$ , the number of spin packets excited by MW pulse is maximal when  $\Omega_R \approx \omega_N - \sigma_e$  which gives us the first maximum of the relaxation rate near  $\omega_N - \sigma_e$ . Also, there appears to be the second maximum at  $\Omega_R \approx \omega_N$ . Its position corresponds to the resonance condition  $\Omega = \omega_N$  (the first term of Eq. (7)) for the spin packet with  $\Omega = \Omega_R$ . This most "coherent" spin packet is responsible for Rabi oscillations at  $\Omega_R t \gg 1$  when other packets  $\Omega > \Omega_R$  are already dephased. The expected width of this second maximum is  $\sim 2\sigma_N$ . All of the features mentioned are present in the experimental relaxation data for  $V_{15}$  molecular magnet [8]. There the central spin corresponds to collective spin  $S = 3/2$  of  $V_{15}$  cluster surrounded by a nuclear bath of  $N = 38$  protons and the values of  $\sigma_e$  and  $\sigma_N$  can be either approximately estimated or obtained from the fit to experimental decay data.

### Conclusions

A phenomenon of electronuclear cross-relaxation in transient regime of EPR was studied theoretically. The relaxation rates of transient nutations were calculated in the framework of the 1<sup>st</sup> order perturbation theory. The qualitative predictions of the theory are justified by recent experimental studies of the relaxation dynamics in  $V_{15}$  molecular magnet [8].

### Acknowledgments

Author is grateful to B.Z. Malkin for advice and fruitful discussions of the results. This work was supported by the RFBR grant 09-02-00930 and by Dynasty foundation.

### References

- [1] I. I. Rabi, Phys. Rev. **51**, 652 (1937).
- [2] R. Boscaino, F. M. Gelardi, J. P. Korb, Phys. Rev. B **48**, 7077 (1993).
- [3] S. Agnello, R. Boscaino, M. Cannas, F. M. Gelardi, R. N. Shakhmurov, Phys. Rev. A **59**, 4087 (1999).
- [4] B. Herzog, E. L. Hahn, Phys. Rev. **103**, 148 (1956).
- [5] E. I. Baibekov, JETP Letters **93**, 292 (2011).
- [6] V. V. Dobrovitski, A. E. Feiguin, R. Hanson, D. D. Awschalom, Phys. Rev. Lett. **102**, 237601 (2009).
- [7] P. C. E. Stamp, I. S. Tupitsyn, Phys. Rev. B **69**, 014401 (2004).
- [8] J. H. Shim, S. Gambarelli, S. Bertaina, T. Mitra, B. Tsukerblat, A. Müller, B. Barbara, arXiv:1006.4960v2.
- [9] A. Abragam, *The Principles of Nuclear Magnetism*, Clarendon Press, Oxford (1961).
- [10] H. C. Torrey, Phys. Rev. **76**, 1059 (1949).

## Synthesis of nanosized PrF<sub>3</sub> powders and their low temperature magnetism study

E.M. Alakshin<sup>1</sup>, R.R. Gazizulin<sup>1</sup>, A.T. Gubaidullin<sup>2</sup>, A.V. Klochkov<sup>1</sup>, S.L. Korableva<sup>1</sup>,  
V.V. Kuzmin<sup>1</sup>, A.M. Sabitova<sup>1</sup>, M.S. Tagirov<sup>1</sup>

<sup>1</sup>Kazan (Volga region) Federal University, Kremlevskaya, 18, 420008, Kazan, Russia

<sup>2</sup>A.E. Arbuzov Institute of Organic and Physical Chemistry of Kazan Scientific Center of Russian Academy of Sciences, Ac. Arbuzov street, 420088, Kazan, Russia

e-mail: [sabitovaalsu@gmail.com](mailto:sabitovaalsu@gmail.com)

### Introduction

The “PrF<sub>3</sub> – liquid <sup>3</sup>He” system is of interest because of the possibility of using the magnetic coupling between the nuclei of the two spin systems for the dynamic nuclear polarization of liquid <sup>3</sup>He. Van Vleck paramagnets are known to have high anisotropy of the effective nuclear magnetogyric ratio and for <sup>141</sup>Pr in PrF<sub>3</sub>  $\gamma_x/2 = 3.322$  kHz/Oe,  $\gamma_y/2 = 3.242$  kHz/Oe,  $\gamma_z/2 = 10.03$  kHz/Oe, while for <sup>3</sup>He  $\gamma/2 = 3.243$  kHz/Oe. As a result, a direct interaction between magnetic moments of equal magnitude at the liquid <sup>3</sup>He–solid state substrate interface becomes possible.

The resonance magnetic coupling between liquid <sup>3</sup>He nuclei and the <sup>141</sup>Pr nuclei in microsized (45  $\mu$ m) Van Vleck paramagnet PrF<sub>3</sub> powder has been discovered by authors [1]. Using nanosized PrF<sub>3</sub> powder would create a highly-coupled <sup>3</sup>He – <sup>141</sup>Pr spin system and could show new aspects of effects discovered earlier. From the other hand, the low temperature magnetism of nanosized PrF<sub>3</sub> powders could exhibit new features, compare to the magnetism of bulk Van Vleck paramagnet PrF<sub>3</sub> due to the great impact of huge surface area of a sample. Besides, the influence of quantum confinement in the case of nanoscopic samples also could give some additional effects. Thus, synthesis of nanosized PrF<sub>3</sub> powders and study of their low temperature magnetism is very interesting goal.

The method of synthesis of PrF<sub>3</sub> nanoparticles described in [2] was tested earlier [3] by authors. Development of various methods for PrF<sub>3</sub> nanoparticles synthesis described in [4].

### The Samples

The crystal structure of the samples has been characterized by X-ray diffraction (XRD) (fig.1). All of the diffraction peaks can be readily indexed from the standard powder diffraction data of the hexagonal phase PrF<sub>3</sub>. Fig.1 also confirms the hexagonal phase of the of PrF<sub>3</sub> particles crystal structure. As shown in fig.1, the narrow and sharp peaks indicate high crystallinity of the samples. Basically, there are no differences in the XRD results between all 6 samples, so chosen different synthesis methods did not affect the crystal structure of nanoparticles, detectable by XRD method.

High-resolution transmission electron microscopy (HRTEM) images for 6 synthesized PrF<sub>3</sub> samples were obtained by using JEM — 4000ex with resolution — 0.16 nm using an accelerating voltage of 400 kV [4]. It is clear, that precursors of chemical reaction have great influence on the shape of synthesized nanoparticles.

The dependence of characteristic size for all 6 synthesized samples of the hydrothermal reaction time is presented on the fig.2.

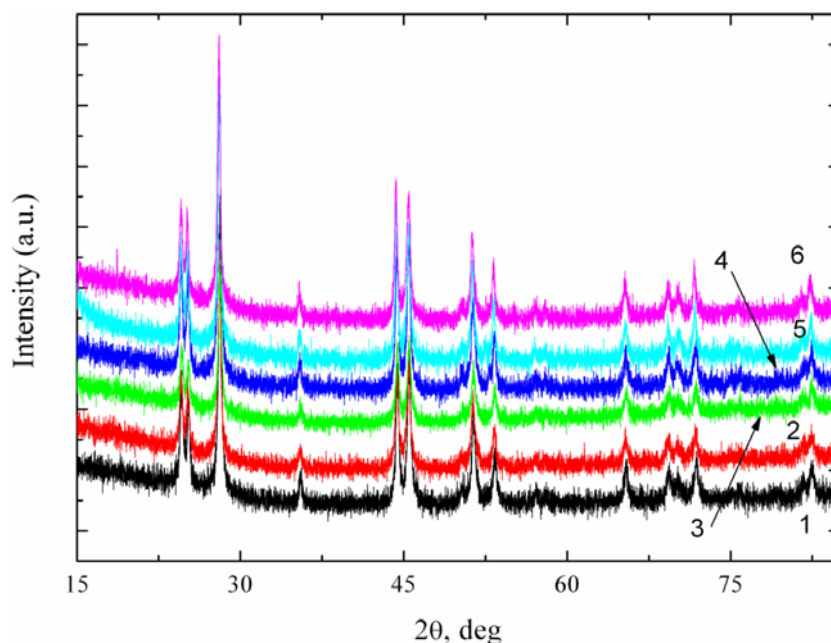


**Fig.1.** XRD results of PrF<sub>3</sub> samples.

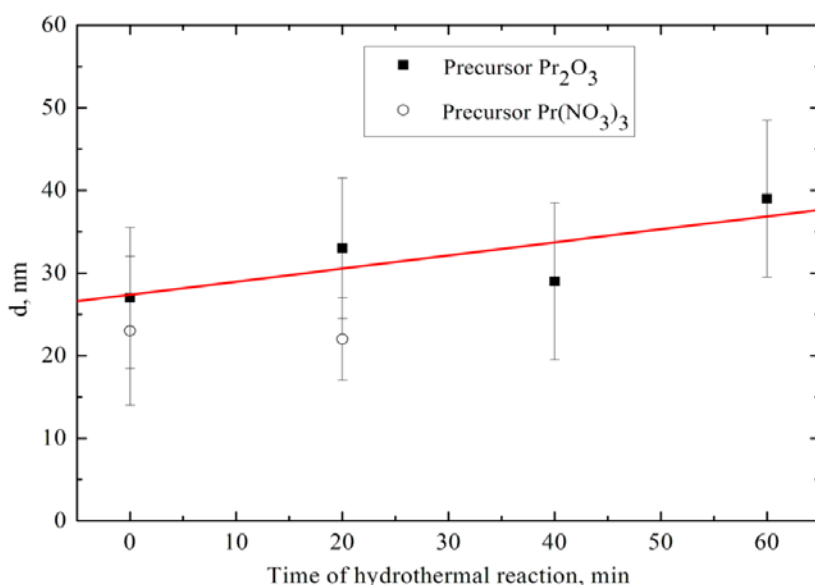


**Fig.2.** The dependence of characteristic size of the hydrothermal reaction time.

### Experiment and Results

The pulse NMR spectrometer is equipped with a resistive electrical magnet that has a magnetic field strength up to 1 T. All experiments were done at the temperature  $T = 1.5$  K, which was achieved by helium bath pumping. The longitudinal magnetization relaxation time  $T_1$  of <sup>141</sup>Pr was measured by the saturation recovery method using a spin-echo signal.

The resonance NMR spectra of the powdered PrF<sub>3</sub> samples were measured at frequencies of 6.63 MHz (fig.3). In conclusion, the NMR <sup>141</sup>Pr spectra at the frequency 6.63 MHz of synthesized PrF<sub>3</sub> nanopowders do not differ significantly. The magnetic field dependences of the longitudinal magnetization relaxation of <sup>141</sup>Pr and <sup>19</sup>F nuclei measured by pulse NMR technique in PrF<sub>3</sub> nanopowders are presented in fig.4. It was shown that the growing of particle sizes and hydrothermal reaction time leads to the increasing of the <sup>19</sup>F and <sup>141</sup>Pr spin-lattice relaxation times.

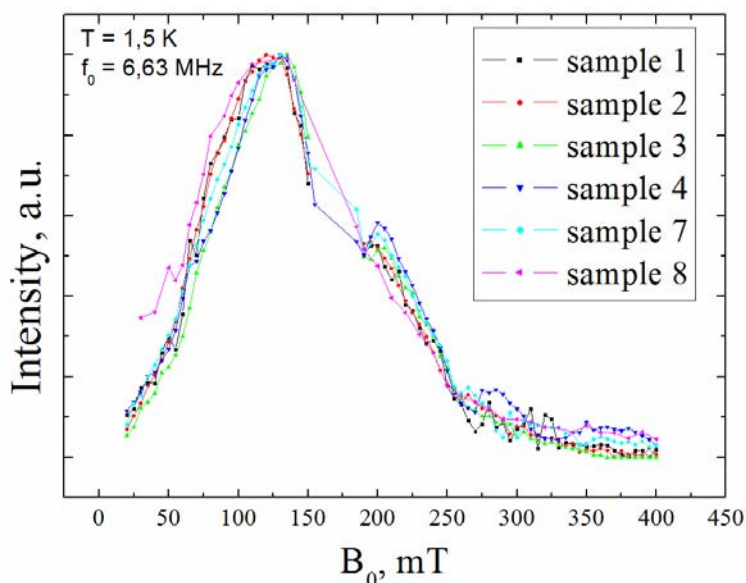


**Fig.3.** Spectra of  $^{141}\text{Pr}$  in  $\text{PrF}_3$  powders at the frequency 6.63 MHz.

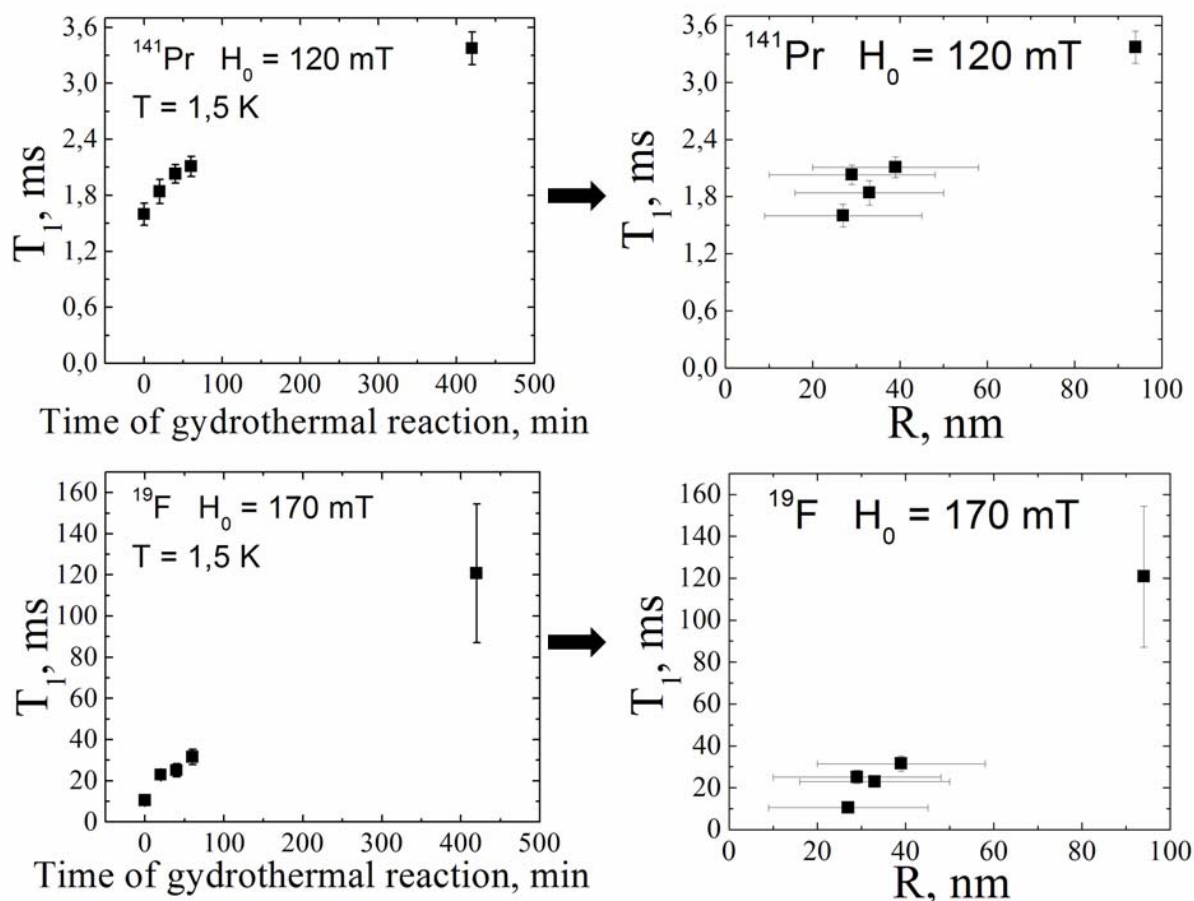


**Fig.4.** The longitudinal magnetization relaxation of  $^{141}\text{Pr}$  in  $\text{PrF}_3$  powders at the frequency 6.63 MHz.

### Acknowledgments

This work is partially supported by the Ministry of Education and Science of the Russian Federation (FTP "Scientific and scientific - pedagogical personnel of the innovative Russia" GK- P900).

**References**

- [1] A.V. Egorov et al., JETP Lett., **86**, 416 (2007).
- [2] L. Ma et al., Materials Letters, **61**, 2765 (2007).
- [3] E.M. Alakshin et al., J. Low. Temp. Phys., **162**, 645 (2011).
- [4] E.M. Alakshin et al., arXiv:**1104.0208** (2011)

## $^{59}\text{Co}$ ZFNMR study of $\text{YBaCo}_2\text{O}_{5+x}$ compound

L.A. Batalova<sup>1</sup>, I.R. Mukhamedshin<sup>1</sup>, A.N.Lavrov<sup>2</sup>

<sup>1</sup>Kazan University, Kremlevskaya str., 18, Kazan, 420008, Russia

<sup>2</sup>Institute of Inorganic Chemistry, Lavrentyeva str., 3, Novosibirsk, 630090, Russia

e-mail: batalova.liliya@yandex.ru

The 3d transition-metal oxides with perovskite-type structure show a wide variety of physical and structural properties, including giant magneto resistance, strong thermopower, temperature-driven spin-state and metal-insulator transitions. A unique feature, making them distinctive from manganites or cuprates, is the spin degree of freedom of Co ions.

To study the interplay between the charge and spin degrees of freedom of cobalt ions the cation-ordered phases of the  $\text{YBaCo}_2\text{O}_{5+x}$  compounds with different oxygen content  $x$  have been synthesized. In such system the changing of oxygen content leads to the doping variation of the  $\text{CoO}_2$  planes and can drastically change the physical properties of cobalt oxides. The phase diagram of the related compound  $\text{GdBaCo}_2\text{O}_{5+x}$  is quite rich and contains different types of charge and magnetic orders [1]. The phase diagram of the  $\text{YBaCo}_2\text{O}_{5+x}$  compound is quite similar to the  $\text{GdBaCo}_2\text{O}_{5+x}$  phase diagram [2] with significant differences in the values of the phase transition temperatures. As an example in fig.1 the temperature dependence of resistivity of  $\text{YBaCo}_2\text{O}_{5.5}$  and  $\text{GdBaCo}_2\text{O}_{5.5}$  compounds are shown - the temperature of metal-insulator transition  $T_{\text{MI}}$  changes from 361 K to 292 K by replacing gadolinium to yttrium ions.

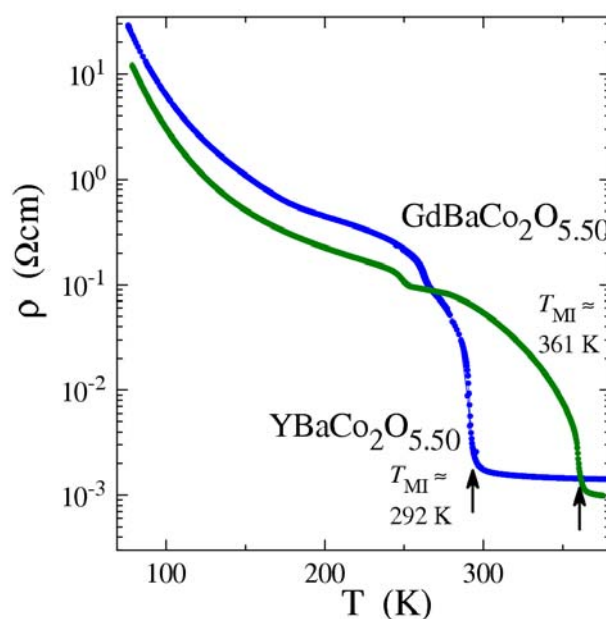


**Fig.1.** Comparison of the temperature dependence of resistivity of  $\text{YBaCo}_2\text{O}_{5.5}$  and  $\text{GdBaCo}_2\text{O}_{5.5}$  compounds.

Depending on the oxygen content the crystal structure of the  $\text{YBaCo}_2\text{O}_{5+x}$  compound also varies. In fig.2a the unit cell of  $\text{YBaCo}_2\text{O}_5$  compound is shown. The structure consists of stacked  $\text{BaO}$ ,  $\text{CoO}_2$ ,  $\text{YO}_x$ ,  $\text{CoO}_2$ , and  $\text{BaO}$  layers along the  $c$ -axis. All Co atoms in this unit cell are in square pyramidal coordination formed by five oxygen atoms (fig.2a) and the average charge state of Co ions is  $2.5+$  with a mix-valence state of  $\text{Co}^{2+}$  and  $\text{Co}^{3+}$ .

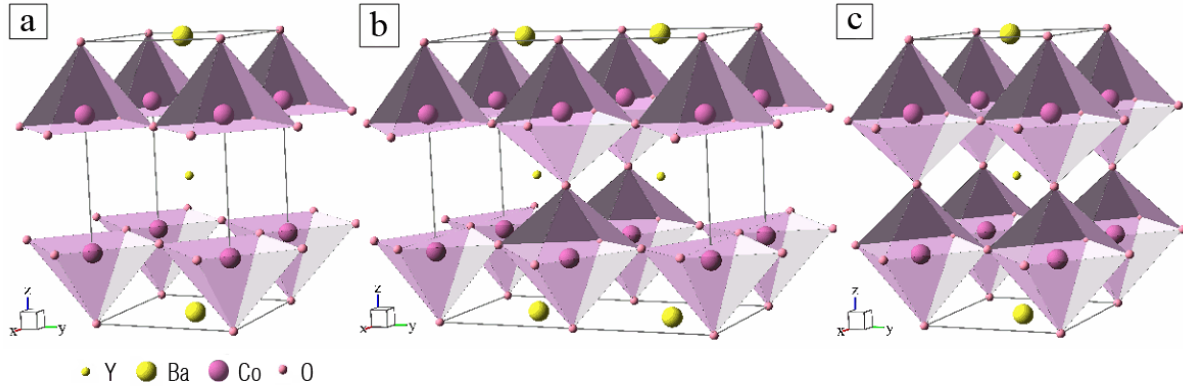


**Fig.2.** The unit cells of  $\text{YBaCo}_2\text{O}_{5+x}$  compound for different oxygen content  $x$ :  
 (a)  $a \times a \times 2a$  ( $x=0$ ), (b)  $a \times 2a \times 2a$  ( $x=0.5$ ), (c)  $a \times a \times 2a$  ( $x=1$ ).

In fig.2b an ideal 122 superstructure of  $\text{YBaCo}_2\text{O}_{5.5}$  is shown. In this unit cell half of Co atoms are in octahedral coordination, and the other half is in square pyramidal coordination (fig.2b). Therefore an alternative appearance of one-dimensional  $\text{CoO}_6$  octahedral and  $\text{CoO}_5$  square pyramidal chains running along the  $b$ -axis produces the 122 superstructure. The average valence of Co ions in such unit cell is  $3+$ .

In fig.2c the crystal structure of  $\text{YBaCo}_2\text{O}_6$  is shown. In this case the average charge state of Co ions is  $+3.5$  with a mix-valence state of  $\text{Co}^{3+}$  and  $\text{Co}^{4+}$ , and all Co atoms are in octahedral coordination.

In this work the several  $\text{YBaCo}_2\text{O}_{5+x}$  samples with the oxygen content  $x = 0.25$ ;  $0.3$ ;  $0.35$ ;  $0.4$ ;  $0.45$ ;  $0.50$  were studied. We have found that all studied samples at liquid helium temperature are magnetically ordered, therefore we observed the so-called Zero Field NMR (ZFNMR) signals of  $^{59}\text{Co}$  in all samples. In fig.3 the ZFNMR spectra of some samples are shown.

The spectra demonstrate the existence of several nonequivalent cobalt positions in the crystal structure as well as rapid change of the local magnetic fields with oxygen content changes. The ZFNMR spectra of  $\text{YBaCo}_2\text{O}_{5.25}$  and  $\text{YBaCo}_2\text{O}_{5.5}$  samples demonstrate relatively narrow lines in the spectra (fig.3) which proves the existence of oxygen order in these phases. In the samples with  $0.3 \leq x \leq 0.45$  the  $^{59}\text{Co}$  ZFNMR is quite broad and non-resolved. Therefore at these oxygen contents the oxygen order either doesn't exist or has more complicated pattern.

The fact that  $^{59}\text{Co}$  ZFNMR spectrum in our  $\text{YBaCo}_2\text{O}_{5.5}$  sample has less number of lines than in the work [3] proves the high quality and phase purity of our samples.

The nuclear spin-lattice and spin-spin relaxation times of  $^{59}\text{Co}$  at several frequencies in different samples also were measured. In fig.3 the values of  $T_1$  and  $T_2$  relaxation times at some frequencies are shown. As one can see the nuclear relaxation of cobalt ions change drastically with oxygen content. In the  $\text{YBaCo}_2\text{O}_{5.5}$  sample the different lines in the ZFNMR spectrum could be attributed to the cobalts with different spin state while in the other samples the situation is more complicated and needs additional study.

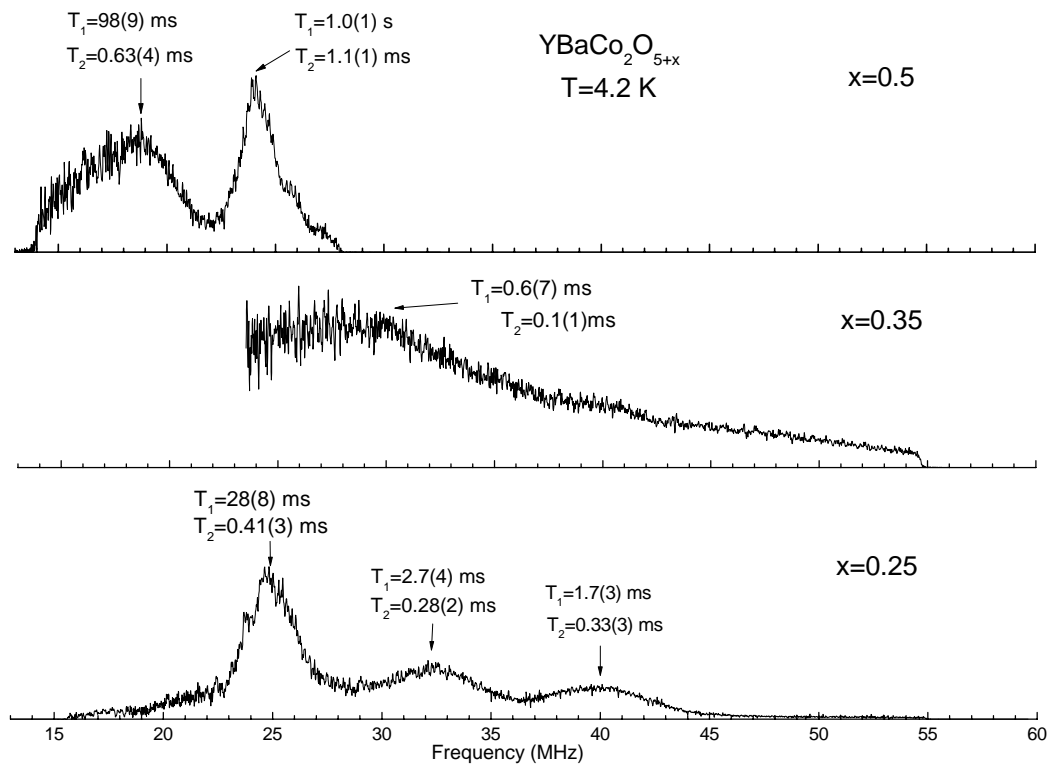


**Fig.3.** The examples of the  $^{59}\text{Co}$  ZFNMR spectra in  $\text{YBaCo}_2\text{O}_{5+x}$  compounds with  $x = 0.25, 0.35$  and  $0.5$ . The nuclear spin-lattice  $T_1$  and spin-spin relaxation  $T_2$  time values at several frequencies are shown.

### Acknowledgements

This work was partially supported by the RFBR (project №10-02-01005-a) and Ministry of Education and Science of the Russian Federation.

### References

- [1] A.A.Taskin *et al.*, Phys. Rev. B **71**, 134414 (2005).
- [2] D. Akahoshi *et al.*, Journal of Solid State Chemistry **156**, 355-363 (2001).
- [3] M. Itoh *et al.*, Physica B **329–333**, 751–752 (2003)

## <sup>59</sup>Co NQR study of Na<sub>0.71</sub>CoO<sub>2</sub> compound

T.A. Platova, I.R. Mukhamedshin, A.V. Dooglav

Kazan (Volga Region) Federal University, 420008, Kremlevskaya str., 18, Kazan, Russia.

e-mail: tanya.platova@gmail.com

The family of layered sodium cobaltates Na<sub>x</sub>CoO<sub>2</sub> ( $0 < x \leq 1$ ) has a rich phase diagram [1,2], which includes the most interesting scientific phenomena of present in condensed matter physics, such as superconductivity [3], spin density waves [4], magnetic frustration in a triangular lattice [5], coexistence of metallic conductivity and Curie-Weiss susceptibility [2]. These oxides may serve as a unique realistic test case for theoretical calculations concerning the doping possibility of a strongly correlated metal with geometrical frustrations [6]. Moreover, high ionic mobility and high Seebeck coefficient [7] allow to consider this compound for potential thermoelectric applications [8, 9].

Cobaltates consist of stacked triangular CoO<sub>2</sub> layers, held together by Na ions in between. Nominally, the oxidation state of cobalt ranges between Co<sup>4+</sup>(3d<sup>5</sup>) and Co<sup>3+</sup>(3d<sup>6</sup>), depending on the sodium content  $x$ .

The present work covers the investigations of Na<sub>≈0.71</sub>CoO<sub>2</sub> compound, or O71 phase in notations of the work [10]. As have been published [11, 12], in the narrow sodium range  $0.67 \leq x \leq 0.75$  three stable phases (H67, O71, H75) and two unstable (H72 and another one with  $x = 0.71 \div 0.72$ ) coexist. This was proved by X-ray analysis, susceptibility measurements, NMR [10] and NQR [12] data for <sup>23</sup>Na and <sup>59</sup>Co nuclei. The susceptibility of these phases differs significantly below 100 K and displays a Curie-Weiss behavior above 100 K [10]. This sodium concentration range bears our attention due to the occurrence of an A-type magnetic ordering at  $x=0.75$  and its absence at lower sodium content  $x < 0.75$ .

In paper [14] the crystal structure and ordering in Co and Na plane in H67 phase was determined. The O71 phase is intermediate between H67 and H75. It is important to understand how the ordering in the Na planes takes place and what kind of Na vacancies, di-vacancies or tri-vacancies, are present there together with the role these vacancies are playing in physical properties of material. This should shed more light on the origin of magnetic ordering and Curie-Weiss behavior.

In the present work we show the results of the NQR investigations of O71 phase. In NQR, nuclei with an electric quadrupole moment have their nuclear spin energy levels split by the electric field gradient (EFG) created by the electronic bonds in the local environment. So this technique is very sensitive to the nature of the bonding around the nucleus.

The standard  $\pi/2 - \tau - \pi$  pulse sequence has been used for forming the nuclear spin echo signal. Detailed NQR spectra were constructed using a Fourier mapping algorithm [15, 16]. Typical NQR spectra of <sup>59</sup>Co of the Na<sub>≈0.71</sub>CoO<sub>2</sub> compound (O71 phase) are shown in fig.1. We found that the number of lines and their intensities in the observed spectrum depend strongly on the delay  $\tau$  between pulses. This corresponds to the fact that the experimental spin-echo intensity depends on the rate of the spin-spin relaxation process. Consequently the fast relaxing nuclei are not observable at long enough delay between the pulses. In the spectrum observed with the shortest possible for our spectrometer at relatively low frequencies  $\tau_S = 45 \mu s$  there are 20 narrow intense lines and several lines with weaker intensity (fig.1). At the same time in the spectrum measured with  $\tau_L = 100 \mu s$ , the intensities of the high frequency lines greatly decrease, while the intensities of low frequency narrow lines at frequency range 2 – 4 MHz do not change much. It is experimentally clear that in the

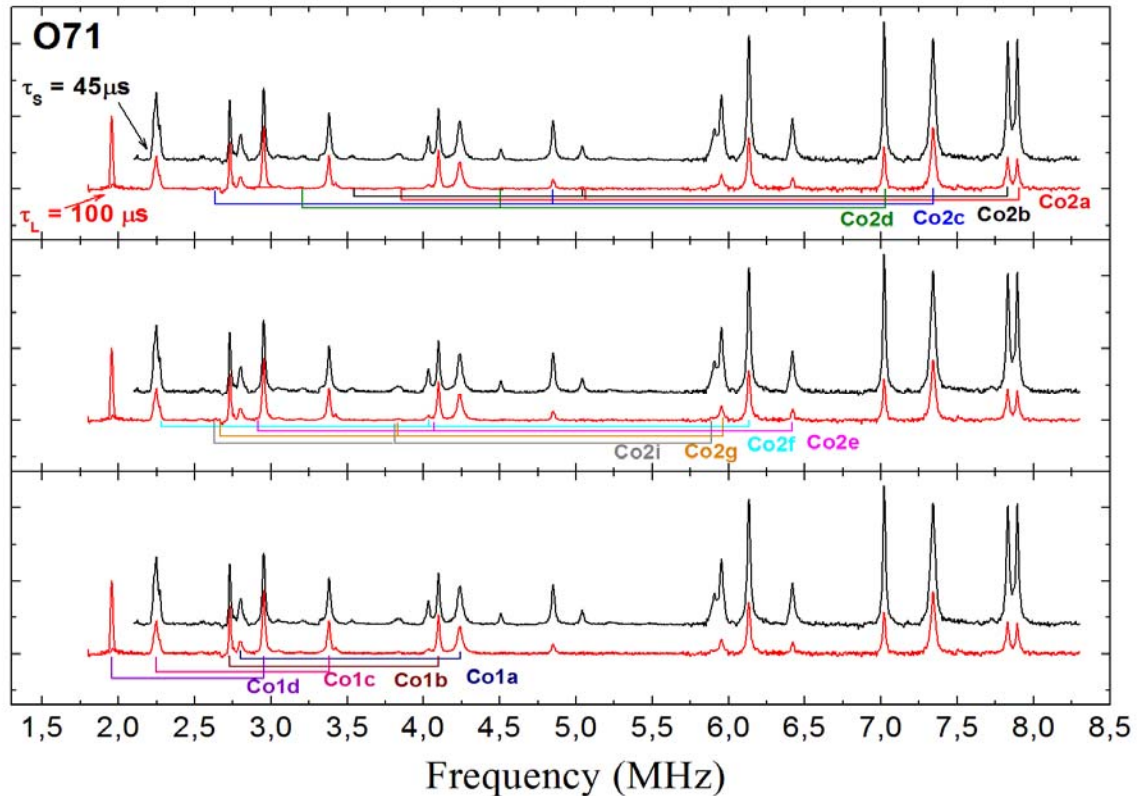


**Fig.1.** NQR spectra of  $^{59}\text{Co}$  in the O71 phase taken at 4.2 K for short ( $\tau_s = 45 \mu\text{s}$ ) and long ( $\tau_L = 100 \mu\text{s}$ ) delay between pulses. The 12 possible non-equivalent cobalt positions have been found from data analysis.

$x \approx 0.71$  phase at least two different types of Co exist – fast and slow relaxing, just as was already established for the  $\text{Na}_{2/3}\text{CoO}_2$  phase [17, 18]. The NQR lines of fast relaxing cobalts are labeled as Co2, slow relaxing — as Co1 in fig.1.

The nuclear spin of  $^{59}\text{Co}$  is  $I = 7/2$ , therefore for a single crystallographic site one should observe three lines in the NQR spectrum. The frequency positions of these lines depend both on quadrupole frequency  $\nu_Q$  and asymmetry parameter  $\eta$  — parameters of quadrupole Hamiltonian [19].

The identification algorithm of Co NQR spectra for H67 phase using the theoretical dependence of NQR frequencies of the allowed transitions on the asymmetry parameter of the EFG tensor for nuclear spin  $7/2$  was demonstrated in Ref. [18]. Such an analysis of  $^{59}\text{Co}$  NQR spectra of  $\text{Na}_{0.71}\text{CoO}_2$  compound allowed us to determine at least 12 non-equivalent Co positions. Frequency values of all transitions for each site, quadrupole frequencies  $\nu_Q$  and asymmetry parameters  $\eta$  are shown in table 1 for Co2 sites and in table 2 for Co1 sites. For simplification, Co positions have been divided in three groups according to the quadrupole frequency value or the frequency of the highest frequency transitions  $\pm 5/2 - \pm 7/2$ . The first group consists of four cobalts, Co2a, Co2b, Co2c and Co2d, with  $\pm 5/2 - \pm 7/2$  transition frequency at 7.89(1), 7.83(1), 7.34(1) and 7.02(1) MHz, respectively. The second group consists of Co2e, Co2f, Co2g and Co2i, with highest transitions at 6.42(1), 6.13(1), 5.95(1) and 5.90(1) MHz, and the cobalts of the third one are labeled as Co1a, Co1b, Co1c and Co1d with  $\pm 5/2 - \pm 7/2$  transitions at 4.24(1), 4.10(1), 3.38(1) and 2.95(1) MHz, respectively. In fig.1 all three groups are presented on the separate copy of spectra and labeled by different colors.

**Table 1.**

	Co2i	Co2g	Co2f	Co2e	Co2d	Co2c	Co2b	Co2a
$\pm 7/2 - \pm 5/2$ , MHz	5.91(1)	5.95(1)	<b>6.13(1)</b>	6.42(1)	7.02(1)	<b>7.34(1)</b>	7.83(1)	7.89(1)
$\pm 5/2 - \pm 3/2$ , MHz	3.80(1)	3.83(1)	<b>4.03(1)</b>	4.12(1)	4.51(1)	<b>4.85(1)</b>	5.04(1)	5.04(1)
$\pm 3/2 - \pm 1/2$ , MHz	2.65(1)	2.69(1)	<b>2.27(1)</b>	2.94(1)	3.21(1)	<b>2.63(1)</b>	3.51(1)	3.85(1)
$\nu_Q$ , MHz	1.99(1)	2.01(1)	<b>2.05(1)</b>	2.16(1)	2.36(1)	<b>2.45(1)</b>	2.64(1)	2.67(1)
$\eta$	0.33(1)	0.33(1)	<b>0.18(1)</b>	0.34(1)	0.34(1)	<b>0.14(1)</b>	0.33(1)	0.39(1)
$T_1$ , ms		1.02(1)	<b>1.32(1)</b>	0.84(1)	1.04(1)	<b>1.79(1)</b>	0.95(1)	0.89(1)
$T_2$ , mks	62(10)	90(10)	<b>155(10)</b>	110(10)	120(10)	<b>170(10)</b>	93(5)	88(5)

**Table 2**

	Co1d	Co1c	Co1b	Co1a
$\pm 7/2 - \pm 5/2$ , MHz	2.95(1)	3.38(1)	4.10(1)	4.24(1)
$\pm 5/2 - \pm 3/2$ , MHz	1.95(1)	2.25(1)	2.73(1)	2.80(1)
$\pm 3/2 - \pm 1/2$ , MHz	1.054(1)	1.15(1)	1.37(1)	1.52(1)
$\nu_Q$ , MHz	0.98(1)	1.12(1)	1.36(1)	1.41(1)
$\eta$ , NQR	0.14(1)	0.07(1)	0.04(1)	0.14(1)
$T_1$ (ms)	49(5)	25(1)	24(1)	12(1)
$T_2$ (mks)	395(10)	382(10)	340(10)	350(10)

As it comes out from the interpretation of spectrum, the Co positions could be divided in three groups with different values of asymmetry parameter: six Co2 (a, b, d, e, g and i) with  $\eta \approx 0.34(5)$ , four Co2c, Co2f, Co1a and Co1d with  $\eta \approx 0.15(3)$  and two sites with nearly axial symmetry, Co1b and Co1c, with  $\eta \approx 0.03(3)$ .

To study the nuclear spin-lattice relaxation (NSLR) process we have used the magnetization inversion recovery method with three pulses. The first pulse tilts the magnetization by 180 degrees, the second and third pulses give a spin-echo. For approximation of the recovery of the longitudinal nuclear magnetization theoretical spin-lattice relaxation functions have been used. These functions were calculated for the case of magnetic relaxation due to weak isotropic fluctuating magnetic fields. Parameters of relaxation function depend on the asymmetry parameter of the site and on the NQR transition. All studies of longitudinal relaxation have been done at  $\pm 5/2 - \pm 7/2$  transition for each site for which the relaxation functions are as follows:

$$\eta = 0.34: M = M_0 \left\{ 1 - B \cdot \left[ 0.26 \cdot \exp(-17.8t/T_1) + 0.54 \cdot \exp(-9t/T_1) + 0.2 \cdot \exp(-3t/T_1) \right] \right\}$$

$$\eta = 0.15: M = M_0 \left\{ 1 - B \cdot \left[ 0.17 \cdot \exp(-19.9t/T_1) + 0.62 \cdot \exp(-9.8t/T_1) + 0.21 \cdot \exp(-3t/T_1) \right] \right\}$$

$$\eta = 0.03: M = M_0 \left\{ 1 - B \cdot \left[ 0.14 \cdot \exp(-21t/T_1) + 0.65 \cdot \exp(-10t/T_1) + 0.21 \cdot \exp(-3t/T_1) \right] \right\}$$

with the parameter  $B$  depending on the exact tilt angle of nuclear magnetization by the first pulse. The experimental values of  $T_1$  are shown in table 1.

The nuclear spin-spin relaxation (NSSR) was studied by monitoring the spin-echo intensity as a function of the time delay  $\tau$  between  $\pi/2$  and  $\pi$  pulses. In general the decay of transverse magnetization as a function of time  $t = 2\tau$  can be fitted by the equation:

$M = M_0 \exp\left[-(t/T_2)^n\right]$ . The NSSR process is characterized by the relaxation time  $T_2$  and the parameter  $n$ , which characterizes the decay shape which usually varies between Lorentzian ( $n = 1$ ) and Gaussian ( $n = 2$ ). In our case the parameter  $n$  was close to 1. The experimental  $T_2$  values for all Co sites are shown in tables 1 and 2.

As one can see, the  $T_1$  and  $T_2$  values for Co2 sites differ by one order of magnitude from those of Co1 sites. This experimental fact proves previous suggestion of the existence of fast and slow relaxing cobalt sites.

## Conclusions

Since the NQR lines of  $^{59}\text{Co}$  nuclei are well resolved and rather narrow (20 – 40 kHz), we conclude that in the O71 phase Na ions are well ordered in the Na planes. At least 12 non-equivalents Co sites were singled out for the O71 phase. Moreover, sites could be sorted by the magnetic properties: positions marked as Co1 (a, b, c, d) are characterized by slow spin-lattice and spin-spin relaxations rates and correspond to non-magnetic sites, while Co2 (a – i) positions are characterized by fast NSLR and NSSR relaxation rates and correspond to magnetic ones. This is in good agreement with previous investigations of other phases [2, 10]. So the existence of charge disproportionation into  $\text{Co}^{3+}$  and  $\text{Co}^{\approx 3.5+}$  is a quite common picture for the high sodium content range ( $x > 0.5$ ) of the sodium cobaltates.

Therefore the physical picture for O71 phase is quite similar to that of the H67 phase [14, 18]; the difference between them is the number of non-equivalents sites and existence of the sites with  $\eta \approx 0.14$  for O71 phase. This could be due to more complicated organization of di-vacancies in Na plane in the O71 phase. The similar physical properties of H67 and O71 phases benefit this suggestion. Up to now we have not succeeded to find the precise structure of the O71 phase, as we have done it for the H67 phase [11, 13]. So ordering in Na planes and full crystalline structure of  $\text{Na}_{\approx 0.71}\text{CoO}_2$  compound is still an open question.

## Acknowledgments

This work was partially supported by the RFBR (project №10-02-01005-a) and Ministry of Education and Science of the Russian Federation.

## References

- [1] M.L. Foo *et al.*, PRL **92**, 247001 (2004).
- [2] Lang G. *et al.*, PRB **78**, 155116 (2008).
- [3] K. Takada *et al.*, Nature (London) **422**, 53 (2003).
- [4] J. Wooldridge *et al.*, J. Phys.: Condens. Matter **17**, 707-718 (2005).
- [5] Ivanova N.B. *et al.*, Phys Usp, **179**, 837 (2009).
- [6] Ch. Piefke *et al.*, cond-mat, v11006.4493, (2010).
- [7] I. Terasaki, *et al.*, PRB **56**, R12685 (1997).
- [8] H.D. Bhatt *et al.* Thin Solid Films **350**, 249 (1999).
- [9] J-W. Moon *et al.* Mater. Lett. **48**, 225 (2001).
- [10] Alloul H. *et al.*, EPL **82** 17002 (2008)
- [11] Meng Ying S. *et al.*, J. Chem. Phys. **128**, 104708 (2009)
- [12] Platova T. A., *et al.*, JETP let., Vol. **91/8**. 457-460 (2010)

## PROCEEDINGS

- [13] G.J. Shu et al., Phys Rev B 76, 184115 (2007).
- [14] H. Alloul, *et al.*, EPL 85, 47006 (2009).
- [15] W. G. Clark, M *et al.*, Rev. Sci. Instrum. 66, 2453 (1995).
- [16] A. P. Bussandri, and M. J. Zuriaga, J. Magn. Reson. 131,224 (1998).
- [17] I.R.Mukhamedshin *et al.*, Phys.Rev.lett. **94**, 247602 (2005)
- [18] Platova T. A., *et al.*, Phys. Rev. B 80, 224106 (2009).
- [19] C.P. Slichter, *Principles of Magnetic Resonance*, 2nd ed., Springer, New York, (1980).

## Electronic and magnetic properties of activated carbon fibers and carbon nanofibers: ESR and magnetic susceptibility data

N.S. Saenko<sup>1</sup>, M.A. Ziatdinov<sup>1,2</sup>

<sup>1</sup>Institute of Chemistry of FEB RAS, 159 Prospekt 100-letiya, Vladivostok, Russia.

<sup>2</sup>Tokyo Institute of Technology, Tokyo, Japan

e-mail: saenko@ich.dvo.ru

### Introduction

Nanoscale carbon systems possess the set of unusual electronic properties and, therefore, are promising materials for different areas of nanotechnology. In recent years, the results of the experimental data analysis for nanoscale carbon systems has revealed that many of the principal electronic properties are determined by the topology of  $sp^2$  carbon orbital [1-4], which depends, in particular, on the nature and distribution of structural defects, including edges of nanocarbon system.

According to the calculations [2, 3], the magnetic properties of nanographene and stack of nanographenes (nanographite) may differ significantly from those of bulk graphite due to the presence of edge  $\pi$ -electron states, which are localized near the peripheral regions of zigzag shape and are spin-polarized. When molecules of some substances are absorbed by nanoporous carbon materials, consisted of nanographites, the  $\pi$ -electron states can transform because of interaction between guest molecules and nanographites. As a result, magnetic properties of nanographites can change, as well as magnetic properties of nanoporous carbon structures formed by them.

In this work the results of investigation of electronic and magnetic properties of the activated carbon fibers (ACFs) and the carbon nanofibers by ESR and magnetic susceptibility methods are presented.

### Experimental data and discussion

Previously, with the set of complementary physical methods (HR TEM, Raman spectroscopy, X-ray powder diffraction and small-angle X-ray scattering) it was shown that studied PAN-based ACFs consist of three-dimensional disordered network of nanographite domains, separated from each other by nanopores. Each nanographite consists of 3 - 4 nanographene layers. The mean in-plane size of nanographite is 1 - 1.5 nm. There are two types of nanopores in ACFs: the pores with average size 1.2 nm and the pores with average size 10 nm.

The ESR and magnetic susceptibility data show (fig.1 and fig.2) that there are two types of spin carriers in ACFs: conduction electrons and localized centers, which are characterized by the same values of  $g$ -factor and lineshape asymmetry parameter  $A/B$ . The concentration  $N_s$  of the localized spins was found from the magnetic susceptibility data: only one localized spin per 2500 carbon atoms (fig.2). Thus, by comparing the integral intensities of resonance signals from conduction electrons ( $I_e$ ) and localized spins ( $I_s$ ), we can estimate the density of states near the Fermi level for nanographite:  $D(E_F) = (I_e/I_s) \cdot (N_s/k_B T)$ . The calculations show that  $D(E_F)$  for nanographites is several times higher than the same value for the bulk graphite. The anomalous high density of states near the Fermi level of nanographite is in good agreement with the theoretical predictions on the presence of edge  $\pi$ -band [2, 3].

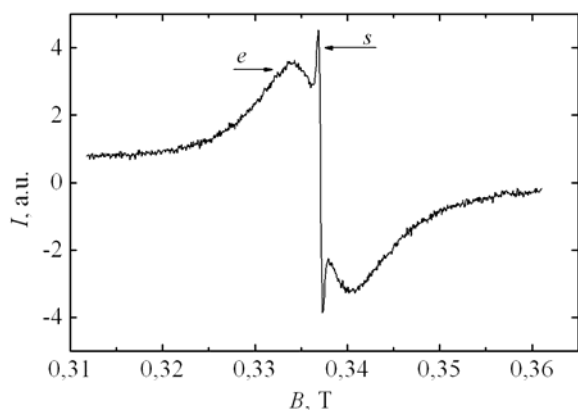


**Fig.1.** The ESR spectrum of ACFs at 120 K (e – signal from conduction electrons, s – signal from localized spins).

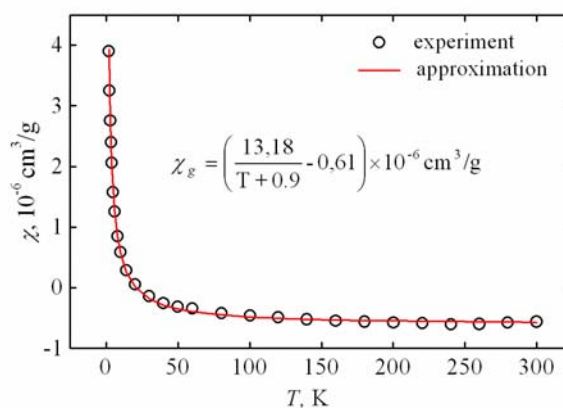


**Fig.2.** The temperature dependence of the static magnetic susceptibility for ACFs.

The absence of narrow signal linewidth temperature dependence for non-evacuated sample indicates that the localized spins are in the interlayer space of nanographites. Furthermore, the Curie-Weiss type temperature dependence of the magnetic susceptibility (fig.2) gives evidence that they are presented in the nanographites in form of small clusters.

After abrupt free air puffing into the reactor with specimen the anomalous decrease of the conduction electron spin-lattice relaxation time ( $1/T_1 \sim \Delta B$ ) was observed (fig.3). Subsequently, the spin-lattice relaxation time restored to the initial value by the exponential law with the characteristic time  $t_0 = 17.9$  hours. The additional experiments show, that the reason of these phenomena is the difference in diffusion constants for oxygen and water molecules. The absorption of the latter by fibers leads to the increase of the spin-lattice relaxation time.

At absorption of fluorine and chlorine molecules by ACFs the linewidth of conduction electron signal decreases, while the  $g$ -factor value increases up to 2.0032(1) (see, for example, fig.4). The XPS data show that at absorption of these halogens by fibers the part of edge carbon atoms forms the covalent bonds with them [5]. It was assumed that this is the reason for the above mentioned changes of conduction electron characteristics.

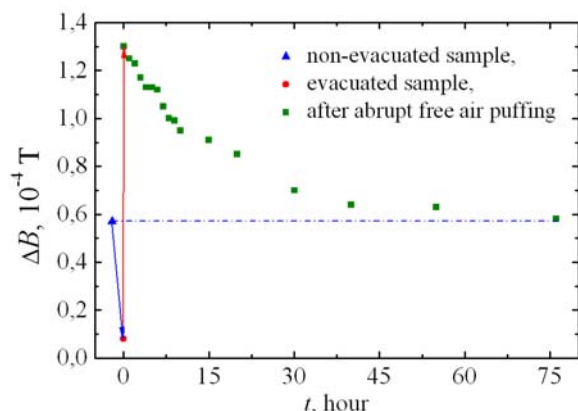


**Fig.3.** The time evolution of CCSR signal linewidth  $\Delta B$  after abrupt free air puffing into the reactor with ACFs.

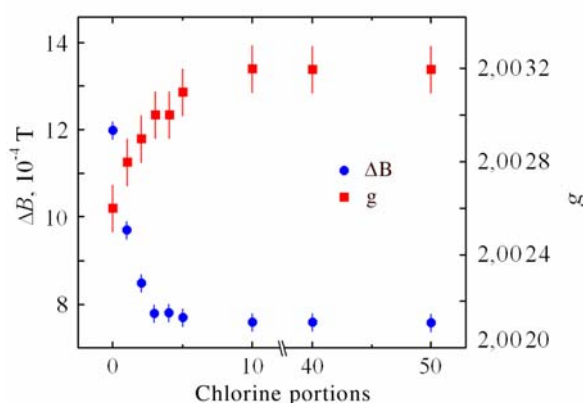


**Fig.4.** The  $g$ -factor value and linewidth of CCSR signal for ACFs from the number of chlorine portions introduced into the reactor.

From high resolution transmission electron microscopy (HR TEM) data it follows, that

studied carbon nanofiber material consist of multiwall carbon nanotubes with length less than 2.5  $\mu\text{m}$ , and diameter less than 70 nm. The dark areas presented in image of initial fibers point out the presence of the nanodimensional particles of nickel catalyst, which was used in synthesis of the investigated material. The average size of nanotubes has been reduced after treating in the strong sulfuric acid within 10 days resulting from surface layer dissolution and total vanishing of thin nanotubes. The dark areas also have disappeared after this treating.

The static magnetic susceptibility of the investigated carbon nanofiber material may be considered as a sum of two components: carbon nanofibers and ferromagnetic impurities (fig.5a). It was assumed that the static magnetic susceptibility of carbon nanofibers composed of paramagnetic and diamagnetic susceptibilities. The former is similar to the static magnetic susceptibility of quasi-2D graphite [6, 7] and the latter may be attributed to the localized spins. The approximation of diamagnetic susceptibility was performed in terms of the band-model of quasi-2D graphite with 2D band parameter  $\gamma_0 = 3$  eV. The best results of fitting procedure were obtained with degeneracy temperature of extrinsic carriers  $T_0 = 164$  K and parameter which takes into account “smearing” of density of states near the Fermi level  $\delta = 73$  K. The concentration of extrinsic carriers for nanofibers was estimated to be  $1.6 \times 10^{10} \text{ cm}^{-2}$ . In low-temperature range localized paramagnetic centers make dominating contribution in magnetic susceptibility and its behavior was fitted by Curie law (fig.5b). The approximated value of Curie constant  $1.4 \times 10^{-5} \text{ emu K/g}$  corresponds to only one paramagnetic center per 2200 carbon atoms.

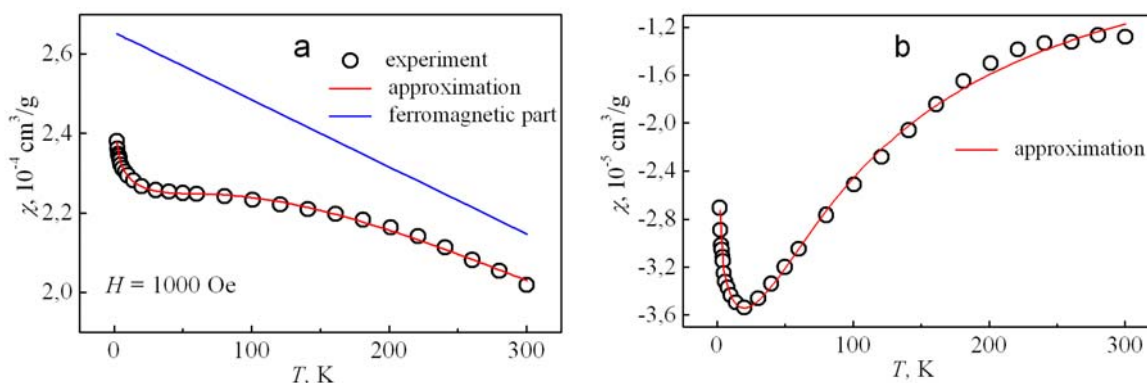


**Fig.5.** The temperature dependence of the static magnetic susceptibility for carbon nanofibers (a - original and b - after subtraction of ferromagnetic component, respectively).

The ESR signal of synthesis product is characterized by the effective value of  $g$ -factor  $\approx 2.24$  and this signal was attributed to divalent state of nickel (fig.6). The ESR signal from nickel remains even after the sample treating in the strong sulfuric acid within 10 days.

To reveal effect of oxygen molecules on the broadening of the ESR signal of carbon nanofibers, the ESR spectrum of the evacuated sample has been acquired and noticeable changes of signal width have not been detected. This fact points out that there is weak interaction between paramagnetic carriers in carbon nanofibers and oxygen molecules adsorbed onto surface. The spectrum of fluorinated carbon nanofibers (fig.7) shows the additional narrow resonance signal with the  $g$ -factor value very close to the free electron one. This signal is likely to belong to the electrons localized on  $p_z$ -orbitals of carbon atoms, near positions “attacked” by fluorine atoms.

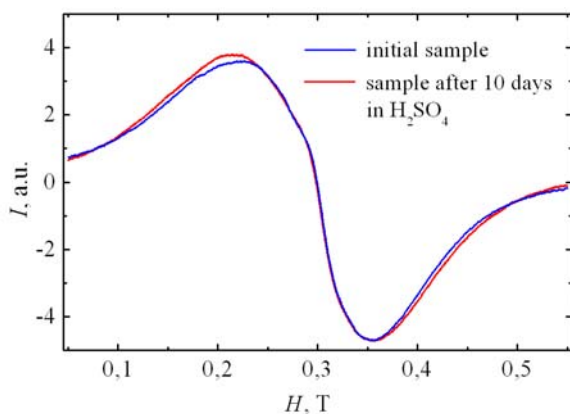


**Fig.6.** The ESR spectrum of carbon nanofibers before and after treating by the strong sulfuric acid at room temperature.

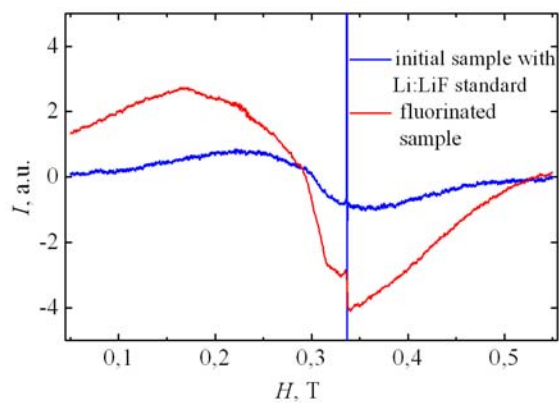


**Fig.7.** The ESR spectrum of carbon nanofibers after fluorination at room temperature.

## Conclusion

It was found that the density of electronic states near the Fermi level for nanographites, structural blocks of ACFs, is more than that in macroscopic graphite. So, in nanographites, a stable localized edge  $\pi$ -states, generating peak density of states near the Fermi level, are realized. When molecules of oxygen, chlorine and fluorine are absorbed by ACFs, the  $\pi$ -electron states transformed because interaction of between these molecules and nanographites. This interaction leads also to the change of magnetic properties of nanographites and ACFs formed by them.

Basing on analysis of magnetic properties of carbon nanofibers synthesized by catalytic methane pyrolysis, the concentration of paramagnetic centers and extrinsic 2D carriers, the degeneracy temperature of extrinsic carriers and the “smearing” degree near the Fermi level have been estimated. It was concluded that in applied technique of carbon nanofibers synthesis the catalyst particles are intercalated in tubular cavities and interlayer spacing, i.e. the synthesis products are ferromagnetic nanocomposites.

## Acknowledgements

The authors gratefully acknowledge prof. Rakov E.G. for providing carbon fibers samples. This work was supported by the Russian Foundation for Basic Research (Grant No. 08-03-00211-a) and the Presidium of Far Eastern Branch of Russian AS (Grant No. № 09-I-P18-07).

## References

- [1] Dresselhaus M.S. et al. Science of fullerenes and carbon nanotubes. N.Y.: Academic Press, 1996.
- [2] Fujita M. et al. J. Phys. Soc. Jpn. **65**, 1920 (1996).
- [3] Nakada K. et al. Phys. Rev. B. **54**, 17954 (1996).
- [4] Kobayashi Y. et al. Phys. Rev. B. **71**, 193406 (2005).
- [5] Ziatdinov A.M. and Nikolenko Yu.M. Bull. FEB RAS **2**, 23 (2009).
- [6] Kotosonov A.S. Pis'ma v ZhETF **70**, 468 (1999).
- [7] Likodimos V. et al. Phys. Rev. B. **68**, 045417 (2003).

## Magnetic polarons in $\text{CaMnO}_{3-x}$ : the $^{17}\text{O}$ NMR study

Z.N. Volkova<sup>1</sup>, S.V. Verkhovskii<sup>1</sup>, A.P. Gerashenko<sup>1</sup>, K.N. Mikhalev<sup>1</sup>,  
A.Y. Yakubovskii<sup>2</sup>, A. Trokiner<sup>3</sup>

<sup>1</sup>Institute of Metal Physics, Ural Branch of Russian Academy of Sciences, Ekaterinburg 620041, Russia

<sup>2</sup>Russian Research Centre «Kurchatov Institute», Moscow 123182, Russia

<sup>3</sup>Laboratoire de Physique du Solide, LPEM UPR5, CNRS, E.S.P.C.I., Paris 75231, France

e-mail: litvinovaz@mail.ru

### Introduction

$\text{CaMnO}_{3-x}$  ( $x < 0.01$ ) is a lightly electron doped G-type antiferromagnetic (AF) with canted structure in the ordered state. It was shown that a homogeneous canted AF state should be unstable with respect to an electron phase separation in doped manganites [1] where the doped electron can become “dressed” with a ferromagnetic (FM) polarized cloud of neighboring manganese magnetic moments of the AF lattice. The electron travels with its magnetic polarization cloud through the lattice forming the magnetic polaron (MP) [2].

In this work we present  $^{17}\text{O}$  NMR and magnetic susceptibility results evidencing the existence of magnetic polarons in the AF ( $T_N = 123$  K) and in the paramagnetic (PM) states of a  $\text{CaMnO}_{3-x}$  ( $x < 0.01$ ) sample.

### Magnetic susceptibility and $^{17}\text{O}$ NMR isotropic shift in the PM phase

The temperature behavior of bulk magnetic susceptibility  $\chi = M/H$  is represented in fig.1(a). Above  $T_N = 123$  K  $\chi$  follows the Curie-Weiss law  $\chi(T) \sim (T - \theta)^{-1}$  with  $\theta = -370(20)$  K. The  $T$ -independent part of the magnetic susceptibility  $\chi_0 = 0.10(2)$  memu/mol is negligible in accordance with the corresponding  $\chi_0$  estimated [3].

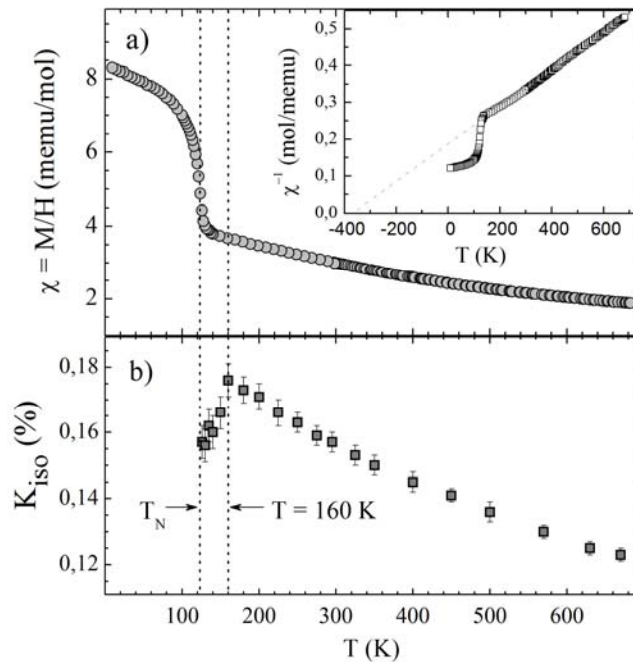


**Fig.1.** (a) magnetic susceptibility  $\chi = M/H$  versus temperature  $T$ ;  
inset of (a):  $\chi^{-1} = H/M$  versus temperature  $T$ ;  
(b) isotropic  $^{17}\text{O}$  NMR shift  $K_{\text{iso}}$  versus temperature  $T$

The almost linear plot  $\chi^{-1}(T) = H/M(T)$  (inset in fig.1(a)) shows that the mean-field behavior holds down to  $T_N$ . The linear fit of  $H/M$  data yields an effective magnetic moment  $\mu_{eff} = 4.0(4) \mu_B$  per Mn close to the expected value for  $Mn^{4+}$  ( $S = 3/2, L = 0$ ) ion in the cubic crystal field. Thus in the PM phase the bulk magnetization is almost completely due to the localized  $t_{2g}$ -spins of the  $Mn^{4+}$  ion [4].

$^{17}O$  nuclei have a spin  $I = 5/2$  and above  $T_N$  the interaction of the  $^{17}O$  quadrupole moment  $e^{17}Q$  with the electric field gradient  $eV_{ii}$  of the charge environment determines the spectrum pattern with five well resolved peaks of  $2I$  transitions [4]. The width and asymmetry of the central ( $m_I = +1/2 \leftrightarrow -1/2$ ) transition depend on the relative values of the magnetic shift components  $\{K_X; K_Y; K_Z\}$  while the position is mainly defined by the isotropic shift  $K_{iso} = 1/3 \text{Sp}\{K_\alpha\}$  ( $\alpha = X, Y, Z$ ).

The thermal dependence of  $K_{iso}$  represented in fig.1(b) evidences two distinct behaviors above and below  $T \sim 160$  K. Above 160 K  $K_{iso}(T)$  decreases with the same  $\theta$  value as the bulk magnetic susceptibility when  $T$  increases. But the proportionality of the local spin density to  $\chi(T)$  is broken below 160 K. We believe that in the PM state far above  $T_N$  the spin density of the mobile doped electrons is equally shared between manganese ions and the local spin density in the regular lattice of the  $Mn^{4+}$  ions follows a Curie-Weiss law. Below  $T \sim 160$  K the doped electrons start to be involved in strong correlations with localized Mn spins and form the magnetic polarons which are evidenced in the AF phase of the sample [4]. Being involved in strong ferromagnetic correlations the motion of these doped electrons is much slower than that for the remaining carriers.

### $^{17}O$ NMR in the AF phase

Below  $T_N$  the  $^{17}O$  NMR spectrum consists of two broad lines with very different resonance frequencies and intensities. The main line is close to Larmor frequency  $\nu_0$  and evidently originates from oxygens in the AF matrix of  $CaMnO_3$ . The less intense line is largely shifted toward high frequency. The local field  $^{17}h_{loc}$  corresponding this frequency range is due to FM-correlated Mn magnetic moments (FM domains). The intensity of FM line is about 3 % of the total NMR spectrum.

In the FM domains it was found that the Mn spins are perfectly aligned from  $^{17}O$  linewidth and from the line shift that the  $e_g$  electron is responsible for the  $^{17}O$  local field through the  $O(2s2p_\sigma) - Mn(e_g)$  hybridized state [4]. A nearly perfect alignment of the Mn spins is expected for MPs.

The low frequency dynamic of the Mn spins was studied in the MPs by measuring the  $^{17}O$  spin echo decay rate  $T_2^{-1}$  on the zero field NMR line (fig.2). The characteristic time of the echo-decay  $T_2$  is defined as the time at which the echo-signal  $E$  drops to  $1/e$  of its starting value.  $T_2^{-1}$  is almost constant from 4 K to 40 K and increases above 40 K so that at  $T > 93$  K the FM signal is lost due to too short  $T_2$ . The component  $(T_2^{-1})_a \equiv [T_2^{-1}(T) - T_2^{-1}(4K)]$  shows a thermal activated behavior  $\sim \exp(-E_a/k_B T)$  with

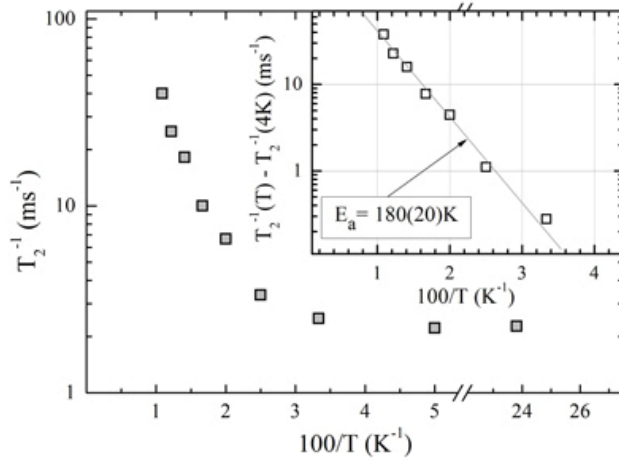


**Fig.2.**  $^{17}O$  spin echo decay rate  $T_2^{-1}$  versus  $T^{-1}$  measured in zero field NMR in the FM domains of  $CaMnO_{3-x}$ ; the inset shows the activated component  $[T_2^{-1}(T) - T_2^{-1}(4K)]$  versus  $1/T$

$E_a = 180(20)$  K  $\approx 15$  meV (inset in fig.2). According to the  $^{17}\text{O}$  echo-decay data the MP starts to move above 40 K in a slow diffusion regime keeping its static properties almost unchanged in agree with the model of small size self trapped magnetic polarons [2]. As  $E_a$  is far smaller than the binding energy of the polaron ( $E_b \approx 100$  meV [5]) the stability of the MP is ensured when it moves through the AF lattice.

### Acknowledgments

This work is supported by the Russian Foundation for Basic Research (grant Ns 08-02-00029, 09-02-00310).

### References

- [1] A. Moreo and et al, Science **283**, 2034 (1999).
- [2] H. Meskine, S. Satpathy, J. Phys. Condens. Matter **17**, 1889 (2005).
- [3] J.A. Souza and et al, Phys. Rev. B **76**, 024407 (2007).
- [4] A. Trokiner and et al, Phys. Rev. B **79**, 214414 (2009).
- [5] S. Verkhovskii and et al, Phys. Rev. B **81**, 144415 (2010).

**Local magnetic susceptibility in the multiferroic CuCrO<sub>2</sub>:  
<sup>63,65</sup>Cu NMR study**

A.G. Smolnikov<sup>1</sup>, V.V. Ogloblichev<sup>1</sup>, A.Yu. Yakubovsky<sup>2</sup>, Yu.V. Piskunov<sup>1</sup>,  
 S.V. Verkhovskii<sup>1</sup>, A.P. Gerashenko<sup>1</sup>, K.N. Mikhalev<sup>1</sup>, K. Kumagai<sup>3</sup>, S. Barilo<sup>4</sup>

<sup>1</sup>Institute of Metal Physics, UD RAS, Ekaterinburg 620990, Russia

<sup>2</sup>Russian Research Centre, "Kurchatov Institute", Moscow, 123182, Russia

<sup>3</sup>Department of Physics, Faculty of Science, Hokkaido University, Sapporo 060-0810, Japan

<sup>4</sup>Institute of Solid State and Semiconductor Physics, Minsk 220072, Belarus

e-mail: smolnikov@imp.uran.ru

Physical properties of the system with the triangular antiferromagnetic lattice (TLA) CuCrO<sub>2</sub>, have been intensively studied recently both experimentally and theoretically. The problem of installation of an antiferromagnetic order in TLA in such systems leads to the strong geometrical spin frustration which leads to some interesting properties.

CuCrO<sub>2</sub> is crystallized into hexagonal layered structure which belongs to spatial group *R-3m* [1]. Trivalent ions of *chrome* Cr<sup>3+</sup> (S=3/2), forming TLA, are located in the centre of correct octahedrons CrO<sub>6</sub> from oxygen which are connected by monovalent ions of *copper* Cu<sup>1+</sup>. In the nearest environment of copper there are six atoms of the chrome that form two triangles developed from each other on 180 degrees.

In early works on neutron diffraction on a powder [2], authors have shown, that in CuCrO<sub>2</sub> more low than 24 K appears 120° angles a magnetic structure with a proportional vector of distribution  $Q = (1/3, 1/3, 0)$ . However, in later work on dispersion of neutrons [1] it is said, that magnetic structure CuCrO<sub>2</sub> is incommensurable to a vector of distribution  $Q = (k, k, 0)$  ( $k = 0.329$ ).

The ferroelectric polarization, *P*, emerging in the magnetic phase of CuCrO<sub>2</sub>, is directed parallel to the triangular-lattice plane. The puzzling direction of *P*, which is inconsistent with the spin-current model [4], rises a problem of the microscopic origin of the magneto-electric coupling existing in the TLA compounds, the most typical examples of the frustrated planar spin systems.

We present the results of <sup>63,65</sup>Cu NMR research into paramagnetic and ordered states of a single crystal of the antiferromagnet CuCrO<sub>2</sub> that has a triangular lattice consisting of Cr atoms. <sup>63,65</sup>Cu NMR spectra were taken in a wide range of temperatures (4-300) K and of magnetic fields  $H = (0-94)$  kOe directed in the plane *ab* and along the *c* axis of the crystal. The components of electric field gradient (EFG) tensor and of magnetic shift tensor ( $K_{ab,c}$ ) were obtained. The temperature dependences of  $K_{ab}(H||ab)$ ,  $K_c(H||c)$  are well described by the Curie-Weiss law for paramagnetic state and they resemble the magnetic susceptibility ( $\chi_{ab,c}$ ) behavior. The hyperfine field at copper sites  $H_{loc,ab,c} = 33$  kOe/ $\mu_B$  has been determined using the  $K_{ab,c}$  vs  $\chi_{ab,c}$  diagrams. The direction of the principle axis of EFG is aligned with the *c*-axis. The quadrupole frequency  ${}^{63}\nu_Q = 27.0(4)$  MHz and the parameter of asymmetry  $\eta$  are equal to 0. Below  $T = 24.2(3)$  K, the NMR line sharply broadens and with further decreasing *T*, the NMR spectrum becomes consisting of two peaks characteristic of incommensurate phases. The distance between the edge peaks in orientation  $H||c$  is five times more than in  $H||ab$ .

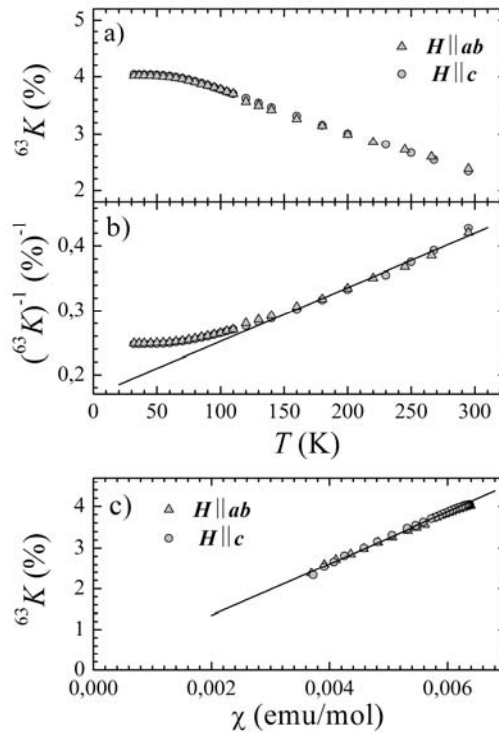


**Fig.1.** Temperature dependence of the  $^{63}\text{Cu}$  NMR line shift  $^{63}K_{ab,c}$  (a),  $(^{63}K_{ab,c})^{-1}$  (b) and the parametric  $K_{ab,c}$  versus  $\chi_{ab,c}$  dependence (c) in the paramagnetic state of the  $\text{CuCrO}_2$  single crystal differently oriented in magnetic field  $H$ .

This work was supported in part by Russian Academy of Sciences Ural Branch (grant for young scientists (V.V.O.)), by the Russian Foundation for Basic Research (Grants No 11-02-00354, 09-02-00310), by the Belarusian State Fund for Fundamental Research (grants No. F10R-152 and F09K-017), by the President of Russia through the grant for young scientists (MK-1232.2011.2).

### References

- [1] M. Poienar et. al., Phys. Rev. B **79**, 014412 (2009).
- [2] H. Kadowaki et. al., J. Phys.: Condens. Matter **2**, 4485 (1990).
- [3] S. Seki et. al., Phys. Rev. Lett. **101**, 067204 (2008).
- [4] Katsura et. al., Phys. Rev. Lett. **95**, 057205 (2005)

## Phototransformation of acetylene derivatives of lappaconitine studied by NMR and CIDNP techniques

V.I. Klimentiev, N.E. Polyakov, T.V. Leshina, A.A. Stepanov, S.F. Vasilevsky

Institute of chemical kinetics and combustion, Novosibirsk, 630090, Russia

e-mail: viktracer@ngs.ru

### Introduction

Lappaconitine (LA0, fig.1), a natural alkaloid extracted from aconite (*Aconitum Septentrionale Koelle*), is widely used in pharmacology as a hypertensive and anti-arrhythmic drug [1]. It is known that the activity of LA is connected to its ability to bind the site 2 of sodium channels, thereby blocking the channel [2]. A serious drawback of many blockers of ion channels, including lappaconitine, is high toxicity, including phototoxicity. Under the influence of light LA can decompose to form free radicals, causing skin disease [3]. In this regard, it is a challenge to search new approaches that reduce the side effects of the drug. One such approach is the introduction of the substitute in the anthranilic fragment of the LA. In this study we have synthesized a new class of acetylenic derivatives of lappaconitine and studied the effect of substitutes in the 4-th position of LA on the rate of photodecomposition in the reactions of intramolecular electron transfer.

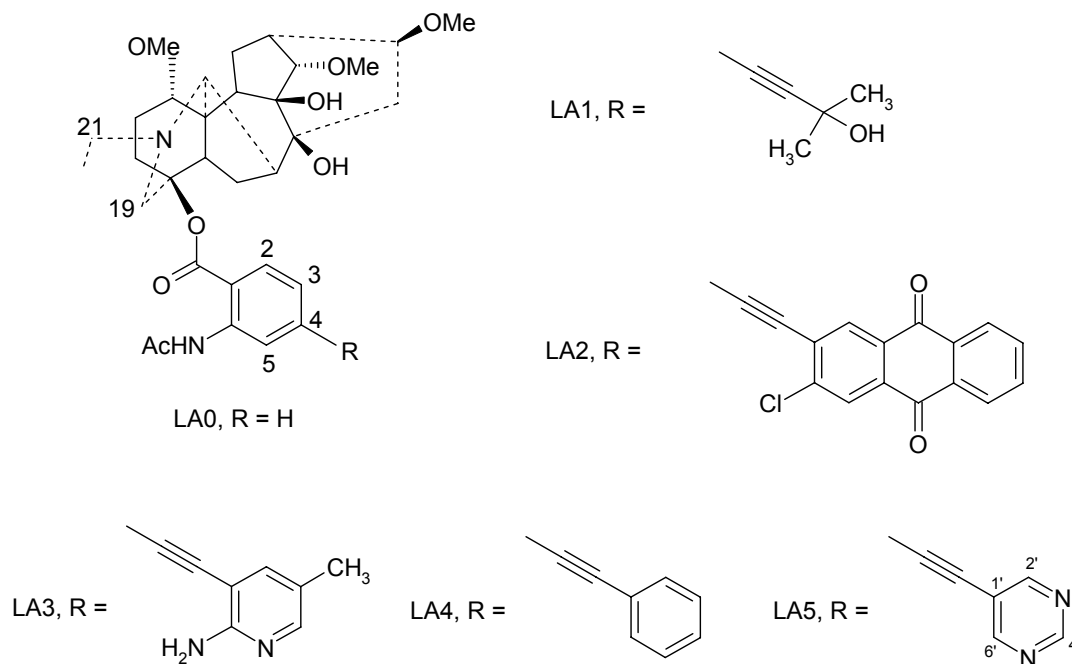
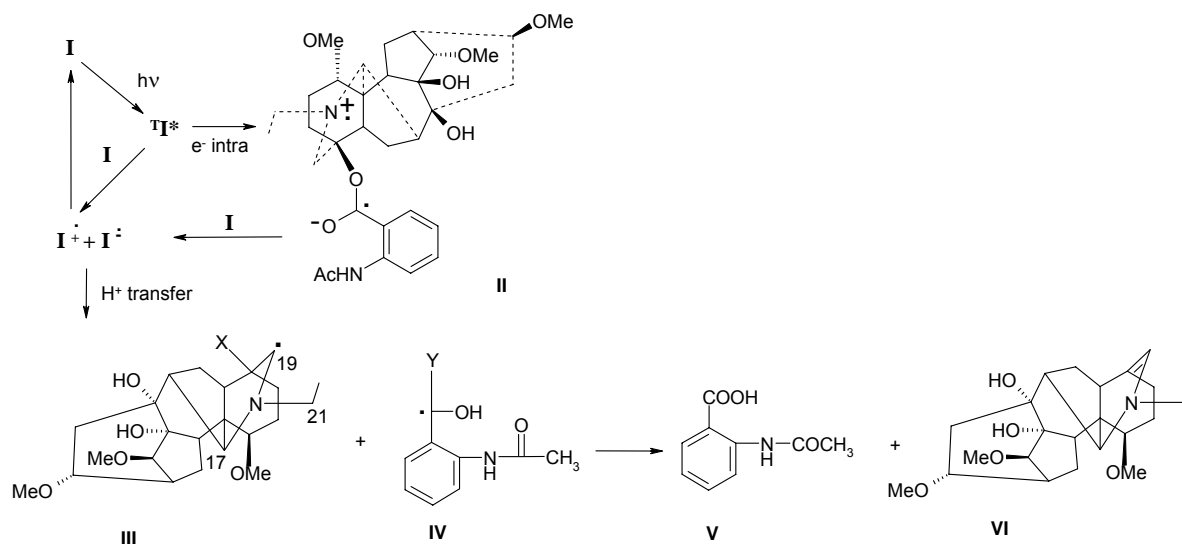


**Fig.1.** The structures of acetylenic derivatives of lappaconitine.

The mechanism of photodegradation of unsubstituted LA has previously been studied in [4]. In these processes, the first and crucial act in lappaconitine photodegradation was the electron transfer from the nitrogen atom N-20 to the anthranilic fragment with the formation of rigidly bound ion-radical pair (Scheme 1).

Using Chemically Induced Dynamic Nuclear Polarization (CIDNP) technique [5] it was shown that the formation of the final products **V** and **VI** occurs through successive stages of the intermolecular electron and proton transfer with the subsequent fragmentation of neutral



**Scheme 1.** The scheme of lappaconitine (I) phototransformation after photoexcitation by UV light, established in [4]. X - anthranilic fragment of and Y - aliphatic fragment of LA.

radicals [4, 6]. We supposed that the introduction of acetylenic substitutes may affect the rate of electron transfer and lead to a redistribution of electron density in the anthranilic fragment in the radical anion and neutral radical. This, in turn, can serve the cause of decrease in the rate of proton transfer to an oxygen atom and increase the strength of ester bond. All these factors may result in increase the stability of LA.

### Experimental Section

Deuterated solvents ( $CD_3CN$  (99.5% D),  $CD_3OD$  (99.5% D), Aldrich) were used as supplied. Lappaconitine derivatives were synthesized according to [7]. All NMR experiments (including CIDNP measurement) were performed using DPX-200 Bruker NMR spectrometer equipped with photo probe. An EMG 101 MSC Lambda Physik excimer laser was used as the light source ( $\lambda = 308$  nm, pulse duration 15 ns, average pulse energy 100 mJ). Since the background (equilibrium) NMR signals in the pulse CIDNP experiments were suppressed, only the signals of the products demonstrating nuclear polarization could be observed.

### Results and Discussion

The anthranilic fragment is known to be a chromophore in the molecule of LA [4]. It was found that the presence of acetylenic substitutes affects both the position of absorption maximum and extinction coefficient on it (Table 1).

	$\epsilon_{\max}$ , 1/(cm*M)	$\lambda_{\max}$ , nm	$\epsilon_{\text{irr}}$ , 1/(cm*M)
LA0	5200	309.5	5100
LA1	3000	327	1900
LA2	6600	380	14000
LA3	13000	346	4600
LA4	42000	296.5	36000
LA5	14000	300.5	13700

**Table 1.** Extinction coefficients  $\epsilon_{\max}$  of lappaconitine derivatives at the maximum absorption wavelength  $\lambda_{\max}$  and at  $\lambda_{\text{irr}} = 308$  nm.

Analysis of the NMR spectra after laser illumination has shown that during the decomposition of all the lappaconitine derivatives, the products produced are similar to the

products obtained after irradiation of LA0, taking into account acetylenic substitute. The yield of product **VI** in all substituted LA is markedly lower than in LA0 (Table 2).

	The product <b>VI</b> yield	CIDNP of product <b>VI</b>
LA0	0,50	-100
LA1	0,40	-81
LA2	0,35	+9
LA3	0,20	0
LA4	0,15	-24
LA5	0,10	-14

**Table 2.** The relative yield and CIDNP intensity (21-H) of the product **VI** after the same illumination time in methanol.

In CIDNP experiments in methanol the decrease in polarization intensity on the reaction products for LA1-LA5 was observed in comparison with LA0 (Table 2). The CIDNP spectrum detected during irradiation of LA0 is shown in fig.2. The detailed analysis of the mechanisms of CIDNP formation in this reaction has been done in [4].

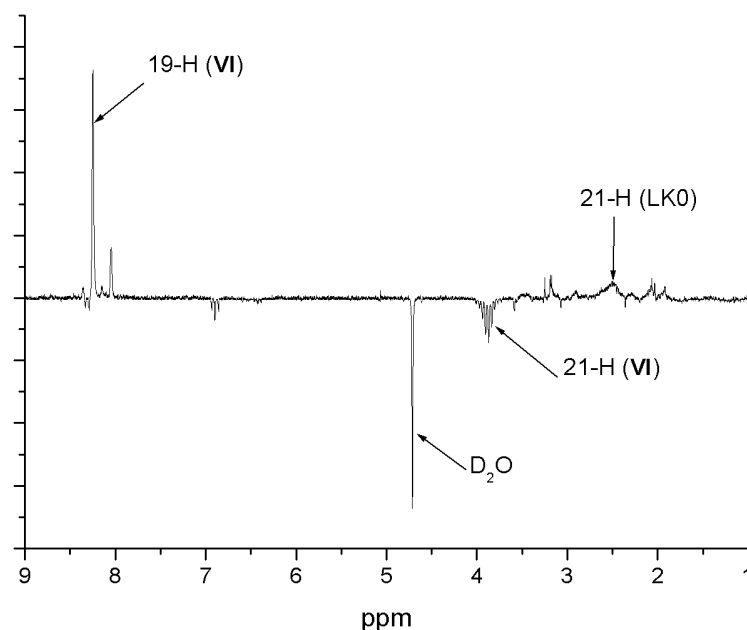


**Fig.2.** CIDNP spectrum recorded in the photolysis of LA0 in CD<sub>3</sub>OD.

CIDNP intensities on product **VI** have no linear correlation with the product yields due to superposition of CIDNP contributions from radical ion pair and neutral radical pair (see Scheme 1).

In addition CIDNP experiments were also conducted in acetonitrile for some lappaconitine derivatives. CIDNP spectra of LA0 and LA1 are almost identical. NMR spectrum of irradiation products of LA1 is also similar to the NMR spectrum of LA0 products. The CIDNP spectrum of LA2 does not show adsorption of 19-H (**VI**), which indicates the absence of the contribution from the neutral radical pair (**III** + **VI**). This means that the break of C-O bond in LA2 occurs in the radical cation in contrast to neutral radical for LA0. We suggest that this reaction begins with electron transfer not to the anthranilic fragment, but to the quinone part.

## Conclusion

Acetylenic moiety play a significant role in the efficacy of intramolecular electron transfer in lappaconitine molecule. The investigation of the “structure-property” dependence is a common approach to creating more effective medicines. Previously, we assumed that the processes of electron transfer play a significant role in the chemistry of lappaconitine *in vivo*, particularly in the mechanism of its therapeutic activity and toxicity. As an example, a correlation between toxicity and electron donor ability of amine fragment (N-20) was observed [6, 8]. The data obtained in this work on improving the stability of esters of anthranilic acid may be useful for the creation of new sunscreen products on their basis [9]. In addition, the stabilization of the radical anion of LA may reduce the overall toxicity and increase its therapeutic effect.

## Acknowledgment

This work was supported by the grants 11-03-01104 of Russian Foundation of Basic Research.

## References

- [1] Dzhakhangirov F. N., Sultankhodzhaev M. N., Tashkhodzhaev B. and Salimov, B. T. *Chem. Nat. Compd. (Engl. Transl.)*, **33**, 190 (1997).
- [2] Wright S. N. *Mol. Pharmacol.*, **59**, 183 (2001).
- [3] Quintero B., Miranda M.A. *Ars Pharmaceutica*, **41**, 27 (2000).
- [4] Polyakov N. E. Leshina T. V. *Russ. Chem. Bull. Int. Ed.*, **56**, 631 (2007).
- [5] Salikhov K.M., Molin Yu.N., Sagdeev R.Z. and Buchachenko A.L. *Spin Polarization and Magnetic Effects in Radical Reactions*, Academiai Kiadó, Budapest, Hungary, (1984).
- [6] Polyakov N.E., Simaeva O.A., Taraban M.B., Leshina T.V., Konovalova T.A., Kispert L.D., Nikitina I.A., Pankrushina N.A., Tkachev A.V., CIDNP and EPR Study of Photo-transformation of Lappaconitine Derivatives in Solution. *J. Phys. Chem. B*, **114**, 4646–4651 (2010).
- [7] Stepanov A.A., Wasilewski S.F., Tolstikov G.A. *Chemistry for Sustainable Development*, [Article in Russian] **8**, 505-510 (2010).
- [8] Tolstikova T. G., Voevoda T. V., Dolgikh, M. P. *Eksp. Klin. Farmakol.* [Article in Russian], **4**, 7 (2001).
- [9] Beeby A., Jones A. E. The Photophysical Properties of Menthyl Anthranilate: A UV-A Sunscreen. *Photochem. Photobiol.*, **72**, 110-115 (2000).

**NMR study of cholesterol complexes with glycyrrhizic acid**

O.Yu. Gluschenko, N.E. Polyakov, T.V. Leshina

Institute of Chemical Kinetics and Combustion, Institutskaya str., 3, Novosibirsk, 630090, Russia

e-mail: olga.gluschenko@gmail.com

**Introduction**

Cholesterol is a natural lipophilic alcohol contained in the cell membranes of most living organisms. It enters the body from two sources: from food and from endogenous synthesis, with the majority (80%) is synthesized by the body. Cholesterol plays an important role in many biochemical processes, in particular, ensures the stability of cell membranes in a wide range of temperatures, and is needed to produce vitamin D and various steroid hormones. In addition, cholesterol participates in the synthesis of bile acids, and according to some sources — affects the activity of the synapses of the brain and the immune system, including protection against cancer. At the same time, cholesterol earned him notoriety for his involvement in the formation of atherosclerotic plaques. To date, it is believed that increased blood levels of cholesterol and low density lipoprotein (LDL) cholesterol are the main factors for risk of atherosclerosis. But there is another insight into the problems of cholesterol: it is like a “repair material” accumulated in the field of microdamage of blood vessels and blocking these lesions. In addition, the oxidation products of cholesterol were found in atherosclerotic plaques, which may play a key role in the pathogenesis of atherosclerosis and other diseases [1-4].

At the moment there are several ways of treatment the atherosclerosis disease. All of them use the drugs which are inhibitors of enzymes responsible for the different stages of cholesterol biosynthesis. They terminate the chain of cholesterol formation, but block also the formation of some other important products of biosynthesis. In addition, these drugs often demonstrate toxic properties. This is why the search for alternative methods of regulation of cholesterol level is in progress. One such approach might be to use natural complexants which are able to bind to cholesterol molecules and affect their properties. At now, only one successful example of such approach is known. It is a complex of cholesterol with cyclodextrins (CDs) which effectively remove cholesterol from membranes [5, 6]. But in this case some negative effects occur. First, this disturbs the structure of membranes, and second, the possibility of crystallization of both the CD and their complexes was detected.

There are several reasons why the interaction of cholesterol with glycyrrhizic acid (GA) may be of interest. First, the GA - the natural complexants that exhibits a wide spectrum of biological activity. It forms inclusion compounds with many drugs and is widely used in medicine [7]. Secondly, unlike the CD, there is no evidence indicating toxicity of GA. Thirdly, there are some data on the influence of GA on the biosynthesis and properties of cholesterol [8]. In experiments on animals with atherosclerosis, GA and its salts reduce cholesterol, LDL and triglycerides level [8]. Fourthly, there are data that indicate the ability of GA to reduce the oxidation of cholesterol [9]. However, the molecular mechanism of these effects is currently unknown. Complex formation of cholesterol with GA may shed light on these facts and open a new way to treatment of atherosclerosis. The purpose of this study is to investigate the possibility of complexation of cholesterol with GA by NMR relaxation technique.

## Results and Discussion

In this study the complex formation between cholesterol and glycyrrhizic acid was observed for a first time. The complexes were prepared by mixing the starting materials in deuterated methanol. For the calculation of stability constants and thermodynamic parameters of the complex the samples with different ratios of cholesterol and GA: 5 mM/5 mM, 10 mM/5 mM and 5 mM/10 mM were analyzed at two temperatures: 300°K and 320°K. The formation of complexes was studied by NMR relaxation technique. All NMR experiments were performed using DPX-200 Bruker NMR spectrometer (200 MHz <sup>1</sup>H operating frequency) equipped with temperature control.  $T_2$  relaxation time of cholesterol and GA (the corresponding protons are marked with \* in fig.1 and fig.2) was measured by means of Carr-Purcell-Meiboom-Gill sequence:  $p(90^\circ) - (\tau - p(180^\circ) - \tau)n$  - acquisition, where  $\tau = 0.6$  ms and  $n$  was varied from 0 to 2000.

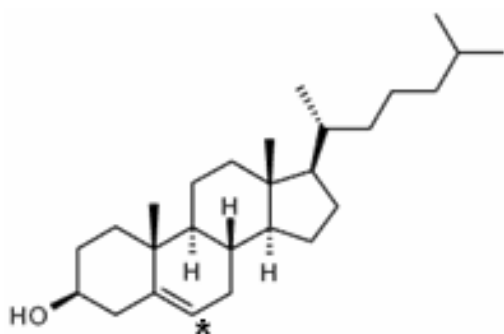


**Fig.1.** Cholesterol.

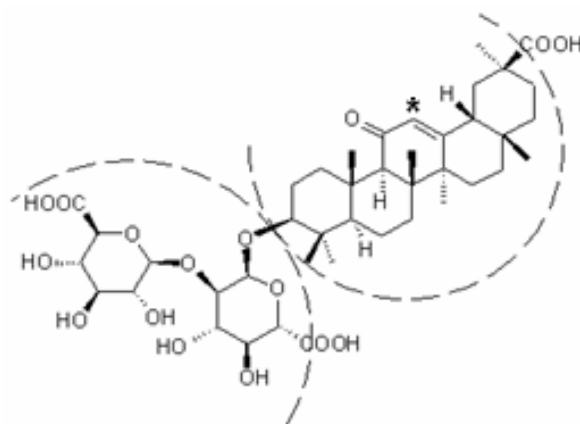


**Fig.2.** Glycyrrhizic acid.

It is known that the relaxation times of protons are very sensitive to molecular mobility. The formation of complex decreases the mobility of molecules, and this leads to a significant decrease in the relaxation time of protons. In general, the complex formation results in bi-exponential or even three-exponential relaxation kinetics, if there are several different types of aggregates in solution. Measurement of the pre-exponential factors allows to determine the fraction of molecules located in the complex and hence to calculate the stability constants and stoichiometry of the complex. In general the stability constant of the reaction:  $nChol+mGA \leftrightarrow Chol_nGA_m$  is determined as  $K = \frac{[Chol_nGA_m]}{[Chol]^n[GA]^m}$ , where [Chol] is the free cholesterol concentration, and [GA] is the concentration of free GA. The values of m and n were calculated using the optimization program of experiments with different ratios of  $[Chol]_0$  and  $[GA]_0$ .

$T_2$  relaxation kinetics for both precursors in the free state is mono-exponential with characteristic times of  $T_2 \sim 300$  ms for cholesterol and  $T_2 \sim 400$  ms for GA protons. As an example, fig.3 shows the kinetic of relaxation of proton at the double bond (marked by \* in fig.1)) of pure cholesterol. After mixing the cholesterol with GA three-exponential kinetics for the protons of both substances appear: the fastest component has a characteristic decay time in order of several milliseconds, the second component in the order of several tens of milliseconds and the third component - the order of several hundred milliseconds (fig.4). Over time, the shortest component disappears. While the process of establishing the equilibrium takes a few days, it accelerates when the temperature rises to 60° C. Fig.5 shows the kinetic of the echo signal decay for the sample stored for one day at room temperature.

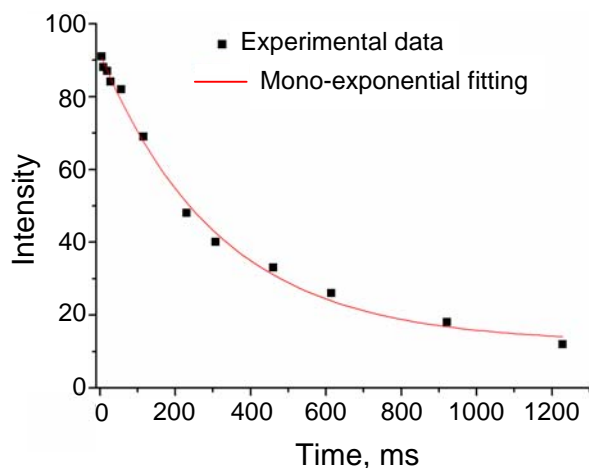


**Fig.3.** Decay kinetics of echo signal for pure cholesterol in methanol.

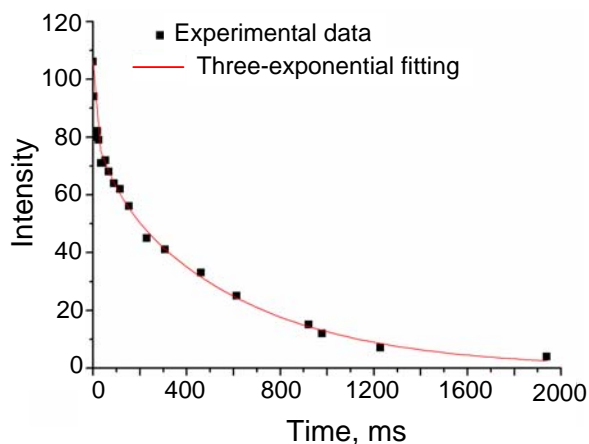


**Fig.4.** Decay kinetics of echo signal of cholesterol in the presence of GA in methanol.

We assume that the component with shortest relaxation time corresponds to large aggregates consisting of several molecules of cholesterol and GA. The same order of magnitude of relaxation time is observed, in particular, for micelles solution. Over time, they

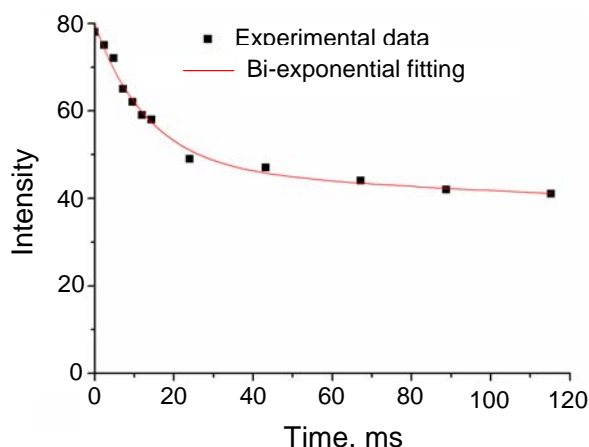


**Fig.5.** Decay kinetics of echo signal of cholesterol in the presence of GA in methanol after store of one day at RT.

are likely to disintegrate into smaller complexes, which correspond to the relaxation time of several tens of milliseconds. Long component of several hundred milliseconds corresponds to the free states of the substances involved in the complex.

The stoichiometry and stability constants of the complex were determined by the fitting of decay kinetics at different concentrations of cholesterol and GA after the establishment of equilibrium. The resulting stoichiometry is 1:2 (one molecule of cholesterol on the two molecules of GA). This result is consistent with existing data on the complexation of GA with other

substances [10-11]. The calculated stability constant for this stoichiometry is  $K_{12} = (3 \pm 0.6) \times 10^3 \text{M}^{-2}$ . From the temperature dependence of the stability constant the thermodynamic parameters were calculated:  $\Delta G(300^\circ \text{K}) = -20 \pm 4 \text{ kJ/mol} \times \text{K}$ ;  $\Delta H = 0.4 \pm 0.1 \text{ kJ/mol}$ ; and  $\Delta S(300^\circ \text{K}) = 68 \pm 14 \text{ J/mol} \times \text{K}$ . It is seen that the entropy factor makes the main contribution to the complex stability. This could mean that the desolvation of the cholesterol molecule occurs during the complex formation. It should be kept in mind that all measurements were made in methanol solution. One can expect that in aqueous solution the binding of cholesterol with GA will be significantly enhanced by the hydrophobic interaction.

## Conclusion

Thus, the formation of stable aggregates of cholesterol with glycyrrhizic acid was observed for a first time. The measurement of  $T_2$  relaxation time of the protons of cholesterol and GA shows the existence of several types of aggregates: complexes with stoichiometry 1:2 and more large aggregates which disappear at higher temperature. Taking into account also

the ability of GA to gain the permeability of cage membranes, where near 90% of cholesterol is located, this study might be the beginning of new approach development to the regulation of the cholesterol level.

### Acknowledgment

This work was supported by the Priority Program for Basic Research RAS. Project No 4: “Study of supramolecular complexes of plant metabolites and their derivatives with hypocholesterolemic agents by physicochemical methods”, 2009-2011.

### References

- [1] Leonarduzzi G., Sottero B., Galli G. *The journal of nutritional biochemistry*. 2002, **13**, 700-710.
- [2] Ostlund R., Racette S., Stenson W. *Nutr. Rev.* 2002, **60**, 349-359.
- [3] Usui K., Hulleman J. D., Paulsson J. F., Siegel S. J., Powers E. T., Kelly J. W. *Proceedings of the National Academy of Sciences*. 2009, **106**, 44.
- [4] Wentworth P., Nieva J., Takeuchi C., Galve R., Wentworth A., Dilley R., DeLaria G., Saven A., Babior B., Janda K., Eschenmoser A., Lerner R. *Science*. 2003, **302**, 1053-1057.
- [5] Alcalde M. A., Antelo A., Jover A., Mejjide F., Tato J. V. *Journal of inclusion phenomena and macrocyclic chemistry*. 2009, **63**, 309–317.
- [6] Kilsdonk E. P. C., Yancey P. G., Stoudt G. W., Bangerter F. W., Johnson W. J., Phillips M. C., Rothblat G. H. *The journal of biological chemistry*. 1995, **270**, 17250-17256.
- [7] Fiore C., Eisenhut M., Krausse R., Ragazzi E., Pellati D., Armanint D., Bielenberg J. *Phytotherapy research*. 2008, **22**, 141–148.
- [8] Tolstikov G.A., Baltina L.A., Shults E.E., Pokrovskii A.G. *Russ. J. Bioorg. Chem.* 1997, **23**, 625-642.
- [9] Fuhrman B., Buch S., Vaya J., Belinky P., Coleman R., Hayek T., Aviram M. *The american journal of clinical nutrition*. 1997, **66**, 267-275.
- [10] Polyakov, N.E.; Khan, V.K.; Taraban, M.B.; Leshina, T.V. *J. Phys. Chem. B*, 2008, **112**, 4435-4440.
- [11] Polyakov, N.E.; Leshina, T.V.; Salakhutdinov, N.F.; Kispert, L.D. *J. Phys. Chem. B*. 2006, **110**, 6991-6998.

## **Electron Spin Resonance in Heterostructures with a InGaAs quantum well and Mn $\delta$ -Doped GaAs Layer**

A.I. Dmitriev<sup>1</sup>, A.D. Talanste<sup>1</sup>, S.V. Zaitsev<sup>2</sup>, R.B. Morgunov<sup>1</sup>

<sup>1</sup>Institute of Problems of Chemical Physics RAS, 142432, Acad. Semenov av., Chernogolovka, Russia.

<sup>2</sup>Institute of Solid State Physics RAS, 142432, Acad. Ossipyan st., Chernogolovka, Russia.

e-mail: aid@icp.ac.ru

Magnetic quasi-two-dimensional (2D) Ga<sub>1-x</sub>Mn<sub>x</sub>As heterostructures deserve special attention from the viewpoint of spintronics because they create conditions for injecting spin-polarized carriers in light emitting diodes. The direct implantation of Mn into the 2D channel leads to low mobility of charge carriers and suppresses radiative recombination. The spatial separation of charge carriers and the Mn  $\delta$ -doped GaAs layer results in a considerable increase in the mobility of carriers in the 2D channel by more than two orders of magnitude.

Direct measurements of the magnetization (or magnetic susceptibility) of heterostructures containing a single Mn  $\delta$ -doped GaAs layer are rather scarce and pertain to periodic structures containing a number of Mn  $\delta$ -doped GaAs layer separated by GaAs layers. Early, devoted to measurements of magnetization, the total magnetic moment of heterostructures usually containing several magnetic subsystems was determined. The interpretation of such data involves considerable difficulties and requires the introduction of additional assumptions already at the stage of subtraction of the diamagnetic contribution from the crystal matrix, not to mention the contributions from structural defects in the sample volume, substrate, interlayer boundaries, etc. This problem can be solved by using, along with a superconducting quantum interference device (SQUID), the electron spin resonance (ESR) allowing the separation of contributions from subsystems to the magnetic susceptibility of a sample. We are not aware of any works on electron spin resonance in heterostructures with quantum wells.

In this work, we used both a SQUID and ESR spectrometer to study the temperature dependences of the magnetic susceptibility of GaAs semiconductor heterostructures containing an InGaAs quantum well and a Mn  $\delta$ -doped GaAs layer. The contributions from different magnetic subsystems of the heterostructure to the magnetic susceptibility were separated by the method of ESR [1, 2]. The aim of the work was to separate the contribution of the ferromagnetic Mn  $\delta$ -doped GaAs layer to the magnetic susceptibility of a sample, to obtain the main parameters of the ferromagnetic resonance of this layer, and to find other subsystems that are sensitive to the ferromagnetic ordering in the Mn  $\delta$ -doped GaAs layer. Investigation of photoluminescence of a quantum well showed that the circular polarization of light is sensitive to the ferromagnetic ordering in the Mn  $\delta$ -doped GaAs layer. This allowed us to detect ferromagnetism by the independent optical method.

InGaAs/GaAs heterostructures with a Mn  $\delta$ -doped GaAs layer were grown by the combined method of stepwise epitaxial growth. In the first stage the GaAs buffer layer, the C  $\delta$ -doped GaAs layer, the undoped GaAs layer, the undoped InGaAs quantum well, and finally the separating GaAs layer were successively grown on a GaAs (001) substrate by metal-organic hydride epitaxy (fig.1). In the next stage the Mn  $\delta$ -doped GaAs layer and the GaAs cover layer were successively grown in the same reactor by laser sputtering of Mn and GaAs targets. The method for manufacturing and certifying InGaAs/GaAs heterostructures with a Mn  $\delta$ -doped GaAs layer is described in detail in [3]. We studied in our paper three types of

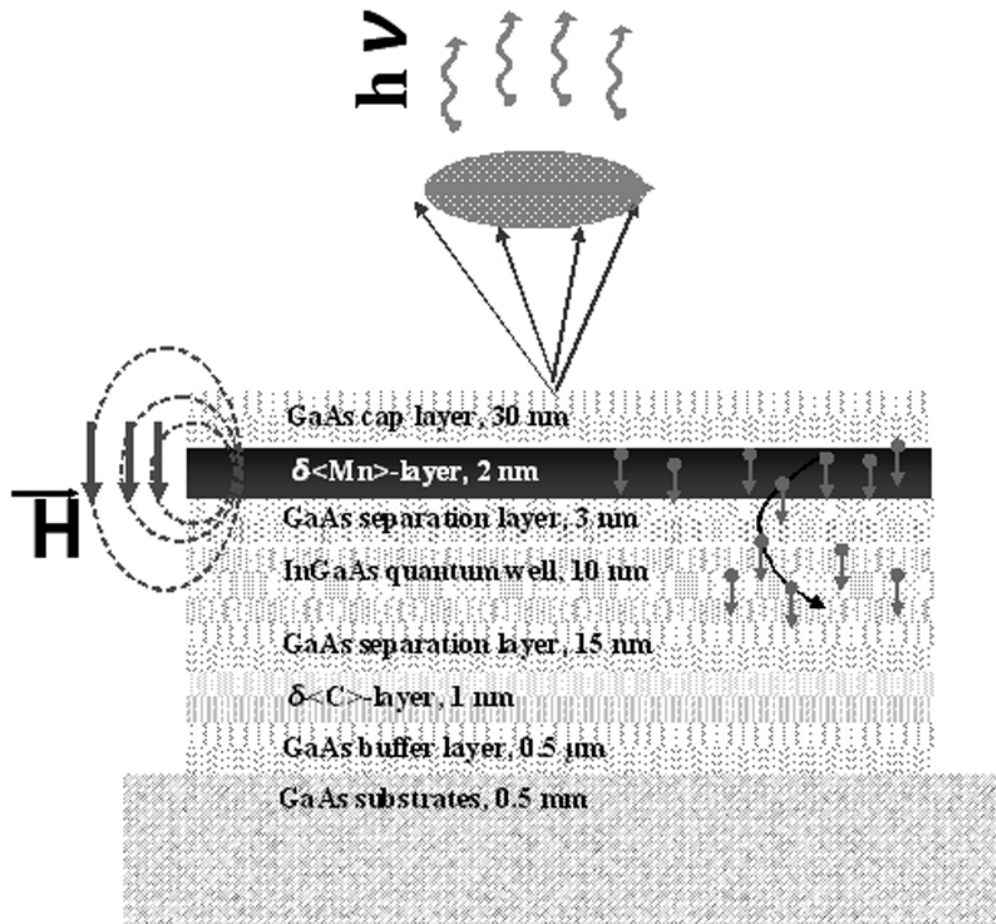


**Fig.1.** Schematic view of a heterostructure grown on a GaAs substrate. Heterostructure consist from GaAs buffer layer, C  $\delta$ -doped GaAs layer, GaAs separation layers, InGaAs quantum well, Mn  $\delta$ -doped GaAs layer and GaAs cap layer. Magnetic field  $H$  of Mn  $\delta$ -doped GaAs layer with spin-polarized holes and polarized photoluminescence of InGaAs quantum well are shown.

samples: a heterostructure containing an InGaAs/GaAs quantum well and a Mn  $\delta$ -doped GaAs layer on a GaAs (001) substrate, a control heterostructure sample containing a C  $\delta$ -doped GaAs layer instead of a Mn  $\delta$ -doped GaAs layer on a GaAs (001) substrate, and a control GaAs (001) substrate sample without a heterostructure. By using these samples, we could successively determine contributions from the substrate, crystal matrix with defects, and the C  $\delta$ -doped GaAs layer itself. The C  $\delta$ -doped GaAs layer was used to determine the contribution of boundaries between layers and paramagnetic defects in the sample volume not related to the ferromagnetism of the Mn  $\delta$ -doped GaAs layer.

The magnetic moments of samples were measured with an MPMS 5XL SQUID magnetometer (Quantum Design) in a constant magnetic field  $H = 1$  kOe. The temperature was changed from 2 to 300 K. Electron spin resonance spectra were recorded with a Bruker EMX spectrometer operating in the 9.4 GHz range at a modulation frequency of 100 kHz and constant magnetic field changing from 50 to 14 kOe. The temperature was changed from 4 to 300 K in an ESR 900 Oxford Instruments cryostat.

The degree of circular polarization of photoluminescence was measured in a magnetic field of  $H = 0$ -50 kOe in a cryostat with a superconducting magnet in Oxford Instruments cryostat. Photoluminescence was excited with a 632.8 nm He-Ne laser and recorded in the

Faraday geometry with a charge-coupled device and a monochromator. Circularly polarized photoluminescence was studied by the standard method using a linear polarizer and a quarter-wavelength plate.

The electron spin resonance spectra of the three samples are shown in fig.2. The spectrum of sample with the Mn  $\delta$ -doped GaAs layer at low temperatures contains several lines. The intensity of lines 1 and 3 drastically decreases with increasing temperature, and they are not observed at temperatures above 40 K. Isotropic lines 2, 4-6 are also observed in sample with the C  $\delta$ -doped GaAs layer instead of the Mn  $\delta$ -doped GaAs layer and in a GaAs substrate (fig.2). This means that they are related to the same paramagnetic centres of an uncontrollable impurity contained in all three samples.

Electron spin resonance line 3 in sample with the Mn  $\delta$ -doped GaAs layer was not observed in other samples without the Mn  $\delta$ -doped GaAs layer (fig.2). The number of spins

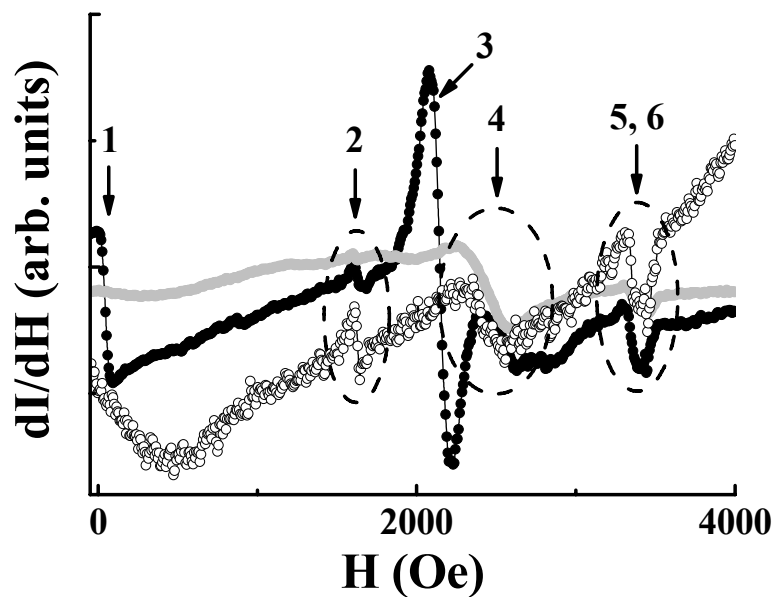


**Fig.2.** Electron spin resonance spectra for samples with the Mn  $\delta$ -doped GaAs layer (black symbols), with the C  $\delta$ -doped GaAs layer instead of the Mn  $\delta$ -doped GaAs layer (grey symbols) and GaAs substrate (open symbols) at temperatures 15 K. The numbers denote lines in the spectra.

for line 3 determined from the calculated area under the absorption curve (second integral) by comparison with this number for the calibrating blue vitriol sample proved to be 100 times greater than the number of spins calculated from the concentration of independent noninteracting manganese ions at 4 K. Therefore, at low temperatures the ferromagnetic correlations of the spins of the Mn  $\delta$ -doped GaAs layer are observed.

The explanation of line 3 by ferromagnetic resonance in MnAs, Mn<sub>3</sub>As<sub>2</sub> or other Mn containing alloys (which can be formed due to segregation of manganese on a surface and formation of compounds with arsenic during the growth of heterostructures) can be excluded. First, these materials exhibit different ferromagnetic resonance spectra. Second, the Curie temperature of these alloys is noticeably higher than the Curie temperature  $T_C \approx 35$  K observed in our experiments. In our opinion, this line is caused by the ferromagnetic resonance in the Mn  $\delta$ -doped GaAs layer. This is demonstrated by the temperature dependence of line 3, which disappears above  $T_C$ . This conclusion is also confirmed by the axial anisotropy of line 3 with the axis of easy magnetization in the layer plane.

Thus, we have separated the contributions of the magnetically ordered Mn  $\delta$ -doped GaAs layer with the Curie temperature  $T_C \approx 35$  K, the C  $\delta$ -doped GaAs layer, paramagnetic defects in GaAs, and impurity centres in a substrate to the magnetic susceptibility of two-dimensional InGaAs/GaAs semiconductor heterostructures with the Mn  $\delta$ -doped GaAs layer. The temperature dependence of the dynamic magnetic susceptibility of the Mn  $\delta$ -doped GaAs layer is consistent with the results of static measurements of the magnetic moment that is described by the “3/2” Bloch law. Effect of Mn  $\delta$ -doped GaAs layer magnetization on photoluminescence polarization of quantum well in GaAs-based heterostructures was found [2].

### Acknowledgments

Support by the Grant of the President of Russia MK-1764.2011.3.

### References

- [1] A.I. Dmitriev, R.B. Morgunov, S.V. Zaitsev, JETP 112 (2011) 317.
- [2] A.I. Dmitriev, A.D. Talantsev, S.V. Zaitsev, Yu.A. Danilov, M.V. Dorokhin, B.N. Zvonkov, O.V. Koplak, R.B. Morgunov, JETP 112 (2011) in print.
- [3] M.V. Dorokhin, Yu.A. Danilov, P.B. Demina, V.D. Kulakovskii, O.V. Vikhrova, S.V. Zaitsev, B.N. Zvonkov, J. Phys. D 41 (2008) 245110.

## Structural transition in lanthanum gallate and transformation of the fine structure of the EPR spectrum of a Gd<sup>3+</sup> impurity center

A.V. Fokin, V.A. Vazhenin, V.B. Guseva, A.P. Potapov, M.Yu. Artyomov

Ural State University, Pr. Lenina 51, 620083 Ekaterinburg, Russia.

e\_mail: andrey.fokin@rambler.ru

Investigation of LaGaO<sub>3</sub> powders and single crystals using X-ray and neutron scattering proved the existence of the structural phase transition  $P_{bnm}(D_{3h}^{16}) \leftrightarrow R\bar{3}c(D_{3d}^6)$  at 420 – 430 K between the phases with a distorted perovskite-like structure. In [1,2], we studied the EPR spectra of Gd<sup>3+</sup> ions substituting La<sup>3+</sup> and Mn<sup>4+</sup>, Fe<sup>3+</sup>, and Mn<sup>2+</sup> ions in the positions of Gd<sup>3+</sup>. The parameters of the spin Hamiltonian of Gd<sup>3+</sup> and Mn<sup>4+</sup> centers, whose symmetry groups change from  $m(C_s)$  to  $32(D_3)$  and from  $\bar{1}(C_i)$  to  $\bar{3}(S_6)$ , respectively, have been determined in both phases. This work is focused on studying the structural transition in lanthanum gallate by EPR. Measurements were carried out on a Bruker EMX Plus X-band EPR spectrometer. The accuracy of the temperature measurement was  $\pm 1$  K. We studied manganese-doped LaGaO<sub>3</sub> single crystals (with a concentration of manganese dioxide in a charge of 0.5 and 5.0 mol % and a purity of initial chemicals of no worse than 99.99%) grown by G. B. Lutts at Norfolk University (Virginia, United States) in a weakly oxidizing atmosphere with the use of Czochralski method. Temperature transformation of the EPR spectrum of the samples during heating and cooling in the vicinity of the structural transition at  $\mathbf{B} \parallel \mathbf{y} \parallel \mathbf{c}$ , where  $\mathbf{B}$  is the magnetic field induction,  $\mathbf{c}$  is the crystallographic axis in group  $P_{bnm}(D_{3h}^{16})$  and  $\mathbf{y}$  is the magnetic axis in the low-temperature phase (deviation from  $\mathbf{B} \parallel \mathbf{y}$  is  $\approx 3^\circ$ ) was investigated.

The coexistence of phases during heating and cooling takes place at 450 K and 447 K respectively. A drastic abrupt change in the positions of the EPR signals of Gd<sup>3+</sup> and Mn<sup>4+</sup>, combined with the presence of the temperature hysteresis and coexistence of phases, indicates the first order structural transition. Constancy of the resonance positions of the electronic transitions in both phases, except for the structural transformation point, indicates a weak temperature dependence of the fine structure parameters. A colossal change in the parameters of the second rank spin Hamiltonian, including the sign change of  $b_{20}$  of the Mn<sup>4+</sup> centers (Table 1), occurs almost entirely at the structural transition temperature. Within the accuracy of measurements, we did not observe any temperature dependence of the line-width of Gd<sup>3+</sup> centers in both phases. A similar behavior of the EPR spectra of the cubic and tetragonal (in the paraphrase) Gd<sup>3+</sup> centers (an abrupt change in the resonance positions, coexistence of the

**Table 1.** Second\_order parameters (in MHz) of the spin Hamiltonians of Gd<sup>3+</sup> and Mn<sup>4+</sup> centers in two phases of lanthanum gallate in the coordinate system of the low-temperature phase; two signs of  $b_{21}$  of the Gd<sup>3+</sup> center correspond to two magnetically nonequivalent centers;

Параметр	Gd <sup>3+</sup>		Mn <sup>4+</sup>	
	300K	438K	300K	438K
b <sub>20</sub>	-2276	-1772	3556	-3100
b <sub>21</sub>	$\pm 4278$	0	950	0
b <sub>22</sub>	-91	1772	-1650	3100
c <sub>21</sub>	0	-10023	3900	-17535
c <sub>22</sub>	0	0	-1730	0

spectra due to the adjacent phases and the absence of line broadening in the vicinity of the transition) was observed in cesium strontium trichloride CsSrCl<sub>3</sub>, which undergoes a set of first-order ferroelastic transitions  $O_h^1 \rightarrow D_{4h}^5 \rightarrow D_{2h}^{17} \rightarrow C_{2h}^2$  at temperatures of 390, 379, and 366 K, respectively [3, 4], as a result of the condensation of the components of rotational modes  $M3$  and  $R25$  [5].

As is known, the EPR spectrum of a high-spin center contains unique information on the structure of the local environment of

the defect, which obviously differs from the structure of the defect-free crystal. The problem of extracting structural information from the spectrum, i.e., finding the relation between the spectral parameters and the parameters of the local environment can be solved by developing an adequate microscopic theory. However, this approach encounters serious difficulties. This explains a large number of works attempting to couple the parameter of the zero-field splitting of a high-spin paramagnetic center to the coordinates of the ligand environment by empirical relations. The most popular version of such coupling is the superposition approximation, which assumes additivity of the contributions of the nearest anions to the fine-structure parameters  $b_{nm}$  [6, 7]. In the present work, the transformation of paramagnetic centers due to the structure transition in lanthanum gallate is used to test this approach.

The most known superposition approximation for the fine-structure constants of the ground state suggested by Newman [6, 7]:

$$b_{2m} = \sum_d K_{2m}(\theta_d, \phi_d) \cdot \bar{b}_2(R_d) \quad (1)$$

$$\bar{b}_n(R_d) = \bar{b}_n(R_0)(R_0/R_d)^{t_n} \quad (2)$$

where  $K_{nm}(\theta_d, \phi_d)$  is the angular structure factor,  $R_d$ ,  $\theta_d, \phi_d$  are the spherical coordinates of ligands, and  $R_0$  is the sum of ionic radii of the ligand and the central ion,  $\bar{b}_n(R_0)$  and  $t_n$  are the two intrinsic parameters. Although the intrinsic parameters remain constant only for paramagnetic centers within the sets of isostructural crystals, dozens of researchers use this formalism to analyze the experimental parameters of both second and fourth-order zero-field splitting of  $d$ - and  $f$ - ions. Levin [8] validated the use of the superposition approximation for the parameters of the second-rank fine-structure tensor of  $S$ -state rare-earth ions and proposed the new version of Eq. (2):

$$\bar{b}_2(R_d) = \bar{b}_{2p}(R_0)(R_0/R_d)^3 + \bar{b}_{2s}(R_0)(R_0/R_d)^k \quad (3)$$

where the first and second terms are the contributions of the electrostatic field of the ligand point charge and the short-range metal–ligand interaction respectively,  $k \approx 10$ ,  $\bar{b}_{2p}$ ,  $\bar{b}_{2s}$  are the model parameters. Monoclinic-to-trigonal transformation of  $Gd^{3+}$  centers under the structural transition makes lanthanum gallate a model object for comparing the effectiveness and adequacy of the above superposition approximations.

The second-order fine-structure parameters of  $Gd^{3+}$  centers in  $LaGaO_3$  at room temperature in the system of coordinates  $\mathbf{x} \parallel \mathbf{a}$ ,  $\mathbf{y} \parallel \mathbf{c}$ ,  $\mathbf{z} \parallel \mathbf{b}$  ( $\mathbf{a}$ ,  $\mathbf{b}$ ,  $\mathbf{c}$  are the axes in group  $P_{bnm}(D_{2h}^{16})$ ) are listed in Table 1. Equations (1) and (3) taking into account the coordinates of twelve oxygen atoms surrounding the lanthanum ion, which follow from the structural data [9], yield the expressions for the parameters (at  $R_0 = 234$  pm):  $b_{20}$ ,  $b_{21}$ ,  $b_{22}$ . Equating these

**Table 2.** Intrinsic parameters  $\bar{b}_{2p}$ ,  $\bar{b}_{2s}$ , mean-square deviations  $S$ , and predicted values of  $b_{20}$  ( $\mathbf{z} \parallel C3$ ) (all values are given in MHz) for  $Gd^{3+}$  centers in the rhombohedral phase of  $LaGaO_3$  in the Levin approximation (3)

$\bar{b}_{2p}(R_0)$	$\bar{b}_{2s}(R_0)$	S	$b_{20}$	Structure of the environment
-25000	13850	816	-1190	[7]
-25110	12000	750	-1260	[7]+relaxation according to (4)
-12905[8]	6897[8]	-	-1050	[7]+relaxation according to (4)
-	-	-	-3544	Experiment [1]

expressions to the experimental data results in a redundant system of equations for two intrinsic parameters. The best least-squares fit of these expressions to the experimental data was obtained for intrinsic parameters (Table 2)

The inconsistency of the system of equations for and can be due to the difference in the environment of the paramagnetic ion from the structure of the perfect crystal [9] caused by lattice relaxation. Bearing in

mind a substantial difference between the radii of the impurity and the substitution ion (in the case of nine surrounding atoms,  $R(\text{Gd}^{3+}) = 110.7$ ,  $R(\text{Ln}^{3+}) = 121.6$  pm]), it is natural to assume the presence of, along with other distortions, a fully symmetric deformation of the environment of the paramagnetic defect. According to [14], to take this deformation into account, one has to replace  $\bar{R}_d$  in Eq. (3) by

$$\bar{R}_d = R_d - \Delta R, \quad \Delta R = 1/2\{R(\text{Ln}^{3+}) - R(\text{Gd}^{3+})\}. \quad (4)$$

As a result, the mean-square deviation decreases and the intrinsic parameters become  $\bar{b}_{2p} = -25110$  MHz and  $\bar{b}_{2s} = 12000$  MHz. Substitution of the latter values of the intrinsic parameters into Eqs. (1), (3) with the coordinates of ligands in the high-temperature phase [9] deformed according to Eq. (4) yields the  $b_{20}$  value (Table 2), which is closer to the experimental one than without the deformation. It should be mentioned that Levin [8] quotes the values of  $b_{20}$  and for the  $\text{Gd}^{3+}$  centers in the oxygen environment with  $R_0 = 234$  pm, which agree in the order of magnitude and sign with our values; their use in the high-temperature phase of  $\text{LaGaO}_3$  leads to a reasonable (order of magnitude and sign) value of  $b_{20}$  (Table 2). Intrinsic parameters, mean-square deviations  $S$ , and predicted values of  $b_{20}$  for  $\text{Gd}^{3+}$  centers in the rhombohedral phase of  $\text{LaGaO}_3$  in the Levin and Newman approximations are listed in Tables 2 and 3 respectively.

**Table 3.** Intrinsic parameters  $\bar{b}_n(R_0)$ ,  $t_2$ , mean-square deviations  $S$ , and predicted values of  $b_{20}$  ( $\mathbf{z} \parallel \text{C3}$ ) (all values are given in MHz) for  $\text{Gd}^{3+}$  centers in the rhombohedral phase of  $\text{LaGaO}_3$  in the Newman approximation

$\bar{b}_n(R_0)$	$t_2$	$S$	$b_{20}$	Source
3590	7.7	2010	-1670	This work, 1 ver.
-2540	-1	1710	340	This work, 2 ver.
-6000	0.4	-	-	CaO[7]
-6000	0.8	-	-	SrO[7]
-3000	1	-	-	YVO[7]

We also performed calculations in the Newman version (2) of the superposition approximation for the oxygen environment relaxed according to Eq. (4). The results are summarized in Table 3 along with the intrinsic parameters of  $\text{Gd}^{3+}$  centers in oxides from [7]. Two sets of parameters with nearly the same mean-square deviation  $S$  were obtained in the orthorhombic phase by solving the system of equations, which puts a question of choosing a physically reasonable solution. At this point, we should

emphasize that mean-square deviations  $S$  yielded by the present calculation, which characterize the quality of the solutions, are substantially higher than the values in Table 2. This indicates larger errors of the intrinsic parameters. Bearing in mind the above errors, the first set of intrinsic parameters is close to the values obtained in [7] for the centers in CaO, SrO, and YVO<sub>4</sub>. However, the use of these parameters in the rhombohedral phase yields  $b_{20}$  very far from the experiment (Table 3). The second set of parameters predicts the  $b_{20}$  value for the  $\text{Gd}^{3+}$  center in the high-temperature phase in fair agreement with the experiment (Table 3) but the intrinsic parameters have nothing in common with the values for  $\text{Gd}^{3+}$  in oxide crystals [7].

The intrinsic parameters of the model found above were used to predict zero-field splitting of  $\text{Gd}^{3+}$  centers in perovskite-like compounds  $\text{BaTiO}_3$  [10]) and  $\text{LaAlO}_3$  [11], which are formed due to structural transitions from phase  $\text{O}_{1h}$ . A  $\text{Gd}^{3+}$  ion occupies the position of barium ( $C_{4v}$ ) and lanthanum ( $D_3$ ) ion in  $\text{BaTiO}_3$  and  $\text{LaAlO}_3$ , respectively. Zero-field splitting parameters  $b_{20}$  of gadolinium centers in these crystals were found in [12,13]. These predictions taking into account fully symmetric relaxation of the environment according to Eq.(4) and the respective experimental data are listed in Table 4. Clearly, the superposition model in the Levin approximation (3) gives for  $\text{BaTiO}_3$  the result (the sign and order of magnitude of  $b_{20}$ ) close to the experimental one, whereas the agreement of two versions of the

**Table 4.** Calculated and experimental parameters of the zero-field splitting of  $Gd^{3+}$  centers ( $\Delta R$  is the radial relaxation of the environment)

Crystal	Approximation	$\Delta R$ , pm	$b_{20}$ , MHz	
			calculation	experiment
BaTiO <sub>3</sub>	Levin	10	-630	-878[11]
	Newman, 1 version		-15	
	Newman, 2 version		-240	
LaAlO <sub>3</sub>	Levin	5	-480	1113[12]
	Newman, 1 version		-410	
	Newman, 2 version		70	

gadolinium center in LaAlO<sub>3</sub>. It is reasonable to perform similar procedure also for the rhombohedral phase of LaGaO<sub>3</sub>, where the predicted zero-field splitting is very approximate (see above). Twelve oxygen ions surrounding La<sup>3+</sup> in these compounds (point group  $D_3$ ) include a hexagon of ions with  $\theta_1 = 90^\circ$  and two oxygen triangles with  $\theta_2 \approx 35^\circ$ ,  $\theta_{31} = (180 - \theta_2)^\circ$ , where  $\theta$  is the polar angle. Within the said point group, one can vary only the parameters  $\theta_2$ , the angle between  $C_3$  and the gadolinium-ion bond axis in the oxygen triangle. It turned out that perfect agreement with the experiment can be achieved within the

**Table 5.** Relaxation of the angular coordinates of the ligand environment of the  $Gd^{3+}$  ions required for the agreement with the experiment

Crystal	Approximation	$\Delta\theta_2$ , deg
LaAlO <sub>3</sub>	Levin	0.8
	Newman, 1ver	-7
	Newman, 2ver	2
LaGaO <sub>3</sub>	Levin	-1.2
	Newman, 1ver	11
	Newman, 2ver	-10

Levin approximation (3) by small ( $\approx 1^\circ$ ) angular distortions. In the versions of the Newman approximation (2), similar result can be achieved by an order of magnitude larger and, most probably, nonrealistic distortions.

The latter estimates in the Levin approximation (3) seemingly cannot be yet treated as reliable information on the character and magnitude of the distortions of the crystalline environment under the ion substitution. The values in Table 5 can result from errors in the intrinsic model parameters. Nevertheless, it can be stated with confidence that the Levin version (3) of the superposition model describes considerably better

zero field splitting of gadolinium in perovskite-like crystals, as compared to the Newman version (2).

## References

- [1] V. A. Vazhenin, A. P. Potapov, V. B. Guseva, and M. Yu. Artyomov, *Fiz. Tverd. Tela* (St. Petersburg) **51** (5), 869 (2009) [*Phys. Solid State* **51** (5), 917 (2009)].
- [2] V. A. Vazhenin, A. P. Potapov, V. B. Guseva, and M. Yu. Artyomov, *Fiz. Tverd. Tela* (St. Petersburg) **52** (3), 480 (2010) [*Phys. Solid State* **52** (3), 515 (2010)].
- [3] V. A. Vazhenin and M. Yu. Artemov, *Fiz. Tverd. Tela* (St. Petersburg) **39** (2), 377 (1997) [*Phys. Solid State* **39** (2), 323 (1997)].
- [4] V. A. Vazhenin, V. B. Guseva, and M. Yu. Artemov, *Fiz. Tverd. Tela* (St. Petersburg) **41** (2), 247 (1999) [*Phys. Solid State* **41** (2), 219 (1999)].
- [5] K. S. Aleksandrov, A. T. Anistratov, B. V. Beznosikov, and N. V. Fedoseeva, *Phase Transitions in Crystals of Halide ABX<sub>3</sub> Compounds* (Nauka, Novosibirsk, 1981) [in Russian].
- [6] D.J. Newman, W. Urban. *Adv. Phys.* **24**, 793 (1975).

## PROCEEDINGS

- [7] Crystal Fiedl Handbook / Eds D.J. Newman, B. Ng. Cambridge University Press, Cambridge (2000). P. 151.
- [8] L.I. Levin. Phys. Status Solidi B 134, 275 (1986).
- [9] C.J. Howard, B.J. Kennedy. J. Phys.: Cond. Matter **11**, 3229 (1999).
- [10] F. Jona and D. Shirane, *Ferroelectric Crystals* (Pergamon, Oxford, 1962; Mir, Moscow, 1965).
- [11] B.C. Chakoumakos, D.G. Schlom, M. Urbanik, J. Luine. J. Appl. Phys. **83**, 1979 (1998).
- [12] L. Rimai, G.A. de Mars. Phys. Rev. **127**, 702 (1962).
- [13] W. Low, A. Zusman. Phys. Rev. **130**, 144 (1963).
- [14] Shao-Yi Wu, Hua-Ming Zhang, Guang-Duo Lu, Zhi Hong Zhang. Pramana — J. Phys. **69**, 451 (2007).

**Diagnostics of radiating ions-radicals in bioorganic materials  
using a method of an electronic paramagnetic resonance at Q-range.  
The spectra shapes**

L.V. Khaidarshina, V.I. Pudov

Institute of Metal Physics, UB RAS, 620990, S. Kovalevskaya 18, Ekaterinburg, Russia.

e-mail: Haidarshina@imp.uran.ru

This work was carried out as a part of the researches directed to creation of a basis for development of new methods of medical diagnostics and the laboratory analysis.

The specific ions-radicals are formed in bone tissue under the influence of temperature, ionizing radiation etc. that become apparent at the magnetic resonance spectra. The phenomenon of increase of the paramagnetic centres concentration was found out under some diseases in comparative trials of the samples of healthy tissue and pathologically changed one using the X-range spectrometers. [1,2,3]. The effect has nonspecific character i.e. is not accompanied by a change of the spectrum form for thermochemical radicals which originate during annealing [2,3]. The similar phenomenon was also observed in the samples treated by ionizing radiation [1].

The comparative X-range EPR-researches of ion-radicals concentration dynamics for healthy bone tissue and pathologically one were carried out in [1] at complex effect of the radiation and heating (an irradiation with the subsequent annealing at different temperatures). At complex method, the annealing temperature rise, the multicomponent radiation spectrum degenerates in a single line that is typical for a thermochemical spectrum. The method appeal consists in that the maximal EPR-signals intensity from thermochemical ions-radicals is formed at much smaller temperatures (150° – 300°C) in comparison with a classical method of thermal generation (400° – 500°C, [2,3]). An additional data are given by the spectra dynamics which looking differing for the healthy bone tissue and the pathogenic one. Unfortunately, lack of data about the form and structure of registered multicomponent spectra reduces the information value of the research. Therefore, the conclusion of [1] is that it is desirable to supply the work by the spectra shapes researches using high-resolution Q-range spectrometers.

This work is the continuation of [1]. The purpose of research was acquisition and the analysis of the radiation spectra shape for a bone tissue at absence of heat treatment and in the temperature range of transition to a thermochemical spectrum.

At the first stage the shape of EPR-spectra registered after an irradiation of normal bone tissue (a spongy part of a femoral joint) and pathologically changed one (coxarthrosis) was investigated. Research was carried out using the modified Q-band radiospectrometer RE-1308 (37 GHz, Russia). Samples were made of a material of the same collection which was used in [1,2] that has allowed to avoid the problems concerned with variability of properties of objects with a biological origin.

At fig.1 the EPR-spectra obtained after an irradiation of healthy bone tissue ("Norm") and pathologically changed one ("Pathology") are presented. The results do not need for the special analysis: in both cases, spectra are completely similar to each other in every detail. The form of spectra is typical for the radiation ions-radicals formed in apatite-like materials to which the bone tissue belongs. These spectra are usually characterized by three primary extrema [4]. G-factor values for these extrema are presented in table 1. The literary data [4] on g-factor variations of radiation spectra of the bone remains are given in the same place for comparison.

The research result is the evidence that shapes of radiation-induced EPR-spectra of bone

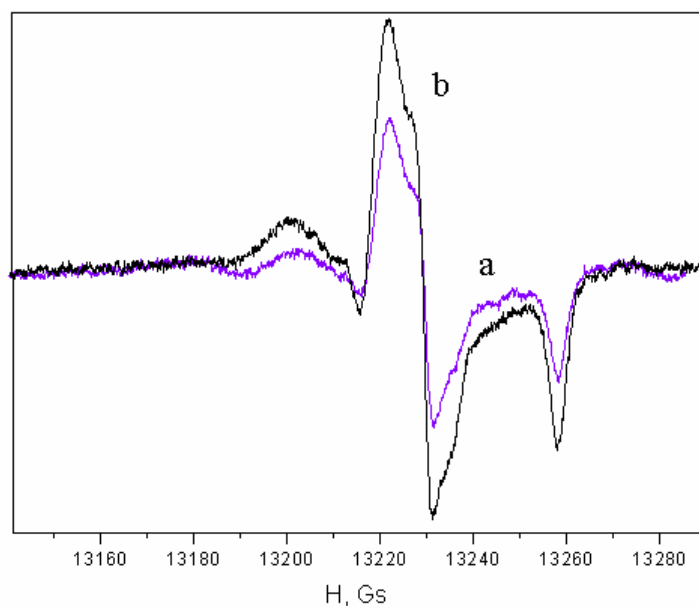


**Fig.1.** Radiation EPR-spectra for the samples of a healthy bone tissue (a) and pathologically changed one (b).

tissue at norm and at a pathology do not differ among themselves. Hence, the differences in radiation spectra of healthy tissue and pathologically changed one [1], similarly to the spectra of thermochemical radicals [2], are caused by a nonspecific increase of concentration of the paramagnetic centers.

**Table 1.** The characteristics of EPR-spectra for the samples of a healthy bone tissue and pathologically changed one at different kinds of treatment.

№	Sample	Treatment	g1	g2	g3
1	Norm	Irradiation	2,0039	2,0025	1,9984
2	Pathology	Irradiation	2,0039	2,0025	1,9984
3	Pathology	Irradiation + heat treatment	2,0043	2,0026	1,9984
4	Parameter variations [4]	Irradiation	2,0036 – 2,0045	2,0005 – 2,0022	1,9977 – 1,9984

The second stage included the analysis of a spectrum of annealing temperatures transition region. The special sample containing all types of radicals was prepared for this purpose. The sample of a bone tissue was annealed at temperature of 420°C. The EPR-spectrum of a sample represented the single line typical for thermochemical radicals. Further the sample was irradiated. A radiation component, similar to fig.1, appeared at the spectrum. At last stage a sample was annealed at 220° C (the region of radiation spectrum degeneration [1]), this result is presented at fig.2a, and a radiation component is feebly marked.

For obtained EPR-spectrum (curve "a") analysis we have tried to use an approach of EPR-dosimetry [5]. The EPR-signal is numerically decomposed (by a fitting) on radiation and background components, the last one is then subtracted. In our case the background component can be interpreted as a single line from a thermochemical ion-radical. The result of decomposition to components is presented at fig.2. As one can see, the remained signal (curve b) after subtraction of a single line spectrum (curve c) corresponds to the typical radiating spectrum similar to that presented at fig.1. G-factor values for radiation ions-radicals for the primary maxima (see table 1) are lightly differ.

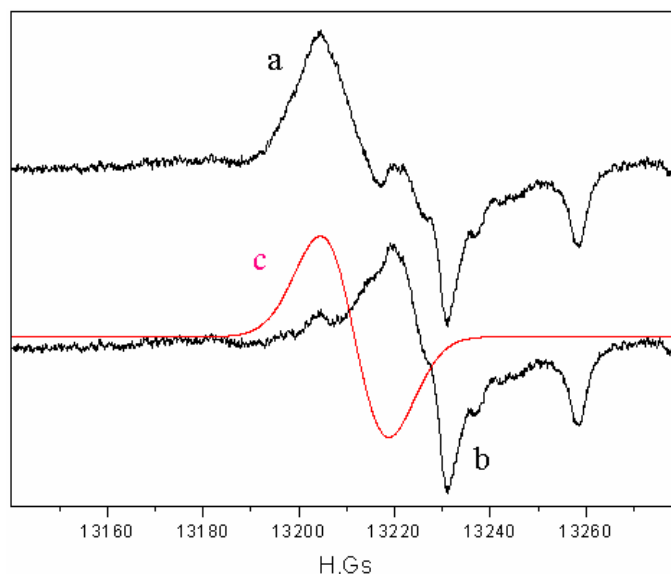


**Fig.2.** EPR-spectra of a bone tissue sample after an irradiation and annealing at 220°C (a) and decomposition to radiation component (b) and thermochemical one (c).

The researches have shown, that the effect of increase of concentration of the paramagnetic centres at pathological change of a human bone tissue (by the example of coxarthrosis) is nonspecific both for thermochemical and for radiating ions-radicals. At the combined radiation-thermal influence the specific form of radiation spectrum component is kept in a qualitative kind right up to annealing temperatures, corresponding to radiation spectrum degeneration. The obtained results actually dictate a priority direction of the further researches: realization of detailed, component-wise comparative analysis of EPR-spectra dynamics at radiation-thermal processing of healthy and pathologically changed human bone tissues. The complex use of X- and Q-range spectrometers will be very effective for this task.

## References

- [1] Khaydarshina L. V. Diagnostics of radiating ions-radicals in bioorganic materials via a method of an electronic paramagnetic resonance. Actual problems of magnetic resonance and its application. XIII International Youth Scientific School. Kazan University, 2010, p. 85-88.
- [2] Khaydarshina L. V. EPR-researches of biomaterials using the data of thermochemical ion-radicals. Actual problems of magnetic resonance and its application. XIII International Youth Scientific School. Kazan University, 2010, p. 140-142.
- [3] Votyakov S. L., Lemesheva S. L., Golovanova O. A. Thermochemical ions-radicals in organic component of a human bone tissue, influence of pathogenic changes. Materials of the III Russian conference with international participation. Syktyvkar 2009, p. 162–165.
- [4] Вотяков С. Л., Киселева Д.В., Щапова Ю.В., Смирнов Н.Г., Садыкова Н.О. Физико-химические характеристики ископаемых костных остатков млекопитающих и проблема оценки их относительного возраста. Часть 2. Екатеринбург, 2009, с. 35-42.
- [5] ГОСТ Р 22.3.04-96 Метод определения поглощенных доз внешнего гамма-излучения по спектрам электронного парамагнитного резонанса зубной эмали. /Method of absorbed radiation doses measurement using ESR-spectra of tooth enamel./ Изд. стандартов, 1997, 30 с.

## High-frequency EPR of the polynuclear compounds of Cu(II)

N.N. Efimov, V.V. Minin, E.A. Ugolkova, N.V. Zauzolkova, I.L. Eremenko,  
V.M. Novotortsev

N. S. Kurnakov Institute of General and Inorganic Chemistry, Russian Academy of Sciences,  
119991, Leninskiy prospekt, Moscow, Russian Federation

e-mail: nnefimov@narod.ru

Recently, interest has grown in design and magnetic properties of bi- and polynuclear molecules and molecule based on the coordination polymers with mono or multidimensional frameworks. These compounds are very useful for developing new functional molecule-based materials, for example the high nuclearity transition metal complexes are of current importance as new nanometric substances and a single molecule magnets. Therefore the synthesis of bi- and polynuclear compounds containing magnetic transition metal ions has become the focus of intense research activities in coordination chemistry [1].

We investigated polynuclear compounds  $\{[(\text{EtOH})_2\text{Cu}_2(\text{CHDAA})_2]\cdot\text{EtOH}\}_n$  (**1**) and  $[\text{K}_2(\eta^1\text{-H}_2\text{O})_6(\eta^1\text{-py})_8\text{Cu}_{16}(\eta^1\text{-H}_2\text{O})_2(\mu_4\text{-CHDAA})_{16}]\cdot\text{EtOH}\cdot\text{MeCN}\cdot 3\text{H}_2\text{O}$  (**2**) which were synthesized and characterized by single crystal XRD data (see fig.1 and fig.2 respectively) and partly characterized previously [2]. The crystal structure of the both compounds mainly consists of the binuclear fragment of copper(II) with four paddle-wheel carboxylates bridging (O-C-O).

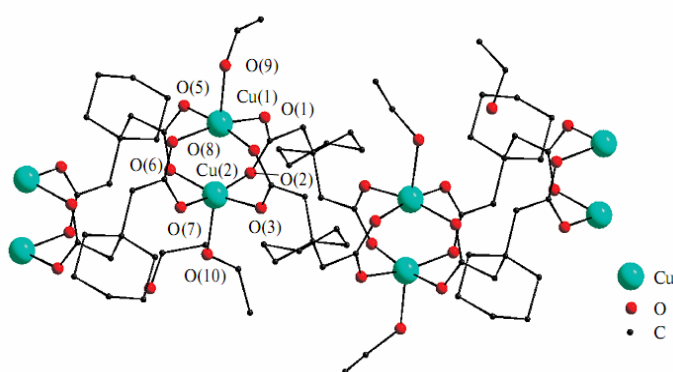


**Fig.1.** Fragment of the polymer chain **1**.

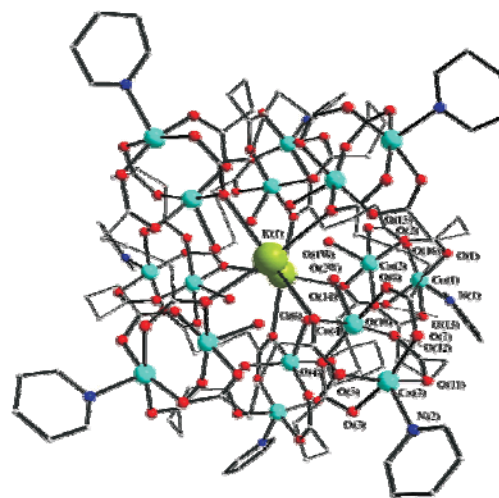


**Fig.2.** Crystal structure of **2**.

X- and W-band EPR spectra of powdered samples were recorded by a Bruker Elexsys-E680X spectrometer. Spectra simulation was performed using the Belford's eigenfield method [3].

The X-band EPR spectra of polynuclear compounds of copper(II) pivalates studied in this work are typical for the systems in the triplet state with total spin  $S = 1$  (see fig.3). The triplet states can be formed in the polynuclear complexes of copper (II) in the presence of strong exchange interaction between metal ions. The  $S = 1$  EPR signals of **1** and **2** confirm the existence of the paddle-wheel binuclear structure. As can be seen from fig.3, the EPR spectra of the studied substances are very similar what may be caused by weak influence of similar channels of exchange interaction in these compounds. A weak signal at 340 mT (in the case of **1** and **2**) is caused by presence of contamination by the monomer complexes. In fig.3a, you

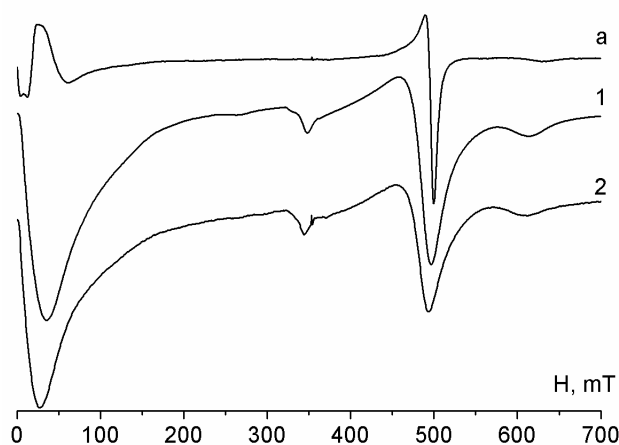


**Fig.3.** X-band EPR spectra of **dimer** (a), **1** (1) and **2** (2) (T = 298 K).

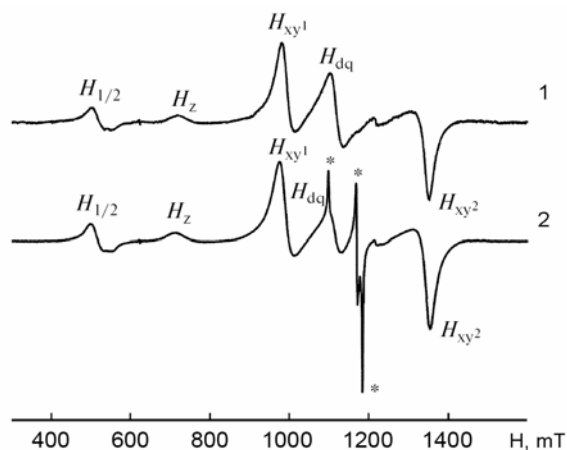


**Fig.4.** Q-band spectra of **1** (1) and **2** (2) (T = 298 K) [2].

can see the EPR spectrum of a simple paddle-wheel Cu(II) binuclear structure with four O-C-O bridges (**dimer**).

In the case of the triplet state, the SH is represented in the following form [4]:

$$H = g_{\parallel}\beta H_z S_z + g_{\perp}\beta(H_x S_x + H_y S_y) + D(S_z^2 - 1/3 S(S+1)). \quad (1)$$

We carried out high-frequency electron paramagnetic resonance measurements in order to investigate the effect of the magnitude of  $h\nu$  on the electronic structure of the compounds and to quantitatively determine the zero-field-splitting (zfs) parameters of the spin Hamiltonian (SH) [1].

The main part of the W-band EPR spectra is present on fig.5. The weak half-field (near 1.5 T) signal due to forbidden transition ( $\Delta m_s = 2$ ) is not presented.

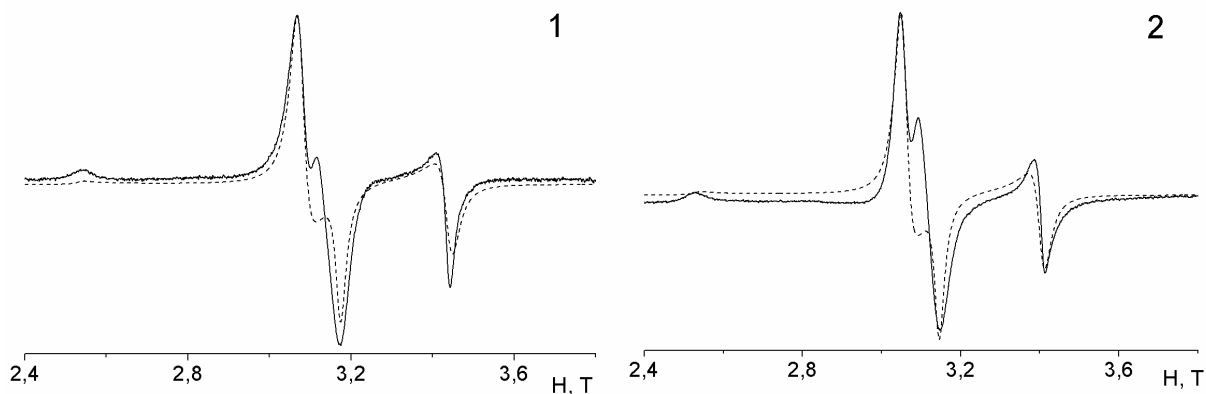


**Fig.5.** The main part of W-band EPR spectra of **1** (1) and **2** (2) (strong line) and its best-fit (dashed line) (T = 298 K).

The positions of the observed resonances in X-, Q- [2] and W-band for **1** are plotted in the  $h\nu$  versus field plot displayed in fig.6. Best-fit of the simulated spectra in X- and W-band (See dashed line on fig.5) to the experimental data allow us to quantitatively determinate zfs parameters of the SH (see table 1).

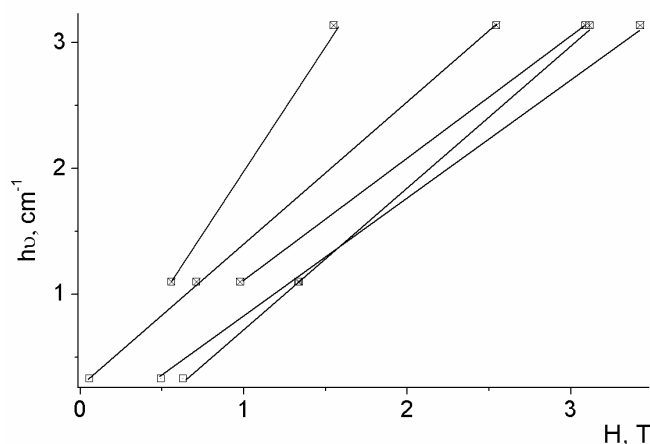


**Fig.6.** The  $h\nu$  dependence of the main EPR peaks of **1** observed at 298 K.  
(The Q-band data taken from [2].)

**Table 1.** Parameters of the spin Hamiltonian.

sample	dimer		1			2		
	X	W	X	Q [2]	W	X	Q [2]	W
$g_{\parallel}$	2.375	2.370	2.360	2.38	2.355	2.365	2.38	2.355
$g_{\perp}$	2.077	2.070	2.064	2.07	2.050	2.075	2.07	2.060
$D$ (cm <sup>-1</sup> )	0.372	0.369	0.351	0.368	0.340	0.337	0.374	0.337

### Acknowledgment

This work was supported by Russian Foundation for Basic Research (Grant N 09-03-12122, 09-03-12228, 09-03-90441, 09-03-90446)

### References

- [1] D. Gatteschi, R. Sessoli and J. Villain. *Molecular Nanomagnets*. // Oxford University press. 2006.
- [2] N.V. Zauzolkova et al. // *Rus. Chem. Bullet.* 2010. 59 (6). P. 1186.
- [3] G.G. Belford, R.L. Belford, J.F. Burkhalter. // *J. Magn. Reson.* 1973. 11. P. 251.
- [4] A. Abragam, B. Bleaney. *Electron Paramagnetic Resonance of Transition Ions* // Dover: New York, 1986.

## Spin probe orientation distribution functions in aligned nematic liquid crystal

T.S. Yankova, N.A. Chumakova, D.A. Pomogailo, A. Kh. Vorobiev

Department of Chemistry, Lomonosov Moscow State University, 119991, Leninskiye gory, 1/3, Moscow, Russian Federation

e-mail: ya.tatiana@gmail.com

### Introduction

Spin probe method is widely used for investigation of alignment and rotational mobility of liquid crystals [1 (Chapter 3), 2, 3]. This method is based on analysis of EPR spectra of spin probes – nitroxide radicals introduced into liquid crystalline media.

Characteristic of orientational ordering is an orientation distribution function (ODF). It shows a fraction of particles oriented in angle interval  $(\alpha+d\alpha, \beta+d\beta, \gamma+d\gamma)$ . A method for determination of an orientation distribution function (ODF) of spin probes was developed previously [4]. ODF is expanded in a series of spherical harmonics:

$$\rho(\beta, \gamma) = \sum_{l=0}^{\infty} \left( \frac{1}{2} a_{l0} P_l(\cos \beta) + \sum_{k=1}^l P_{lk}(\cos \beta) [a_{lk} \cos k\gamma + b_{lk} \sin k\gamma] \right) \quad (1)$$

Here  $P_l(\cos \beta)$  — Legendre polynomials,  $P_{lk}(\cos \beta)$  — associated Legendre functions. Angles  $(\beta, \gamma)$  relate g-tensor frame of a spin probe molecule with a sample frame. Expansion coefficients  $a_{lk}$ ,  $b_{lk}$  are determined via numerical simulation of EPR spectra. ODF expressed as Eq. (1) corresponds to distribution of orthorhombic spin probes in an axial sample. In the most general case an ODF depends on three angles  $(\alpha, \beta, \gamma)$ . The method [4] is used for investigation of alignment in frozen media, in the absence of molecular mobility.

The most widespread approach for investigation of ordered media by EPR spectroscopy implies rotational diffusion of a spin probe in a field of an orienting potential  $U(\alpha, \beta, \gamma)$ , which is created by an orienting media [1 (Chapter 3)]. However this approach is not optimized for investigations of orientation distribution of molecules in samples in the absence of molecular mobility. The orientation distribution function in this case is presented as a Boltzmann's exponent:

$$\rho(\alpha, \beta, \gamma) = \frac{e^{-U(\alpha, \beta, \gamma)/k_b T}}{\int e^{-U(\alpha, \beta, \gamma)/k_b T} d\alpha d\beta d\gamma} \quad (2)$$

Within this approach the orientational axis of spin probe molecule is assumed to coincide with one of the axes of rotational diffusion tensor. The orienting potential is expanded in a series of spherical Wigner's D- functions:

$$\frac{U(\alpha, \beta, \gamma)}{k_b T} = \sum_{l,m,k} \varepsilon_{mk}^l D_{mk}^l(\alpha, \beta, \gamma) \quad (3)$$

Potential expansion coefficients and coefficients of rotational diffusion are sought for parameters of numerical simulation of EPR spectra.

In this work we combine these two approaches to determine orientation distribution functions of spin probes in a liquid crystalline media at conditions of presence and absence of rotational mobility.

### Sample preparation

Liquid crystal 4'-penty-4-cyanobiphenyl (5CB) from Sigma Aldrich was used without further purification. Nematic phase was found within temperature interval 295-308 K.

Stretched porous polyethylene (PE) films were produced by the procedure described in [5]. The material was kindly granted by Prof. G.K. Elyashevitch (Institute of Macromolecular Compounds, RAS). Pores of this material with diameter  $\sim 200$  nm are elongated mainly uniaxially. This material aligns liquid crystals embedded in it due to the action of internal surface of the pores [6].

Stable nitroxide radical 2,5-dimethyl-2-undecyloxyphenyl-5-[4-(4-undecyloxybenzenecarbonyloxy)phenyl]-pyrrolidine-1-oxide R (fig.1), was synthesized as described elsewhere [7] and kindly granted by Prof. R. Tamura (Kyoto University). The concentration of the spin probe introduced into 5CB was less than  $10^{-3}$  M to avoid dipole-dipole broadening of EPR spectrum lines. This nitroxide radical has rigid central core. It has been shown earlier [8] that being introduced into oriented liquid crystalline media, this spin probe exhibits rather strong angular dependence of EPR spectrum. Hence it is a promising orientation-sensitive spin probe.

The liquid crystal with admixture of the spin probe was readily soaked into the film due to the surface tension. Then ten layers of filled film were stacked and co-aligned to form the sample.

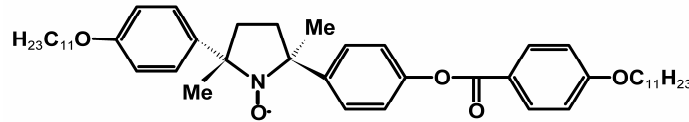


**Fig.1.** Spin probe 2,5-dimethyl-2-undecyloxyphenyl-5-[4-(4-undecyloxybenzenecarbonyloxy)phenyl]-pyrrolidine-1-oxide

### EPR spectra numerical simulation. Determination of orientation distribution function.

EPR spectra recorded at different angles between magnetic field vector and the sample anisotropy axis were simulated jointly. The procedure for numerical simulation of EPR spectra in the absence of molecular mobility is described in detail in [4]. We have modified the procedure to determine the orientation distribution of the axis of a spin probe, which is ordered to the maximum extent. In this case ODF depends on one angle and can be expanded in a series of Legendre polynomials:

$$\rho(\beta) = \sum_l \frac{1}{2} c_l P_l(\cos \beta) \quad (4)$$

It was proved that expansion parameters  $c_l$  are related with expansion parameters  $a_{lk}$ ,  $b_{lk}$  of expansion (1) through Eqns. (5):

$$\begin{aligned} a_{lk} &= c_l \frac{(-1)^k (l-k)!}{(l+k)!} \cos k\varphi P_{lk}(\cos \theta) \\ b_{lk} &= -c_l \frac{(-1)^k (l-k)!}{(l+k)!} \sin k\varphi P_{lk}(\cos \theta) \end{aligned} \quad (5)$$

Sought for parameters of this procedure are expansion coefficients of the ODF of the spin probe orientational axis  $c_l$  and angles  $(\theta, \varphi)$  which relate orientational axis of the spin probe with g-tensor principal axes.

To take into account rotational mobility of spin probes in ordered media within Brownian diffusion approach, we used a procedure suggested in [9]. Orientation distribution is expressed as a function (2), sought for parameters of numerical simulation are expansion coefficients of an orienting potential (3), rotational diffusion coefficients and angles which

relate principal axes of diffusion tensor and principal axes of g-tensor of the spin probe ( $\theta'$ ,  $\varphi'$ ).

**Results and discussion**

EPR spectra of the spin probe in 5CB embedded into porous PE film recorded at 77 K and at 295 K are shown in fig.2. The difference between them is accounted for rotational mobility of the spin probe molecules at 295 K.

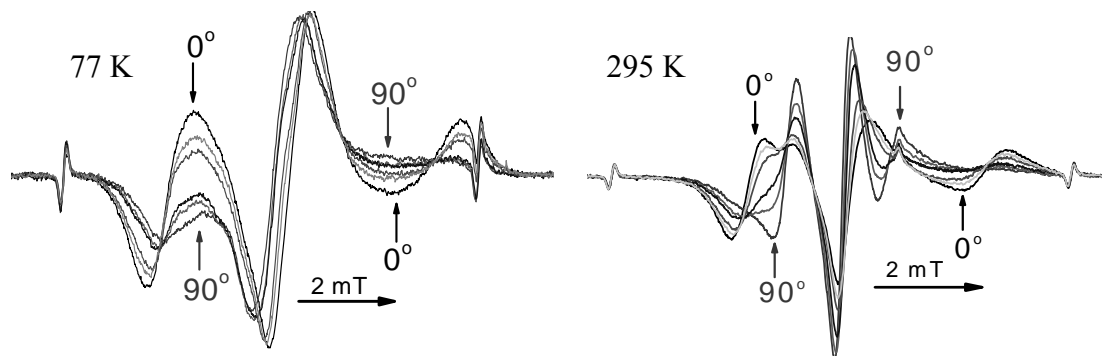


**Fig.2.** EPR spectra of spin probe R in liquid crystal 5CB embedded into porous PE film recorded at different angles between the sample anisotropy axis and magnetic field

Orientation distribution function of the spin probe at 77 K is shown in fig.3. The ODF shows distribution of medium director in g-tensor frame of probe molecule. Angles ( $\theta$ ,  $\varphi$ ) shows tilt of orientational axis of the molecule relative to g-tensor frame.

If equilibrium is achieved at any temperature, then in accordance with Eq. (3), orienting potential expansion coefficients go up with decreasing of temperature. It means that orientational distribution of the spin probes at 77 K should be more anisotropic, than at 295 K. However, our experiments have not validated this statement. To compare ODF at 295 K and at 77 K we expanded ODF determined at 295 K, expressed via Eq. (2) in a series of spherical harmonics. The first coefficients of the series are presented in Table. Taking into account the

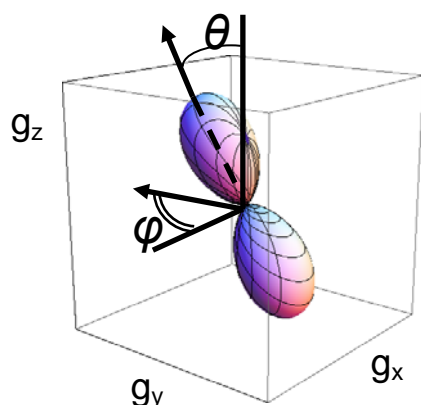


**Fig.3.** Orientation distribution function (77 K) of spin probe R in 5CB embedded into porous PE film

**Table.** ODFs parameters

	77 K	295 K
$c_2$	2.48±0.12	2.24±0.10
$c_4$	0.76±0.87	1.17±0.10
$c_6$	-	0.36±0.04
$c_8$	-	.....
$F$	0.50±0.02	0.42±0.02
	$\theta = (32\pm 1)^\circ$	$\theta' = (38\pm 1)^\circ$
	$\varphi = (90\pm 9)^\circ$	$\varphi' = (90\pm 18)^\circ$

values of coefficients obtained for ODFs at 295 K and 77 K, one can conclude that ODFs at 295 K and at 77 K are rather similar. Only slight increasing of order parameter  $F$  with decreasing of temperature takes place. Therefore, molecular orientation distribution at 77 K approximately corresponds to nematic liquid crystalline state at room temperature. It means

that rapidly cooled liquid crystal is in non-equilibrium supercooled state. Orientational characteristics of molecules in cooled liquid crystal do not meet condition of Boltzmann's equilibrium (2) that lies in the base of the approach [1, Chapter 3].

Angles ( $\theta'$ ,  $\varphi'$ ), which relate diffusion frame and g-tensor frame, determined at 295 K were found to be in qualitative agreement with angles ( $\theta$ ,  $\varphi$ ) which give direction of orientational axis of the spin probe in g-tensor frame, determined at 77 K (see Table). The vicinity of orientational axis and principal axis of rotational diffusion for this spin probe is accounted for rodlike shape of the molecule.

### Acknowledgements.

This work was supported by the Russian Foundation for Basic Research, grants No. 09-03-00900. The authors thank Prof. R. Tamura for provision of paramagnetic probe and Prof. G.K. Elyashevitch for provision of stretched porous polyethylene films.

### References

- [1] L.J.Berliner, Ed., Spin Labeling: Theory and applications, academic Press, New York, 1976, L.J.Berliner, Ed.
- [2] E. Meirovitch, D. Igner, E. Igner, G. Mora, J. H. Freed, *J. Chem. Phys.* 77 (1982) 3915-3938.
- [3] G.R. Luckhurst, *Thin Solid Films* 509 (2006) 36 – 48.
- [4] A. Kh.Vorobiev, N.A. Chumakova, *J. Magn. Reson.* 175 (2005) 146-157.
- [5] G. Elyashevich, A. Kozlov, I. Moneva, *Polymer Science, series B* 40 (1998) 71-74 [Vysokomol. Soyed., 40 (1998) 483-486, in Russian].
- [6] A. Bobrovsky, V. Shibaev, G. Elyashevich, E. Rosova, A. Shimkin, V. Shirinyan and K.-L. Cheng, *Polym. Adv. Technol.* 21 (2010) 100–112.
- [7] N. Ikuma, R. Tamura, S. Shimono, Y. Uchida, K. Masaki, J. Yamauchi, Y. Aoki, H. Nohira, *Adv. Mater.* 18 (2006) 477-480.
- [8] N.A. Chumakova, A.Kh. Vorobiev, Ikuma N., Uchida Y., Tamura R., *Mendeleev Commun.* 18 (2008) 21-23.
- [9] D. E. Budil, S. Lee, S. Saxena, J. H. Freed, *J. Magn. Reson. Series A* 120 (1996) 155–189.

**NMR study of ball-milled TiH<sub>2</sub> with C, B, and BN additives**O.A. Babanova<sup>1</sup>, A.V. Soloninin<sup>1</sup>, A.V. Skripov<sup>1</sup>, O.S. Morozova<sup>2</sup>, A.V. Leonov<sup>3</sup><sup>1</sup>Institute of Metal Physics, Ural Division of the Russian Academy of Sciences, 620041, S. Kovalevskoi 18, Ekaterinburg, Russia<sup>2</sup>Semenov Institute of Chemical Physics, Russian Academy of Sciences, 119991, Kosygina 4, Moscow, Russia<sup>3</sup>Lomonosov Moscow State University, Chemical Department, 119899, Leninskie Gory, Moscow, Russia

e-mail: Babanova@imp.uran.ru

**Introduction**

Nanostructured metal hydrides prepared by ball milling are becoming increasingly important for hydrogen storage applications. In particular, the ball milling of a number of metal hydrides with catalytic additives has been shown to result in a significant acceleration of hydrogen absorption and desorption [1,2]. However, little is known about the mechanisms responsible for the changes in hydrogen reaction kinetics due to the milling. Since a diffusive motion of hydrogen is crucial to the hydriding and dehydriding reactions, it is of special interest to study the parameters of H diffusion in nanostructured hydrides. Microscopic information on the H jump motion in metal – hydrogen systems can be obtained from nuclear magnetic resonance measurements [3].

The aim of this work is to study the effects of ball milling on the H jump rates in titanium dihydride with C, B, and BN additives. Titanium dihydride, TiH<sub>2</sub>, has a high density of absorbed hydrogen; however, the hydrogen desorption temperature for this material appears to be too high for H storage applications. In fact, the maximum of the first H desorption peak for the coarse-grained TiH<sub>2</sub> is observed near 750 K [1]. The ball milling of TiH<sub>2</sub> with C, B, and BN additives has been found to lead to a significant reduction of the H desorption temperature [4,5]. In the present work, we use <sup>1</sup>H and <sup>11</sup>B NMR measurements to address the question of whether these changes in H desorption are related to changes in the atomic-level H mobility.

**Results and discussion**

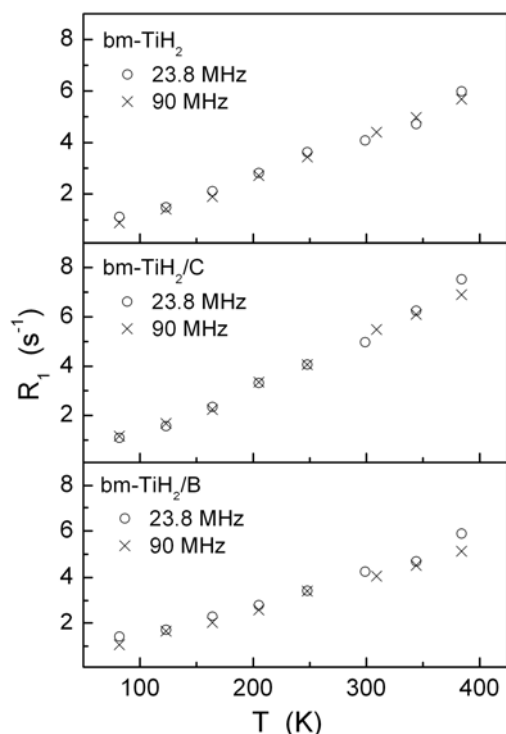
Commercial titanium dihydride powder (Aldrich, 99% purity), highly oriented pyrolytic graphite (99% purity), amorphous boron (98.5% purity), and hexagonal boron nitride, *h*-BN (99% purity), were used as the starting materials for preparing nanostructured TiH<sub>2</sub> with additives. The milling time was 62 min (for the samples of TiH<sub>2</sub> without additives and with C additive) and 66 min (for the samples of TiH<sub>2</sub> with B and BN additives). In all cases, the fraction of an additive was 16.6 mass %. According to X-ray diffraction analysis at room temperature, the coarse-grained TiH<sub>2</sub> was tetragonal ( $a = 4.47 \text{ \AA}$ ,  $c = 4.40 \text{ \AA}$ ) and all the bm-samples had the structure of a cubic titanium dihydride with the lattice parameter of about 4.45 Å and the average grain size of 12 – 14 nm.

The proton spin-lattice relaxation rate  $R_1$  in metal-hydrogen systems is determined by the sum of contributions resulting from the interactions of proton spins with conduction electrons  $R_{1e}$  and from the internuclear dipole-dipole interactions modulated by H motion  $R_{1d}$  [3]. At low temperatures the hydrogen diffusion is ‘frozen’ and the measured values of  $R_1$  are determined by

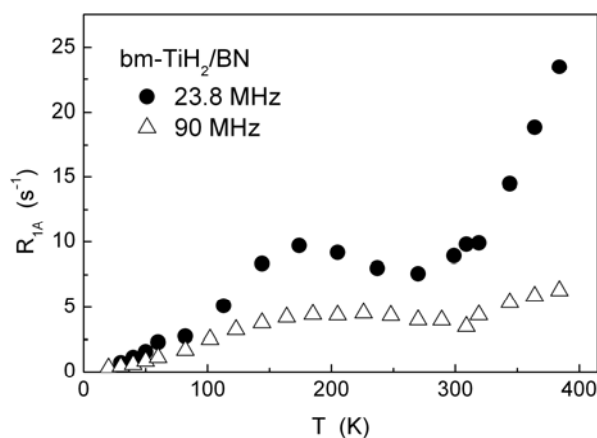
the electronic (Korringa) contribution  $R_{1e}$ . The motional contribution  $R_{1d}$  becomes more important in the temperature range where the H jump rate  $\tau_d^{-1}$  is between  $10^7$  and  $10^{11} \text{ s}^{-1}$ .

Fig.1 shows the temperature dependences of  $R_1$  at resonance frequencies  $\omega/2\pi = 23.8$  and 90 MHz for the ball-milled (bm-)  $\text{TiH}_2$  without additives and for the bm- $\text{TiH}_2$  with C and B additives. A common feature of the  $R_1$  data for these bm-samples is the absence of any significant frequency dependence of  $R_1$  in the studied temperature range of 82 – 384 K. This suggests that the measured relaxation rates are determined by the electronic contribution  $R_{1e}$ ; no motional contributions can be discerned.

The behavior of the  $^1\text{H}$   $R_1(T)$  for the bm- $\text{TiH}_2$  with BN is found to differ significantly from that for the other samples studied. The recovery curve of nuclear magnetization for bm- $\text{TiH}_2/\text{BN}$  deviates markedly from a single-exponential function over the entire temperature range of our measurements. This suggests a coexistence of protons having different relaxation rates. Fig.2 shows the temperature dependences of the ‘average’ spin-lattice relaxation rates  $R_{1A}$  defined by the  $1/e$  point of the recovery curve at  $\omega/2\pi = 23.8$  and 90 MHz. It can be seen from this figure that the values of  $R_{1A}$  are frequency-dependent, increasing strongly with the decreasing frequency. Furthermore, the temperature dependence of  $R_{1A}$  at 23.8 MHz shows a well-defined peak near 170 K and a steep rise at  $T > 320$  K. Such a behavior is typical of metal –hydrogen systems where mobile protons participate in two jump processes with different characteristic rates (for example, a fast localized jump motion and a slower jump process leading to long-range diffusion). Thus, the data shown in fig.2 suggest that at least a fraction of H atoms in bm- $\text{TiH}_2/\text{BN}$  are mobile on the frequency scale of  $\omega$ .



**Fig.1.** Temperature dependences of the proton spin-lattice relaxation rates measured at 23.8 and 90 MHz for the bm- $\text{TiH}_2$ , bm- $\text{TiH}_2/\text{C}$  and bm- $\text{TiH}_2/\text{B}$ .



**Fig.2.** Temperature dependences of the ‘average’ proton spin-lattice relaxation rates measured at 23.8 and 90 MHz for the bm- $\text{TiH}_2/\text{BN}$ .

For parametrization of our proton spin-lattice relaxation data for bm-TiH<sub>2</sub>/BN, the recovery curves have been described by two exponential terms. The temperature dependences of the fast relaxation component,  $R_{1F}$ , for the two-exponential fits to the data at 23.8 and 90 MHz are shown in fig.3. It should be noted that the two-exponential spin-lattice relaxation suggests a weak interaction between protons showing the fast and slow recovery. The  $R_{1F}$  peak (fig.3) indicates that, for a fraction of H atoms, the jump rate reaches the value of about  $2 \times 10^8 \text{ s}^{-1}$  at 170 K. Such a fast jump process can hardly be ascribed to long-range H diffusion; more likely, it represents some localized motion of H atoms.

In order to describe the temperature dependence of the motional contribution to  $R_{1F}$ , the electronic contribution  $(R_{1F})_e$  have been estimated. Using the  $R_{1F}$  data at 90 MHz, the upper limit of the electronic contribution is estimated as  $(R_{1F})_e / T \approx 0.019 \text{ s}^{-1}\text{K}^{-1}$ . The motional contribution  $(R_{1F})_d$  obtained by subtracting  $(R_{1F})_e$  from the measured  $R_{1F}$  is shown in fig.4 as a function of the inverse temperature. For parametrization of the  $(R_{1F})_d$  data, we have used the Bloembergen – Purcell – Pound model with a Gaussian distribution of the activation energies [6]. The motional parameters of this model, the average activation energy  $E_a=0.11 \text{ eV}$ , the distribution width  $\Delta E_a=0.06 \text{ eV}$ , and pre-exponential factor  $\tau_{d0}^{-1} = 9.4 \times 10^{12} \text{ s}^{-1}$  have been determined from the simultaneous fit of this model to the data at 23.8 and 90 MHz.

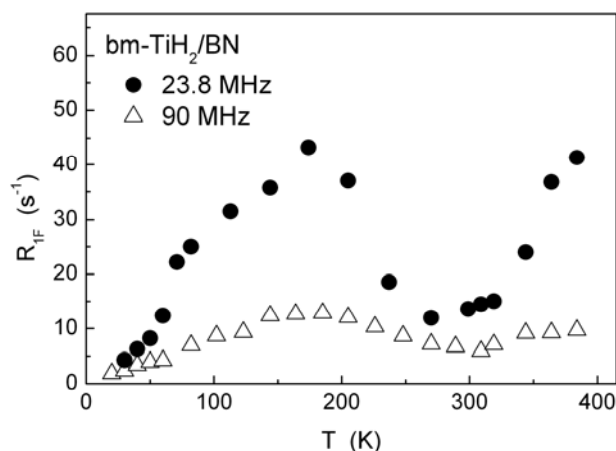


**Fig.3.** Temperature dependences of the fast component of the proton spin-lattice relaxation rate at 23.8 and 90 MHz for the bm-TiH<sub>2</sub>/BN.

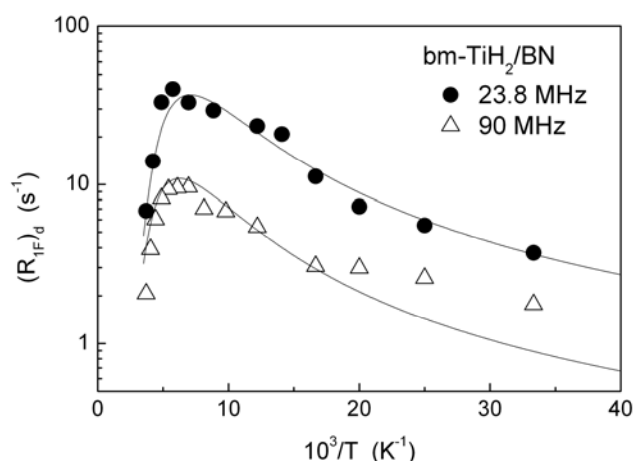


**Fig.4.** Dipolar contributions to the fast component of the <sup>1</sup>H  $R_1(T)$  at 23.8 and 90 MHz for the bm-TiH<sub>2</sub>/BN. The solid curves show the simultaneous fit of the BPP model with a Gaussian distribution of the activation energies to the data.

On the basis of the proton NMR data, we can conclude that the mobility of H atoms in bm-TiH<sub>2</sub>/BN is much higher than in the cg-TiH<sub>2</sub> and bm-TiH<sub>2</sub>, bm-TiH<sub>2</sub>/C, and bm-TiH<sub>2</sub>/B. Our experimental results for bm-TiH<sub>2</sub>/BN are consistent with a coexistence of two H jump processes with different characteristic rates. The faster process with the characteristic H jump rate of about  $2 \times 10^8 \text{ s}^{-1}$  at 170 K represents a localized motion of a fraction of H atoms in this system. The slower process responsible for the frequency-dependent rise of the spin-lattice relaxation rate at  $T > 320 \text{ K}$  can be attributed to long-range H diffusion. This process is presumably related to the kinetics of hydrogen absorption and desorption. It should be stressed that, according to our data, the majority of H atoms in bm-TiH<sub>2</sub>/BN are involved in this motion.

The  $^{11}\text{B}$  spin-lattice relaxation measurements for bm-TiH<sub>2</sub>/B and bm-TiH<sub>2</sub>/BN have been carried out. For all these systems, the recovery of the  $^{11}\text{B}$  magnetization deviates from a single-exponential behavior. For both bm-TiH<sub>2</sub>/B and bm-TiH<sub>2</sub>/BN, the  $^{11}\text{B}$  spin-lattice relaxation rate increases monotonically with the temperature increase. If there are some H jump processes in the vicinity of B atoms, one would expect motional contributions to the  $^{11}\text{B}$  spin-lattice relaxation rate associated with the modulation of the B – H dipolar and quadrupolar interactions. The absence of any peaks in the temperature dependence of the  $^{11}\text{B}$  spin-lattice relaxation rate for bm-TiH<sub>2</sub>/BN (not shown) suggests that the fast H motion in this system occurs outside the immediate vicinity of B atoms. This conclusion is consistent with the results of X-ray emission spectroscopy (XES) experiments [5] showing no signs of B – Ti bonds in the sample prepared by ball milling Ti/BN in H<sub>2</sub>/He flow. In other words, the XES results indicate that B atoms do not penetrate into the TiH<sub>2</sub> lattice in this system. However, N atoms can occupy interstitial sites in Ti or TiH<sub>2</sub> lattices forming N – Ti bonds in the ball-milled Ti/BN in H<sub>2</sub>/He flow. It is likely that interstitial N atoms play the key role in the acceleration of H motion in our bm-TiH<sub>2</sub>/BN system. If the ball milling leads to the appearance of interstitial N atoms in the distorted TiH<sub>2</sub> regions near grain boundaries, these N atoms may act as trapping centers for hydrogen. In this case, the fast localized motion of a fraction of H atoms in bm-TiH<sub>2</sub>/BN could be naturally attributed to H jumps in a double-well (or multi-well) potential formed around interstitial N atoms. Lattice distortions induced by interstitial N atoms may also lead to the reduction of the potential barriers for long-range H diffusion.

## References

- [1] Kurmaev, E.Z.; Morozova, O.; Khomenko, T.I.; Borchers, C.; Nemnonov, S.N.; Harada, Y.; Tokushima, T.; Osawa, H.; Takeuchi, T; Shin,S.//*J. Alloys Compd.* **2005**, *395*, 240-246.
- [2] Borchers, C.; Khomenko, T.I.; Morozova, O.S.; Galakhov, V.A.; Kurmaev, E.Z.; McNaughton, J.; Yablonskikh, M.V.; Moewes, A.//*J. Phys. Chem. B* **2006**, *110*, 196.
- [3] Barnes, R.G. In *Hydrogen in Metals III*; Wipf, H., Ed.; Springer: Berlin, 1997; pp 93-151.
- [4] Borchers, C.; Morozova, O.S.; Khomenko, T.I.; Leonov, A.V.; Kurmaev, E.Z.; Moewes, A.; Pundt, A.//*Chem. Phys. Lett.* **2008**, *465*, 82-85.
- [5] Borchers, C.; Morozova, O.S.; Khomenko, T.I.; Leonov, A.V.; Postnikov, A.V.; Kurmaev, E.Z.; Moewes, A.; Pundt, A.//*J. Phys. Chem. C* **2008**, *112*, 5869-5879.
- [6] Markert, J.T.; Cotts, E.J.; Cotts, R.M.//*Phys. Rev. B* **1988**, *37*, 6446-6452.

## Paramagnetic resonance of ions $\text{Pb}^{3+}$ in ferroelectric $\text{Pb}_5\text{Ge}_3\text{O}_{11}$

V.A. Vazhenin, A.N. Ivachev, M.Yu. Artyomov, and A.P. Potapov

Center of classic education, Ural Federal University, Lenin ave. 51, Yekaterinburg, 620000  
Russia

e-mail: ivachev@e1.ru

The photorefractive effect in pure reduced (annealed in oxygen or hydrogen) and doped (Cu, Nd, Ba, Ni, Fe, Yb, Rh) lead germanate  $\text{Pb}_5\text{Ge}_3\text{O}_{11}$  was detected and studied in [1–8]. In [9], photoinduced  $\text{Pb}^{3+}$  centers ( $^2\text{S}_{1/2}$  state) in lead germinate (LG) were studied. The authors of [9] founded out, that the photorefractive effect in  $\text{Pb}_5\text{Ge}_3\text{O}_{11}$  can be associated with  $\text{Pb}^{2+}$  lead matrix ion recharging, and released electrons are trapped by unknown traps. In [9], the parameters of Zeeman, hyperfine, and superhyperfine (with two nearest lead nuclei) interactions of  $\text{Pb}^{3+}$  centers were also determined.

Our work is devoted to the EPR study of lead ion recharging upon exposure to light in lead germanate single crystals containing a number of cationic and anionic impurities and those with deviations from stoichiometry, the determination of the parameters of the superhyperfine interaction with long-range  $^{207}\text{Pb}$  nuclei,  $\text{Pb}^{3+}$  localization, and discussion of the nature of electron traps stabilizing  $\text{Pb}^{3+}$  ions.

The spectra of paramagnetic  $\text{Pb}^{3+}$  ions were measured using an EMX Plus (Bruker) EPR spectrometer of three-centimeter range. The error of sample temperature maintenance and measurement was  $\pm 1$  K. Lead germinate single crystals were grown by P6 the Czochralski method and were not polarized before measurements. Crystals with Fe (0.2%), Cu (0.3%), Ti (1%), Eu (0.05%), Ag (0.01%), Si (15%), chlorine, bromine, fluorine impurities, and samples with deficient (61.75% PbO) and excess (64.5% PbO) lead oxide (the stoichiometric composition is 62.5% PbO) were studied. Cationic impurities were added to the mixture; chlorine, bromine, and fluorine were introduced into the crystal upon annealing in a corresponding atmosphere at a temperature close to the melting temperature. Samples were uniformly exposed to light of a 35-W xenon lamp and light-emitting diodes with emission maxima at 410 and 470 nm at a temperature of 100–120 K. Light was incident on the sample through a special window of a microwave cavity of the spectrometer.

The exposure of the lead germanate sample to both the xenon lamp and light-emitting diodes in the above temperature range leads to the formation of a characteristic EPR spectrum shown in fig.1. To avoid overlapping the arising spectrum and signals of  $\text{Gd}^{3+}$  and  $\text{Cu}^{2+}$  centers, measurements were performed in the orientation close to  $\text{B} \parallel \text{C}_3$  (B is the magnetic field strength). The central group and signals with positions indicated by arrows in fig.1b represent the superhyperfine structure of even (nuclear spin is  $I = 0$ )  $\text{Pb}^{3+}$  isotopes, caused by the interaction with eight nearest lead nuclei. Transitions of the odd  $^{207}\text{Pb}^{3+}$  isotope ( $I = 1/2$ , natural abundance is 22.6%,  $A_{\parallel} = 34.64$  GHz,  $A_{\perp} = 34.77$  GHz [9]) with the same superhyperfine structure are observed in the magnetic fields with strengths of  $\approx 550$  and  $\approx 1100$  mT. Appearance of other paramagnetic centers during exposure was not detected by us at  $T = 100$ – $200$  K and the authors of [9] at  $T \approx 20$  K, which points to trapping of two electrons or strong broadening of the EPR spectrum of the trapped electron in a wide temperature range.

During exposure to light-emitting diodes,  $\text{Pb}^{3+}$  signals increase for an hour; an increase in the intensity of these signals when using the xenon lamp ceases in 15 min. The  $\text{Pb}^{3+}$  center concentration in samples doped with titanium, estimated by comparing the total intensities of

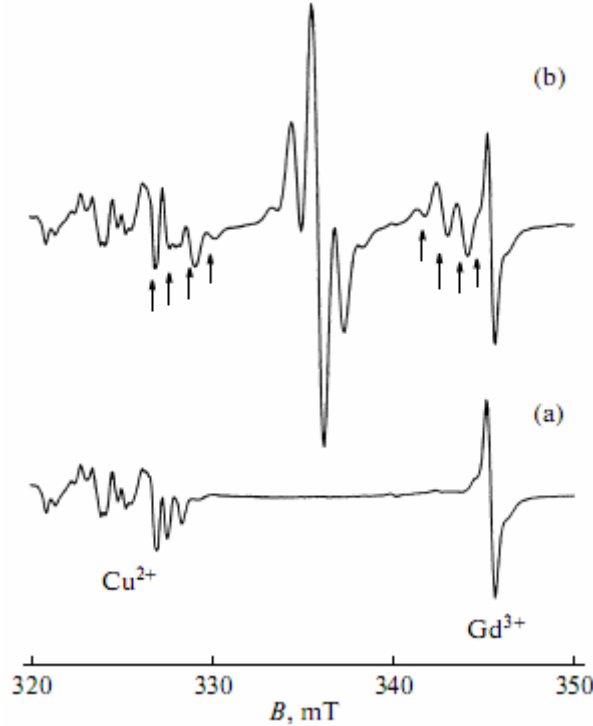


**Fig.1.** EPR spectrum (derivative of absorption signals) of  $\text{Pb}^{3+}$  centers with nuclear spin  $I = 0$  in the  $\text{Pb}_5\text{Ge}_3\text{O}_{11}$  crystal doped with 1 mol %  $\text{TiO}_2$  and containing uncontrolled iron, gadolinium, and copper impurities (a) before and (b) after 5-min exposure to a xenon lamp at  $T = 120$  K in the orientation close to  $B \parallel C_3$ .

the observed spectrum and the EPR spectrum of the  $(\text{Cd}_{0.95}\text{Mn}_{0.05})\text{Te}$  single crystal is  $\sim 10^{16}$  spins/cm<sup>3</sup>.

As the temperature increases, an exponential decrease (with time constant  $\tau$ ) in the intensity of these centers is observed; in this case, the spectral shape and linewidth are almost unchanged to 175 K. We plotted temperature dependence of the annealing time constant of  $\text{Pb}^{3+}$  centers in LG crystals with silver and fluorine impurities; the activation energy of this process is 0.12(3) eV. In [9], the  $\text{Pb}^{3+}$  center annealing was detected by optical absorption decay in the region of the transition to the conduction band from the  $\text{Pb}^{3+}$  ion state. Measurements of the thermal behavior of the annealing time in pure LG crystals yielded the activation energy of 0.16 eV; in crystals doped with barium, it is 0.22 eV.

The symmetry axially of Zeeman, hyperfine (HFI) and superhyperfine (SHFI) interactions of  $\text{Pb}^{3+}$  centers at  $z \parallel C_3$  suggests that lead ions at sites with symmetry  $C_3$  are recharged upon exposure to light. There are six such sites in the unit cell of the LG ferroelectric phase. In their environment (see fig.3 in [9]), all these sites have two axial lead ions localized at the  $C_3$  axis and six ions arranged at vertices of the triangular twisted prism [10, 11]. The coordinates of the lead environment of six trigonal  $\text{Pb}^{2+}$  sites differ appreciably. Therefore, the observation of only one  $\text{Pb}^{3+}$  center indicates recharging of lead ions at only one  $C_3$  site. At  $B \perp C_3$ , side groups of signals in fig.1 almost reproduce the shape of the central group, since the SHFI parameters  $A_{\perp}$  with axial lead nuclei a and b are almost identical:  $= 130.9 \times 10^{-4} \text{ cm}^{-1}$  and  $= 130.4 \times 10^{-4} \text{ cm}^{-1}$  [9]. The noticeable difference between  $= 155.4 \times 10^{-4} \text{ cm}^{-1}$  and  $= 130.2 \times 10^{-4} \text{ cm}^{-1}$  [9] at  $B \parallel C_3$  leads to splitting of side quintets, due to which the observed spectrum is formed (fig.1). The best description of the spectrum shape caused by the superhyperfine interaction with two nonequivalent triads of  $^{207}\text{Pb}$  nuclei of the prism (central region of the spectrum in fig.1) corresponds to the isotropic interaction parameters As

equal to 2.2 mT ( $20.5 \times 10^{-4} \text{ cm}^{-1}$ ) and 0.8–1.0 ( $(7.5\text{--}9.3) \times 10^{-4} \text{ cm}^{-1}$ ). Thus, the observed  $\text{Pb}^{3+}$  center exhibits the almost identical isotropic SHFI with two axial lead nuclei and the significantly different SHFI with  $^{207}\text{Pb}$  nuclei in two prism triangles.

As the authors of [12], let us suppose that the isotropic SHFI depends only on the distance and has the form of the simple power function  $A_s \sim R^{-n}$ . Using averaged distances to axial lead ions (0.356 nm) and lead ions in the prism (0.425 nm) and the average ratio of their SHFI parameters of 137/14.5, we obtain  $n \approx 13$ . The existence of spontaneous polarization in the crystal and the decrease in the effective ionic radius during recharging  $\text{Pb}^{2+} \text{ Pb}^{3+}$  will, most likely, result in a lead ion displacement along the trigonal axis. It is conceivable that the  $\text{Pb}^{3+}$  ion is displaced to the position equidistant from axial lead ions, causing the closeness of the corresponding SHFI values; in this case, the distances to lead ions in the prism triangle become rather different, providing the observed difference between interaction parameters.

An analysis of the lead environment of six trigonal sites shows that the lead ion at the site Pb5 satisfies to the greatest extent the above conditions. Its displacement during recharging toward Pb4 by  $\approx 0.01$  nm (other ions are considered as immobile) makes identical the distances to axial lead ions Pb4 and Pb6; the distances to ions in the prism become equal to 0.434 and 0.408 nm. In this case, for the ratio  $A_s$  for nuclei at Pb2 and Pb1 sites ( $A_{si} \sim R_i^{-13}$ ), the value of 2.23 is expected, whereas experiments yield the value  $A_{s1}/A_{s2} = 2.2/0.9 \approx 2.44$ . Taking into account the roughness of the used approximation of the radial dependence of the isotropic superhyperfine interaction, the closeness of the obtained ratios is a quite good argument in favor of recharging of the  $\text{Pb}^{2+}$  ion localized at the Pb5 site.

Crystals doped with iron exhibit a significantly lower (by a factor of  $\approx 5$ , Table 1) concentration of  $\text{Pb}^{3+}$  centers generated during exposure than pure samples. A  $\text{Pb}^{3+}$  concentration higher by a factor of 4–5 (in comparison with pure samples) was observed upon exposure of crystals annealed in fluorine and chlorine atmospheres and titanium-doped crystals. Other impurities have a slight effect on photoinduction of  $\text{Pb}^{3+}$  centers (Table 1).

**Table 1.** Intensity of the  $\text{Pb}^{3+}$  spectrum (in relative units) arisen after exposure to a xenon lamp at 120 K in initial and modified samples

Sample modification	Intensity
Initial, stoichiometric (62.5% PbO)	1
Doping with iron (0.2%)	1/5
Deficiency PbO (61.75%)	1/5
Doping with silver (0.01%)	2
Doping with europium (0.05%)	2
Annealing in a bromine-containing atmosphere	1
Doping with copper (0.3%)	2
Doping with silicon (15%)	2
Excess PbO (64.5%)	4
Annealing in a chlorine-containing atmosphere	4
Doping with titanium (1%)	5
Annealing in a fluorine-containing atmosphere	5

It is clear that the concentration of  $\text{Pb}^{3+}$  centers induced by uniform light is limited by the number of traps capable of trapping electrons which have left  $\text{Pb}^{2+}$ . The authors of [13, 14] concluded the LG conductivity is hole-type, and holes are localized at lead ions. There is also assumed the existence of an appreciable concentration of  $\text{Pb}^{3+}$  centers in crystals with deficient lead oxide, which exhibit a significantly higher conductivity than that observed in

stoichiometric samples. A small contribution to the conductivity is made by oxygen ion motion in channels along the  $C_3$  axis in the structure formed by lead ions [14].

In the samples with deficient lead oxide, studied in the temperature range of 100–300 K, the  $Pb^{3+}$  ion resonance was not detected. Exposure of these samples to the xenon lamp at 110 K gives rise to a weak EPR spectrum of  $Pb^{3+}$ , comparable in intensity to the spectrum of iron-doped LG. Before exposure, crystals with excess lead oxide also do not exhibit  $Pb^{3+}$  centers; however, exposure induces an intense  $Pb^{3+}$  spectrum comparable to the signals arising in samples with fluorine and chlorine impurities (Table 1).

Hence, the observed efficient recharging of lead in the crystals containing fluorine cannot stabilize with the formation of F- or F<sup>+</sup>-centers [15], i.e., by photo-electron localization at oxygen vacancies. The significant scatter of the annealing activation energy of  $Pb^{3+}$  centers in crystals with different doping (0.12, 0.16 and 0.22 eV, see Section 3) suggests that there exist several types of electron traps. In our opinion, in addition to impurity defects, the role of an electron trap can also be played by the  $Ge^{4+}$  ion capable of trapping two electrons.

### References

- [1] P. V. Ionov, V. V. Voronov, and V. T. Gabrielyan, *Fiz.Tverd. Tela (Leningrad)* 17 (4), 1144 (1975) [*Sov. Phys. Solid State* 17 (4), 728 (1975)].
- [2] W. Krolkowski, M. Cronin-Golomb, and B. S. Chen, *Appl. Phys. Lett.* 57, 7 (1990).
- [3] L. Pryadko, O. Gnatovsky, V. Linnik, and T. Semenets, *Proc. SPIE–Int. Soc. Opt. Eng.* 2795, 208 (1996).
- [4] L. Pryadko, O. Gnatovsky, V. Linnik, and Z. Yanchook, *Proc. SPIE–Int. Soc. Opt. Eng.* 3488, 259 (1997).
- [5] X. Yue, S. Mendricks, Yi Hu, H. Hesse, and D. Kip, *J. Appl. Phys.* 83, 3473 (1998).
- [6] X. Yue, S. Mendricks, T. Nikolajsen, H. Hesse, D. Kip, and E. Kratzig, *J. Opt. Soc. Am. B* 16, 389 (1999).
- [7] S. Mendricks, X. Yue, R. Pankrath, H. Hesse, and D. Kip, *Appl. Phys. B: Lasers Opt.* 68, 887 (1999).
- [8] O. Gnatovsky, V. Linnik, and L. Pryadko, *Semicond. Phys., Quantum Electron. Optoelectron.* 4, 199 (2001).
- [9] H. J. Reyher, M. Pape, and N. Hausfeld, *J. Phys.: Condens. Matter* 13, 3767 (2001).
- [10] M. I. Kay, R. E. Newnham, and R. W. Wolfe, *Ferroelectrics* 9, 1 (1975).
- [11] Y. J. Iwata, *J. Phys. Soc. Jpn.* 43, 961 (1977).
- [12] M. Moreno, M. T. Barriuso, and J. A. Aramburu, *Appl. Magn. Reson.* 3, 283 (1992).
- [13] V. M. Duda, A. I. Baranov, A. S. Ermakov, and R. C. T. Slade, *Fiz. Tverd. Tela (St. Petersburg)* 48 (1), 59 (2006) [*Phys. Solid State* 48 (1), 63 (2006)].
- [14] A. S. Ermakov and V. M. Duda, *Ukr. J. Phys.* 55, 218 (2010).
- [15] N. N. Kristofel', *Theory of Small Radius Impurity Centers in Ionic Crystals* (Nauka, Moscow, 1974), p. 15 [in Russian].

## NMR studies of mechanisms and stereochemistry of new dimerization and cascade oligomerization reactions of dimethyl 2-phenylcyclopropan-1,1-dicarboxylate catalyzed by Lewis acids

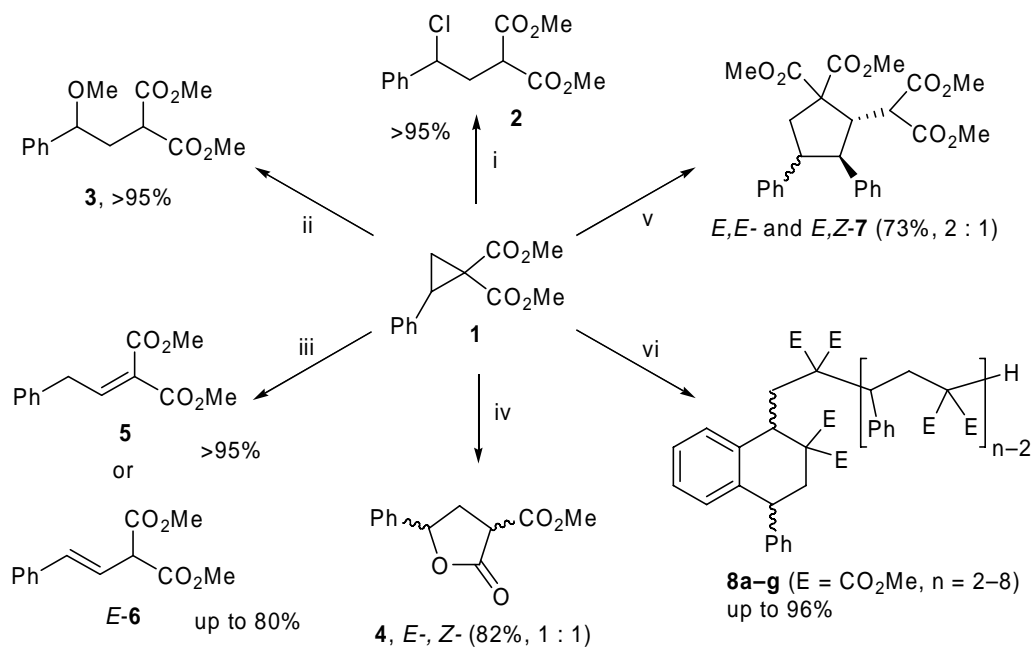
R.A. Novikov<sup>1,2</sup>, V.V. Kachala<sup>1</sup>, V.P. Timofeev<sup>2</sup>, Yu.V. Tomilov<sup>1</sup>

<sup>1</sup>N.D. Zelinsky Institute of Organic Chemistry, Russian Academy of Sciences, 47 Leninsky prosp., 119991 Moscow, Russian Federation.

<sup>2</sup>V.A. Engelhard Institute of Molecular Biology, Russian Academy of Sciences, 32 Vavilov st., 119991 Moscow, Russian Federation.

e-mail: novikovfff@bk.ru

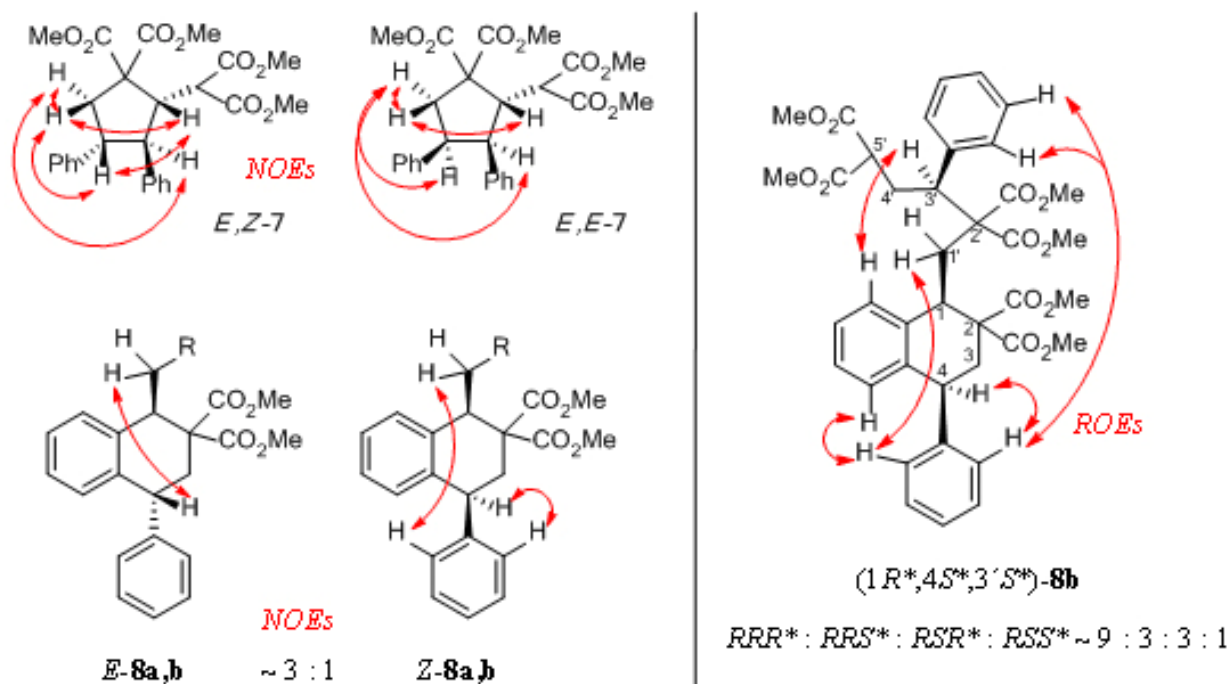
Recently, we have been found new routes to transform donor-acceptor cyclopropanes in the presence of Lewis acids. In fact, the reaction of dimethyl 2-phenylcyclopropane-1,1-dicarboxylate **1**, a typical representative of this class of compounds, with an equimolar amount of anhydrous GaCl<sub>3</sub> gives, depending on the reaction time, (2-phenylethylidene)malonate **5** or styrylmalonate **6** after hydrolysis, whereas in the presence of 15–20 mol.% GaCl<sub>3</sub> the starting cyclopropane undergoes dimerization to give the malonic derivative of 3,4-diphenylcyclopentane-1,1-dicarboxylate **7**.



**Reagents and conditions:** (i) SnCl<sub>4</sub>, TiCl<sub>4</sub> or EtAlCl<sub>2</sub>; (ii) GaCl<sub>3</sub> (5 mol.%), MeOH; (iii) GaCl<sub>3</sub> (1 eq), CH<sub>2</sub>Cl<sub>2</sub>, 0°C, 5 min; then 12 h, rt; (iv) GaCl<sub>3</sub> (1 eq), H<sub>2</sub>O (1 eq), CH<sub>2</sub>Cl<sub>2</sub>; (v) GaCl<sub>3</sub> (20 mol.%), CH<sub>2</sub>Cl<sub>2</sub>, rt, 30 min; (vi) SnCl<sub>4</sub>•THF (2 eq) or GaCl<sub>3</sub>•THF (1 eq), CH<sub>2</sub>Cl<sub>2</sub>, rt, 12h

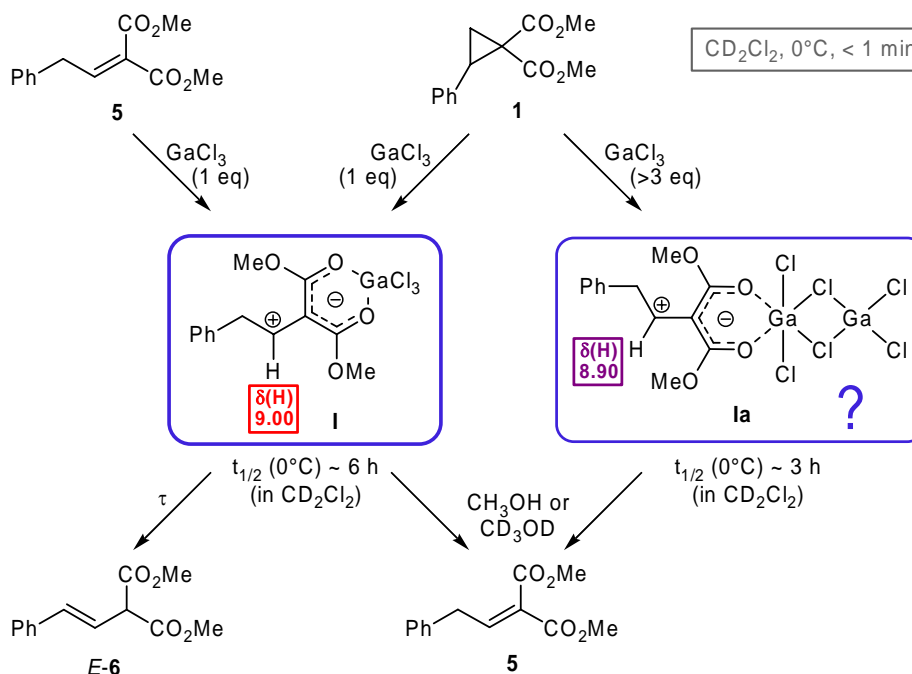
In the presence of the  $\text{GaCl}_3 \cdot \text{THF}$  complex, the same cyclopropane gives a substituted 4-phenyltetraline-2,2-dicarboxylate **8a** in high yield, whereas in the presence of  $\text{SnCl}_4 \cdot \text{THF}$  it gives the dimer specified above along with products of chain oligomerization **8a-g**, the degree of which can be controlled by changing the concentration of the starting cyclopropane in the solution.

The positions of substituents in the compounds **7** and **8a-g** were exactly determined based on NMR  $^1\text{H}$  and  $^{13}\text{C}$  using COSY, TOCSY, HSQC, and HMBC two-dimensional correlation spectra. The spatial arrangement of the substituents was determined from  $^1\text{H}$  NOESY and ROESY two-dimensional correlation spectra. Key cross-peaks of these spectra indicated by arrows on the picture below.

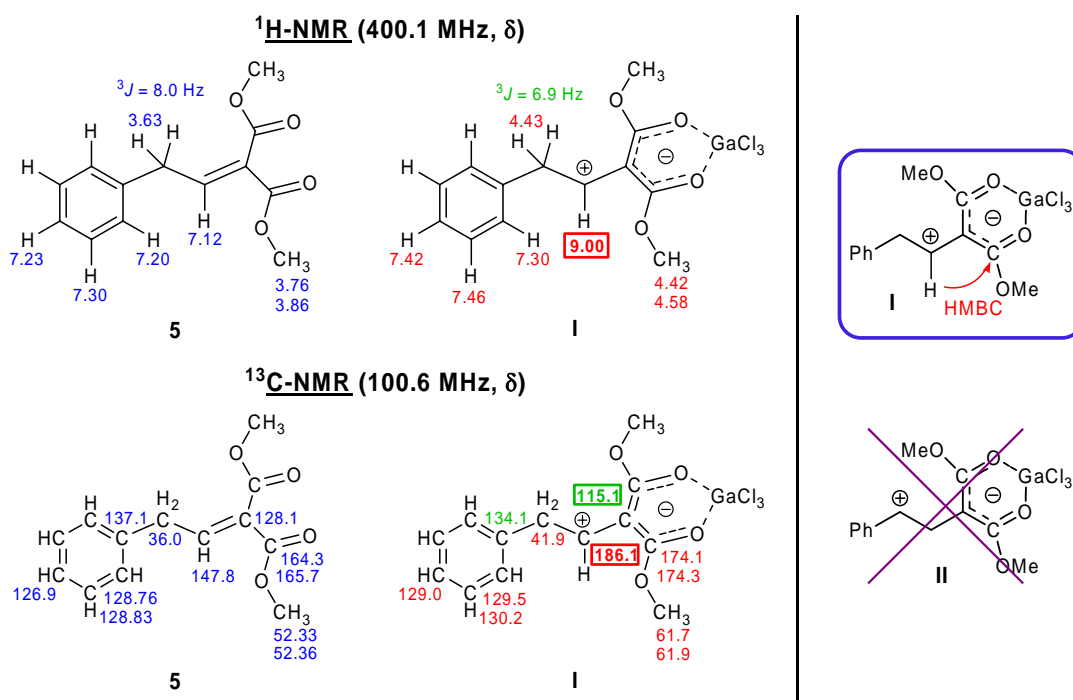


We have suggested and investigated the possible mechanisms of the occurring transformations with the use of low-temperature NMR spectroscopy to fix the intermediates. We have found that during the interaction of the donor-acceptor cyclopropane **1** with  $\text{GaCl}_3$  in NMR tube could be fixed the formation of two complexes **I** and **Ia** depending on the ratio of reagents, quite stable at lower temperatures.

PROCEEDINGS

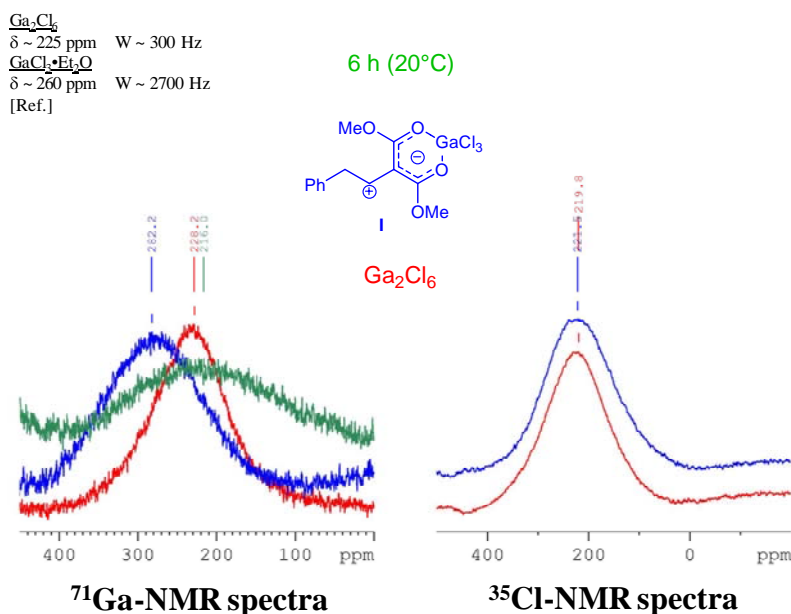


The structure of the complexes was proved by NMR spectroscopy on  $^1\text{H}$ ,  $^{13}\text{C}$ ,  $^{71}\text{Ga}$  and  $^{35}\text{Cl}$  nucleus. Thus, in the  $^1\text{H}$  and  $^{13}\text{C}$  NMR spectra of complex **I** and **Ia** compared with alkene **5** was occurring a very strong shift of some signals in low field, indicating a high delocalization of the positive charge on the carbon atom. Two-dimensional correlation HMBC spectrum shows that the complex exists in the structure **I**, but not **II**, although the latter structure initially seemed more likely.

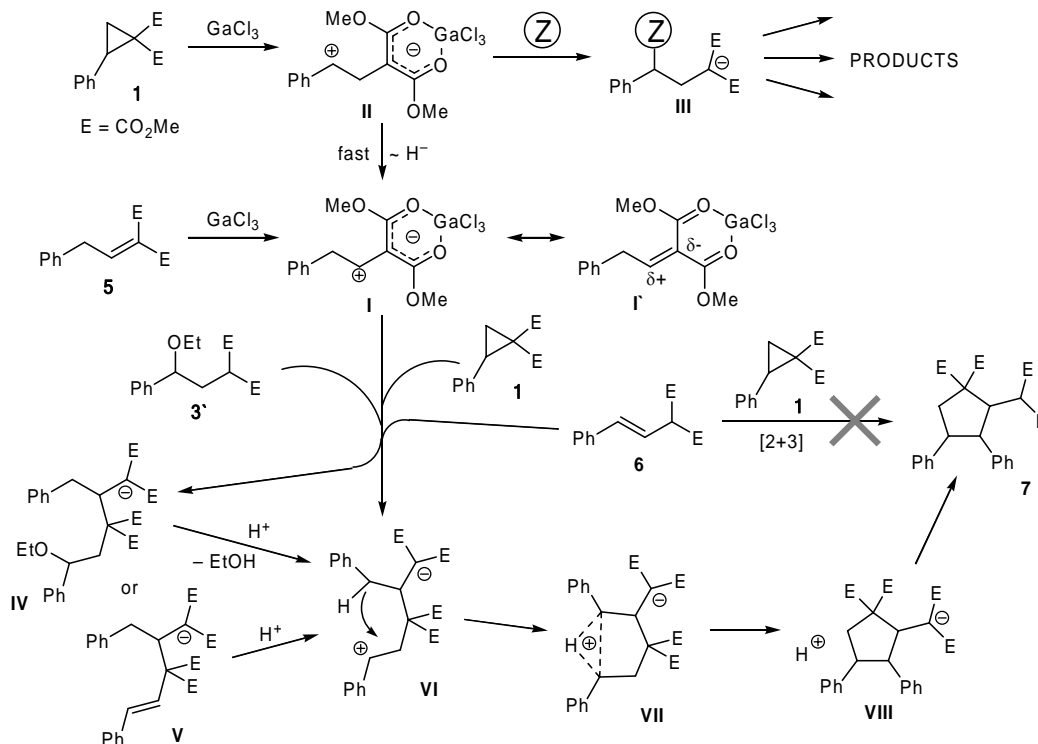


# PROCEEDINGS

Comparison of the changes in the  $^{71}\text{Ga}$  and  $^{35}\text{Cl}$  NMR spectra with literature data for various gallium compounds allows us to establish the coordination sphere of Ga atom in the complex **I**.

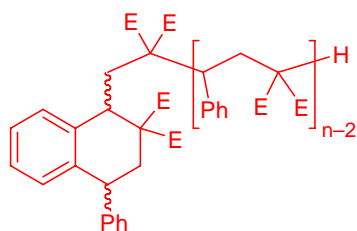


Based on obtained data about the structure of the formed intermediate complexes, as well as stereochemistry and products of the reaction for a some variety initial compounds, we have suggested a plausible mechanisms of the occurring transformations. The possible mechanism has been very difficult and now it is not completely clear.



## PROCEEDINGS

For a study the cascade oligomerization reaction of cyclopropane **1** in tetralines **8a–g** we in particular used 2D  $^1\text{H}$ -DOSY NMR spectra, which allow to distinguish molecules on their diffusion in the solution, and therefore on its molecular weight. An example is shown on the picture.

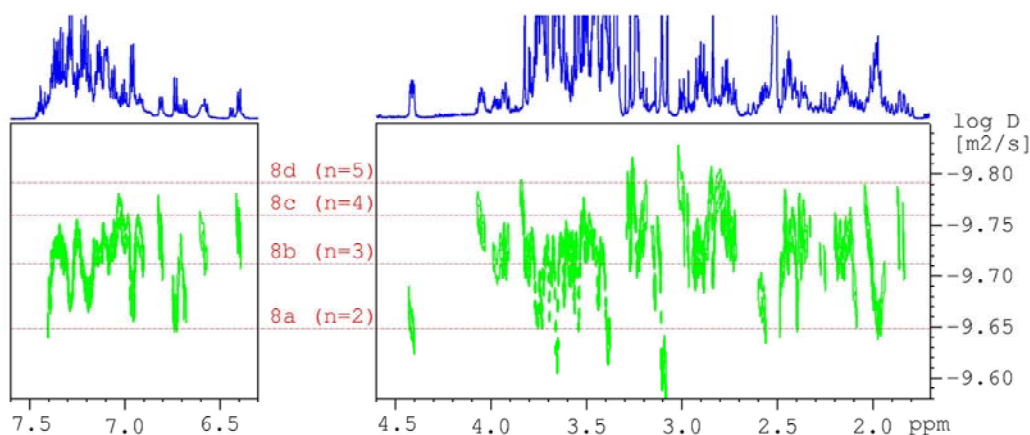


### $^1\text{H}$ -DOSY NMR spectra

Cond.: conc. **1** 0.17 mol/l

**8a–d** (E = CO<sub>2</sub>Me, n = 2–5)

**8a** : **8b** : **8c** : **8d** ~ 4 : 7 : 3 : 1



In conclusion, we have found some new transformations of donor-acceptor cyclopropanes in the presence of Lewis acids, and also we have studied and suggested the plausible mechanisms of these reactions.

This work was financially supported by Government Contract 02.740.11.0258

### References

- [1] Tomilov, Yu. V.; Novikov, R. A.; Nefedov, O. M. *Tetrahedron*, **2010**, *66*, 9151.
- [2] Novikov, R. A.; Korolev, V. A., Timofeev, V. P.; Tomilov, Yu. V. *Tetrahedron Lett.*, **2011**, (in press).

## ESR study of the spin-gap magnet PHCC: magnetic resonance of the $S=1$ quasiparticles in the effective crystal field

V.N. Glazkov<sup>1,2</sup>, T. Yankova<sup>3,2</sup>, J. Sichelschmidt<sup>4</sup>, A. Zheludev<sup>2</sup>

<sup>1</sup>Kapitza Institute for Physical Problems RAS, 119334 Moscow, Russia

<sup>2</sup>Laboratory for Neutron Scattering and Magnetism, ETH-Zurich, Zurich, Switzerland

<sup>3</sup>Chemical Department, Moscow State University, Moscow, Russia

<sup>4</sup>Max Planck Institute for Chemical Physics of Solids, Dresden, Germany

e-mail: glazkov@kapitza.ras.ru

Spin-gap magnets, i.e. magnets with a singlet ( $S=0$ ) ground state separated from the excited triplet ( $S=1$ ) states by an energy gap of exchange origin, are actively studied now. These systems remain in the disordered, but strongly correlated, spin-liquid state down to lowest temperatures. The spin-gap state appears within different theoretical models. It frequently requires specific geometry of the exchange bonds, as in the case of systems of coupled antiferromagnetic dimers, or invokes unusual quantum effects, as in the case of the Haldane magnet. The energy gap makes singlet ground state stable against weak perturbations of these models (e.g. magnetic field, or additional spin-spin interactions). This stability allows formation of spin-gap state in the real crystals.

Spin-gap magnet PHCC (abbreviated from piperazinium hexachlorodocuprate,  $(C_4H_{12}N_2)(Cu_2Cl_6)$ ) is an example of such a system. Its magnetic properties are due to the two-dimensional networks of magnetic ions  $Cu^{2+}$  coupled by superexchange interactions via chlorine ions. Neighboring planes are decoupled from each other since they are separated by non-magnetic piperazinium spacers. The exchange interactions can be envisioned as a set of strongly coupled ladders running along  $a$ -axis of triclinic crystal. Strongest exchange bond is formed on the rungs of the ladder, corresponding exchange integral value is 1.3 meV. [1]

Existence of the gap in the excitations spectrum of PHCC was confirmed by static

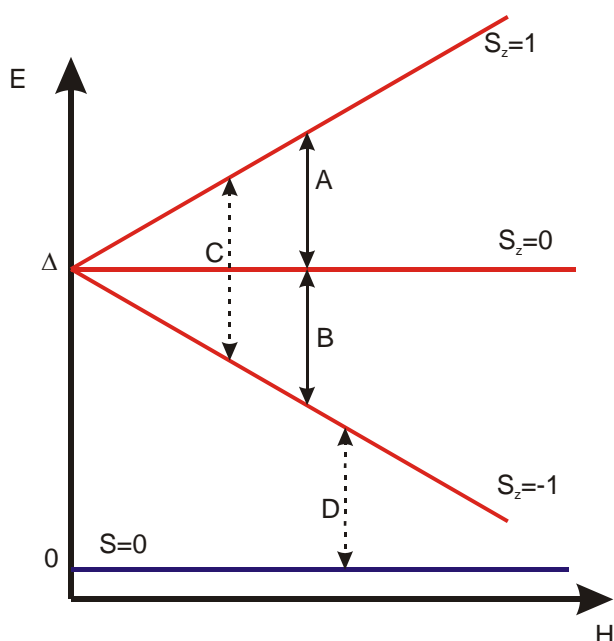


**Fig.1.** Schematic field dependence of the energy levels of a spin-gap magnet. Vertical lines mark possible resonance transitions.

measurements and by neutron scattering experiments. Magnetization measurements demonstrate decrease of the susceptibility at low temperatures, which corresponds to the freezing out of the triplet excitations with decreasing temperature. Inelastic neutron scattering experiments directly demonstrates presence of the gap of about 1 meV [1].

Electron spin resonance technique is an effective method to study the low energy dynamics of a spin-gap magnet. Schematic field dependence of the energy levels of a spin-gap magnet and possible resonance transitions are shown on the fig.1. It is possible to observe transitions between field-split sublevels of triplet excitations

(transitions A, B and C) and transition from singlet ground state to one of the triplet states (D). Resonance absorption at the transitions A, B and C should follow thermally activated behavior since population of these sublevels is strongly temperature dependent. Additionally, selection rules for ESR absorption demands that  $\Delta S_z = \pm 1$ . Thus, transitions C and D are forbidden transitions as long as only Heisenberg and Zeeman terms are present in the Hamiltonian. Additional anisotropic interactions could allow microwave absorption at these transitions and make them observable in ESR experiments. These anisotropic interactions could also lift degeneration of triplet sublevels in zero field. The zero-field splitting of triplet sublevels results in the difference of the resonance fields at the same microwave frequency (same energy difference) for the transitions A and B, which allows to make a detailed study of anisotropic interactions in a spin-gap system by means of resonance technique. Electron spin resonance allows to study these fine effects with a precision hardly accessible by other experimental methods (microwave frequencies used in the experiment (10 – 100 GHz) corresponds to the energy scale of 0.05 – 0.5 meV).

Our ESR experiments were carried out at the microwave frequencies from 9 GHz to 140 GHz. Low-frequency X-band experiments (9.4 GHz) were performed on the commercial Bruker ELEXYS600 spectrometer equipped with a helium flow cryostat. High frequency measurements were done using home-made transmission type ESR spectrometers equipped with cryomagnet yielding field up to 6 T. Single crystalline samples of PHCC were grown by cooling of the saturated solution or from the seed by the temperature gradient technique. Samples demonstrate well developed natural facets which allow easy orientation of the sample in the experiment. Samples were characterized by X-ray methods (Bruker APEX II diffractometer) and by static magnetization measurements (Quantum Design MPMS system). We have found crystallographic structure to be the same as reported in the literature.  $M(T)$  curves (right panel of fig.2) demonstrates freezing out of the susceptibility at low

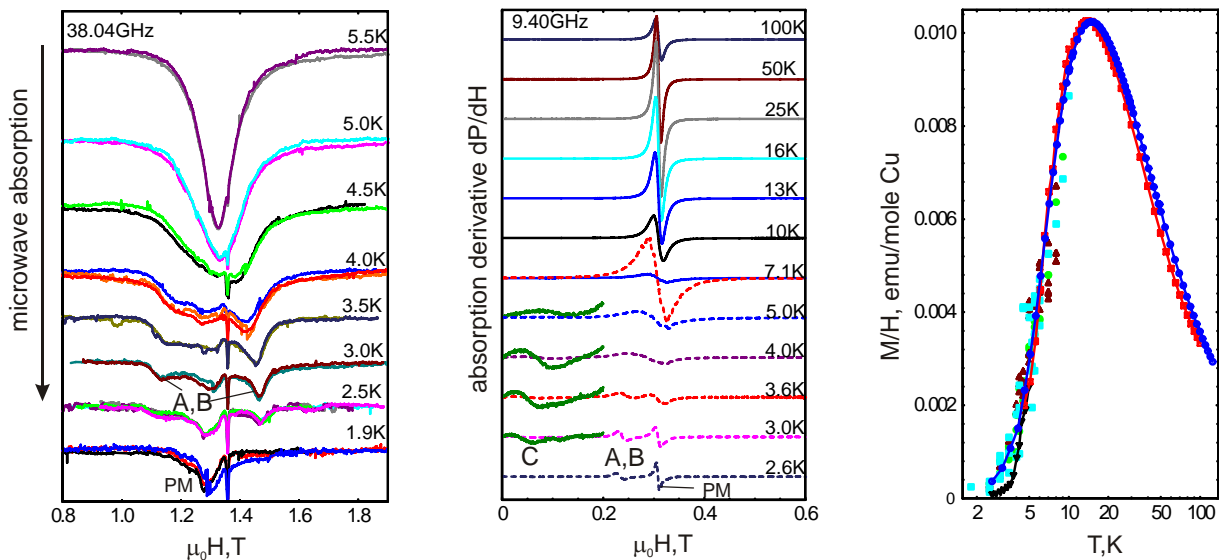


**Fig.2.** (Left panel) Examples of measured ESR absorption in high-frequency experiments.  $f = 38$  GHz,  $H \parallel a^*$ . Narrow line is a DPPH marker ( $g = 2.0$ ). (middle panel) Examples of ESR signals measured on X-band (9.4 GHz) spectrometer. Dashed lines below 7 K are y-scaled by a factor of 10, as compared to high-temperature lines. Low-field fragments of low temperature lines are y-scaled by a factor of 100, as compared to high-temperature lines. (right panel) Comparison of the static susceptibility (circles) and integrated intensity of ESR absorption (squares - X-band experiments, other symbols - high frequency

temperatures, as expected for a spin-gap system. Residual magnetization at 2K allows to estimate uncontrolled defects concentration as  $4 \cdot 10^{-4}$  per copper ion.

Temperature dependence of resonance lines is illustrated in fig.2. As temperature decreases, intensity of the resonance absorption decreases. This allows to identify observed absorption as one due to the inter-triplet transitions. At low temperatures ESR line splits into several components. Component with intensity increasing on cooling can be naturally ascribed to the residual paramagnetic defects. Components fading with cooling corresponds to the inter-triplet transitions A,B and C. Their splitting reflects above mentioned zero-field splitting of the triplet sublevels. We did not observe any absorption corresponding to the singlet-triplet transition (D, in terms of fig.1).

At low temperatures excitations can be considered as an  $S = 1$  quasiparticles traveling in some effective crystal field. In case of PHCC, the analysis of this effective crystal field is hindered by its low symmetry, that allows orientations of the anisotropy axes to be arbitrary with respect to the crystal axes. To solve this problem we have measured frequency-field diagrams in different orientations and a detailed orientation dependences of the resonance field at different temperatures (see fig.3 and fig.4).

These curves were jointly analyzed in the model that treats both anisotropic interactions and magnetic field as a perturbations of the triplet state. This model is described by the Hamiltonian:

$$\hat{H} = \Delta + \mu_B \hat{S} \hat{g} \mathbf{H} + D \hat{S}_{Za}^2 + E (\hat{S}_{Xa}^2 - \hat{S}_{Ya}^2)$$

here  $\Delta$  — is an energy gap,  $D$  and  $E$  are the anisotropy constants and  $\hat{g}$  is a g-tensor.

This Hamiltonian can be solved for eigenvalues, yielding resonance frequencies in the

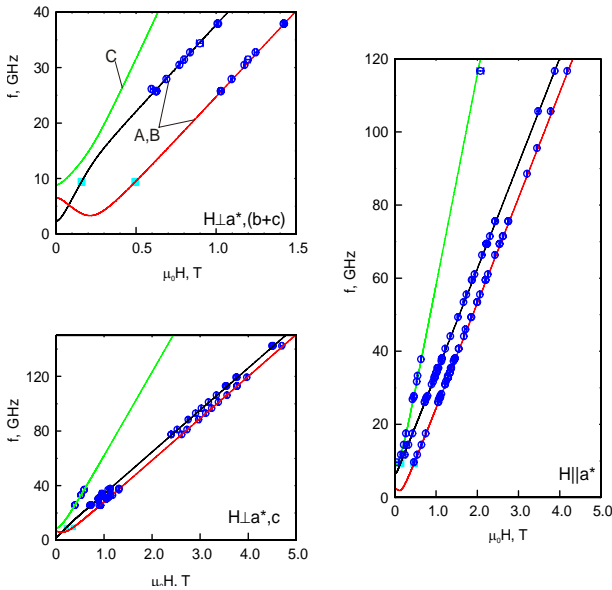


**Fig.3.**  $f(H)$  diagrams of PHCC at 3.0 K.

Symbols — experiment, curves — model calculations (see text). Two parallel modes corresponds to the A and B transitions of fig.1, mode with doubled slope — to the forbidden C transition.

given field. The resonance frequencies can be then compared with experimental data shown on fig.3 and fig.4. Best fit was searched using standard minimization procedure. Fit parameters include values of anisotropy constants, main values of g-tensor and Euler angles of g-tensor frame and of the anisotropy axes. Fit procedure was tested for stability by randomly varying starting point of minimization routine. The number of fit parameters can be slightly reduced by assuming axially of the g-tensor (general g-tensor model yields two of the main values very close to each other). This axially is not forced by macroscopic symmetry and, most probably, is caused by some details of microscopic structure of PHCC.

Best fit parameters of this model are:  $g_{\parallel} = 2.280$  and  $g_{\perp} = 2.048$ , g-tensor main axis polar angles are  $\Theta = 105^{\circ}$  and  $\varphi = 55^{\circ}$  (with respect to the XYZ basis introduced on fig.5). The effective anisotropy is of the easy axis type, anisotropy parameters values are  $D = -7900$  MHz and  $E = -1340$  MHz,

Euler angles for the anisotropy axes  $X_a Y_a Z_a$  are  $\alpha = -44^{\circ}$ ,  $\beta = -106^{\circ}$ ,  $\gamma = -12.5^{\circ}$ .

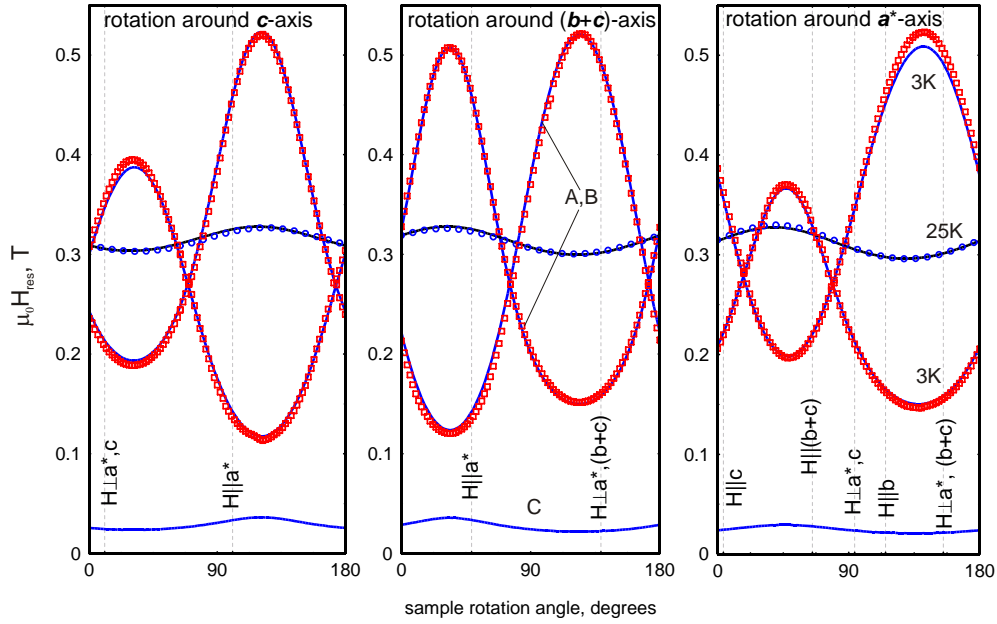


**Fig.4.** Angular dependences of the resonance field in PHCC.  $f = 9.4 \text{ GHz}$ ,  $T = 3.0 \text{ K}$ . Circles – experimental data at 25 K, squares – experimental data at 3.0 K, curves – model calculations (see text).

Orientation of the found axes with respect to the crystal is illustrated on fig.5. Theoretical  $f(H)$  curves and angular dependences of the resonance field are shown on the fig.3 and fig.4, they demonstrate perfect agreement with the experiment.

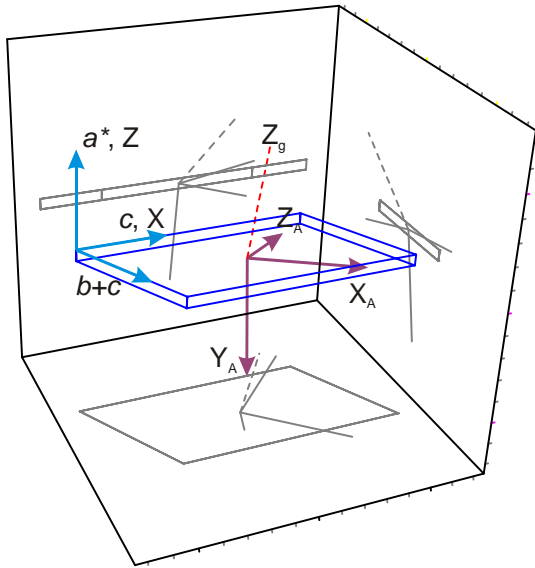


**Fig.5.** Orientations of the different axes of the perturbative model with respect to the crystal and to the laboratory frame of reference.

In conclusion, we have determined parameters of the effective crystal field acting on the  $S=1$  quasiparticles in the spin-gap magnet PHCC. These results could allow better insight into physical properties of this particular system.

This work was supported by RFBR grant 09-02-00736-a.

## References

- [1] M.B.Stone, C.Broholm, D.H.Reich, P.Schiffer, O.Tchernyshyov, P.Vorderwisch and N.Harrison, *New Journal of Physics* **9** (2007) 31

## Multiple quantum Rabi oscillations in quasi-harmonic high spin system

S. Bertaina<sup>1</sup>, L. Chen<sup>2,3</sup>, N. Groll<sup>2,4</sup>, I. Chiorescu<sup>2</sup>

<sup>1</sup>IM2NP-CNRS (UMR 6242), Université Aix-Marseille, 13397 Marseille Cedex, France.

<sup>2</sup>Department of Physics and The National High Magnetic Field Laboratory, Florida State University, Tallahassee, FL 32310, USA.

<sup>3</sup>Department of Chemistry and Chemical Biology, Cornell University, Ithaca, NY 14853-1301, USA

<sup>4</sup>Materials Science Division, Argonne National Laboratory, 9700 S. Cass Avenue, IL 60439, USA.

e-mail: sylvain.bertaina@im2np.fr

Coherent EPR attracts regain of interest because of its potential application to performed quantum algorithms [1]. Multi-level systems are proposed to the implementation of the Grover algorithm [2]. Here we show how a quasi-harmonic high spin  $Mn^{2+}$  ( $S = 5/2$ ) diluted in the cubic crystal MgO can be coherently manipulated and how using only one frequency we can induce Rabi oscillations between all kind of transitions (from  $\Delta M_S = 1$  to 5).

In EPR, transitions exist with regard of the selection rule:  $\Delta M_S = 1$  (Fermi golden rule). However when anisotropy is small enough, this rule fall down and multiple quantum transition can appear. In continuous wave EPR (incoherent), this effect has been observed many years ago [3] but up to recently [4] no observation of the coherent behavior of such transitions has been reported.

Measurements of Rabi oscillations have been done on a pulsed EPR spectrometer Bruker Elexys 680 at room temperature. The system used: MgO:Mn<sup>2+</sup> is well known and is describe by the Hamiltonian:

$$H = \frac{a}{6} [S_x^4 + S_y^4 + S_z^4 - S(S+1)(3S^2 - 1)/5] + \gamma \vec{H}_0 \vec{S} - A \vec{S} \vec{I} + \gamma \hbar \vec{S} \cos(2\pi ft)$$

With  $a = 55.7$  MHz,  $A = 244$  MHz,  $f = 9.6$  GHz,  $\gamma = g\mu_B/h$

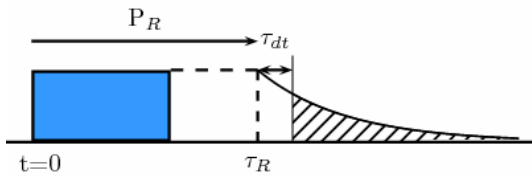


**Fig.1.** Pulse sequence. An intense pulse  $P_R$  is applied at  $t=0$  and stop at  $t=\tau_R$ . An FID is induced and recorded.

In pulse EPR spectrometer, magnetic field is set to have the one-photon resonance condition  $\gamma H_0 = f$ . A MW pulse rotate coherently the magnetization, when the MW is stop, a free induction decay signal is recorded and give the magnetization state at the end of the pulse.

Fig.2 shows Rabi oscillation observed in  $Mn^{2+}$ . At low microwave power, only the standard 1-photon Rabi oscillation is observed. When the microwave field is increase a second kind of Rabi oscillations with a lower frequency is induced: the 3-photon Rabi oscillation.

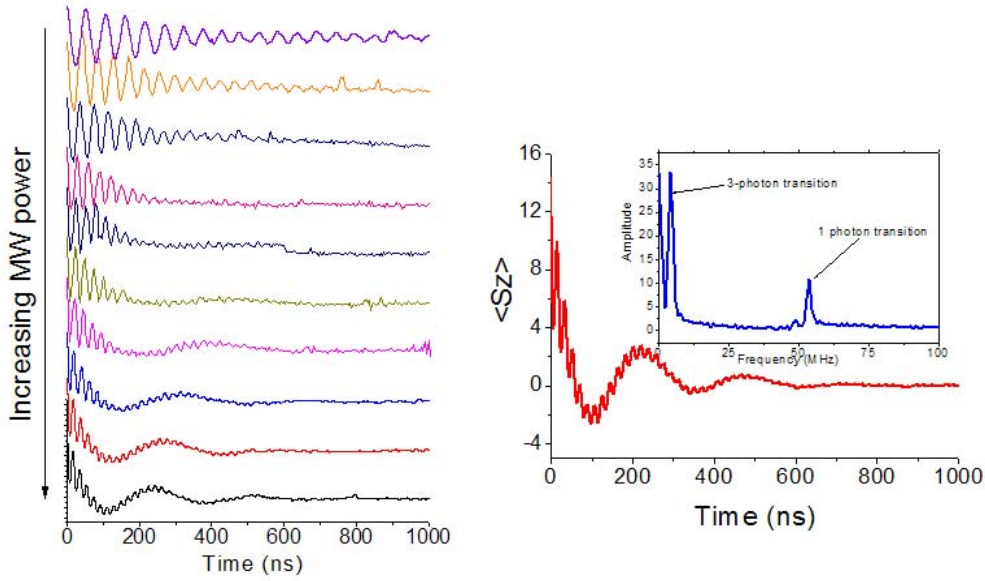


**Fig.2.** Rabi oscillation of magnetization in  $Mn^{2+}$  at room temperature for a static magnetic field  $H_0 \parallel [111]$ . When MW power is increased, a second kind of oscillation appears: the 3-photon Rabi oscillations.

Contrary to the coherent dynamic of a two level system, the multi-photon Rabi oscillation is very anisotropic with orientation of static magnetic field and its frequency behavior is non linear with microwave field.

To quantify this dynamic we develop a model based on the crystal field parameters and the rotating frame transformation [1].

Fig.3 shows the frequency distribution of multiple photon Rabi oscillations when the static field is oriented in the axis [110] of the crystal.

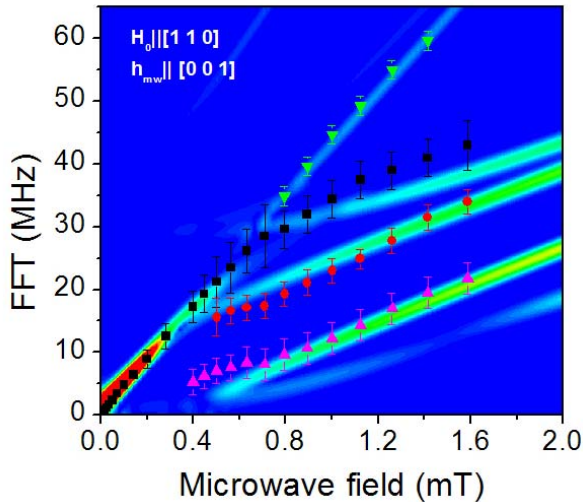


**Fig.3:** Rabi frequencies of  $Mn^{2+}$  spin, as a function of drive field, obtained by FFT of detected coherent oscillations. The error bars are the FFT linewidths.

Points are experimental data coming from the Fourier transform of the Rabi oscillation signal. The contour plot is the numerical calculation using our model (no fit parameter has been used). Numerical model is in very good agreement with data. Thus this will allow us to fully describe coherent multi-photon dynamic of any spin only using crystal field parameter.

In conclusion, we have shown that coherent manipulation of non consecutive level can be made in an electron-spin system using coherent multi-photon transition. This result is a great step for the implementation of the quantum Grover algorithm.

**References**

- [1] Leuenberger, M.N. et al. Quantum Information Processing with Large Nuclear Spins in GaAs Semiconductors. *Physical Review Letters* **89**, 1-4(2002).
- [2] Grover, L. Quantum Mechanics Helps in Searching for a Needle in a Haystack. *Physical Review Letters* **79**, 325-328(1997).
- [3] Sorokin, P., Gelles, I. & Smith, W. Multiple Quantum Transitions in Paramagnetic Resonance. *Physical Review* **112**, 1513-1515(1958).
- [4] Bertaina, S. et al. Multiphoton Coherent Manipulation in Large-Spin Qubits. *Physical Review Letters* **102**, 50501-50504(2009).

## The effect of spin-lattice relaxation on the intensities of multiple-quantum NMR coherences and entanglement in solids

E.B. Fel'dman, A.N. Pyrkov

Institute of Problems of Chemical Physics of Russian Academy of Sciences, Chernogolovka, Moscow Region, Russia, 142432

e-mail: pyrkov@icp.ac.ru

### Introduction

Multiple-quantum (MQ) coherences in a system of dipolar coupled spins can be detected by MQ NMR methods [1, 2]. In the simplest cases (one-dimensional spin chains and rings, a system of spin-carrying atoms (molecules) in nanopores), analytical and numerical methods were developed [3, 4] in order to calculate the intensities of MQ NMR coherences. Usually spin-lattice relaxation is not taken into account at investigations of MQ NMR dynamics because the characteristic times of spin-lattice relaxation are longer than the characteristic time of MQ NMR dynamics [2]. At the same time, MQ NMR methods have been also used in order to measure the decoherence for highly correlated spin states [5, 6] and to study the scaling of the decoherence rate with the number of correlated spins [5]. Since the decoherence rate of a cluster of correlated spins increases with an increase in the number of spins [5] it is not obvious if a scalable quantum computer [7] on the basis of NMR methods is possible. The MQ NMR methods can help us to answer this question. It was shown also [8] that MQ NMR allows us to find a relationship between the MQ coherence intensity of the second order and a measure of the quantum entanglement which is the main resource of quantum computers [7]. However, this relationship was found without taking into account effects of spin-lattice relaxation [8]. Undoubtedly a theory of spin-lattice relaxation in MQ NMR experiments is necessary for solving such problems. Such theory can also be useful for traditional problems of NMR (paramagnetic impurities, internal molecular motions, etc.) [9].

In the present paper we develop a phenomenological theory of spin-lattice relaxation for a system consisting of two dipolar coupled spins in the MQ NMR experiment at low temperatures. We calculate the intensities of MQ coherences of the zeroth and plus/minus second orders and discuss the effects of spin-lattice relaxation on MQ NMR dynamics. We show that the developed approach is also applicable for linear spin chains when the approximation of nearest neighbor interactions is used. We discuss a connection of quantum entanglement with the intensity of MQ NMR coherence of the second order at different spin-lattice relaxation times.

### MQ NMR of spin pairs with spin-lattice relaxation at low temperature

In this work we consider the experiment with the MQ Hamiltonian and start with the thermodynamically equilibrium density matrix:

$$H_{MQ} = -\frac{D}{2}(I_1^+ I_2^+ + I_1^- I_2^-), \quad \rho_{eq} = \frac{\exp\left(\frac{\hbar w_0}{kT} I_Z\right)}{Z} \quad (1)$$

where  $I_i^+, I_i^-$  are rising and lowering operators respectively,  $D$  is the coupling constant,  $Z$  is the partition function. Then the Liouville equation with the phenomenological term on the preparation period of the MQ NMR experiment [1] is

$$\frac{d\rho}{d\tau} = -i[H_{MQ}, \rho] - \frac{\rho(\tau) - \bar{\rho}}{T_1}, \quad (2)$$

where  $\bar{\rho}$  is the thermodynamically equilibrium density matrix on the preparation period,  $T_1$  is the time of spin-lattice relaxation and  $\tau$  is the duration of the preparation period. We will consider the millikelvin temperature region, where one can suppose [10] that  $\frac{\hbar D}{kT} \ll 1$  and  $\bar{\rho} = 1/4$ . We propose that the evolution period is short and we can neglect spin-lattice relaxation on this period. Taking into account that  $Tr(I_z \bar{\rho}) = 0$  one can find that only MQ NMR coherences of zeroth and plus/minus second orders emerge in the our system and their intensities  $J_0(\tau), J_{\pm 2}(\tau)$  are

$$\begin{aligned} J_0 &= \tanh(\beta/2) \cos^2(D\tau) \exp(-2\tau/T_1), \\ J_{\pm 2}(\tau) &= \frac{1}{2} \tanh(\beta/2) \sin^2(D\tau) \exp(-2\tau/T_1). \end{aligned} \quad (3)$$

Note that all performed calculations are also valid for any equilibrium density matrix  $\bar{\rho}$  which commutes with operators  $H_{MQ}$  and  $I_z$ .

It is also interesting to note that an analogous approach can be applied to a linear chain of N interacting spins in the approximation of nearest neighbour interactions [11].

### Quantum entangled states in MQ NMR

It is well known [8] that entanglement is a main resource for quantum devices (in particular, quantum computers). MQ NMR is one of the numerous methods of obtaining entangled states [8, 12]. It turned out [8] that intensity of the MQ NMR coherence of the second order (without spin-lattice relaxation) is intimately connected with the concurrence [13] which describes quantitatively entanglement of quantum systems. In order to calculate the concurrence [13] at the end of the preparation period one should determine the matrix  $\tilde{\rho}(\tau)$  as following

$$\tilde{\rho}(\tau) = (\sigma_{y1} \otimes \sigma_{y2}) \rho^*(\tau) (\sigma_{y1} \otimes \sigma_{y2}), \quad (4)$$

where  $\rho^*(\tau)$  is the complex conjugate matrix  $\rho(\tau)$  of Eq. (2) in the standard basis  $\{|00\rangle, |01\rangle, |10\rangle, |11\rangle\}$  and  $\sigma_{yi} = 2I_{yi}, (i=1,2)$  is the Pauli matrix.

The concurrence  $C$  of the two-spin system with the density matrix  $\rho(\tau)$  of Eq. (2) equals to [13]:

$$\begin{aligned} C &= \max\{0, 2\lambda - \lambda_1 - \lambda_2 - \lambda_3 - \lambda_4\}, \\ \lambda &= \max\{\lambda_1, \lambda_2, \lambda_3, \lambda_4\}, \end{aligned} \quad (5)$$

where  $\lambda_1, \lambda_2, \lambda_3$  and  $\lambda_4$  are the square roots of the eigenvalues of the matrix product  $\rho(\tau)\tilde{\rho}(\tau)$ . Although this product is not Hermitian, it has real nonnegative eigenvalues [14]. We found that the concurrence  $C(\tau)$  in our system is

$$C(\tau) = \max\left\{0, \frac{\exp(-\tau/T_1)}{2 \cosh^2(\beta/2)} (|\sin(D\tau)| \sinh \beta - 1) - \frac{1 - \exp(-\tau/T_1)}{2}\right\}. \quad (6)$$

This expression coincides with the one obtained in [8] when the spin-lattice relaxation time tends to infinity. The entangled state emerges at temperatures

$$T < T_E = \frac{\hbar w_0}{k \ln \left( \frac{\sqrt{2+a}}{2-\sqrt{2+a}} \right)}, \quad (7)$$

where  $a = e^{\tau/T_1} - 1$ . If one takes  $w_0 = 2\pi 500 * 10^6 s^{-1}$  the entangled state emerges at the temperature  $T_E \approx 27mK$  when  $T_1 \rightarrow \infty$  [8]. According to Eq. (7) the entangled states emerge at  $2 > e^{\tau/T_1} - 1$ , i.e. at  $\ln 3 > \tau/T_1$ . The temperature  $T_E$  decreases with the decrease in the spin-lattice relaxation time.

In order to obtain the entanglement measure of the two-qubit system we average over the state of the first spin and obtain a reduced density matrix for the second spin [13]. The reduced density matrix thus depends on the fluctuations of the first spin. These fluctuations give rise to the fluctuations of the entanglement measure [15].

The rms fluctuations,  $\Delta E$  of the entanglement entropy of two-qubit system are [15]

$$\Delta E = C \log_2 \left\{ \frac{1}{C} \left( 1 + \sqrt{1 - C^2} \right) \right\}, \quad (8)$$

where the concurrence  $C$  is determined by Eq. (6). Dependencies of the sum of the MQ NMR coherences of the plus/minus second order, the concurrence  $C(\tau)$  and the entanglement fluctuations on the dimensionless spin-lattice relaxation rate  $\tau/T_1$  at  $\beta = 6$  are shown in fig.1. At long spin-lattice relaxation times the concurrence approximately coincides with the sum of the intensities of the MQ NMR coherence of the plus/minus second order as it was obtained in [8]. At  $DT_1 \gg 1$  MQ NMR dynamics determines the entanglement and its fluctuations. Spin-lattice relaxation is the dominant factor when  $DT_1 \leq 1$ . We note also that the concurrence decreases with a decrease of the spin-lattice relaxation time and entanglement fluctuations are getting more important. In conclusion we emphasize that quantum entanglement can be studied with MQ NMR methods and the effect of spin-lattice relaxation

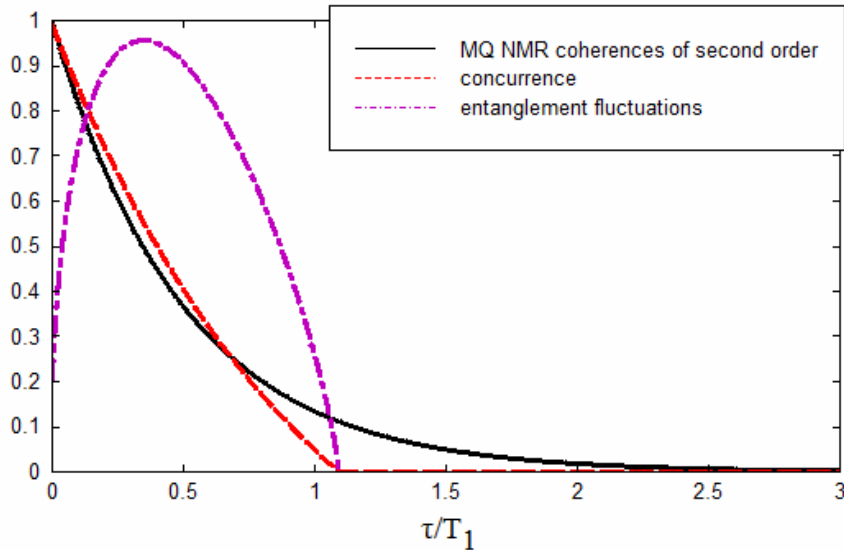


**Fig.1** The sum of the MQ NMR coherences of the plus and minus second orders (solid line), concurrence (dash line), the entanglement fluctuations (dash-dot line) versus the dimensionless spin-lattice relaxation rate  $\tau/T_1$ . The spin-spin coupling constant  $D = 4\pi 1307 s^{-1}$ , the duration of the preparation period  $\tau = 0.00086s$ ,  $D\tau = 9\pi/2$  and  $\beta = 6$ .

on MQ NMR coherences is important both for traditional magnetic resonance [9] and quantum information processing [7].

### Acknowledgments

We are grateful to D.E. Feldman for many helpful discussions. This work was supported by the Program of the Presidium of Russian Academy of Sciences No. 7 (the program "Development of the methods for obtaining chemical substances and creating new materials").

### References

- [1] J. Baum, M.Munowitz, A.N. Garroway, and A. Pines, Multiple-quantum dynamics in solid state NMR, *J. Chem. Phys.* 83 (1985) 2015-2025.
- [2] G. Cho, J.P. Yesinowski, H-1 and F-19 multiple-quantum NMR dynamics in quasi-one-dimensional spin clusters in apatites, *J. Phys. Chem.* 100 (1996) 15716-15725.
- [3] E.B. Feldman, S. Lacelle, Multiple quantum nuclear magnetic resonance in one-dimensional quantum spin chains, *J. Chem. Phys.* 107 (1997) 7067-7084.
- [4] S.I. Doronin, A.V. Fedorova, E.B. Fel'dman, et al., Multiple quantum NMR dynamics of spin-1/2 carrying molecules of a gas in nanopores, *J. Chem. Phys.* 131 (2009) 104109.
- [5] H.G. Krojanski, D. Suter, Scaling of decoherence in wide NMR quantum registers, *Phys. Rev. Lett.* 93 (2004) 090501.
- [6] H. Cho, P. Cappellaro, D.G. Cory, et al., Decay of highly correlated spin states in a dipolar-coupled solid: NMR study of CaF<sub>2</sub>, *Phys. Rev. B* 74 (2006) 224434.
- [7] M.A. Nielsen, I.L. Chuang, *Quantum computation and quantum information*, University Press, Cambridge, 2000
- [8] E.B. Fel'dman, A.N. Pyrkov, Evolution of Spin Entanglement and an Entanglement Witness in Multiple-Quantum NMR Experiments, *JETP Letters*, 88 (2008) 398-401.
- [9] A. Abraham, *The principles of nuclear magnetism*, Clarendon Press, Oxford, 1961.
- [10] A. Abraham, M. Goldman, *Nuclear magnetism: order and disorder*, Clarendon Press, Oxford, 1982.
- [11] E.B. Fel'dman, I.I. Maximov, Multiple quantum dynamics in linear chains and rings of nuclear spins in solids at low temperatures, *J. Magn. Reson.* 157 (2002) 106-113.
- [12] G.B. Furman, V.M. Meerovich, V.L. Sokolovsky, Entanglement and multiple quantum coherence dynamics in spin clusters, *Quantum information processing* 8 (2009) 379-386.
- [13] W.K. Wootters, Entanglement of formation of an arbitrary state of two qubits, *Phys. Rev. Lett.* 80 (1998) 2245-2248.
- [14] R.A. Horn, C.R. Johnson, *Matrix Analysis*, University Press, Cambridge, 1985.
- [15] E.B. Fel'dman, M.A. Yurishchev, Fluctuations of quantum entanglement, *JETP Letters* 90 (2009) 70-74.

## Hyperfine interactions in (La,Y)TiO<sub>3</sub> system

P.A. Agzamova<sup>1</sup>, A.E. Nikiforov<sup>2</sup>, Yu.V. Leskova<sup>2</sup>

<sup>1</sup>Institute of Metal Physics, 620041, S. Kovalevskaya st., Yekaterinburg, Russian Federation

<sup>2</sup>Ural State University, 620083, Lenin av., Yekaterinburg, Russia

e-mail: polina.agzamova@usu.ru

### Introduction

The interaction of spin and orbital degrees of freedom in transition-metal (TM) oxides has attracted much attention for a long time.

Among various *3d*-TM oxides, RTiO<sub>3</sub> (R=rare-earth element or Y) have been proposed as one of the most appropriate systems, due to relative simplicity of electronic states of this compounds (the nominal valence of Ti is 3+ with *3d<sup>1</sup>* configuration). Moreover, Ti<sup>3+</sup> ions are relative to Jahn-Theller ions, which possess unusual magnetic properties.

It is known, that in wide temperature range and for different R = rare-earth element or Y titanates possess orthorhombic crystal structure with *Pnma* space group, often called “quasicubic”. The GdFeO<sub>3</sub>-type distortions (*T<sub>1g</sub>* distortions) [1,2], which are present in these crystals, are believed to control magnetic structures and properties of the compounds through the influence on their orbital ground state.

LaTiO<sub>3</sub> is known as an antiferromagnetic insulator with *T<sub>N</sub>* ~ 140 K [3], while YTiO<sub>3</sub> is known as a ferromagnetic insulator with *T<sub>C</sub>* ~ 25 K [4].

Many experimental and theoretical studies suggested that the degeneracy of *t<sub>2g</sub><sup>1</sup>* configuration in YTiO<sub>3</sub> is lifted by the *d*-type Jahn-Theller distortions and ‘antiferromagnetic’ orbital ordering, and it causes the ferromagnetism in YTiO<sub>3</sub>. By contrast, no orbital ordering has yet been observed in LaTiO<sub>3</sub>. The origin of G-type antiferromagnetic ordering and the orbital state at the ground state in LaTiO<sub>3</sub> have been unclear.

One of the local experimental methods to the investigation of titanates properties is nuclear magnetic resonance (NMR) obtained on both magnetic (<sup>47,49</sup>Ti) and nonmagnetic (<sup>139</sup>La, <sup>89</sup>Y) ions [5-11].

In the paper [8] <sup>47,49</sup>Ti, <sup>139</sup>La and <sup>89</sup>Y measurements have been performed to clarify the orbital ordering and the local magnetic properties of the Y and La sites. Authors found that the Ti NMR spectrum in YTiO<sub>3</sub> is successfully explained by an orbital ordering model proposed by the unrestricted Hartree-Fock and the band calculations. On the other hand, the Ti NMR spectrum in LaTiO<sub>3</sub> is explained without orbital ordering. The internal field at the La site is canceled out because of the local symmetry in the antiferromagnetic state of LaTiO<sub>3</sub>.

In this paper we have proposed the theoretical explanation of obtained NMR data to fully understand the orbital ordering and magnetic properties of YTiO<sub>3</sub> and LaTiO<sub>3</sub>.

We concentrate our attention on the local magnetic properties investigation of the Y and La site.

We have proposed the theoretical models, which allow to explain magnetic hyperfine field formation within frameworks of microscopic viewpoint.

### Hyperfine interaction

For a description of the NMR spectrum observed at the La or Y nucleus in an orthorhombic coordinate system, we use a spin Hamiltonian of the form:

$$H = \nu_Q \left[ (3I_z^2 - I(I-1)) + \eta(I_x^2 - I_y^2) \right] - \gamma \hbar (\mathbf{H}_{ex} + \mathbf{H}_{dip} + \mathbf{H}_{hf}) \cdot \mathbf{I}, \quad (1)$$

where  $\mathbf{H}_{ex}$  is the external magnetic field,  $\mathbf{H}_{dip}$  is the field induced by the dipole-dipole interaction of the nucleus with the surrounding magnetic ions,  $\mathbf{H}_{hf}$  is the internal field (the field of the hyperfine interaction (HFI) with the nearest titan ions),  $\nu_Q$  is the nuclear quadrupole interaction constant, and  $\eta$  is the asymmetry parameter of the nuclear quadrupole interaction tensor.

The position of the lanthanum or yttrium ion is described by the symmetry point group Ch. Therefore, in the orthorhombic coordinate system the induced field due to the hyperfine interaction, expressed in terms of the components of the magnetic structure vectors, take the form

$$\begin{aligned} \mathbf{H}_{hf} &= A^F \mathbf{F} + A^A \mathbf{A} + A^G \mathbf{G} + A^C \mathbf{C} \\ A^F &= \begin{pmatrix} A_{aa}^F & 0 & A_{ac}^F \\ 0 & A_{bb}^F & 0 \\ A_{ca}^F & 0 & A_{cc}^F \end{pmatrix}; \quad A^C = \begin{pmatrix} A_{aa}^C & 0 & A_{ac}^C \\ 0 & A_{bb}^C & 0 \\ A_{ca}^C & 0 & A_{cc}^C \end{pmatrix}; \\ A^A &= \begin{pmatrix} 0 & A_{ab}^A & 0 \\ A_{ba}^G & 0 & A_{bc}^A \\ 0 & A_{cb}^A & 0 \end{pmatrix}; \quad A^G = \begin{pmatrix} 0 & A_{ab}^G & 0 \\ A_{ba}^G & 0 & A_{bc}^G \\ 0 & A_{cb}^G & 0 \end{pmatrix}; \\ \mathbf{F} &= \mathbf{S}_1 + \mathbf{S}_2 + \mathbf{S}_3 + \mathbf{S}_4, \quad \mathbf{A} = \mathbf{S}_1 - \mathbf{S}_2 + \mathbf{S}_3 - \mathbf{S}_4, \\ \mathbf{G} &= \mathbf{S}_1 - \mathbf{S}_2 - \mathbf{S}_3 + \mathbf{S}_4, \quad \mathbf{C} = \mathbf{S}_1 + \mathbf{S}_2 - \mathbf{S}_3 - \mathbf{S}_4 \end{aligned} \quad (2)$$

Let us find the values of the coefficients.

The effective magnetic hyperfine interaction Hamiltonian on the nucleus of nonmagnetic ion (lanthanum or yttrium) for (La,Y) – Ti pair depends on spin state of titan. The Hamiltonian form is chosen to fit the coincidence of hyperfine fields obtained by the molecular orbitals method and by the effective Hamiltonian method.

In the local coordinate system with Oz axis parallel to (La,Y) – Ti bond the effective Hamiltonian may be represented at the sum of isotropic and anisotropic contributions:

$$H_{MHF}^{eff} = A^{is} \frac{1}{2S} (\mathbf{IS}) + A^{an} \frac{1}{2S} [3I_z S_z - (\mathbf{IS})] \quad (3)$$

Here  $A^{is}$  is the operator of isotropic HFI associated with (La,Y)  $s$ -shell polarization;  $A^{an}$  is the operator of anisotropic HFI associated with (La,Y)  $p_\sigma$ - and  $p_\pi$ -shells polarization;  $S$  is the  $3d$ -ion spin.

$$\begin{aligned} A^{is} &= B^{is}(\theta, \varphi) \cdot f_S(R) \cdot A_S^{(0)} \\ A^{an} &= A_\sigma + A_\pi = (B_\sigma^{anis}(\theta, \varphi) \cdot f_\sigma(R) + B_\pi^{anis}(\theta, \varphi) \cdot f_\pi(R)) \cdot A_p^{(0)}, \end{aligned} \quad (4)$$

where  $B^{is}(\theta, \varphi)$ ,  $B_\sigma^{an}(\theta, \varphi)$ ,  $B_\pi^{an}(\theta, \varphi)$  are the angle dependences,  $(\theta, \varphi)$  is angle between (La,Y) – Ti bond direction and quantization axis;  $f_S(R)$ ,  $f_\sigma(R)$ ,  $f_\pi(R)$  are the overlap integrals, which characterize the spin density transfer on  $s$ -,  $\sigma$ - and  $\pi$ -direction correspondingly;  $A_S^{(0)}$ ,  $A_p^{(0)}$  are hyperfine interaction values.

To take the influence of all the nearest titan ions into account, we transform the local coordinate system for each titan ion to orthorhombic axis and use a superposition model. Next we calculate the coefficients from Eq. (1) to isotropic and anisotropic parts and written in units of  $a_S$ ,  $a_\sigma$  and  $a_\pi$ . All the values were calculated in accordance with the crystal structures.

When the  $A_x(0.002)F_y(0.006)G_z(0.999)$  magnetic structure of  $\text{LaTiO}_3$  and the  $A_x(0.115)F_y(0.993)G_z(0.008)$  magnetic structure of  $\text{YTiO}_3$  are taken into account, the induced magnetic field at the (La,Y) nuclei is expressed as:

$$\begin{aligned}
 {}^{139}H_{is} &= -\frac{1}{139\gamma\hbar} 0.693 \cdot a_s \cdot F_y, & {}^{89}H_{is} &= -\frac{1}{89\gamma\hbar} 0.582 \cdot a_s \cdot F_y \\
 {}^{139}H_{an} &= -\frac{1}{139\gamma\hbar} \left[ (0.008 \cdot a_\pi + 0.040 \cdot a_\sigma) F_y + (-0.087 \cdot a_\pi - 0.432 \cdot a_\sigma) A_x + \right. \\
 &\quad \left. + (0.015 \cdot a_\pi + 0.067 \cdot a_\sigma) G_z \right] \\
 {}^{89}H_{an} &= -\frac{1}{89\gamma\hbar} \left[ (-0.006 \cdot a_\pi - 0.063 \cdot a_\sigma) F_y + (0.030 \cdot a_\pi - 0.317 \cdot a_\sigma) A_x + \right. \\
 &\quad \left. + (-0.040 \cdot a_\pi - 0.219 \cdot a_\sigma) G_z \right]
 \end{aligned}$$

It is note, that in the absence of external magnetic field the contributions are comparable in magnitude.

The additional contributions, which appears when the polarization of the  $p_{\sigma^-}$  and  $p_{\pi^-}$  shells is taken into account. The concrete form of these contributions is determined by the orbital structures of (La,Y)TiO<sub>3</sub> compounds.

Next, the following parameters of the local electric and magnetic fields for the <sup>139</sup>La and <sup>89</sup>Y centers were obtained:  $v_Q$ ,  $\eta$ ,  $H_{hf}$ ,  $H_{dip}$ . The direction of the local magnetic field coincides with the direction of the orthorhombic axis  $b$ .

## Conclusion

We have proposed a model for calculating the magnetic structure and HFI parameters at the <sup>139</sup>La and <sup>89</sup>Y sites for LaTiO<sub>3</sub> and YTiO<sub>3</sub> correspondingly. The standard approach is supplemented by the inclusion of the anisotropic contribution to the HFI. The obtained structures of the (La,Y)TiO<sub>3</sub> system determines the type of magnetic structure and the form of the anisotropic magnetic field at the lanthanum or yttrium nucleus.

## References

- [1] A.C. Komarek, H. Roth, M. Cwik, W.D. Stein, J. Baier, M. Kriener, F. Bouree, T. Lorenz, and M. Braden, Phys. Rev. B **75**, 224402 (2007).
- [2] M. Cwik *et al.*, Phys. Rev. B **68**, 060401(R) (2003).
- [3] Y. Okada, T. Arima, Y. Tokura, C. Murayama, N. Mori, Phys. Rev. B, **48**, 13, 9677 (1993)
- [4] Y. Taguchi, Y. Tokura, T. Akima, F. Inaba, Phys. Rev. B, **48**, 1, 511 (1993)
- [5] Y. Furukawa, I. Okamura, K. Kumagai, Y. Taguchi, Y. Tokura, J. Low Temp. Phys., **105**, 314, 413-418 (1996)
- [6] Y. Furukawa, I. Okamura, K. Kumagai, Y. Taguchi, Y. Tokura, Physica B, **237-238**, 39-40 (1997)
- [7] Y. Furukawa, I. Okamura, K. Kumagai, T. Goto, T. Fukase, Y. Toguchi, Y. Tokura, Phys. Rew. B, **59**, 16, 10550 (1999)
- [8] M. Itoh, M. Tsuchia, H. Tanaka, K. Motoya, J. Phys. Soc. Jap., **68**, 8, 2783-2789 (1999)
- [9] T. Kiyama, S. Fujisawa, H. Saitoh, M. Itoh, K. Kodama, M. Takigawa, Physica B, **329-333**, 733-735 (2003)
- [10] T. Kiyama, M. Itoh, Phys. Rev. Lett., **91**, 16, 167202 (2003)
- [11] M. Itoh, T. Kiyama, K. Kodama, J. Akimitsu, J. Magn. Mat., **272-276**, 90-91 (2004)

## Temperature dependence of the conduction electron g-factor in silicon

A.A. Konakov, V.A. Burdov, A.A. Ezhevskii, A.V. Soukhorukov, D.V. Guseinov,  
S.A. Popkov

University of Nizhniy Novgorod, 603950, Gagarin ave. 23, Nizhniy Novgorod, Russia

e-mail: anton.a.konakov@gmail.com

Since pioneer demonstration of the spin injection and detection in Si [1], silicon becomes a perspective material for spintronics due to weak spin-orbit interaction, long spin relaxation time and large spin diffusion length in comparison with typical III-V semiconductors such as gallium arsenide. One of the most important characteristics of conduction electrons in various systems with spin-orbit coupling is the spin relaxation rate. The dominant mechanism of the spin relaxation in silicon is the mechanism of Elliott [2] and Yafet [3], where spin flip processes are caused by electron-phonon interaction. Quantitative theoretical studies of the Elliott-Yafet spin relaxation in silicon [4] yields the spin relaxation rate proportional to a third power of temperature. This is in good agreement with the experimental data. The spin relaxation rate can be extracted from the line width of the conduction electron spin resonance (CESR).

Another important characteristic of conduction electrons in magnetic field is their Lande g-factor, which is characterized by the position of the CESR line. First experimental investigations of the conduction electron g-factor were carried by Wilson and Feher [5]. The measured value for “free” carriers was found to be  $g = 1.99875 \pm 0.00010$ . In silicon each conduction valley has only axial symmetry around  $\Delta$ -direction in the reciprocal space, so the g-factor of each valley is a tensor with two, longitudinal and transverse, principal values:  $g_{\parallel}$  and  $g_{\perp}$ , respectively. The measured value  $g$  is isotropic due to the cubic symmetry of the silicon lattice and has the average form over all 6 conduction band valleys:

$$g = \frac{1}{3} g_{\parallel} + \frac{2}{3} g_{\perp}. \quad (1)$$

Roth was first, who theoretically investigated the conduction electron g-factor in silicon [6]. Use of the second-order  $\mathbf{k} \cdot \mathbf{p}$ -method including spin-orbit coupling as the first-order perturbation allows obtaining analytical expressions for g-tensor components, which is  $\mathbf{k}$ -independent for electrons near the bottom of conduction band. Liu [7] applied the method of orthogonalized plane waves to calculate the g-factor according to the mentioned above Roth formula, and obtained a good agreement with experimental data of Wilson and Feher [5]. In fact, no evidence exists in literature on the electron g-factor temperature dependence in silicon. We shall first demonstrate that dependence, which can be explored in the CESR measurements together with the spin relaxation rate.

In the present work the temperature dependence of the electron g-factor in silicon has been investigated both theoretically and experimentally. Theoretical consideration is based on the renormalization of the electron energy by the electron-phonon interaction in the second-order perturbation theory [8]. We take into account only electron-phonon interaction in the second-order perturbation theory that has been first considered by Fan [9], neglecting influence of the Debye-Waller term [10] (interaction of the electron with two phonons in the first-order perturbation theory). The physical grounds for such an approximation will be discussed below.

The electron energy renormalization by the electron-phonon interaction is given by

$$\varepsilon_n(\mathbf{k}) = \varepsilon_n^{(0)}(\mathbf{k}) + \sum_{m, \mathbf{q}, \lambda} \left( N_{\mathbf{q}, \lambda} + \frac{1}{2} \mp \frac{1}{2} \right) \frac{|V_{n\mathbf{k}, m\mathbf{k} \pm \mathbf{q}}|^2}{\varepsilon_n^{(0)}(\mathbf{k}) - \varepsilon_m^{(0)}(\mathbf{k} \pm \mathbf{q}) \pm \hbar \omega_{\mathbf{q}, \lambda}}, \quad (2)$$

where  $\varepsilon_n^{(0)}(\mathbf{k})$  and  $\varepsilon_n(\mathbf{k})$  are unperturbed and renormalized energies of the electron with the band index  $n$  and the wave vector  $\mathbf{k}$ , respectively,  $V_{n\mathbf{k}, m\mathbf{k} \pm \mathbf{q}}$  is the matrix element describing the electron momentum scattering from the  $|n\mathbf{k}\rangle$  state to the  $|m\mathbf{k} \pm \mathbf{q}\rangle$  one accompanied by absorption (+) or emission (-) of the phonon with wave vector  $\mathbf{q}$  and polarization  $\lambda$ ,  $\omega_{\mathbf{q}, \lambda}$  and  $N_{\mathbf{q}, \lambda}$  are the frequency and the occupation number of the phonon. Including spin-orbit interaction one has to take into account an effective spin-up  $|\uparrow\rangle$  or spin-down  $|\downarrow\rangle$  state of the electron [4]. In the absence of magnetic field the spin-up and spin-down states have the same energy (the Kramers degeneracy). So, the expression (2) describes an influence of the electron-phonon interaction on the Kramers degenerate states. The matrix element  $V_{n\mathbf{k}, m\mathbf{k} \pm \mathbf{q}}$  includes both spin preserving and spin flip scattering.

In the external magnetic field  $\mathbf{H}$  oriented along one of the conduction band valleys the electron energy has an additional Zeeman term  $\pm \mu_B g_i H/2$ , where  $\mu_B$  is the Bohr magneton,  $g_i$  is the g-tensor principal value,  $i = \parallel, \perp$  for longitudinal and transverse components, respectively, and  $\pm 1/2$  is the spin-projection on the magnetic field axis. The external magnetic field splits the Kramers conjugate states. In that case renormalization of the electron energy includes also the modification of the Zeeman contribution in addition to the renormalization (2) of the Kramers degenerate part. The electron-phonon correction to this term can be represented effectively as a correction to the g-tensor components  $g_i$ . That is the principle of the conduction electron g-factor renormalization in the imperfect lattice.

Let us discuss the renormalization of the spin-up state energy in the external magnetic field. Spin preserving transitions do not modify the Zeeman energy due to binding the states with the same spin orientation. Only spin flip processes renormalize this term:

$$\varepsilon_n(\mathbf{k}) + \frac{1}{2} \mu_B g_i H = \varepsilon_n^{(0)}(\mathbf{k}) + \frac{1}{2} \mu_B g_i^{(0)} H + \sum_{m, \mathbf{q}, \lambda} \left( N_{\mathbf{q}, \lambda} + \frac{1}{2} \mp \frac{1}{2} \right) \frac{|V_{n\mathbf{k}\uparrow, m\mathbf{k} \pm \mathbf{q}\downarrow}^{(i)}|^2}{\varepsilon_n^{(0)}(\mathbf{k}) + \frac{1}{2} \mu_B g_i^{(0)} H - \left( \varepsilon_m^{(0)}(\mathbf{k} \pm \mathbf{q}) - \frac{1}{2} \mu_B g_i^{(0)} H \right) \pm \hbar \omega_{\mathbf{q}, \lambda}}, \quad (3)$$

where  $g_i^{(0)}$  and  $g_i$  are unperturbed and renormalized values of the g-tensor  $i$ -th component, respectively,  $V_{n\mathbf{k}\uparrow, m\mathbf{k} \pm \mathbf{q}\downarrow}^{(i)}$  is the spin flip matrix element with respect to the spin-up  $|n\mathbf{k}\uparrow\rangle$  and spin-down  $|m\mathbf{k} \pm \mathbf{q}\downarrow\rangle$  states in the  $i$ -th valley. In weak magnetic fields, for which the theory is developed, one usually have:  $\mu_B g_i H \ll \varepsilon_n(\mathbf{k})$ . As a result, the expression (3) can be expanded into series, and the explicit form of the g-factor is

$$g_i = g_i^{(0)} - 2g_i^{(0)} \sum_{m, \mathbf{q}, \lambda} \left( N_{\mathbf{q}, \lambda} + \frac{1}{2} \mp \frac{1}{2} \right) \frac{|V_{n\mathbf{k}\uparrow, m\mathbf{k} \pm \mathbf{q}\downarrow}^{(i)}|^2}{\left( \varepsilon_n^{(0)}(\mathbf{k}) - \varepsilon_m^{(0)}(\mathbf{k} \pm \mathbf{q}) \pm \hbar \omega_{\mathbf{q}, \lambda} \right)^2}. \quad (4)$$

Let us discuss some approximations for the formula (4). First, for the electrons near the conduction-band bottom, emission of virtual phonons results mainly in interband transitions, whose contribution to the expression (4) is weakened due to the great value of the energy forbidden gap. The most dominant processes in the g-factor renormalization have to be the

phonon absorption with subsequent re-absorption. Second, one can remove the summation over the band index due to suppression of interband transitions. On the contrary, intraband spin flip transitions mostly dominate in the g-factor modification. Third, these arguments justify neglecting the Debye-Waller term in the electron energy renormalization (2), which was pointed out when formulating the model. So, the relative g-tensor component modification is

$$\frac{g_i}{g_i^{(0)}} \approx 1 - 2 \sum_{q\lambda} N_{q\lambda} \frac{|V_{\mathbf{k}\uparrow\mathbf{k}\pm\mathbf{q}\downarrow}^{(i)}|^2}{(\varepsilon^{(0)}(\mathbf{k}) - \varepsilon^{(0)}(\mathbf{k} + \mathbf{q}) + \hbar\omega_{q\lambda})^2}, \quad (5)$$

where the band index  $n$ , describing the conduction band, is omitted for simplicity. The minus sign in front of the second term in (5) emphasized decrease of the g-tensor component absolute value, when the interaction with lattice vibrations is taken into account. The measured value  $g$  can be obtained from the expression (1).

Yafet [3] has shown that, for the spin flip processes in silicon,  $V_{\mathbf{k}\uparrow\mathbf{k}\pm\mathbf{q}\downarrow}^{(i)} \sim \mathbf{q}^2$  in contrast to the spin preserving scattering matrix element that is proportional to the first order of the phonon wave vector  $\mathbf{q}$ . So, in Eq. (5) we suppose

$$|V_{\mathbf{k}\uparrow\mathbf{k}\pm\mathbf{q}\downarrow}^{(i)}| = A_i q^2 \sqrt{\frac{\hbar}{2\rho V \omega_{q\lambda}}}, \quad (6)$$

where the factor  $\sqrt{\frac{\hbar}{2\rho V \omega_{q\lambda}}}$  is standard for the electron-phonon scattering matrix element [11],  $\rho$  and  $V$  are the silicon density and the sample volume, respectively,  $A_i$  are constants, which are analogous to the deformation potential components in silicon for spin preserving processes [12]. In case of spin flip processes detailed calculation of these constants is required.

The temperature dependence comes from the occupancy  $N_{q\lambda}$  of the  $\omega_{q\lambda}$  phonon mode, which is given by the Bose-Einstein distribution function in the equilibrium. In the case of sufficiently high temperatures  $T$  (of the order, or higher than) 100 K, the occupancy is represented as

$$N_{q\lambda} \approx \frac{k_B T}{\hbar\omega_{q\lambda}}, \quad (7)$$

where  $k_B$  is the Boltzmann constant. Neglecting the  $\mathbf{k}$ -dependence of the g-factor for electrons near the bottom of the conduction band, and substituting expressions (6) and (7) into Eq. (5), one can obtain the temperature dependence of the g-tensor components:

$$\frac{g_i}{g_i^{(0)}} \approx 1 - \frac{k_B T}{\rho V} \sum_{q\lambda} \frac{|A_i|^2 \mathbf{q}^4}{\omega_{q\lambda}^2 (\hbar\omega_{q\lambda} - \varepsilon^{(0)}(\mathbf{q}))^2}, \quad (8)$$

where  $\varepsilon^{(0)}(\mathbf{q})$  is counted from the conduction band bottom and  $V^{-1} \sum_{q\lambda} \dots$  is, as usual, replaced by  $\int d\mathbf{q} / (2\pi)^3$ .

We have found that, the g-factor of the conduction electrons should almost linearly decrease with temperature if the interaction of the conduction electrons with lattice vibrations is taken into account.

The g-factor of electrons is also investigated experimentally in CESR spectra measurements. We use natural silicon samples doped with Li and P whose concentrations were very close to minimize difference in spin flip process intensity. The experimental results

are presented in fig.1. As temperature increases from zero to  $\sim 80$  K, a monotonous rise of the g-factor takes place. Such a behaviour can be explained by the electron localization on the impurity centres. However at higher temperatures the donors become ionized and the

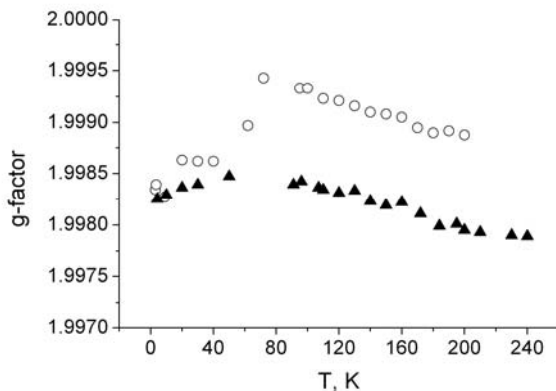


**Fig.1.** Experimental temperature dependence of electron g-factor in Si:Li ( $\circ$ ) and Si:P ( $\blacktriangle$ ) samples with donor concentration  $3.3 \cdot 10^{18} \text{ cm}^{-3}$  and  $3.7 \cdot 10^{18} \text{ cm}^{-3}$ , respectively.

electrons can propagate over the sample. In this temperature range one can see approximately linear decrease of the g-factor, which was predicted theoretically for the conduction electrons. Quantitative comparison with experimental results requires additional detailed calculations.

Generally speaking, modification of the g-factor is caused by virtual phonon-induced spin flip processes occurring between the initial, intermediate, and final electron states, where the final state completely coincides with the initial one. This, presumably, implies that the Elliott-Yafet mechanism of the spin relaxation is the

main one for the considered system.

This work was in part financially supported by RFBR, the Russian Ministry of Education and Science through the programs “RNP” and “Kadry”, and the “Dynasty” Foundation.

## References

- [1] I. Appelbaum, B. Huang, D.J. Monsma, *Nature (London)* **447**, 295 (2007).
- [2] R.J. Elliott, *Phys. Rev.* **96**, 266 (1954).
- [3] Y. Yafet, in *Solid State Physics*, edited by F. Seitz and D. Turnbull (Academic, New York, 1963), Vol. 14, p. 1.
- [4] J.L. Cheng, M.W. Wu, J. Fabian, *Phys. Rev. Lett.* **104**, 016601 (2010).
- [5] D.K. Wilson and G. Feher, *Phys. Rev.* **124**, 1068 (1961).
- [6] L.M. Roth, *Phys. Rev.* **118**, 1534 (1960).
- [7] L. Liu, *Phys. Rev. Lett.* **6**, 683 (1961).
- [8] P.B. Allen, M. Cardona, *Phys. Rev. B* **23**, 1495 (1981).
- [9] H.Y. Fan, *Phys. Rev.* **82**, 900 (1951).
- [10] E. Antončík, *Czech. J. Phys.* **5**, 449 (1955).
- [11] A. Anselm, *Introduction to semiconductor theory* (Prentice-Hall, Englewood Cliffs, NJ, 1981).
- [12] C. Herring, E. Fogt, *Phys. Rev.* **101**, 944 (1956).

**EPR study of spin relaxation in the single-layer graphene**

K. Tadyszak, M. Augustyniak-Jabłokow, M. Maćkowiak

Institute of Molecular Physics, PAS , Smoluchowskiego 17, 60-179 Poznań, Poland.

e-mail: krzysztof.tadyszak@ifmpan.poznan.pl

Any future application of graphene in spintronics is based on the expectation of long relaxation times. Theoretical considerations are focused on conduction electrons [1-4]. According to theoretical predictions, the most effective relaxation process is electron scattering on impurities and it is characterised by spin relaxation times as long as  $\tau_s \sim 10^{-6} - 10^{-3}$  s depending on the impurity concentration and the applied electrical field, but temperature independent. As possible relaxation mechanisms, the electron-electron interactions [2] and interactions with polar-optical surface phonons are also considered [3].

However, the experimental times derived from the magnetoconductivity measurements are in the range of 100-200 ps [5-8]. It is speculated that such short relaxation times can be due to metallic adatoms introduced in the process of sample preparation.

Another source of data on the values of the spin relaxation times is Electron Paramagnetic Resonance (EPR). This method has not been previously used in the study of graphene as it requires small, but significant amount of the material.

However, despite the fact that graphene is just a single layer of graphite, these two materials have significantly different electronic structure. In graphite the EPR signal originates mainly from conduction electrons. But in a similar EPR experiment, at low magnetic field of about 300 mT and without an external electrical field, the graphene sample is in the vicinity of the neutrality point and the concentration of the conduction electron,  $N_e$ , should be close to zero. Even if the experimentally found  $N_e$  [9-10] has a finite value it is still lower than the predicted concentration of the defects in the pristine graphene. Therefore, the EPR signal of graphene will be mainly due to electrons localized on defects and the measured relaxation times will describe the localized paramagnetic centres.

Here we present preliminary results of our investigation of the pristine single-layer graphene obtained by substrate-free gas-phase synthesis with average flake size of about  $\sim 550$  nm [11]. The EPR sample was prepared by deposition of graphene flakes on the amorphous SiO<sub>2</sub> in argon atmosphere. After transfer to the quartz tube the sample was degassed and sealed under vacuum to avoid contact with atmospheric oxygen. A narrow signal with the RT line width  $\Delta B_{pp} = 0.06$  mT and intensity significant for measurements appeared after several days of storage in vacuum.

The temperature dependence of the EPR signal intensity from the sample with a small concentration of paramagnetic centres  $2 \times 10^{19}$  spin/g follows the Curie law down to  $\sim 10$  K confirming our predictions that the EPR signal originates from the localized, not the conduction electrons. In our preliminary EPR study of graphene with the higher spin concentration  $\sim 10^{20}$  spin/g we have studied temperature dependences of the resonance line parameters [12]. We have found, that the line shape of the EPR signal is Lorentzian in the whole temperature range. This is due to exchange interactions between localized and conduction electrons. Thus the EPR line is homogeneously broadened where all unpaired electrons experience the same time-averaged local fields due to their delocalization and spin exchange. The decay of the magnetization cannot be refocused in an echo experiment. Electron spin echo can be excited for inhomogeneously broadened EPR lines only. For this

reason we were not able to obtain the spin echo. Relaxation times studies were performed by analysis of the free induction decay (FID).

Pulsed EPR measurements were performed with a Bruker ESP 380E FT/CW spectrometer equipped with an Oxford CF935 flow helium cryostat in temperature range 4.2 K – 150 K. Two types of pulsed experiments were carried out: the first one was the free induction decay time  $T_2^*$  investigation. After  $\pi/2$  (16ns) pulse we measured the magnetization decay as a function of temperature. Typical free induction decay curve is shown in fig.1. The solid line is the monoexponential fit. It is interesting to point out that the value of spin-spin relaxation time depends on the concentration of spins (fig.2). Further studies of this effect are in progress.

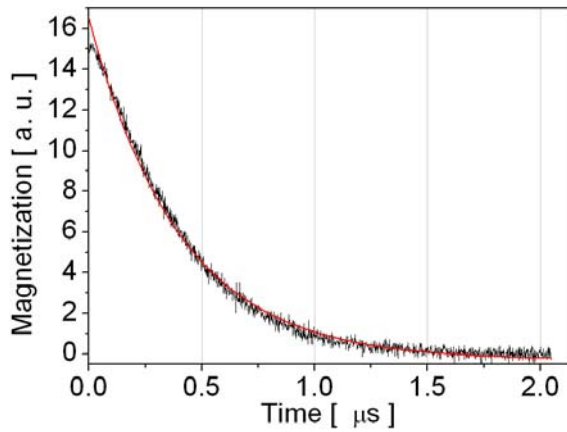


**Fig.1.** An example of an FID from the single-layer graphene at  $T=5K$ . The solid line represents the monoexponential fit.

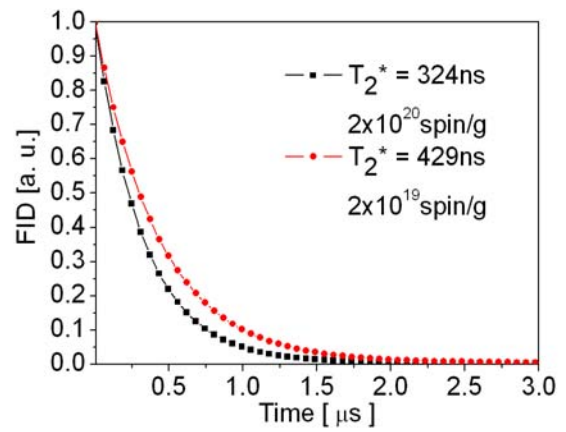


**Fig.2.** Free induction decays showing shortening of the spin-spin relaxation time with increasing defects concentration. ( $T=5K$ )

The second experiment was a study of the spin-lattice relaxation time  $T_1$ . The sequence used was  $\pi$  (80ns) –  $\tau$  –  $\pi/2$  (16ns) –  $t$ . The typical inversion recovery curve obtained at  $T=5K$  is shown in fig.3. The solid line is the monoexponential fit. The magnetization at very long  $\tau$  values represents the so-called “initial magnetization” of the spin system.

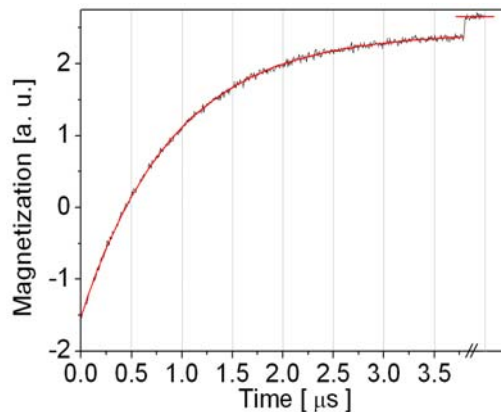


**Fig.3.** Typical inversion magnetization recovery curve in single-layer graphene ( $T=5K$ ). The solid line is the monoexponential fit.

Temperature dependences of the measured spin-lattice and spin-spin relaxation rates in single layer graphene are shown in fig.4. The relaxation rate is relatively fast at very low

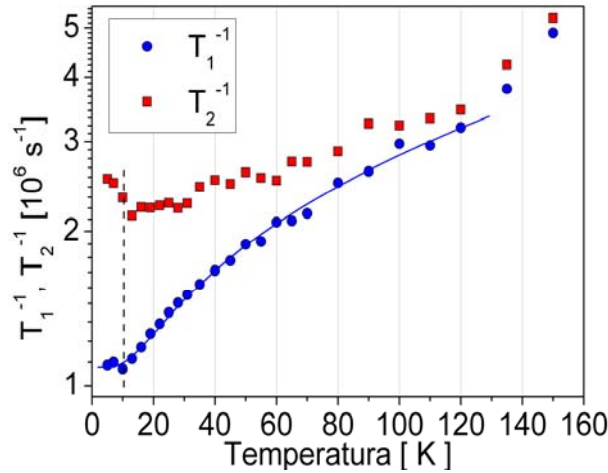


**Fig.4.** Spin-lattice relaxation rate  $1/T_1$  and spin-spin relaxation rate  $1/T_2$  as a function of temperature. The solid line is the best fit to Eq.(1) with thermally activated process having activation energy of  $30.4 \text{ cm}^{-1}$ .

temperatures and slowly grows with temperature. The spin-lattice relaxation rate in temperature range 10 K – 130 K is well described by the following equation [13]:

$$\frac{1}{T_1} = a + b \operatorname{cosec}\left(\frac{\Delta}{kT}\right) = 1.08848 \cdot 10^6 [\text{s}^{-1}] + 0.79 \cdot 10^6 [\text{s}^{-1}] \cdot \operatorname{cosec}\left(\frac{44.33[\text{K}]}{T}\right). \quad (1)$$

Relaxation theories predict that this mechanism can be related to the thermal excitations between two local conformations having energy splitting  $\Delta = 30.4 \text{ cm}^{-1}$ . We are not able to identify the molecular origin of these conformational states. The EPR signal of graphene is mainly due to electrons localized on defects and the measured relaxation times will describe the localized paramagnetic centres. Thus, the probable relaxation mechanism may involve excitations between local conformations of the vacancy defects. But there are also other possibilities, which should be taken into consideration. In graphene the carrier-mediated exchange interaction between localized centres leads to the antiferromagnetic coupling [12]. The localized spins could relax via the conduction electrons (as in Korringa-type relaxation). We are planning more experimental studies (relaxation measurements for graphene with different types and concentrations of defects) to distinguish between possible relaxation mechanisms.

Spin-spin relaxation time for homogeneously broadened EPR line may be evaluated on the basis of Bloch equation:

$$T_2^* = \frac{0.131306 \cdot 10^6}{g \cdot \Delta B [\text{G}]} [\text{s}] \quad (2)$$

Using the temperature dependence of EPR line width  $\Delta B_{pp}$  measured by us previously by CW method [12] we calculated the spin-spin relaxation time values. Results for the sample with twenty times higher concentration of paramagnetic centres are presented in fig.5 and compared with the relaxation times measured by the pulse methods. It is interesting to see that in the temperature region, where  $T_1$  is comparable to  $T_2$ , the line width is well reproduced only by relaxation mechanisms. The low temperature differences can be due to the difference in the spin concentration and transition to the state of the diluted antiferromagnet [12]. Temperature dependence of CW EPR line width is shown in fig.6 for comparison.

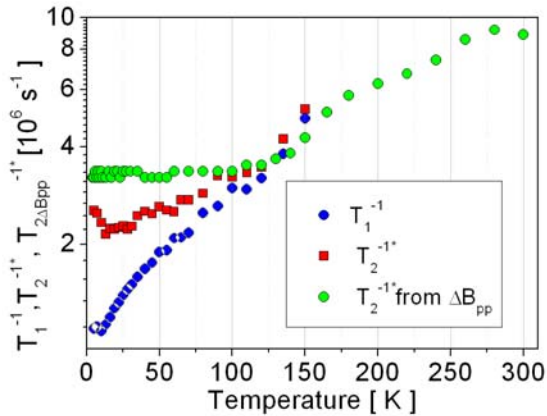


**Fig.5.** Comparison of the measured and calculated relaxation times.

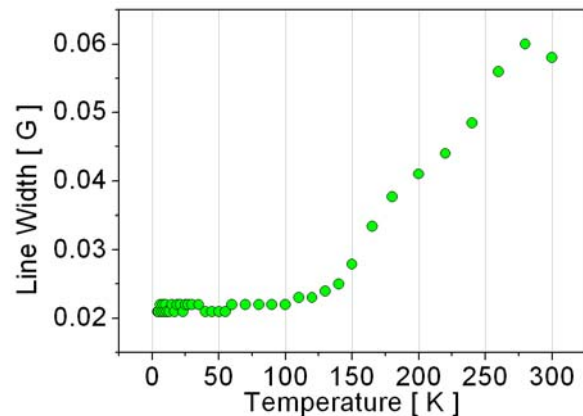


**Fig.6.** Temperature dependence of CW EPR line width of the sample with spin concentration  $4 \times 10^{20}$  spin/g [12].

In conclusion we point out that the electron spin relaxation studies by pulse EPR methods provide valuable information about the dynamics of the electron states in nanocarbon materials. The need of the further investigation is undisputable.

### Acknowledgment

The authors wish to thank Prof. dr hab. Stanisław K. Hoffmann for very valuable and inspiring discussions.

### References

- [1] D. Huertas-Hernando, F. Guinea, A. Brataas, Eur. Phys. J. Special Topics 148, 177 (2007).
- [2] C. Ertler, S. Konschuh, M. Gmitra, J. Fabian, Phys. Rev. B **80**, 041405 (2009).
- [3] Y. Zhou, M. W. Wu, Phys. Rev. B **82**, 085304 (2010).
- [4] B. Dóra, F. Murányi, F. Simon, Europhysics Letters **92** 17002 (2010).
- [5] N. Tombros, C. Józsa, M. Popinciuc, H. T. Jonkman, B. J. van Wees, Nature, **448**, 571, (2007).
- [6] N. Tombros, S. Tanabe, A. Veligura, C. Józsa, M. Popinciuc, H.T. Jonkman, and B.J. van Wees, Phys. Rev. Lett. **101**, 046601 (2008).
- [7] M. Popinciuc, C. Józsa, P.J. Zomer, N. Tombros, A. Veligura, H.T. Jonkman, and B.J. van Wees, Phys. Rev. B **80**, 214427 (2009).
- [8] C. Józsa, T. Maassen, M. Popinciuc, P. J. Zomer, A. Veligura, H.T. Jonkman, and B.J. van Wees, Phys. Rev. B **80**, 241403(R) (2009).
- [9] L.A. Ponomarenko, R. Yang, R.V. Gorbachev, P. Blake, A.S. Mayorov, K.S. Novoselov, M.I. Katsnelson, A. K. Geim, Phys. Rev. Letters, 105, 136801 (2010).
- [10] S. Dröscher, P. Roulleau, F. Molitor, P. Studerus, C. Stampfer, K. Ensslin, T. Ihn, Appl. Phys. Letters **96**, 152104 (2010).
- [11] A. Dato et al., Nano Letters. **8** 2012 (2008).
- [12] M.A. Augustyniak-Jabłokow, K. Tadyszak, M. Maćkowiak, Y.V. Yablokov, submitted to Phys. Status Solidi, Rapid Research Letters.
- [13] S. Lijewski, M. Wencka, S.K. Hoffmann, M. Kępiński, W. Kempieński, M. Śliwińska-Bartkowiak, Phys. Rev. B **77**, 014304 (2008).

**<sup>51</sup>V NMR Study of the Multiferroic Ni<sub>3</sub>V<sub>2</sub>O<sub>8</sub>**

V.V. Ogloblichev<sup>1</sup>, A.G. Smolnikov<sup>1</sup>, S.V. Verkhovskii<sup>1</sup>, Yu.V. Piskunov<sup>1</sup>,  
A.P. Gerashenko<sup>1</sup>, K.N. Mikhalev<sup>1</sup>, A.Yu. Yakubovsky<sup>2</sup>, K. Kumagai<sup>3</sup>, S. Barilo<sup>4</sup>

<sup>1</sup>Institute of Metal Physics, UD RAS, Ekaterinburg 620990, Russia

<sup>2</sup>Russian Research Centre, "Kurchatov Institute", Moscow, 123182, Russia

<sup>3</sup>Department of Physics, Faculty of Science, Hokkaido University, Sapporo 060-0810, Japan

<sup>4</sup>Institute of Solid State and Semiconductor Physics, Minsk 220072, Belarus

e-mail: ogloblichev@imp.uran.ru

Compound with chemical formula M<sub>3</sub>V<sub>2</sub>O<sub>8</sub> (M=Cu, Ni, Co) are intensively studied last time [1,2], because of frustrated magnetic nature with complicated magnetic structure in ordered state including incommensurate magnetic and ferroelectric state. These systems with Kagome-type crystallographic structure are supposed to be susceptible to relatively weak interactions, as such, there are expected to demonstrate new and unusual long- and short-range magnetic order.

Ni<sub>3</sub>V<sub>2</sub>O<sub>8</sub> (NVO) represents a typical example of magnetic Kagome-staircase phases with the spin moment of magnetic ions (Ni<sup>2+</sup>)  $S = 1$ . This oxide has an orthorhombic crystal structure *Cmca* [1, 2, 3]. The structure consists of two different types of Ni<sup>2+</sup> ions: Ni<sub>S</sub> - "spine" and Ni<sub>C</sub> - "cross tie", which form the chains of the Kagomé staircases along *a*-axis in the *ac*-plane. The nonmagnetic V<sup>5+</sup> ions occupy structurally equivalent sites surrounded with six Ni<sub>S</sub> and three Ni<sub>C</sub> magnetic neighbors.

The paramagnetic state in Ni<sub>3</sub>V<sub>2</sub>O<sub>8</sub> exists down to 10K. The Ni ions form several magnetic phases with different types of long-range order at low temperatures  $T < 10$ K. According to the neutron diffraction study [1] the high-temperature incommensurate (HTI) paraelectric phase with longitudinal sinusoidal spin density wave (SDW) of Ni<sub>S</sub> spins predominantly polarized along *a*-axis changes below 6.4 K into the low-temperature incommensurate (LTI) ferroelectric phase where the Ni<sub>S</sub> and Ni<sub>C</sub> moments point the cycloid spiral in *ab*-plane with the wave vector again along *a*. In zero magnetic field the phases with commensurate antiferromagnetic order: the high-temperature phase (CAF) and the low-temperature one (C'AF) appear below 4 K.

Nuclear Magnetic Resonance (NMR) measurements performed on a single crystal of NVO to study the local magnetic susceptibility and the electronic structure, which provide important information about the magnetic transition and the charge ordering. The <sup>51</sup>V NMR spectra were measured by a field sweep for the temperature range  $T = (3 - 300)$  K and magnetic fields  $H_0 = (2 - 9.4)$  T directed along the *a, b, c* axes of crystal. Temperature dependences of the NMR line shapes and shifts have been determined in four phases (PM, LTI, HTI, C) [1]. The borders of the phase diagram measured by means of NMR are in a good agreement with earlier magnetic and neutron data [1].

In a paramagnetic phase the spectrum consists of a single quadrupole splitted <sup>51</sup>V NMR line. The components of electric field gradient (EFG) tensor and of magnetic shift tensor ( $K_{a,b,c}$ ) were obtained. The temperature dependences of  $K_a(H|a)$ ,  $K_b(H|b)$ ,  $K_c(H|c)$  are well described by a Curie-Weiss law in the paramagnetic phase and they resemble the magnetic susceptibility ( $\chi_{a,b,c}$ ) behavior. The hyperfine field at vanadium sites  $H_{loc,a} = 1.23$  T/ $\mu_B$ ,  $H_{loc,b} = 1.01$  T/ $\mu_B$ ,  $H_{loc,c} = 1.18$  T/ $\mu_B$  have been determined by using the  $K_{a,b,c}$  vs  $\chi_{a,b,c}$  diagrams. The direction of the principle axis of EFG is lying in *bc*-plane and has an angle 54(3)° with

respected to the  $c$ -axis. The quadrupole frequency  $\nu_Q = 160(15)$  kHz and parameter of asymmetry  $\eta = (V_{xx} - V_{yy})/V_{zz}$  is 0.4(1).

Below  $T = 9.4(4)$  K the single NMR line sharply broadens and with further decreasing  $T$  the NMR spectrum consisting of several peaks with nonzero spectral intensity between them (fig.1). Such a line shape is characteristic for incommensurate phases [4]. In HTI phase the spectrum has an asymmetric appearance with two peaks. The separation between the edge peaks in orientation  $H||a$ ,  $H||c$  is twice as large than that in  $H||b$ . This separation ( $h_1 - h_2$ ) is proportional to the amplitude of the order parameter [3]. By plotting  $h_1 - h_2$  vs  $T_{HTI} - T$  on a doubly logarithmic scale we obtained the critical exponent  $\beta_a = 0.37(2)$ ,  $\beta_c = 0.33(2)$ . In LTI phase the  $^{51}\text{V}$  NMR spectrum consist four peaks. We assume that it is related to an additional nickel ordering in the sites "cross tie". This ordering leads to the occurrence of magnetic nonequivalent sites of vanadium ions.

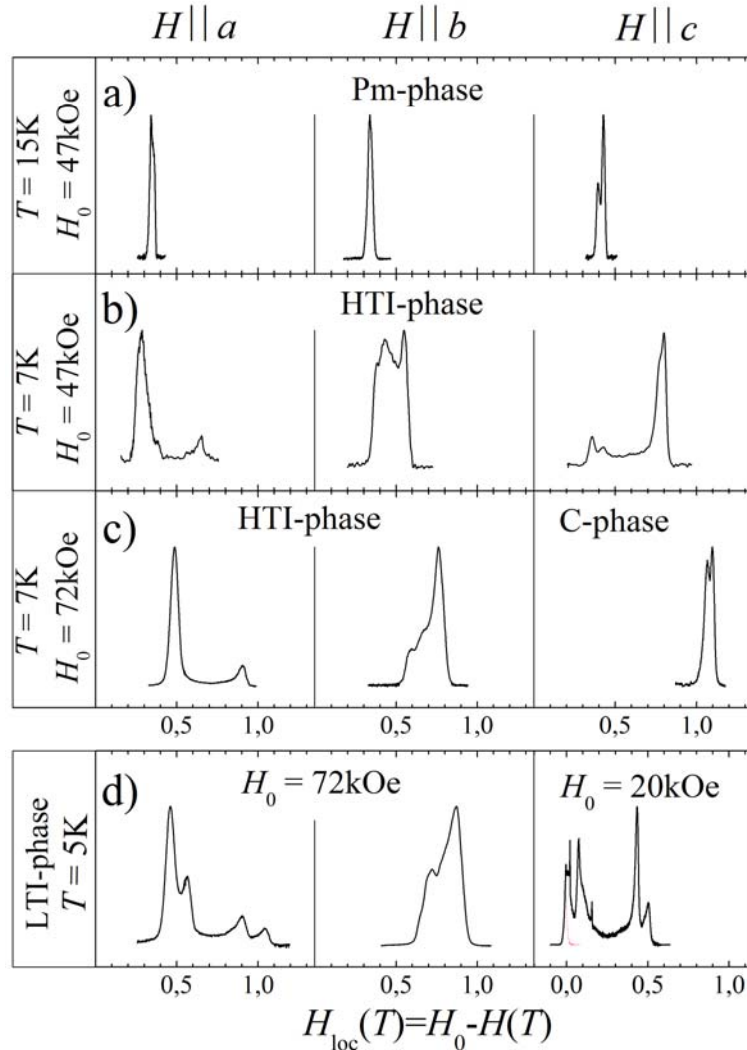


**Fig.1:**  $^{51}\text{V}$  NMR spectra measured in the  $\text{Ni}_3\text{V}_2\text{O}_8$  single crystal at different orientations of the  $a$ ,  $b$ ,  $c$  axes with respect to magnetic field direction  $H$  in (a) – paramagnetic phase, (b), (c) – high temperature incommensurate (HTI) and canted antiferromagnetic (C) phase, (d) – low temperature incommensurate (LTI) phase.

This work was supported in part UB RAS (grant for young scientists (V.V.O.)), by the RFBR (grants No 0902-00310a), by the BRFFR (grants No. F08R-177, F09K-017) and by grant from the President of Russia for young scientists (MK-1232.2011.2).

**References**

- [1] M. Kenzelmann *et al.*, Phys. Rev. B **74**, 014429 (2006).
- [2] N. Rogado *et al.*, Solid State Commun. **124**, 229 (2002).
- [3] V. Ogloblichev *et al.*, Phys. Rev. B, **81**, 144404 (2010).
- [4] R. Blinc, Phys. Rep. **79**, 331 (1981).

**EPR Meets MD: Dynamics of Myosin Motor Domain**

Ya.V. Tkachev<sup>1,2</sup>, R.V. Agafonov<sup>2</sup>, Yu.E. Nesmelov<sup>3</sup>

<sup>1</sup>V.A. Engelhardt Institute of Molecular Biology RAS, 119991, 32 Vavilov str. Moscow  
Russia

<sup>2</sup>University of Minnesota, BMBB Dept., US, Minneapolis 55455, 420 Church St SE

<sup>3</sup>University of North Caroline, US, Charlotte 28223 9201 University City Blvd

e-mail: yat.imb@gmail.com

Studying protein macromolecules by means of spin labeling technique may reveal significant dynamical and structural properties. Unfortunately, information held in an EPR spectrum of nitroxide probe attached to biomolecule is a squeeze of the extremely complex internal motion of the protein, thus it is impossible to get its detailed description. Number of special methods and their combinations has been developed, particularly site-directed spin labeling (SDSL) and double electron resonance (DEER) to partially overcome this difficulty. Introduction of spin labels into different locations allows promising use of DEER as 'ruler', but requires extensive bioengineering for producing and testing protein mutants. There is an attractive idea of joining Molecular Dynamics (MD) simulation with EPR. MD provides detailed system dynamics, and number of attempts has been made (*eg*, [6, 7]) to calculate spectra directly from trajectory data. Still there is no currently reliable algorithm developed to date for this purpose.

We successfully applied both EPR and MD to study the mechanism of myosin action. Myosin is a molecular motor with a key role in a biological motility. It is responsible for muscle contraction and cell locomotion. Its functionality is based on the structural transitions of S1 subfragment (myosin head, which selectively binds to actin filaments depending on its conformation). Transition is modulated by ATP molecule binding followed by hydrolysis, it is reversible and occurs in cyclic manner, pulling myosin filament and producing force. Nowadays the intermediate structures of this acto-myosin cycle are known (M - apo, M.ADP, M.ATP (M.ADP.BeFx), M.ADP.Pi), but the exact mechanism of their mutual conversions remains unclear.

This mechanism has been studied by pulsed ELDOR (DEER) together with molecular dynamical simulation [1]. Myosin works in cyclic manner, changing its conformation twice per cycle. From X-ray structures [2] and spectroscopy [4] it is known that light chain-binding domain of the myosin head rotates relative to catalytic domain upon power/recovery stroke. This renders myosin head bent in the recovery stroke and straight in power stroke. Relay helix (residues 462-501), connecting converter with catalytic domain, is, therefore, of special interest in myosin. Myosin mutants from *Dictyostelium discoideum* with two cystein residues

(K498C, D515C) and (K498C, A639C), has been selectively labeled by spin labels, and distance between N and C ends of relay helix change during recovery stroke were measured by DEER. DEER decays were fitted with help of Deer Analysis toolbox [3], and resulting distributions are shown in fig.1. It is clear that nucleotide analog binding (emulating the recovery stroke) leads to shorter distances and narrower distribution, that is, relay helix undergoes disorder to order transition.

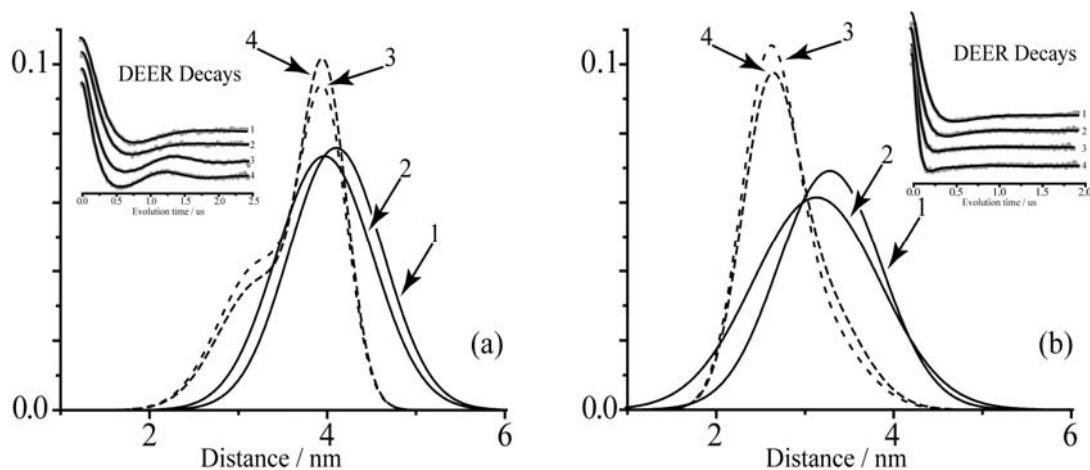


**Fig.1.** Distance distributions determined from DEER decays for A639C.K498C (a) and D515C.K498C (b) myosin mutants, trapped in different nucleotide analog states: apo (1), ADP (2), ADP.BeFx (3), ADP.AIF4 (4).

We suggest that relay helix may acts like molecular switch driving the conformational change in binding interface of the myosin head. To go into the details of its structural changes, we performed MD simulations with full-atom CHARMM force field with explicit TIP3P water within NAMD package [5]. Trajectories of 20 ns length were calculated after system equilibration in pre-recovery (straight) and post-recovery (bent) states. Simulation analysis revealed that relay helix, as well as the profile of its interaction with proximal residues undergoes significant transformations upon power/recovery stroke. It bends like the entire myosin head, during recovery stroke, due to  $\alpha$  to  $\pi$  transition of single helical turn (residues 484-489). This leads to distance contraction within residue pairs K498-D515 and K498-A639 (fig.2), which correlates well with our experimental DEER data. At the same time, although regularity of hydrogen bond network inside relay helix is disrupted, its dynamics become less chaotic (backbone RMS fluctuation decrease, fig.3, and distance distributions become narrower, fig.2). This can be explained by closing the switch II loop connected to relay helix, upon nucleotide binding. Besides that, electrostatic interactions of relay helix with relay loop, converter, and lower 50k domain changes significantly, making bent conformation more favoring and less disordered in post-recovery stroke.

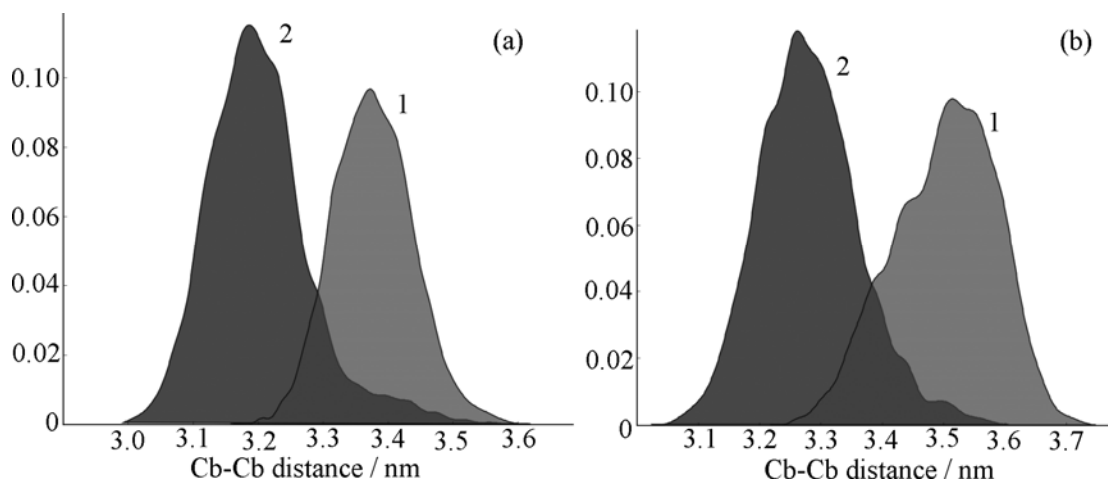


**Fig.2.** Distance distributions between  $C_{\beta}$  atoms of residue pairs A639 - K498 (a) and D515 - K498 (b). Measured from 20 ns trajectories of S1 subfragment in pre-recovery (1) and post-recovery (2) states.

By introducing optical probes (IADEANS/DABCYL) into the same locations as spin labels, fast transient kinetics of conformation change driven by ATP binding and hydrolysis, were measured by FRET. This study resolved that this conformation change is caused by ATP binding, while hydrolysis is much slower and occurs at later stages of the cycle, and this gives a good starting point for further MD study.

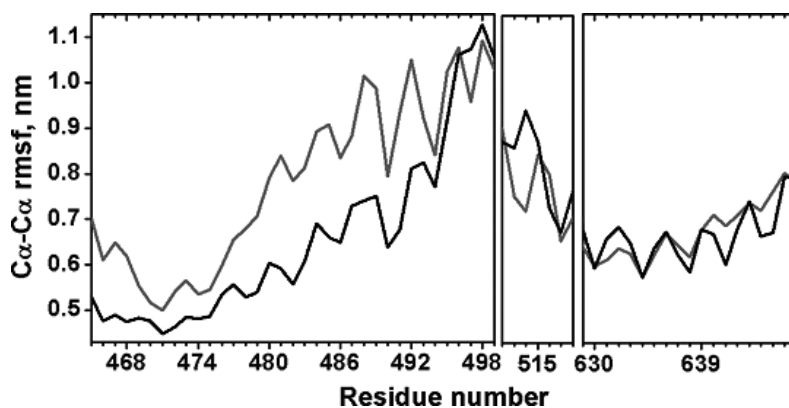


**Fig.3.** RMS fluctuation of  $\alpha$ -carbons in pre-recovery (gray line) and post-recovery (black line) states. Significant differences are seen only in relay helix.

In conclusion, this study displays a successful merging an EPR experiment with Molecular Dynamics simulation on basis of geometrical properties (distances) and degree of protein internal motion disordering. In this study we discovered what transformations (bending and ordering) occur at the relay helix of myosin head, by means of pulsed ELDOR, and clarified the details of these transformations by full-atom MD simulations. The wider distribution of interprobe distances in the pre-recovery stroke states indicates flexibility of the N-terminal part of the relay helix, when the switch II loop in the nucleotide binding site is open. These results provide direct information about the structural dynamics of the relay helix

in myosin in solution, providing insight into the interaction between myosin's active site and force-generating region.

**References**

- [1] Agafonov R.V., Negrashov I.V., Tkachev Y.V., Blakely S.E., Titus M.A., Thomas D.D., Nesmelov Y.E. Proc Natl Acad Sci U S A., 106, 21625-21630 (2009)
- [2] Rayment I, et al. Science 261, 50–58 (1993)
- [3] Jeschke G, et al.: Appl Magn Reson 30, 473–498 (2006)
- [4] Baker J.E., Brust-Mascher I., Ramachandran S., LaConte L.E., Thomas D.D. Proc. Natl. Acad. Sci. USA 95:2944–2949 (1998)
- [5] Phillips J.C., et al. J. Comput. Chem. 26:1781–1802. (2005)
- [6] Stoica I. J.: Phys. Chem. B, 108, 1771 (2004)
- [7] Budil D. E., Sale K. L., Khairy K. A., Fajer P. G.: J. Phys. Chem. A, 110, 3703 (2006)

# TABLE OF CONTENTS

## Table of Contents

<b>Program</b> .....	4
<b>Proceedings</b> .....	9
<b>P.G. Baranov, A.A. Soltamova, I.V. Il'in, F.M. Shakhov, S.V. Kidalov, A.Y. Vul', B.V. Yavkin, G.V. Mamin, S.B. Orlinskii, N.I. Silkin,</b> "Self-organization of sintered detonation nanodiamonds as revealed by high-frequency EPR spectroscopy".....	9
<b>E.M. Alakshin, R.R. Gazizulin, A.V. Klochkov, V.V. Kuzmin, M.S. Tagirov, D.A. Tayurskii, N. Mulders,</b> "Low temperature adsorption of $^3\text{He}$ on silica aerogel surface and its influence on $^3\text{He}$ spin kinetics".....	11
<b>T.R. Safin, E.M. Alakshin, Yu.M. Bunkov, A.V. Klochkov, R.R. Gazizulin, V.V. Kuzmin, M.S. Tagirov,</b> "The experimental technique for observing magnon BEC".....	15
<b>E.M. Alakshin, Yu. M. Bunkov, R.R. Gazizulin, A.V. Klochkov, V.V. Kuzmin, T.R. Safin, M.S. Tagirov,</b> "The observation of magnon BEC in solid antiferromagnet $\text{CsMnF}_3$ ".....	18
<b>L.K. Aminov, A.A. Ershova, S.L. Korableva, I.N. Kurkin, B.Z. Malkin, A.A. Rodionov,</b> "Super-Hyperfine Structure of EPR Spectra of $\text{Ce}^{3+}$ , $\text{Nd}^{3+}$ and $\text{U}^{3+}$ Ions in Double Fluorides $\text{LiRF}_4$ ( $R=\text{Y, Lu, Tm}$ )".....	20
<b>D.T. Sitdikov, G.V. Mamin, S.B. Orlinskii, N.I. Silkin, R.V. Yusupov, T.N. Yusupova,</b> "Multifrequency EPR of Asphaltenes".....	24
<b>D.D. Gabidullin,</b> "Radiofrequency synthesizer design for magnetic resonance imaging system's spectrometer".....	27
<b>N.A. Krylatykh, Ya.V. Fattakhov,</b> "Simulation of Magnetic Resonance Imaging Experiments".....	29
<b>T. Zinkevich, R. Kurbanov<sup>2</sup>, A. Krushelnitsky,</b> "General $R_1/R_{1\rho}$ equations for the NMR relaxation data analysis in solids".....	31
<b>A.Y. Manin, S.V. Efimov, V.V. Klochkov,</b> "Obtaining spatial structure of cyclosporine (Csa) in chloroform using 2D NMR".....	35
<b>V. Sahin, L. Salakhutdinov, Yu. Talanov,</b> "ESR Research of High-temperature Superconductor $\text{Bi}_2\text{Sr}_2\text{Ca}_{1-x}\text{Y}_x\text{Cu}_2\text{O}_8$ ".....	38
<b>E.I. Baibekov,</b> "Theory of electronuclear cross-relaxation in transient regime of EPR".....	42
<b>E.M. Alakshin, R.R. Gazizulin, A.T. Gubaidullin, A.V. Klochkov, S.L. Korableva, V.V. Kuzmin, A.M. Sabitova, M.S. Tagirov,</b> "Synthesis of nanosized $\text{PrF}_3$ powders and their low temperature magnetism study".....	46
<b>L.A. Batalova, I.R. Mukhamedshin, A.N. Lavrov,</b> " $^{59}\text{Co}$ ZFNMR study of $\text{YBaCo}_2\text{O}_{5+x}$ compound".....	50
<b>T.A. Platova, I.R. Mukhamedshin, A.V. Dooglav,</b> " $^{59}\text{Co}$ NQR study of $\text{Na}_{0.71}\text{CoO}_2$ compound".....	53

## TABLE OF CONTENTS

<b>N.S. Saenko, M.A. Ziatdinov</b> , “Electronic and magnetic properties of activated carbon fibers and carbon nanofibers: ESR and magnetic susceptibility data”.....	58
<b>Z.N. Volkova, S.V. Verkhovskii, A.P. Gerashenko, K.N. Mikhalev, A.Y. Yakubovskii, A. Trokiner</b> , “Magnetic polarons in $\text{CaMnO}_{3-x}$ : the $^{17}\text{O}$ NMR study”.....	62
<b>A.G. Smolnikov, V.V. Ogloblichev, A.Yu. Yakubovsky, Yu.V. Piskunov, S.V. Verkhovskii, A.P. Gerashenko, K.N. Mikhalev, K. Kumagai, S. Barilo</b> , “Local magnetic susceptibility in the multiferroic $\text{CuCrO}_2$ : $^{63,65}\text{Cu}$ NMR study”.....	65
<b>V.I. Klimentiev, N.E. Polyakov, T.V. Leshina, A.A. Stepanov, S.F. Vasilevsky</b> , “Phototransformation of acetylene derivatives of lappaconitine studied by NMR and CIDNP techniques”.....	67
<b>O.Yu. Gluschenko, N.E. Polyakov, T.V. Leshina</b> , “NMR study of cholesterol complexes with glycyrrhizic acid”.....	71
<b>A.I. Dmitriev, A.D. Talanstev, S.V. Zaitsev, R.B. Morgunov</b> , “Electron Spin Resonance in Heterostructures with a InGaAs quantum well and Mn $\delta$ -Doped GaAs Layer”.....	75
<b>A.V. Fokin, V.A. Vazhenin, V.B. Guseva, A.P. Potapov, M.Yu. Artyomov</b> , “Structural transition in lanthanum gallate and transformation of the fine structure of the EPR spectrum of a $\text{Gd}^{3+}$ impurity center”.....	79
<b>L.V. Khaidarshina, V.I. Pudov</b> , “Diagnostics of radiating ions-radicals in bioorganic materials using a method of an electronic paramagnetic resonance at Q-range. The spectra shapes”.....	84
<b>N.N. Efimov, V.V. Minin, E.A. Ugolkova, N.V. Zauzolkova, I.L. Eremenko, V.M. Novotortsev</b> , “High-frequency EPR of the polynuclear compounds of Cu(II)”..	87
<b>T.S. Yankova, N.A. Chumakova, D.A. Pomogailo, A. Kh. Vorobiev</b> , “Spin probe orientation distribution functions in aligned nematic liquid crystal”.....	90
<b>O.A. Babanova, A.V. Soloninin, A.V. Skripov, O.S. Morozova, A.V. Leonov</b> , “NMR study of ball-milled $\text{TiH}_2$ with C, B, and BN additives”.....	94
<b>V.A. Vazhenin, A.N. Ivachev, M.Yu. Artyomov, and A.P. Potapov</b> , “Paramagnetic resonance of ions $\text{Pb}^{3+}$ in ferroelectric $\text{Pb}_5\text{Ge}_3\text{O}_{11}$ ”.....	98
<b>R.A. Novikov, V.V. Kachala, V.P. Timofeev, Yu.V. Tomilov</b> , “NMR studies of mechanisms and stereochemistry of new dimerization and cascade oligomerization reactions of dimethyl 2-phenylcyclopropan-1,1-dicarboxylate catalyzed by Lewis acids”.....	102
<b>V.N. Glazkov, T. Yankova, J. Sichelschmidt, A. Zheludev</b> , “ESR study of the spin-gap magnet PHCC: magnetic resonance of the $S=1$ quasiparticles in the effective crystal field”.....	107
<b>S. Bertaina, L. Chen, N. Groll, I. Chiorescu</b> , “Multiple quantum Rabi oscillations in quasi-harmonic high spin system”.....	111
<b>E.B. Fel’dman, A.N. Pyrkov</b> , “The effect of spin-lattice relaxation on the intensities of multiple-quantum NMR coherences and entanglement in solids”.....	114
<b>P.A. Agzamova, A.E. Nikiforov<sup>2</sup>, Yu.V. Leskova</b> , “Hyperfine interactions in $(\text{La}, \text{Y})\text{TiO}_3$ system”.....	118

## TABLE OF CONTENTS

<b>A.A. Konakov, V.A. Burdov, A.A. Ezhevskii, A.V. Soukhorukov, D.V. Guseinov, S.A. Popkov, “Temperature dependence of the conduction electron g-factor in silicon”</b> .....	121
<b>K. Tadyszak, M. Augustyniak-Jabłokow, M. Maćkowiak, “EPR study of spin relaxation in the single-layer graphene”</b> .....	125
<b>V.V. Ogloblichev, A.G. Smolnikov, S.V. Verkhovskii, Yu.V. Piskunov, A.P. Gerashenko, K.N. Mikhalev, A.Yu. Yakubovsky, K. Kumagai, S. Barilo, “<sup>51</sup>V NMR Study of the Multiferroic Ni<sub>3</sub>V<sub>2</sub>O<sub>8</sub>”</b> .....	129
<b>Ya.V. Tkachev, R.V. Agafonov, Yu.E. Nesmelov, “EPR Meets MD: Dynamics of Myosin Motor Domain”</b> .....	132

# **ACTUAL PROBLEMS OF MAGNETIC RESONANCE AND ITS APPLICATION**

**XIV International Youth Scientific School**

## **Program Proceedings**

Подписано в печать 10.06.11.  
Бумага офсетная. Печать ризографическая.  
Формат 60x84 1/8. Гарнитура «Times New Roman». Печ. л. 8,62  
Тираж 95 экз. Заказ 32/6

Отпечатано с готового оригинал-макета  
в типографии Издательства Казанского университета

420008, г. Казань, ул. Профессора Нужи́на, 1/37  
тел. (843) 233-73-59, 292-65-60